

6. SITE 735¹

Shipboard Scientific Party²

HOLE 735A

Date occupied: 14 November 1987
Date departed: 15 November 1987
Time on hole: 30 hr 15 min
Position: 32°43.315'S, 57°15.864'E
Bottom felt (rig floor, m; drill pipe measurement): 738.0
Distance between rig floor and sea level (m): 11.1
Water depth (drill pipe measurement from sea level, m): 726.9
Total depth (rig floor, m): 745.0
Penetration (m): 7.0
Number of cores (including cores with no recovery): 1
Total length of cored section (m): 7.0
Total core recovered (m): 0.10
Core recovery (%): 1.4
Basement:
Depth (mbsf): 0
Nature: metagabbro

HOLE 735B

Date occupied: 15 November 1987
Date departed: 11 December 1987
Time on hole: 25 days 22 hr 45 min
Position: 32°43.395'S, 57°15.959'E
Bottom felt (rig floor, m; drill pipe measurement): 731.0
Distance between rig floor and sea level (m): 11.1
Water depth (drill pipe measurement from sea level, m): 719.9
Total depth (rig floor, m): 1231.7
Penetration (m): 500.7
Number of cores (including cores with no recovery): 88
Total length of cored section (m): 500.7
Total core recovered (m): 434.81
Core recovery (%): 86.8
Basement:
Depth (mbsf): 0
Nature: gabbro, metagabbro, mylonite, troctolite, trondhjemite
Measured velocity (km/s): 7.1

HOLE 735C

Date occupied: 4 December 1987
Date departed: 5 December 1987

Time on hole: 5 hr 15 min
Position: 32°43.40'S, 57°15.45'E
Bottom felt (rig floor, m; drill pipe measurement): 753.9
Distance between rig floor and sea level (m): 11.1
Water depth (drill pipe measurement from sea level, m): 742.8
Total depth (rig floor, m): 753.9
Penetration (m): 0
Number of cores (including cores with no recovery): 0
Total length of cored section (m): 0
Total core recovered (m): 0
Core recovery (%): 0

Principal results: Site 735 is located on a shallow platform in about 700 m of water on the east rim of the Atlantis II Transform. This platform, about 9 km long in a north-south direction and 4 km wide, is one of a series of uplifted blocks that are connected by saddles to form a long, linear ridge parallel to the Atlantis II Transform.

The platform at Site 735 has a flat surface, which suggests that it is a wave-cut feature. Its position in the magnetic anomaly pattern on the east transform wall suggests a crustal age of about 12 Ma. A television/sonar survey of the seafloor revealed basement outcrops locally mantled with thin sediment. Many of the outcrops have a well-developed, steeply dipping foliation and are cut by a regular pattern of faults or joints.

From an unsupported test spud-in and using the coring motor, we recovered 0.1 m of gabbro from Hole 735A. We then deployed the hard-rock guidebase, and drilling commenced in Hole 735B. The coring motor was used to start the hole and to drill to a depth of 60 meters below seafloor (mbsf). A standard rotary coring system then was used to drill to 500 mbsf. The newly developed navidrill was used to cut an additional 0.7 m. The entire 500.7-m-deep hole was drilled in 17 days, resulting in an average rate of penetration of 30 m/day.

A total of 435 m of olivine gabbro, olivine-bearing gabbro, two-pyroxene gabbro, iron-titanium oxide gabbro, troctolite, and micro-gabbro with rare basalt and trondhjemite was recovered from Hole 735B for an average recovery of 87%. These rocks have undergone varying degrees of plastic and brittle deformation, and many have well-developed foliations. Six major lithologic units were recognized in the sequence, based primarily on igneous mineralogy, mineral compositions, and degree and style of deformation.

Lithologic Unit I is a 39.5-m-thick sequence of foliated metagabbro having porphyroclastic to mylonitic textures. Rock types include poorly foliated metagabbro, porphyroclastic metagabbro, mylonite, gneissic metagabbro, and augen gneissic metagabbro. Igneous textures have been completely destroyed, and the rocks now consist chiefly of neoblasts of plagioclase, clinopyroxene, and amphibole. The protolith was probably a two-pyroxene gabbro or olivine gabbro. There are a few iron-titanium oxide-rich layers.

Lithologic Unit II consists of 140.5 m of olivine and olivine-bearing gabbro. The upper contact is drawn at the first appearance of clearly igneous textures, and the lower boundary is a rapid transition to gabbro with more orthopyroxene and more sodic plagioclase. Most of the rocks are mesocumulates. Alternating bands of olivine-rich and olivine-poor gabbro reflect rare modal layering. Chemically, these gabbros are fairly primitive. Interlayered iron-titanium oxide-bearing gabbros are present, as are a few pyroxene-rich layers. Some mylonitic and porphyroclastic intervals are present, particularly in the upper part of the unit.

¹ Robinson, P. T., Von Herzen, R. P., et al., 1989. *Proc. ODP, Init. Repts.*, 118: College Station, TX (Ocean Drilling Program).

² Shipboard Scientific Party is as given in List of Participants preceding the contents.

Lithologic Unit III is a 44-m-thick sequence of olivine gabbro with intervals of iron-titanium oxide gabbro. These gabbros are macroscopically similar to those of Unit II but have significantly more evolved compositions. The upper contact is gradational and is defined mineralogically, but also coincides with a change in chemical composition. A well-developed igneous lamination is steeply dipping in the upper part of the unit but flattens with depth. Mylonitic and foliated zones are common, and the lower contact of Unit III is marked by a 60-cm-thick zone of mylonite.

Lithologic Unit IV is made up of 48 m of iron-titanium oxide-rich gabbro. The upper contact grades into Unit III, and the lower boundary is marked by a 3-m-thick layer of mylonite. These gabbros have more abundant opaque minerals (10% or more) and less olivine than those of Unit III; Fe_2O_3 contents can be as high as 30 wt%, and TiO_2 contents can be as high as 9 wt%. A felsic intrusion breccia having trondjemite veins occurs at two levels in the unit.

Lithologic Unit V consists of 131.5 m of relatively uniform olivine gabbro characterized by a scarcity of iron-titanium oxides and low-calcium pyroxene. Most of the gabbros are mesocumulates, and some exhibit primary grain-size layering. They are mineralogically and chemically similar to those of Unit II. Thin troctolite layers and several plagioclase-rich zones are evident. Zones of brecciation are common and contain felsic veins with epidote and albite.

Lithologic Unit VI is a 97.2-m-thick interval of olivine-rich gabbro having frequent layers of troctolite. The gabbros are similar to those of Unit V but are more olivine-rich. The troctolite and troctolitic gabbros are interlayered with the olivine gabbros, and these were interpreted as intrusive layers. These gabbros are the most mafic rocks encountered in Hole 735B. A few coarse-grained iron-titanium oxide gabbros also are present. Unit VI also has frequent intervals of metagabbro characterized by mylonitic to porphyroclastic textures.

Veins and fractures generally dip 40° to 90° , with a strong peak at 60° to 65° . The mean dip of both veins and foliation decreases downward in the hole, suggesting that deformation took place along listric normal faults that flatten downward.

The rocks from Hole 735B were subjected to varying degrees of metamorphism and alteration. An early stage of dynamothermal metamorphism produced highly foliated porphyroclastic, gneissic, and mylonitic textures. This high-temperature event was followed by brecciation and static alteration associated with brittle deformation. The static alteration was controlled by permeability and is manifested by numerous veins, from 0.5 mm to 2 cm wide, filled largely with hornblende and sodic plagioclase. Clinzoisite, epidote, and minor prehnite occur in the lower parts of the core. A few silicic veins containing diopside, hornblende, sphene, clinzoisite, and albite are also present. In undeformed gabbros, static alteration resulted in development of coronas of hornblende, tremolite, talc, clinzoisite, magnetite, chlorite, sphene, epidote, and phlogopite(?) around the primary igneous minerals. A late stage of oxidative alteration is reflected in carbonate-hematite-smectite pseudomorphs of olivine and orthopyroxene.

Paleomagnetic intensities vary and are generally in the range of other oceanic gabbros, but up to $>2.5 \text{ emu/cm}^3$ in some of the iron-titanium oxide gabbros. Magnetic susceptibilities average about 100×10^{-6} cgs. Again, the highest values are in the iron-titanium oxide gabbros. Natural remanent inclinations are all steep, about equally divided between normal and reverse. Stable inclinations are reversed and average $65^\circ \pm 15^\circ$.

Compressional-wave seismic velocities in the gabbros range from 6.5 to 7.0 km/s. Physical-properties measurements show seismic anisotropy of up to 10%, particularly in some of the foliated rocks. The multichannel seismic experiment indicated that *in-situ* seismic velocity increases somewhat (5%–10%) with depth over the hole. Grain (matrix) densities obtained from logs average about 2.9 g/cm^3 over the hole.

The laterolog showed variations of electrical resistivity of four orders of magnitude downhole (~ 4 to 40,000 ohm-m). The most prominent low-resistivity zone occurs throughout Unit IV and probably results from the effect of the high mineral conductivity of the iron-titanium oxides. Smaller-scale variations (a few meters) in the units below may reflect the same conductivity mechanisms.

The borehole televiwer showed that most of the hole wall is relatively smooth, with occasional linear and sinusoidal features that probably indicate small fractures cutting the borehole.

Four magnetometer sondes were run in the hole: the Schlumberger three-component tool used primarily for hole inclination and orientation, a U.S. Geological Survey (USGS) three-component magnetometer, a USGS susceptibility tool, and a University of Washington/Lamont-Doherty Geological Observatory (UW/LDGO) combined three-component magnetometer and susceptibility tool. The magnetometers showed large and similar variations in the fields measured in the hole, especially in the iron-titanium oxide-rich zone, where the fields are as much as 50% greater and more variable. Susceptibility is also more variable in this zone.

A borehole packer experiment indicated low fluid permeability below about 272 mbsf, with higher values (by several orders of magnitude) above this level. The temperature log showed a very low, or even negative, gradient in the hole, which further suggests the effects of seawater advection, even with low porosity.

More comprehensive studies of the rock samples recovered and the data obtained should better define the origin, tectonics, and physical state of this unique section of material, which we believe represents the lower oceanic crust.

BACKGROUND AND SCIENTIFIC OBJECTIVES

By 13 November 1987, we had spent three weeks searching without success for a location in which to deploy the hard-rock guidebase for drilling a deep hole in peridotite. Attempts to drill at Sites 732, 733, and 734 (Fig. 1) had been frustrated by accumulations of rubble and sediment or by slopes too steep for the hard-rock guidebase. Three remaining backup sites, discussed in the scientific prospectus, included (1) the sediment-filled basins on the floor of the transform, (2) the active nodal basin, and (3) a sediment-filled basin in the northern part of the transform. The sediment-filled basins in the active transform were eliminated from consideration because we thought they might be underlain by the same type of gravel deposits that could not be drilled at Site 732.

We considered the active nodal basin to be of high scientific interest but did not select it because it is a bare-rock site in deep water (5500 m) and thus could not be sampled adequately in the time remaining for Leg 118. Furthermore, our experience in the transform until then suggested that there might be coarse talus deposits in the nodal basin that would be difficult or impossible to drill. We seriously considered the sediment-filled basin, but because we still wished to deploy the guidebase to drill a reentry hole for sampling and logging, we moved to a shoal bench on the east wall of the transform, where the topography indicated many flat surfaces suitable for guidebase deployment. In other transform faults, such shoal features are commonly underlain by mantle peridotite. Because of the short time remaining for the leg, a shallow-water site seemed to have several operational advantages.

After obtaining permission to drill this site, we deployed a beacon and conducted a short television/sonar survey. The survey revealed numerous relatively flat outcrops of foliated igneous rock, separated by small sediment ponds. A test spud-in at Hole 735A recovered a small amount of gabbro. Consequently, we deployed the hard-rock guidebase in preparation for drilling a deep reentry hole.

The principal objectives at Site 735 were (1) to sample a section of basement rock on the wall of the transform, (2) to conduct an array of downhole measurements, and (3) to test the engineering of the hard-rock guidebase and bare-rock drilling capabilities of *JOIDES Resolution*.

GEOLOGIC AND TECTONIC SETTING

Site 735 is located on a shallow platform on the east wall of the Atlantis II Fracture Zone (Fig. 1). This site lies near the center of a remarkably flat area, about 9 km long and 4 km wide, that is elongated in a north-south direction. The top of this feature lies at a water depth of just over 700 m, making it the shal-

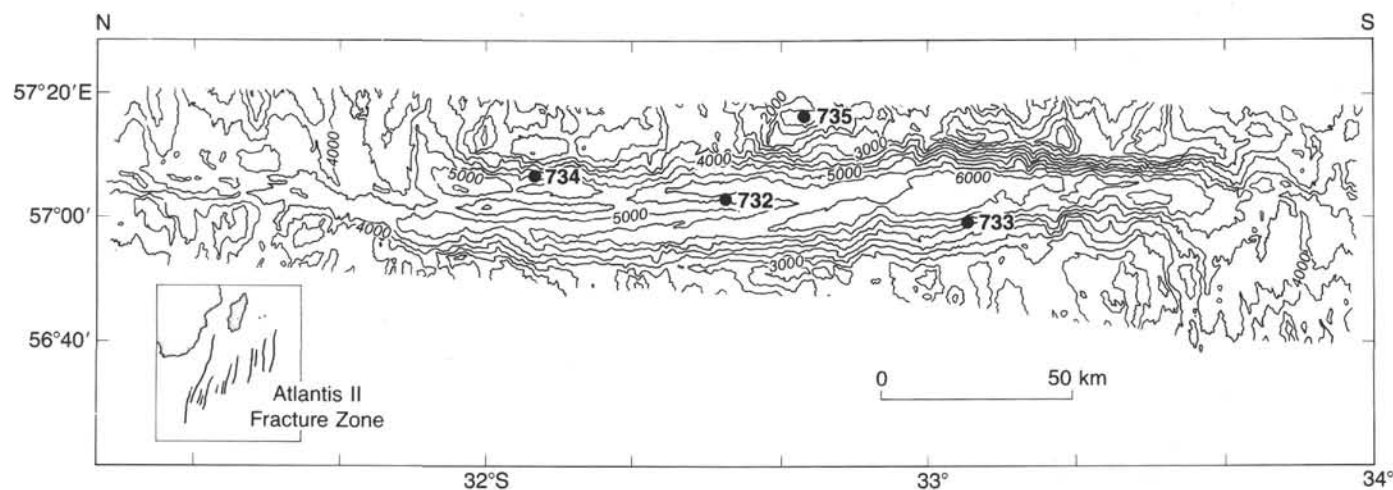


Figure 1. Bathymetric map at 500-m contour intervals of the Atlantis II Fracture Zone, Southwest Indian Ridge, showing Leg 118 drill sites. Survey from *Conrad* cruise 27-09, 1986 (H. Dick, Chief Scientist, with D. Gallo and R. Tyce).

lowest feature associated with the fracture zone. The extremely flat surface of this platform suggests that it is a wave-cut feature that has subsided since formation to its present position. The magnetic anomaly pattern on the east wall of the transform suggests a crustal age of about 12 Ma for this site.

A television/sonar survey of the seafloor in the vicinity of Site 735, conducted from the *JOIDES Resolution*, revealed basement outcrops locally mantled with thin layers of sediment. Many of these outcrops have a well-developed, steeply dipping foliation and are cut by a regular pattern of faults or joints. Subsequent drilling revealed that the exposed basement consists of highly deformed gabbro.

Current models for ridge crest dynamics (e.g., Schouten and Klitgord, 1982) call for a series of ridge segments, each of which is underlain by an axial magma chamber. We believe the fracture zones are relatively cold zones that receive magma largely by lateral injection along the spreading ridge. In this model the far edges of spreading cells (i.e., fracture zones) will have considerably thinner crust sections than the central parts because they will receive less magma. Because of the thin crustal sections and extensive vertical tectonics associated with fracture zones, lower crustal and mantle rock are commonly exposed on the walls of these features.

Site 735 is located on the shoalest of a series of uplifted blocks that are connected by saddles that make up a long, linear ridge parallel to the transform. The entire ridge is elevated from 2 to nearly 6 km relative to the floor of the adjacent transform and from 1 to 4 km relative to the ridge-generated crust lying to the east. The topographic relief along this "transverse ridge" varies considerably, particularly between uplifted blocks, which may be as much as 2 or 3 km higher than the intervening saddles. The uplifted blocks are highly irregular in shape, defined by steep slopes commonly associated with major normal faulting in such terrains, and may represent simple horsts uplifted relative to both the rift valley floor at which the crust originated and the adjacent ocean crust to the east.

Such anomalous topographic features are common features of fracture zones, which in many cases are underlain by upper mantle and lower crustal rocks (Bonatti, 1978; Engel and Fisher, 1975; van Andel et al., 1971). For example, St. Peter and Paul rocks, located on the St. Paul Fracture Zone have a tectonic setting analogous to that at Site 735 and are underlain by similar lithologies. An uplifted block in the Owen Fracture Zone, near its intersection with the Mid-Indian Ridge, exposes mantle lherzolites, harzburgites, and dunites (Bonatti and Hamlyn, 1978).

Many other large fracture zones have similar topographic highs (transverse ridges) underlain by lower crustal and mantle rocks (Bonatti, 1978).

Little is known regarding the processes by which these anomalous topographic features are formed. Uplift of such blocks has been attributed to a combination of thermal conduction across fracture zones from ridge-transform intersections, to compressional and tensional stresses associated with transform faulting, to reduction of the lithospheric head resulting from the thinner crustal sections in transforms, and to serpentinite diapirism. Any or all of these may be contributing factors.

OPERATIONS

Introduction

This site was selected for drilling on the basis of our somewhat meager understanding of the geology and tectonics of other oceanic transform faults, and because of the time and operational constraints that remained for Leg 118. The site is the shallowest region in the vicinity of the Atlantis II Transform, a relatively flat platform at a water depth of about 700 m on the highest part of the eastern wall (Fig. 1). The platform is about 9 km long in the north-south direction and 4 km wide. Its unusual flatness (< 100 m) at minimum depth suggests that it has been wave-cut at sea level and subsequently subsided.

By analogy with other transform faults having high walls, we believed that this site offered a good possibility for drilling ultrabasic or abyssal rock that had been emplaced to high levels. The shallow depth also made operational constraints less demanding, especially because less than four weeks of the leg remained at the time we considered this site to achieve one of our primary objectives of drilling and coring a deep basement hole. The shallow depth meant that deployment of the hard-rock guidebase and round trips of the drill string to change bits, etc., would take much less time. Although the site was not in the original prospectus for the leg, it was approved on the basis of these scientific objectives and logistical constraints.

Approach to Site 735

The site location required a transit of 8.5 hr from Site 734. (All times are local unless stated otherwise.) As usual, we planned to use the seismic-reflection profiling system for both reliable depth soundings and for detection of possible sub-bottom reflectors. This equipment was deployed about 3 km before reaching the first turning point of the beacon location survey (Fig. 2),

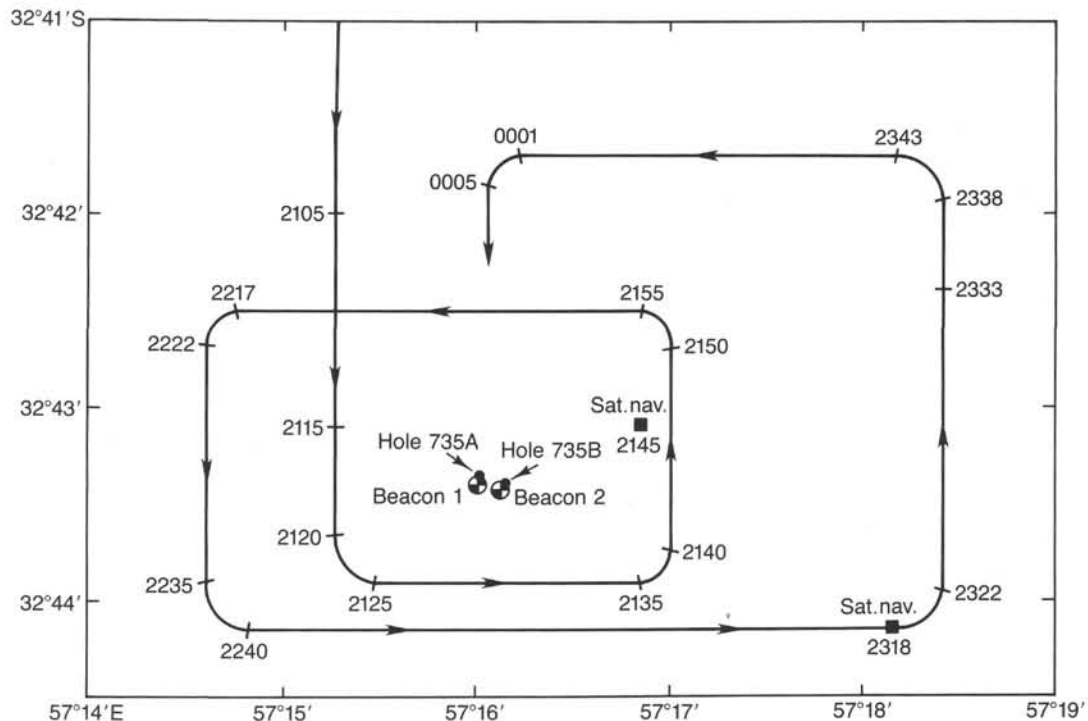


Figure 2. Track line followed until beacon deployment during approach to Site 735. Times along track line are local (UTC + 4 hr) for 13 and 14 November 1987. Navigation was controlled by transit satellite fixes. Beacon and hole locations are indicated. Track line after 0005 hr, 14 November, varied before beacon deployment.

and the ship was slowed to 5–6 kt. Unfortunately, global positioning system (GPS) navigation was not available during this survey, and we had to rely on occasional transit satellite fixes and dead reckoning. Hence, the survey was planned to include several transverse crossings of the shallow platform to confirm its location and geometry, especially since Sea Beam coverage of this feature during the site-survey cruise for this leg was incomplete (H. Dick, pers. comm., 1987).

We crossed the platform at three different locations during the pre-beacon survey. This platform has a relatively flat surface with some occasional irregularities <20 m high (Fig. 3). We planned to stop over the platform after the last crossing, retrieve the seismic profiling gear, and lower the television/sonar to determine the nature of the bottom before deploying the beacon. Unfortunately, the ship drifted off the platform into deeper water during retrieval of the seismic gear and before television/sonar deployment, and we had to wait for 1 hr for another satellite position fix to find our way back to the platform. We then deployed a recallable beacon at 32°43.4'S, 57°15.9'E, over slightly irregular bottom topography for a reference position for the television/sonar survey.

As part of the departure from the site, another brief survey was conducted after logging Hole 735B to determine the exact location of the drill site relative to the east and west slopes of the platform. Again, GPS was not available, but we were able to use the beacon left behind as a relatively accurate reference point for dead reckoning. The site is located approximately 500 m east of the upper slope of the west wall.

Television/Sonar Surveys

After deploying the beacon, a simple box survey, 200 m on a side, was conducted around it to determine the nature of the bottom. The survey revealed irregular outcrops of dark, sometimes foliated rock separated by apparently thin patches of light-col-

ored sediment (Fig. 4). The outcrops of rock protruded only slightly (< few meters) above the level of the sediment patches, and depths varied smoothly over a range of about 30 m along the survey track, deeper to the southwest. This survey took about 4 hr (between 2300 hr UTC, 13 November, and 0300 hr, 14 November 1987), and was relatively straightforward in that the camera remained closely under the ship in the shallow water and moved at relatively slow survey speeds.

Hole 735A (32°43.3'S, 57°15.9'E)

A test spud-in was performed 100 m north and 30 m east of the beacon (Fig. 4) using the positive displacement coring motor (PDCM). The bottom was stable and very hard, with 7 m cored in 11.6 hr before the bit stopped advancing (Table 1). The core barrel could not be pulled with the wireline, so the pipe was tripped to the surface. The pin of the bit sub had failed leaving the bit in the hole. A total of 0.1 m of gabbro was recovered.

Shipboard engineering and operations personnel advised that this site was stable and could be drilled but warned that the coring rate probably would be only one or two cores per day. We decided to deploy the hard-rock guidebase and to drill as deeply as possible in the time remaining.

Hole 735B (32°43.395'S, 57°15.959'E)

Assembly of the hard-rock guidebase began at 1300 hr on 15 November and was completed 42 hr later on 17 November; the entire operation proceeded almost flawlessly. We had to deploy a second acoustic beacon late on 15 November, when the first beacon began to fail. This second beacon landed 230 m away in a southeast direction (Fig. 4), which necessitated moving the ship. Consequently, another brief television/sonar survey was run to confirm the nature of the bottom. The guidebase was landed 50 m north and 50 m east of the second beacon (Fig. 4), about 500 m from the break of slope of the transform valley wall.

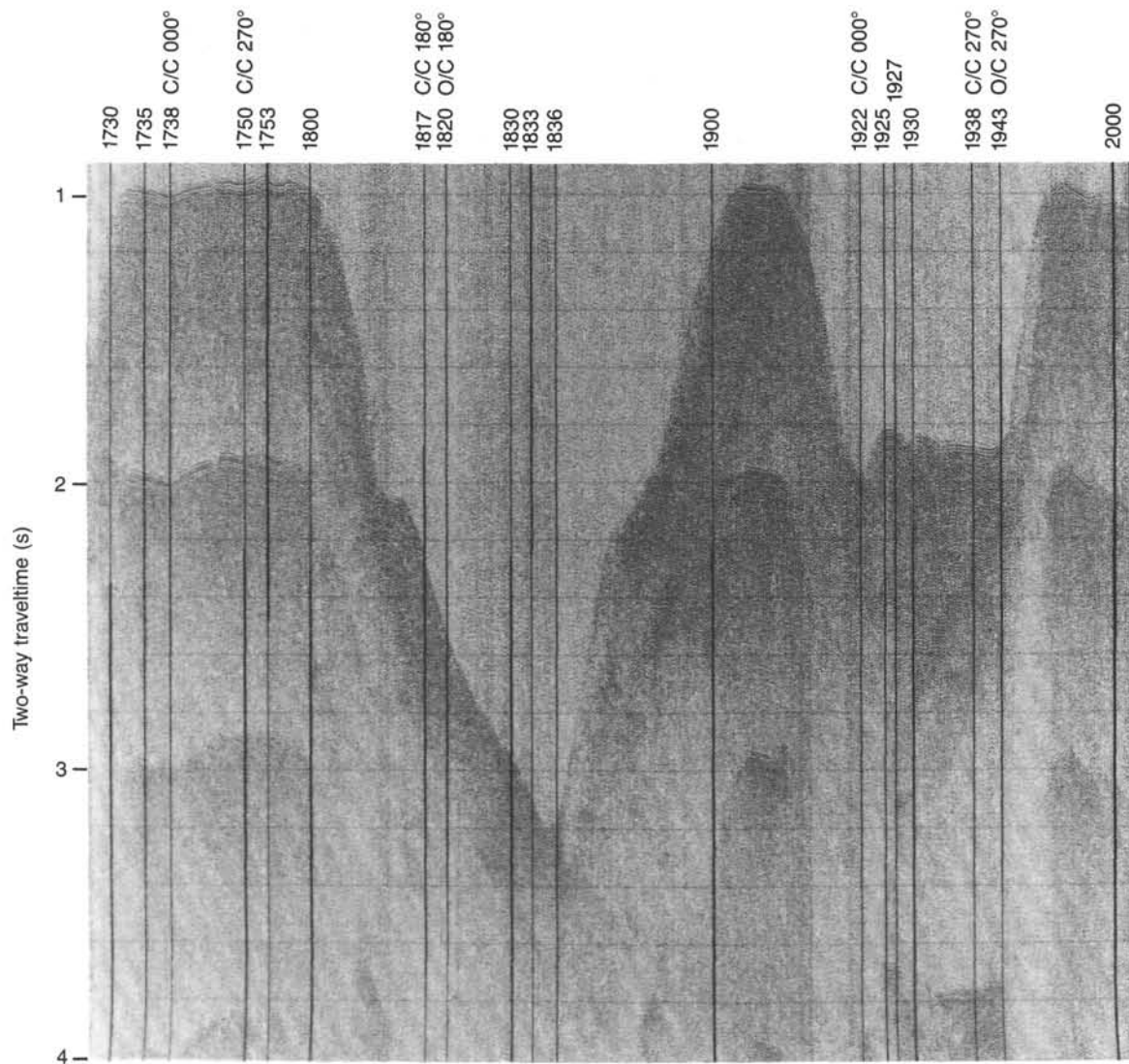


Figure 3. Recording from seismic-reflection profiling system during pre-beacon deployment survey at Site 735 (Fig. 2). Source is a water gun, with recording filtered between 80–250 Hz. Recording window after “shot” is 0 to 4 s. Times printed on recording are UTC, 13 November 1987. c/c = change course.

Table 1 summarizes the drilling and coring operations for Hole 735B. The PDCM was used for the initial unsupported spud-in. As expected, the coring rate was low. Bit 1 advanced the hole 6.5 m (0–6.5 mbsf) in 13 hr. A total of 2.3 m of foliated metagabbro was recovered. The recovery rate for the bit was 35.4%. Once the guidebase had been deployed, we could no longer consider the hole expendable, and consequently, we decided to be prudent and conservative in the number of hours each bit was run. Thus, the first bit was pulled after the first core.

Bit 2 advanced the hole by 14.5 m (6.5–21.0 mbsf) in 14.8 hr. A total of 6.25 m of foliated metagabbro was recovered. The average recovery rate for the bit was 43.1%. When the bit was returned to the surface, we found it was not seriously worn.

Bit 3 was a hybrid bit; the core guide between the cones was composed of geoset diamonds. These guides are designed to trim the core and guide it into the grasp of the core catcher. The bit advanced 18.2 m (21.0–39.2 mbsf) in 14.0 hr. A total of 5.56 m of foliated and massive gabbro was recovered. When the bit was tripped to the surface, we found the cones were in good condition, but the diamonds were severely worn and chipped. The average recovery rate for the bit was 30.5%.

Bit 4 was a Christensen impregnated diamond bit of a design commonly used in the mining industry. However, one this size had never been used for hard-rock drilling. The bit was run for 2.25 hr and advanced the hole 0.2 m (39.2–39.4 mbsf). It was then returned to the surface after a period when no penetration was evident at the rig floor. A total of 0.08 m of gabbro was recovered in the core catcher. The bit was badly worn, and it was clear that this particular design was no match for hard and abrasive gabbro. The recovery rate for this bit was 40.0%.

The diamond bit run terminated at 39.4 mbsf. We believed that this depth of hole was sufficient to justify the running of a rotary-driven bottom-hole assembly (BHA).

The first rotary-driven 9.875 in. bit (bit 5, a Rock Bit Industries type C-7) was run with only 15,000 lb of weight to reduce BHA flexure. Despite its light weight, this bit advanced 16.8 m (39.4–56.2 mbsf) in 19 hr. A total of 13.31 m of foliated and massive gabbro was recovered. The average recovery rate for the bit was 79.2%, a significant increase over the 36.02% average recovery rate of the motor-driven system.

Bit 6 advanced the hole by 12.3 m (56.2–68.5 mbsf). A total of 8.43 m of foliated and massive gabbro was recovered. The average recovery rate for the bit was 68.5%.

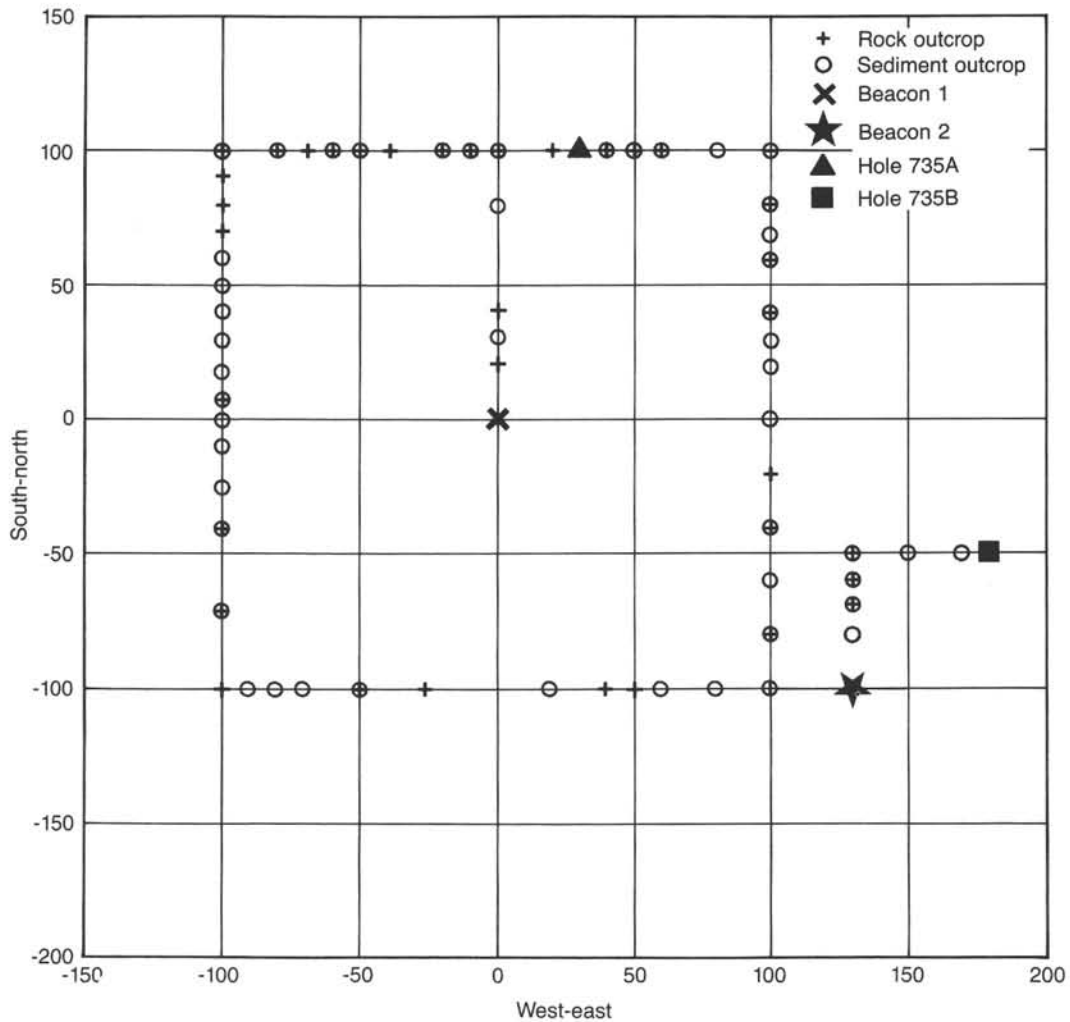


Figure 4. Local survey with television/sonar system at Site 735. Small symbols indicate occurrences of bottom types as recorded on log made during survey. Axes are in meters distance from Beacon 1. Drill-hole locations are as shown.

Table 1. Drilling and coring summary at Site 735.

Core	Date (Nov./Dec. 1987)	Time (local)	Total depth (mbrf)	Depth (mbsf)	Length advanced (m)	Length cored (m)	Length recovered (m)	Recovery (%)
118-735A-1D	15	0900	738.0-745.0	0-7.0	7.0	7.0	0.10	1.4
118-735B-1D	18	0615	731.0-737.5	0-6.5	6.5	6.5	2.30	35.4
2D	18	2000	737.5-745.5	6.5-14.5	8.0	8.0	3.00	37.5
3D	18	2315	745.5-748.5	14.5-17.5	3.0	3.0	1.50	50.0
4D	19	0550	748.5-752.0	17.5-21.0	3.5	3.5	1.75	50.0
5D	19	1200	752.0-755.0	21.0-24.0	3.0	3.0	0.28	9.3
6D	19	1600	755.0-757.0	24.0-26.0	2.0	2.0	0.94	47.0
7D	19	2010	757.0-760.2	26.0-29.2	3.2	3.2	1.30	40.6
8D	19	2330	760.2-764.2	29.2-33.2	4.0	4.0	0.75	18.6
9D	20	0300	764.2-767.2	33.2-36.2	3.0	3.0	1.02	34.0
10D	20	0730	767.2-770.2	36.2-39.2	3.0	3.0	1.27	42.0
11D	20	2100	770.2-770.4	39.2-39.4	0.2	0.2	0.08	40.0
12R	21	0845	770.4-775.5	39.4-44.5	5.1	5.1	4.01	78.6
13R	21	1715	775.5-782.2	44.5-51.2	6.7	6.7	4.22	63.0
14R	22	0200	782.2-787.2	51.2-56.2	5.0	5.0	5.08	101.6
15R	22	1335	787.2-792.8	56.2-61.8	5.6	5.6	2.81	50.2
16R	22	2115	792.8-798.0	61.8-67.0	5.2	5.2	5.26	101.2
17R	23	0200	798.0-799.5	67.0-68.5	1.5	1.5	0.36	24.0
18R	23	1220	779.5-805.7	68.5-74.7	6.2	6.2	3.40	54.8
19R	23	1910	805.7-815.2	74.7-84.2	9.5	9.5	5.58	58.7
20R	23	2330	815.2-820.2	84.2-89.2	5.0	5.0	3.00	60.0
21R	24	0615	820.2-825.0	89.2-94.0	4.8	4.8	2.86	57.2
22R	24	1400	825.0-831.5	94.0-100.5	6.5	6.5	4.76	73.2
23R	24	1815	831.5-836.5	100.5-105.5	5.0	5.0	5.00	100.0

Table 1 (continued).

Core	Date (Nov./Dec. 1987)	Time (local)	Total depth (mbrf)	Depth (mbsf)	Length advanced (m)	Length cored (m)	Length recovered (m)	Recovery (%)
118-735B-24R	24	2230	836.5-841.5	105.5-110.5	5.0	5.0	4.47	89.4
(Cont.) 25R	25	0130	841.5-846.5	110.5-115.5	5.0	5.0	3.69	73.8
26R	25	0650	846.5-852.5	115.5-121.5	6.0	6.0	5.74	95.7
27R	25	1115	852.5-857.5	121.5-126.5	5.0	5.0	4.71	94.2
28R	25	1545	857.5-862.5	126.5-131.5	5.0	5.0	5.03	100.6
29R	26	0300	862.5-867.5	131.5-136.5	5.0	5.0	4.16	83.2
30R	26	0645	867.5-874.5	136.5-143.5	7.0	7.0	5.80	82.8
31R	26	1000	874.5-879.5	143.5-148.5	5.0	5.0	5.16	103.2
32R	26	1230	879.5-884.5	148.5-153.5	5.0	5.0	4.65	93.0
33R	26	1715	884.5-889.5	153.5-158.5	5.0	5.0	5.00	100.0
34R	26	2015	889.5-894.5	158.5-163.5	5.0	5.0	3.96	79.2
35R	27	0525	894.5-902.0	163.5-171.0	7.5	7.5	7.97	106.3
36R	27	1220	902.0-907.0	171.0-176.0	5.0	5.0	4.78	95.6
37R	27	1420	907.0-912.0	176.0-181.0	5.0	5.0	3.88	77.6
38R	27	1745	912.0-917.0	181.0-186.0	5.0	5.0	5.78	105.6
39R	27	1945	917.0-922.0	186.0-191.0	5.0	5.0	4.24	84.8
40R	27	2215	922.0-927.0	191.0-196.0	5.0	5.0	4.92	98.4
41R	28	0030	927.0-932.0	196.0-201.0	5.0	5.0	4.18	83.6
42R	28	0300	932.0-937.0	201.0-206.0	5.0	5.0	5.10	102.0
43R	28	0515	937.0-942.0	206.0-211.0	5.0	5.0	4.68	93.6
44R	28	0745	942.0-947.0	211.0-216.0	5.0	5.0	4.93	98.6
45R	28	1000	947.0-952.0	216.0-221.0	5.0	5.0	5.19	103.8
46R	28	1245	952.0-957.0	221.0-226.0	5.0	5.0	5.15	103.0
47R	28	1500	957.0-962.0	226.0-231.0	5.0	5.0	4.87	97.4
48R	28	1745	962.0-967.0	231.0-236.0	5.0	5.0	4.76	95.2
49R	28	1930	967.0-969.0	236.0-238.0	2.0	2.0	2.52	126.0
50R	29	0510	969.0-974.0	238.0-243.0	5.0	5.0	5.28	105.6
51R	29	0715	974.0-979.0	243.0-248.0	5.0	5.0	4.46	89.2
52R	29	0950	979.0-984.0	248.0-253.0	5.0	5.0	4.89	97.8
53R	29	1405	984.0-989.0	253.0-258.0	5.0	5.0	5.23	104.6
54R	29	1840	989.0-996.0	258.0-265.0	7.0	7.0	6.98	99.7
55R	29	2210	996.0-1001.0	265.0-270.0	5.0	5.0	4.67	93.4
56R	30	0150	1001.0-1006.0	270.0-275.0	5.0	5.0	4.19	83.8
57R	30	0415	1006.0-1011.5	275.0-280.5	5.5	5.5	5.10	93.0
58R	30	0710	1011.5-1016.5	280.5-285.5	5.0	5.0	3.74	74.8
59R	30	0910	1016.5-1021.5	285.5-290.5	5.0	5.0	4.90	98.0
60R	30	1115	1021.5-1026.5	290.5-295.5	5.0	5.0	5.20	104.0
61R	30	1400	1026.5-1031.5	295.5-300.5	5.0	5.0	5.15	103.0
62R	30	1630	1031.5-1036.5	300.5-305.5	5.0	5.0	5.08	101.6
63R	01	0300	1036.5-1046.0	305.5-315.0	9.5	9.5	8.84	93.1
64R	01	0445	1046.0-1051.0	315.0-320.0	5.0	5.0	5.24	104.8
65R	01	0630	1051.0-1056.0	320.0-325.0	5.0	5.0	3.37	74.6
66R	01	0800	1056.0-1061.0	325.0-330.0	5.0	5.0	3.95	79.0
67R	01	0930	1061.0-1066.0	330.0-335.0	5.0	5.0	4.67	93.4
68R	01	1130	1066.0-1072.0	335.0-341.0	5.0	5.0	3.00	50.0
69R	01	1320	1072.0-1077.0	341.0-346.0	5.0	5.0	5.55	111.0
70R	01	1440	1077.0-1082.0	346.0-351.0	5.0	5.0	4.76	95.2
71R	01	1625	1082.0-1087.0	351.0-356.0	5.0	5.0	5.07	101.4
72R	01	1930	1087.0-1096.5	356.0-365.5	9.5	9.5	9.20	96.8
73R	01	2200	1096.5-1106.0	365.5-375.0	9.5	9.5	9.00	94.7
74R	02	0030	1106.0-1115.5	375.0-384.5	9.5	9.5	9.78	102.9
75R	02	0400	1115.5-1125.0	384.5-394.0	9.5	9.5	9.81	103.2
76R	02	0700	1125.0-1134.5	394.0-403.5	9.5	9.5	8.62	90.8
77R	02	1045	1134.5-1140.5	403.5-409.5	6.0	6.0	5.84	97.3
78R	02	1345	1140.5-1145.5	409.5-414.5	5.0	5.0	5.30	106.0
79R	03	0200	1145.5-1155.0	414.5-424.0	9.5	9.5	9.34	98.3
80R	03	0615	1155.0-1164.5	424.0-433.5	9.5	9.5	9.70	102.1
81R	03	0940	1164.5-1174.0	433.5-443.0	9.5	9.5	8.70	91.6
82R	03	1230	1174.0-1183.5	443.0-452.5	9.5	9.5	8.57	90.2
83R	03	1610	1183.5-1193.0	452.5-462.0	9.5	9.5	9.90	104.2
84R	03	1920	1193.0-1202.5	462.0-471.5	9.5	9.5	8.87	93.4
85R	03	2320	1202.5-1212.0	471.5-481.0	9.5	9.5	9.57	100.7
86R	04	0215	1212.0-1221.5	481.0-490.5	9.5	9.5	8.76	92.2
87R	04	0505	1221.5-1231.0	490.5-500.0	9.5	9.5	8.12	85.5
88N	04	1925	1231.0-1231.7	500.0-500.7	0.7	0.7	0.70	100.0
^a 735C-1N	04		753.9-753.9	0-0	0	0	0	0

^a Unable to drill, navidrill core barrel bent.

Bit 7 advanced the hole 25.5 m (68.5-94.0 mbsf) in 18.5 hr. A total of 14.84 m of foliated and massive gabbro was recovered. A noticeable increase in the rate of penetration and recovery became evident. The average recovery rate for this bit was 58.2%.

Bit 8 advanced the hole 37.5 m (94.0-131.5 mbsf) in 24.67 hr. A total of 33.4 m of foliated and massive gabbro was recovered. The average recovery rate for the bit was 89.1%.

Bit 9 advanced the hole 39.5 m (131.5-171.0 mbsf) in 24 hr. A total of 36.7 m of massive gabbro and massive olivine-bearing

ing gabbro was recovered. Bit weight during this run was increased from 15,000 to 22,000 lb. The average recovery rate for the bit was 92.9%.

Bit 10 advanced the hole 67.0 m (171.0–238.0 mbsf) in 38 hr. A total of 64.48 m of massive gabbro, massive olivine-bearing gabbro, and iron-titanium oxide gabbro was recovered. The average recovery rate for the bit was 96.2%.

Bit 11, the last available Type C-7 bit, advanced the hole 67.5 m (238.0–305.5 mbsf) in 30 hr. A total of 64.87 m of massive gabbro and iron-titanium oxide gabbro, veined by trondhjemite, was recovered. The average recovery rate for this bit was 96.1%.

Bit 12, a Type C-57 bit, advanced the hole 109.0 m (305.5–414.5 mbsf) in 29.17 hr. A total of 102.36 m of massive olivine gabbro containing a 4-m-thick brecciated zone and mylonitized gabbro below 403.5 mbsf was recovered. The breccia is filled with massive epidote veins that form a stockwork. The average recovery rate for this bit was 93.9%.

Time available for coring became short. The final bit (Bit 13) was run into the hole on 2 December. By this time, essentially all DSDP/ODP records for coring and recovery of hard rock had been broken, but the depth reached was only 414.5 mbsf, and the prospect of a 0.5-km hole was a tantalizing goal. Progress was good until Core 118-735B-85R (471.5–481.0 mbsf), when the penetration rate decreased and it took 195 min to cut 9.5 m. The prospect of reaching 500 mbsf in the assigned coring time was not good, but the next core, Core 118-735B-86R (481.0–490.5 mbsf), was drilled more quickly and took only 145 min to cut 9.5 m. Our allocated coring time ran out, but the logging scientists "loaned" the drillers the few additional hours required to cut a final core, Core 118-735B-87R (490.5–500.0 mbsf), which took the hole to the goal of 0.5 km depth. This core arrived on deck at 0505 hr on 3 December. A total of 81.53 m of massive olivine gabbro containing zones of troctolite and foliated metagabbro were recovered from the 85.5 m cored (414.5–500.0 mbsf) with this bit in 39 hr. The average recovery rate was 95.4%.

Hole 735B was cored from 0 to 500.0 mbsf using the PDCM and rotary top drive systems. Total recovery for the hole was 434.81 m, an average recovery rate of 86.79%. Recovery with the rotary system alone was 420.62 m, an average recovery rate of 91.28%.

Navidrill Testing in Hole 735B

A period of 24 hr was set aside for testing the navidrill. This system complements the advanced piston corer (APC)/extended-core barrel (XCB) system. A mud-driven motor with a 5-m-long core barrel attached to the bottom is landed inside the bottom drill collar directly above the bit. The core barrel has a thin-walled diamond bit at the bottom that can drill out ahead of the drill pipe. The system is designed to obtain a sample of basement rock at the end of an XCB hole. The tool worked well during land tests but failed two previous tests at sea.

After extensive surface testing, the navidrill cut a 0.7-m-long core in Hole 735B, thereby extending the hole to 500.7 mbsf. A single piece of massive olivine gabbro was recovered. The recovery rate for the navidrill system was 100%. The drill pipe then was pulled above the guidebase, and the ship offset for further test drilling in Hole 735C.

Hole 735C (32°43.4'S, 57°15.5'E)

We attempted a bare-rock spud-in using the navidrill about 70 m away from Hole 735B, but it was unsuccessful. This failure resulted from the BHA apparently being pumped off the seafloor by the hydraulic force of the drill, which resulted in bending of the inner core barrel. Additional testing time was not available; consequently, the hole was abandoned.

Logging in Hole 735B

After ending operations at Hole 735C, the ship returned to Hole 735B to conduct a 5.9-day logging program that began the morning of 5 December. A summary of the various logging runs can be found in Table 2.

The first logging run (run 1) was with the Schlumberger DIT/LSS/GR/CAL tool (dual induction/sonic/natural gamma/caliper tool). The tool worked well between 500 and 269 mbsf but an electrical short developed, which resulted in the loss of the induction and caliper (DIT/GR/CAL) part of the data. However, the sonic log ran well throughout. Run 2 was with the Schlumberger LDT/CNTG/NGT/GPIT/AMS tool (litho-density tool/three-component magnetometer), which logged without incident and produced good data. Run 3 was the Schlumberger GST/ACT/CNTG/NGT/GPIT/AMS tool (geochemical combination/magnetometer). Two complete passes were made on capture mode, which gave excellent data; the inelastic mode did not work.

Run 4 was with the Schlumberger DIT/GR/CAL tool, a repeat run of the tool that partially failed earlier (run 1). Results were good, with resistivities varying between 2 ohm-m and the tool maximum of 2000 ohm-m. Run 5 was with the Schlumberger DLL log, which gave excellent data, with resistivities varying between 2 and 40,000 ohm-m. Run 6 was with the USGS temperature log. This gave good results; temperatures were slightly elevated in the upper part of the hole relative to the bottom. Run 7 was with the LDGO borehole televiwer; these tools failed and no data were collected. Run 8 was the LDGO multichannel sonic (MCS) log, which gave good data, except in the top 100 m of the hole. Run 9 was with the USGS magnetometer log, which gave good results. Run 10 was the UW magnetometer/magnetic susceptibility log, which gave good magnetometer data, but the susceptibility data were very noisy. Run 11 was the USGS magnetic susceptibility log, which logged from 490 mbsf to 49 mbsf, worked well, and gave good data. Run 12 was a repeat run of the MCS log to collect data from the top 100 m of the hole. Logging began at 127 mbsf and continued to the seafloor. The resulting data are good. Run 13 was the second run of the USGS temperature tool; the data were consistent with the first temperature log (run 6). Most of the hole had cooled since the first temperature log.

Run 14 was an experiment using the Woods Hole Oceanographic Institution vertical seismic profile (VSP) tool, the first of three runs using this tool. This run was unsuccessful; there were hydraulic clamping problems with the first tool and noise downhole, and the second tool stopped working. To allow time for fixing these tools, the LDGO borehole televiwer was deployed once more during run 15, which logged the full length of the hole. This time, results were good. The shearing of screws holding the centralizer bracket top plates resulted in these being left in the hole. Run 16 was with the Woods Hole VSP, but again the tool failed. To collect VSP information in the hole, the Schlumberger WST (vertical component VSP) tool was deployed during run 17. There was considerable noise downhole, which was compounded by the unusual shallowness of the site, by noise from the ship, and by noise from the drill pipe. We also found it difficult to set the tool in the smooth-sided hole.

Eventually, 22 shot stations were set at about 20-m intervals using both water and air guns. The resulting data are good. The Woods Hole VSP experiment was run for the third time during logging run 18. The problems were alleviated once the tool was set properly. This time, the experiment was a success; 24 clampings at 15–25-m intervals produced good data. Drill pipe was tripped to the surface at 2045 hr on 9 December. The packer was made up and run into the hole, reentering the guidebase at 0145 hr on 10 December. Six successful inflations were conducted be-

Table 2. Summary of logging operations in Hole 735B.

	Order/start time ¹	Log/experiment
First pipe trip (clean-out/logging bit)		
	0800 5 December	Reentered hole.
(1)	0930 5 December	Schlumberger DIT/LSS/GR/CAL; sonic log good, induction and caliper failed.
(2)	1500 5 December	Schlumberger LDT/CNTG/NGT/GPIT/AMS; data good.
(3)	1815 5 December	Schlumberger GST/ACT/CNTG/NGT/GPIT/AMS; two passes. Data excellent.
(4)	0730 6 December	Schlumberger DIT/GR/CAL; repeat of Run 1. Data good.
(5)	1045 6 December	Schlumberger DLL; data excellent.
(6)	1300 6 December	USGS temperature log 1; good results, temperature higher toward top of hole.
(7)	1630 6 December	LDGO BHTV; both tools failed. No data collected.
(8)	0030 7 December	LDGO MCS; data good except for top 100 m of hole.
(9)	0700 7 December	USGS magnetometer; data good.
(10)	1600 7 December	UW magnetometer/magnetic susceptibility tool; magnetic data good, susceptibility data miscalibrated.
(11)	2015 7 December	USGS magnetic susceptibility tool; data good.
(12)	2315 7 December	LDGO MCS; repeat of Run 8. Good data over missing 100 m of hole.
(13)	0300 8 December	USGS temperature log 2; good data; most of hole cooling since run 1.
(14)	0630 8 December	WHOI VSP; partially successful. Logged bottom of hole, then hydraulic arm clamping problems on one tool, other tool did not work.
(15)	1215 8 December	LDGO BHTV; good data. Centralizer bracket top-plates left in hole.
(16)	2300 8 December	WHOI VSP; unsuccessful, both tools failed.
(17)	0100 9 December	Schlumberger WST; shot 22 stations (about five shots each with water and airgun).
(18)	0245 9 December	WHOI VSP; problems gone when tool set properly; 24 clampings at 15–25 m intervals. Good data.
	2045 9 December	Pull out of hole.
Second pipe trip (packer in BHA)		
	0145 10 December	Reentered hole.
(19)	0345 10 December	Six successful packer sets at 778, 780, 954, 954, 1030, and 1120 mbrf. Slug and flow tests good.
	2200 10 December	Pulled out of hole; time expired.

¹ Start time refers to time logging tool left the rig floor. In the case of the packer experiment, this refers to time the first go-devil was seated in the packer. LDGO = Lamont-Doherty Geological Observatory; WHOI = Woods Hole Oceanographical Institute; BHTV = borehole televiewer. Logs are explained in appropriate sections (this chapter).

fore bringing the pipe to the surface at 2200 hr on 10 December. Data from the packer were excellent and showed that the hole was permeable in the upper part and very impermeable toward the bottom.

The ship departed Site 735 at 0730 hr on 11 December after retrieving the acoustic positioning beacon. Geophysical gear was streamed to determine the position of the hole in relation to the edge of the fracture-zone wall (see end of "Approach to Site 735" section, this chapter).

LITHOSTRATIGRAPHY

Six lithologic units were identified at Site 735 (Fig. 5). The divisions between them are based upon primary igneous modal mineralogy, mineral composition, and degree and style of deformation. A summary of the downhole petrographic and deformational characteristics are included in Figures 6, 7, and 8.

Unit I

Lithologic Unit I is a foliated metagabbro (0.0–0.2 mbsf in Hole 735A, 0.0–39.5 mbsf in Hole 735B; Cores 118-735B-1D through -11D). This unit consists of metagabbro with porphyroclastic to mylonitic textures. There is usually a well-developed foliation dipping at 25° to 35°. Rock types include poorly foliated metagabbro, porphyroclastic gabbro, mylonite, gabbroic gneiss, and augen gneiss. Samples range from very fresh metagabbro containing clinopyroxene and plagioclase porphyroclasts

and neoblasts to amphibole plus plagioclase metagabbro. Both types include orange-red oxidized pseudomorphs after olivine and orthopyroxene. Amphibole- and sodic plagioclase-rich zones clearly crosscut the foliation in several sections, and the amphibole fills fractures that also cut the foliation, indicating that most of the amphibole formed after deformation.

The protolith for most of the metagabbros was a two-pyroxene gabbro or gabbro-norite. Orthopyroxene porphyroclasts make up 1%–10% of several samples (Fig. 6). Olivine remnants occur in intervals, particularly in the lower part of the unit (Fig. 6). In some of the cores, mylonitic bands rich in iron-titanium oxides may have had an opaque-rich gabbro protolith, but no relict mineralogy was determined. Some of these oxide-rich zones are clearly secondary because the oxides fill fractures and pore spaces within the samples. The common occurrence of olivine from Core 118-735B-7R downward (from 27 mbsf) indicates a more magnesium protolith for the rocks. Lithologic Unit I is defined principally by metamorphic criteria because relict igneous textures are not preserved. All Unit I rocks share a common deformational history, even though there were probably several different protoliths.

Unit II

Lithologic Unit II is an olivine-bearing and olivine gabbro (39.5–180.0 mbsf, Cores 118-735B-12R through -37R). The upper boundary of this unit is defined by an abrupt decrease in the

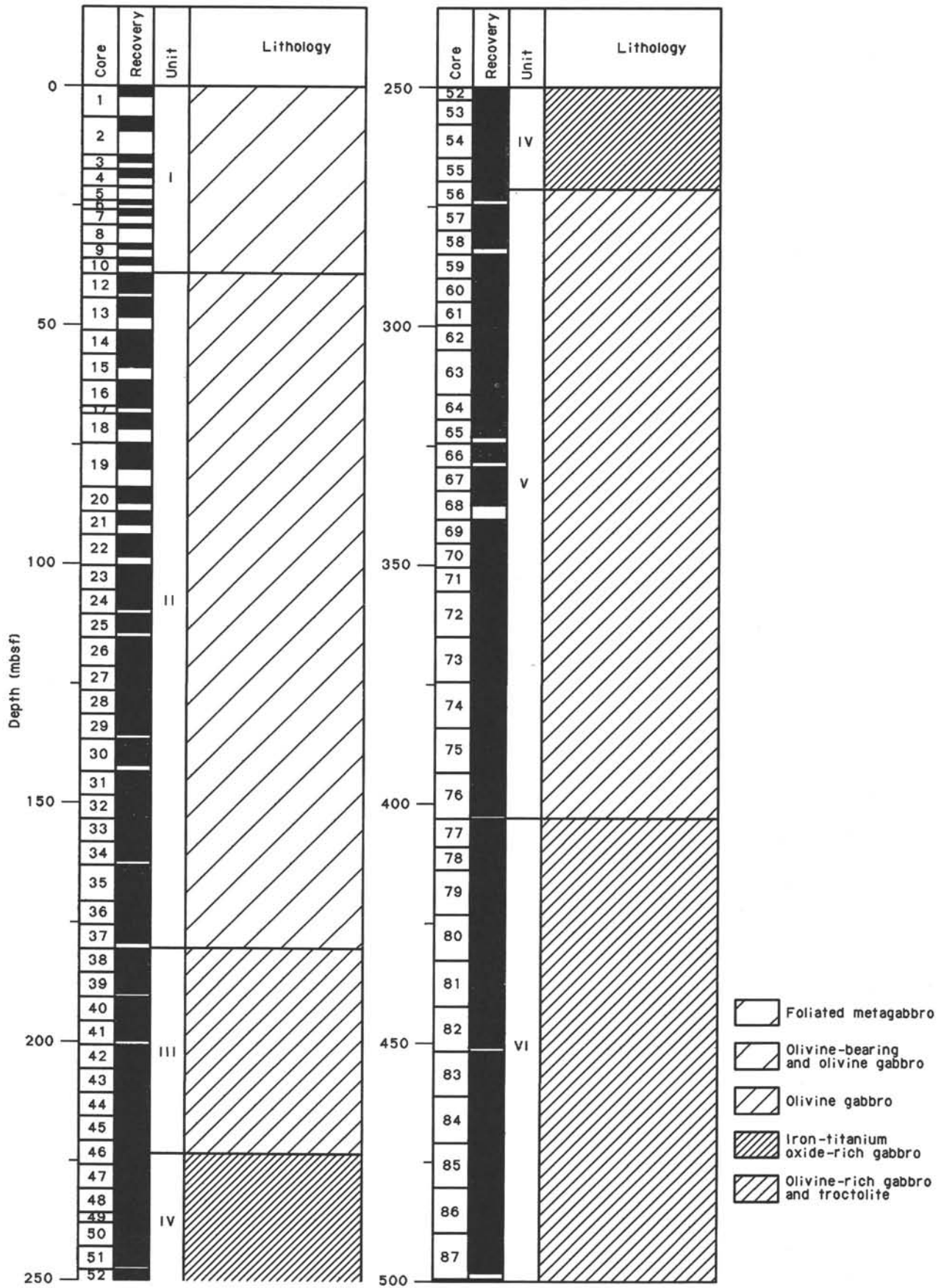


Figure 5. Basement lithostratigraphy of Hole 735B.

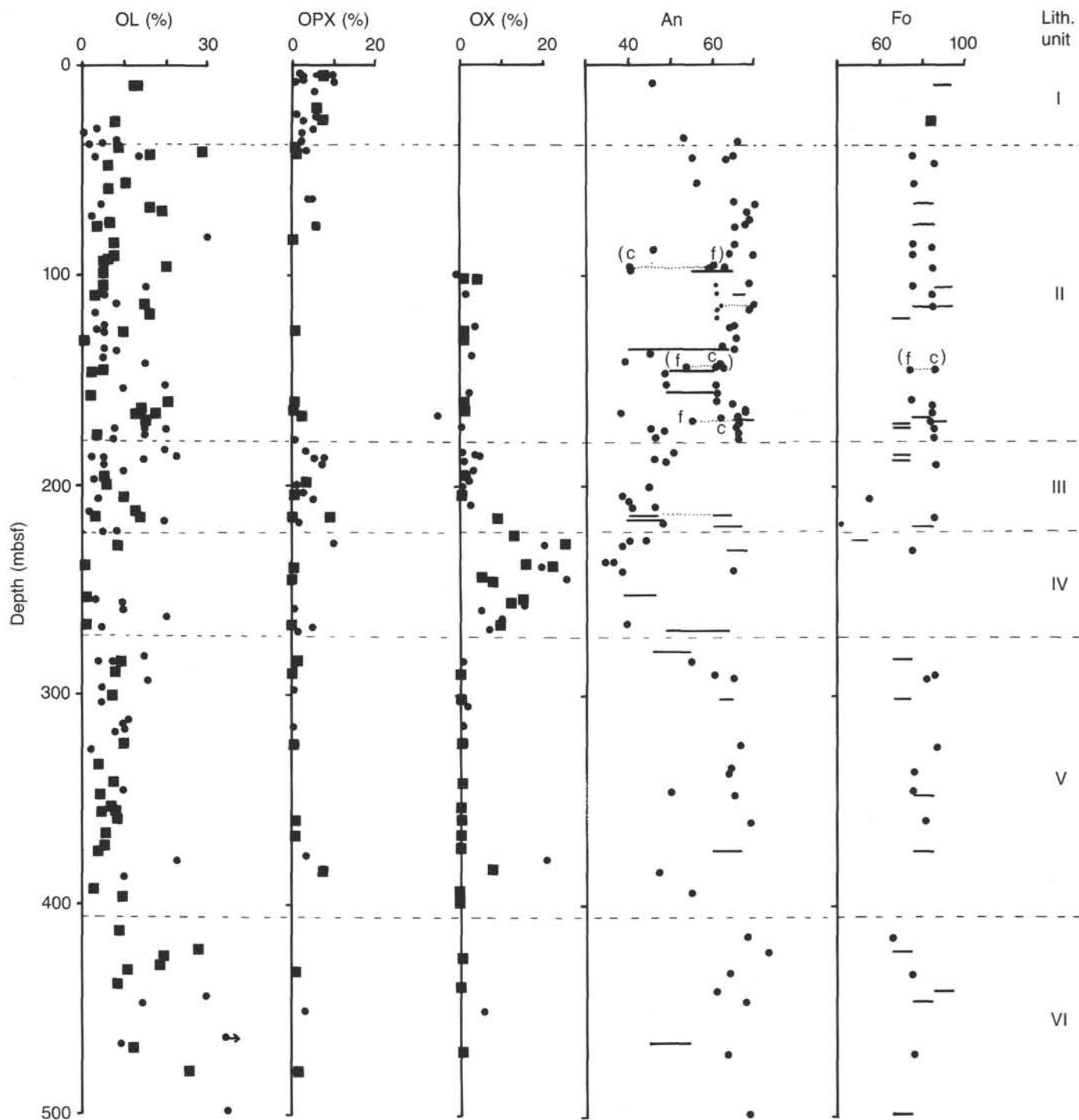


Figure 6. Modal and mineralogic variations with depth in Hole 735B. Anorthite (An) and forsterite (Fo) contents were estimated optically. Large dots for modal percentages of olivine (OL), orthopyroxene (OPX), which includes inverted pigeonites, and iron-titanium oxides (OX) are from point counts; smaller points are visually estimated modes. All modal data are estimates of primary mineral abundances. Extensively altered samples in which the primary modes could not be reasonably estimated are not plotted. Bars in the An and Fo columns indicate ranges within samples that did not give consistent or precise compositions. Pairs joined by dotted lines are for clearly bimodal assemblages in single samples, often coarse-fine contacts (indicated by c or f, respectively).

degree of plastic deformation (Fig. 7) and the appearance of samples having clearly igneous textures. Its lower boundary is defined by a relatively rapid gradation to gabbros containing more orthopyroxene and more sodic plagioclase than the gabbros in Unit II. The exact location of this boundary is somewhat arbitrary. Just below this boundary (in Core 118-735B-38R) are zones of slight deformation. The gradational nature of the pet-

rological data suggests that lithologic Units II and III are part of a continuous magmatic unit. The deformed zone at the top of Unit III may indicate some offset near the Unit II/Unit III boundary.

The principal rock type in Unit II is an olivine-bearing (1%–5% olivine) or olivine (>5% olivine) gabbro. Most of the rocks are mesocumulates in which anhedral and subhedral granular

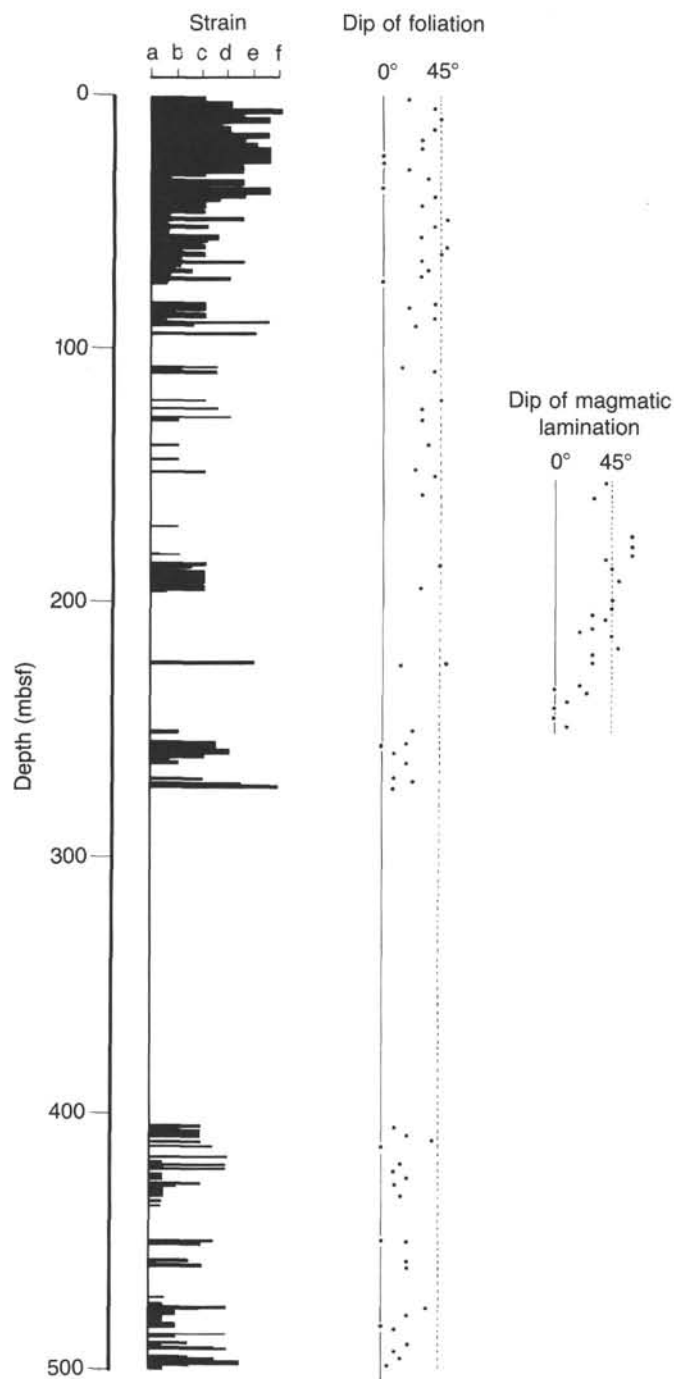


Figure 7. Structural log for Hole 735B. "Strain" column: a = undeformed; b = poorly foliated; c = well-foliated (porphyroclastic); d = augen gneissic; e = augen gneissic with mylonitic bands; and f = mylonitic. Deformation textures were determined by looking at the core and were checked under the microscope when a thin section was available. Due to the scale of the log, only textural intervals 50 cm thick or more are represented.

textures predominate. Clinopyroxene is usually intergranular or subophitic and, in some samples, forms medium- to coarse-grained oikocrysts, most commonly with plagioclase chadacrysts. Olivine chadacrysts are rare. Intervals commonly show magmatic layering, defined principally by size gradations from coarse- to medium- or fine-grained layers. The transitions between layers may

be either sharp or gradational. Igneous laminations are only rarely developed. The magmatic layering is most clearly seen in the lower parts of the unit. Small pods or layers of microgabbro are common (see "Primary Petrography" section, this chapter). Modal layering is sometimes defined by alternating olivine-rich with olivine-poor zones. Short troctolitic intervals occur in Cores 118-735B-12R, -20R, and -26R. The magmatic layering is generally subhorizontal, but occasionally shows dip angles from 10° to 30°.

Thin layers (from one or two to a few centimeters) of iron-titanium oxide-bearing gabbro occur in several locations in the core (Fig. 8). Somewhat thicker intervals of iron-titanium oxide-bearing gabbro occur in Cores 118-735B-21R, -23R, -24R, -32R, and -34R. The rocks in these thicker intervals have igneous textures in which the oxide minerals are closely intergrown with pyroxenes. Inverted pigeonite occurs in pyroxene-rich layers in Cores 118-735B-23R and -35R. These intervals represent crystallization of significantly more evolved liquids than those from which the olivine gabbros crystallized. The few occurrences of iron-titanium oxides are usually associated with sheared zones in which secondary amphibole is abundant. We interpret these as zones of secondary oxide development. These oxide zones commonly have abundant sulfide minerals.

A basalt dike crosscuts the section in Core 118-735B-19R; it is aphyric and has chilled margins adjacent to the gabbro. A large microgabbro dike intrudes the olivine gabbro in Core 118-735B-23R.

The olivine-bearing and olivine gabbros range from 7.0 to 14.0 wt% MgO (see "Geochemistry" section, this chapter). Olivines are magnesium-rich (Fe_{80} , determined optically) and plagioclase compositions average about An_{65} . The plagioclase compositions within single samples or intervals, however, can be quite diverse, ranging from An_{40} to An_{65} . This variation is often associated with adjacent coarse-fine intervals. This, and the range in MgO concentrations, indicate that lithologic Unit II formed in an environment in which there was frequent mixing of magmas having a range of magnesium and calcium contents.

Mylonitic and porphyroclastic intervals are not uncommon in Unit II, particularly in the upper part of the unit (Cores 118-735B-12R to 15R, -16R, -18R, -20R, and -22R; Fig. 7). Most of the remainder of the unit is undeformed or weakly brecciated and underwent only static metamorphism, with development of actinolitic amphibole. Fractures are common throughout the unit and are commonly filled with fibrous green actinolite. Olivine is ubiquitously altered in part to talc-tremolite-magnetite aggregates. Fracture surfaces between individual rock pieces commonly are coated with talc or actinolitic material.

Unit III

Lithologic Unit III is an olivine gabbro, with intervals of iron-titanium oxide gabbro (180.0–224.0 mbsf, Core 118-735B-38R through Section 118-735B-46R-3 at 30 cm). This unit includes long sections of olivine gabbro, with intervals of iron-titanium oxide-rich gabbro having igneous textures and a pronounced igneous lamination. The oxide-rich zones occur in Cores 118-735B-38R, -42R, -43R, and -45R, and are associated with pyroxene-rich intervals (Fig. 6). The upper boundary of the unit is defined by the common occurrence of sodic plagioclase (An_{40-45}), an increase in the appearance and proportions of low-calcium pyroxene and iron-titanium oxides, a decrease in the proportion of olivine, the occurrence of iron-rich olivine, and the development of well-defined, steeply dipping primary igneous layering (Figs. 6 and 7). Although the unit is similar to lithologic Unit I in hand specimen, it is distinct petrographically.

The boundary between Units II and III coincides with a change in the chemical composition of the olivine gabbros (>5% olivine) from gabbros containing 12–13 wt% MgO to gabbros

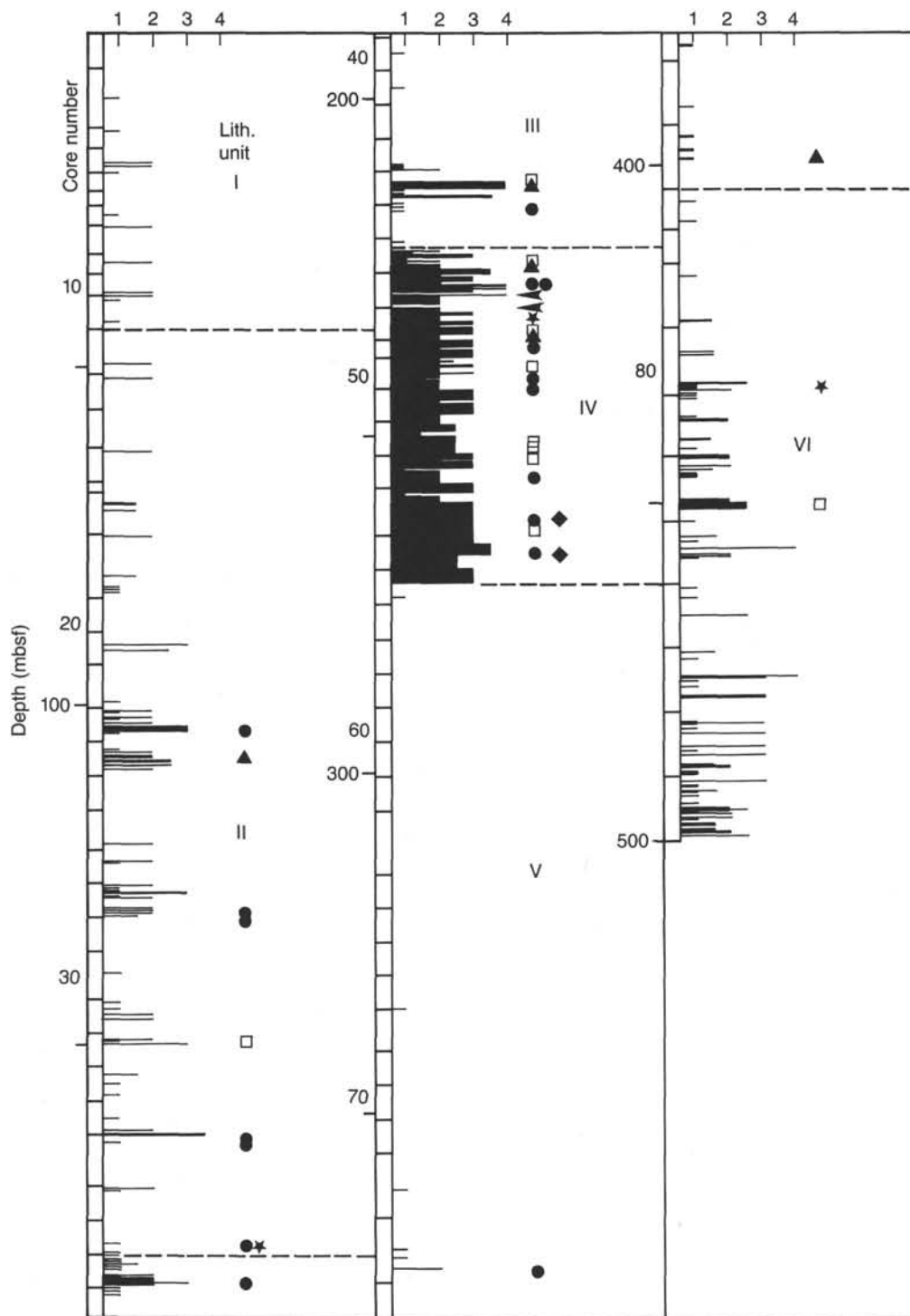


Figure 8. Relative abundance of opaque minerals vs. depth below seafloor. Relative abundances (numbers 1 to 4 on the horizontal scale) correspond to estimates (trace, common, abundant, very abundant) based on visual core descriptions. Symbols indicate different petrographic types based on thin section observations: solid circle = inverted pigeonite-bearing; solid triangle = orthopyroxene-bearing with fairly abundant clinopyroxene lamellae; solid square = orthopyroxene-bearing; solid star = iron-titanium oxide-bearing microgabbro with no calcium-poor pyroxene; solid diamond = apatite-bearing. Arrows indicate two occurrences of olivine gabbro in Unit IV.

containing 8–9 wt% MgO (see “Geochemistry” section, this chapter). There may be some interleaving of more- and less-evolved gabbro in the lower part of Unit III and the uppermost part of Unit IV, as seen by a few more calcic plagioclase compositions in those intervals (Fig. 6).

The igneous lamination in Unit III dips steeply in the upper part of the unit, but flattens until near-horizontal at the contact with Unit IV (Fig. 7). Mylonitic and foliated zones are common in Cores 118-735B-38R and -39R (Fig. 7). The contact between Units III and IV is marked by a 60-cm-thick mylonite zone.

Unit IV

Lithologic Unit IV is an iron-titanium oxide-rich gabbro (224.0–272 mbsf, Section 118-735B-46R-3 at 30 cm through Section 118-735B-56R-3 at 90 cm). This unit represents an interval in which iron-titanium oxide-rich gabbro is the principal rock type (over 75% of recovered material). The contact with Unit III is a shear zone, but significant changes in mineralogy also occur between the two units. The gabbros of Unit IV commonly have more abundant opaque phases (10% or higher) and less olivine than the gabbros of Unit III. Like Unit III, the common plagioclase in these rocks is sodic (An_{35-50}), and some iron-rich olivines also occur (Fig. 6). The pronounced igneous lamination is subhorizontal in most of the unit (Fig. 7). The iron-titanium oxide-rich gabbros have subhedral granular textures, commonly with cumulus plagioclase and clinopyroxene. Olivine commonly is intergranular, and the oxide (a mixture of ilmenite and magnetite) forms intergranular to poikilitic masses enclosing plagioclase and clinopyroxene. Low-calcium pyroxene occurs in some samples and includes both primary orthopyroxene and inverted pigeonite. Olivine is normally as abundant, or slightly more so, than the low-calcium pyroxene. The gabbro is typically coarse- to very coarse-grained. Primary layering is well-defined by a distinct igneous lamination of clinopyroxene and plagioclase, coarse to medium or fine grain-size transitions, and occasional development of pyroxene- or plagioclase-rich bands. Large pyroxene and plagioclase crystals sometimes are elongated perpendicular to the layering (see “Primary Petrography” section, this chapter).

Olivine gabbro occurs infrequently in 20- to 100-cm-thick intervals. Mylonitic zones are uncommon and are concentrated in the upper and lower parts of the unit. A felsic intrusion breccia with a large (4 cm) trondjemitic vein occurs in Sections 118-735B-53R-4 and 118-735B-54R-2.

The lower boundary of the unit is marked by a 2- to 3-m-thick layer of mylonitized oxide-rich gabbro. The mylonitic gabbro has a sharp lower contact with a brecciated olivine gabbro at the top of Unit V.

Unit V

Lithologic Unit V is an olivine gabbro (272.0–403.5 mbsf, Section 118-735B-56R-3 at 90 cm through Core 118-735B-76R). The upper contact of this unit is marked by a brecciated zone below the mylonitized oxide-gabbro. Its lower boundary with Unit VI is defined by the appearance of a pervasive, weak to moderate deformation that persists through most of Unit VI (Fig. 7). It also marks the beginning of a zone characterized by the common occurrence of troctolites and olivine-rich gabbros. Petrologically, the lower boundary is gradational and, like the Unit II/Unit III transition, may be a zone of small offsets of a continuous magmatic section. Overall, Unit V is characterized by a marked lack of deformation. All of the rocks of Unit V are characterized by an abundance of olivine (5% or greater in nearly all samples) and a scarcity of oxides and low-calcium pyroxene (both present but only in trace amounts). Most of the samples are mesocumulates having subhedral granular to anhedral granular textures. Clinopyroxene is intergranular to ophitic and, in some cases, occurs as large oikocrysts. Primary layering is defined by coarse to fine grain-size changes and, less commonly, by lamination of the plagioclase. A troctolitic interval occurs in Sample 118-735B-63R-4, 35–43 cm, Piece 3C. There are a few plagioclase-rich intervals in the unit. This olivine gabbro more commonly has long (2–4 m) intervals of massive, medium- or coarse-grained rock than does the olivine gabbro of Unit II.

MgO ranges from 8 to 16 wt% but typically is between 10 and 12 wt% (see “Geochemistry” section, this volume). Plagioclase

compositions are principally between An_{60} and An_{65} , and olivine averages Fo_{80} (Fig. 6). This unit apparently crystallized from a magma that was better buffered and experienced fewer mixing events than that which formed Unit II.

There are frequent zones of brecciation associated with felsic veins and the growth of epidote and albite. An oxide-rich interval occurs in Sample 118-735B-73R-4, 84–86 cm, Piece 2B, associated with a small shear zone and extensive amphibolitization of the clinopyroxene. Gabbro in this interval contains inverted pigeonite, which suggests a primary iron-rich composition. Near the lower boundary of Unit V in Section 118-735B-74R-6, there is a 50-cm-thick intrusion of microgabbro composed of orthopyroxene, iron-titanium oxide, and apatite. In general, however, Unit IV is remarkably free of iron-titanium oxide-rich zones, in contrast to the olivine gabbro of Unit II (Fig. 8).

Unit VI

Lithologic Unit VI is an olivine-rich gabbro and troctolite (403.5–500.7 mbsf, Cores 118-735B-77R through -88N). This unit is an interval of olivine-rich (commonly >10%) gabbro having frequent layers and intrusions of troctolite (Fig. 6). Olivine-gabbro having mesocumulate texture is the principal rock type; it is similar to the olivine gabbro of Unit V except for the consistently higher modal proportions of olivine. Igneous layering is defined principally by size gradings, which are frequent and well-developed. Pyroxene oikocrysts have maximum linear dimensions up to 10 cm, and both clinopyroxene oikocrysts and large, cumulate plagioclase crystals are commonly oriented perpendicular to the igneous layering.

Interlayered with the gabbro are zones of troctolite and troctolitic gabbro. Troctolites occur in Cores 118-735B-77R, -79R, -83R, and -87R and include both olivine- and plagioclase-rich varieties. A coarse-grained olivine-rich troctolite occurs in Core 118-735B-83R, but the most common troctolite occurrence is as microgabbro dikes or layers that have granular textures. Chromium-spinel occurs in some coarse- and fine-grained troctolites.

Layers and lenses of olivine microgabbro with equigranular textures are also common. These microgabbros occur in Cores 118-735B-74R, -75R, -76R, and -77R. Iron-rich gabbros occur in Core 118-735B-77R. These evolved compositions are rare in the section. Other oxide-rich zones are associated with small shears and zones of extensive amphibolitization. The oxide is typically concentrated in thin zones at the margins of the shears. A trondjemitic vein cuts the gabbro in Core 118-735B-79R.

Lithologic Unit VI has frequent intervals of plastic deformation (Fig. 7). Most of Cores 118-735B-84R through -87R is characterized by mylonitic to porphyroclastic textures. Foliated or mylonitic zones also occur in Cores 118-735B-77R, -78R, -79R, and -80R.

Gabbros in Cores 118-735B-79R through -87R contain an unusual pyroxene, which is pinkish-brown in hand specimen but is indistinguishable in thin section from clinopyroxenes higher in the section. From Core 118-735B-79R downward the rock also commonly contains a dull, emerald green pyroxene that typically has a subophitic or poikilitic texture enclosing plagioclase. These green pyroxenes are most commonly associated with the troctolitic zones. In hand specimen this pyroxene appears to be intergrown with or replaces the brown pyroxene. In the one thin section examined, it is a clear, optically continuous, green clinopyroxene, similar to a chromium diopside. The textures and occurrence of the pyroxenes are discussed in more detail in the “Primary Petrography” section (this chapter).

Units II and III and Units V and VI appear to record two relatively continuous magmatic sections, although there is evidence of minor offsets near each lithologic boundary. The Unit I/Unit II contact is defined by a change in deformation style and may or may not be a major tectonic boundary. The base of

Unit IV clearly is bounded by a major fault. Unit III appears to be chemically and petrographically transitional from the gabbro of Unit II to the iron-titanium oxide-rich gabbro of Unit IV. This unit may represent a magmatic transition, but there is a distinct mylonite zone at the top of Unit IV, and it is possible that the entire section is tectonically interleaved. There is, however, no question that small intervals of olivine gabbro occur in the oxide gabbro, and vice versa, which are clearly of magmatic origin. The contact between Units V and VI is likewise somewhat ambiguous. Unit VI is significantly more sheared than Unit V, and a large microgabbro intrusion occurs near the contact of the two. No clearly definable fault zone can be seen between the two, as with Units IV and V, but we were unable to define unambiguously the contact as magmatic.

STRUCTURE AND DEFORMATION

Introduction

The extent, manner, and intensity of deformation of the rocks drilled in Hole 735B vary considerably downhole. Although both plastic and brittle deformation occurred to varying degrees, there are relatively few open fractures and joints in the rocks recovered. For example, we measured the orientation of fractures and veins in 45 cores, mostly from the upper one-half of the hole and found 687 veins filled with amphibole and other metamorphic minerals and only 25 obvious open joints and fractures. The massive nature of the gabbro and the scarcity of open fractures were largely responsible for the exceptionally high recovery at this site. Nearly one-half the cracks and joint surfaces recorded were found in the upper 10 cores, which may have contributed to the overall lower recovery rates there. However, the lower recovery in the upper sections of the hole may also reflect the use of the mud motor, rather than of the rotary coring system.

About 30% of the gabbros in Hole 735B are plastically deformed, and these occur largely in three main intervals: 0–70, 250–272, and 405–500 mbsf (Fig. 7). Brittle deformation structures in the gabbros include numerous fractures filled with amphibole and result from extension contemporaneous with plastic deformation. These veins are scattered throughout the core, but their density is highest in the upper 220 m. Both deformed and undeformed veins are common. Well-developed igneous lamination, modal layering, and graded bedding were observed in the olivine gabbros and iron-titanium oxide gabbros of lithologic Units II, III, and IV (50–272 mbsf; Fig. 7); such features are also sporadically present in the olivine gabbros and troctolites in the lower portion of Unit VI.

Plastic Deformation Structures

We distinguished five types of textures produced by increasing plastic deformation: (1) poorly foliated, (2) foliated, (3) well foliated or porphyroclastic, (4) augen gneissic, and (5) mylonitic.

In unfoliated or poorly foliated specimens, the foliation is either very faint, marked by the slight elongation of pyroxene in a plagioclase matrix, or not pervasive, with very thin shear zones (< 1 cm wide) crosscutting virtually undeformed gabbros. Foliated and well-foliated or porphyroclastic specimens are characterized by a pervasively shaped fabric of the mafic phases and by partial recrystallization of the plagioclase. Augen gneissic textures (Fig. 9) are defined by a clear and pervasive foliation. The plagioclase grains are extensively kinked and recrystallized, and the pyroxenes form rounded augen with tails of recrystallized grains and/or amphibole. Discrete mylonitic zones less than 0.5 cm wide are present. These rocks exhibit a marked banded appearance, defined by porphyroclastic layers and layers of gneissic material having stripes of alternating recrystal-

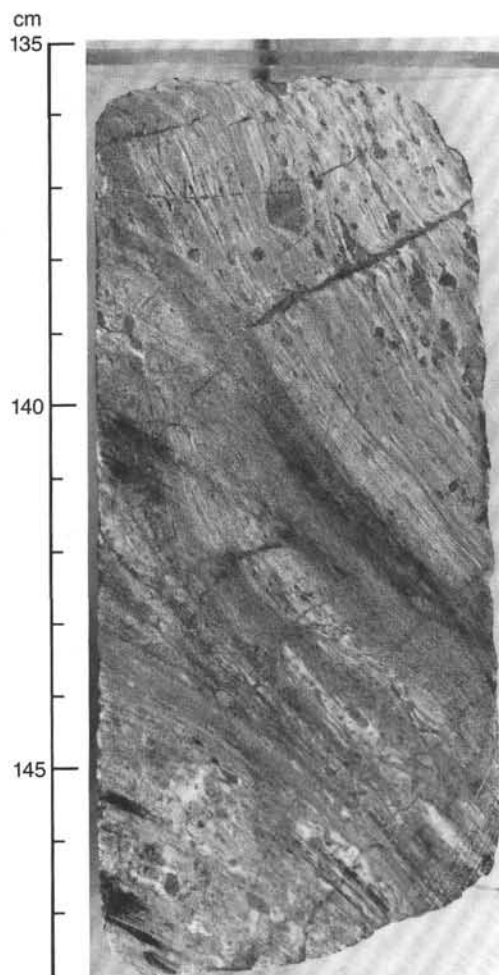


Figure 9. Deformed gabbro with augen gneissic (upper and lower ends of sample) and mylonitic (middle part of sample) textures (118-735B-2D-1, 135–148 cm, Piece 24).

lized mafic minerals and plagioclase. In the mylonitic gabbros (Fig. 9), the rounded pyroxene augen, and/or the clusters of recrystallized olivine grains, appear to float in an extremely fine-grained matrix. The grain size is locally so fine that the foliation is difficult to see.

Undeformed or poorly foliated gabbros commonly are juxtaposed directly with augen gneissic or mylonitic metagabbros (Figs. 10A and 10B). This reflects very high-strain gradients; the poorly foliated and well-foliated gabbros obviously experienced less total strain than the augen gneissic gabbros, which in turn are less strained than the mylonitic gabbros. In Figure 7, the deformation textures are used to estimate the relative strain intensities through the core. However, the relationship between the textural types and the strain is certainly far from linear. The shear strain accommodated by a 10-cm-thick mylonitic band may be greater than that accommodated by a 100-m-thick section of poorly foliated gabbro.

These textures mostly developed at high temperatures in the stability field of clinopyroxene plus brown hornblende \pm olivine \pm orthopyroxene (see "Metamorphism and Alteration" section, this chapter). In the well-foliated gabbros, intracrystalline deformation of the plagioclase porphyroclasts seems to have produced a good preferred orientation. This preferred orientation appears weaker in the augen gneissic and mylonitic gabbros, where the plagioclase porphyroclasts are almost completely re-

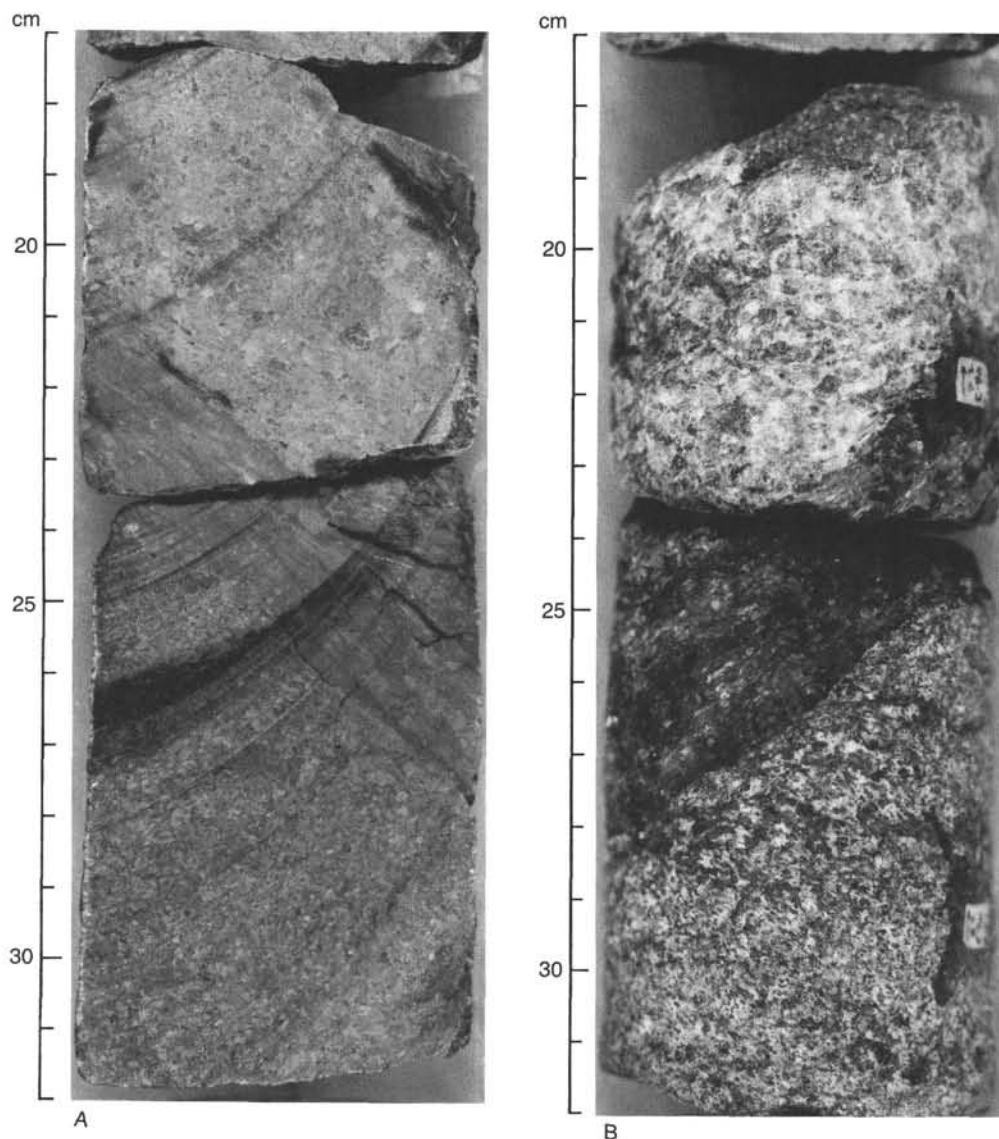


Figure 10. Lower limit of a deformation zone. A. View of split surface. B. View of cored surface. Clear-cut contact between a mylonitic gabbro and an undeformed gabbro with igneous lamination. The mylonitic gabbro contains up to 20% iron-titanium oxides. The igneous lamination, dipping about 20°, is visible on the cored surface (118-735B-46R-3, 17-32 cm, Pieces 2C and 2D).

crystallized to a mosaic of polygonal grains. The clinopyroxene is commonly kinked and partly recrystallized. In the most deformed gabbros, the clinopyroxene porphyroclasts, or augens, appear passively rotated in the fine-grained plagioclase matrix and develop tails of recrystallized grains elongated in the foliation. In the orthopyroxene, intracrystalline plastic deformation locally produces a preferred orientation of the (100) slip planes close to the foliation. But the dominant deformation mechanism in orthopyroxene seems to be kinking and fracturing. Recrystallization of orthopyroxene is only rarely observed (see "Metamorphism and Alteration" section, this chapter). The olivine is plastically deformed, and subgrain boundaries are frequent. The olivine appears to have a crystallographic-preferred orientation in some well-foliated gabbros. In the augen gneissic and mylonitic gabbros, however, recrystallization appears to supercede intracrystalline dislocation creep as the principal deformation mechanism, and the olivine is recrystallized to aggregates of polygonal grains having no apparent subgrain bounda-

ries or preferred orientation. Overall, recrystallization or fracturing of the primary minerals is ubiquitous in the most strongly deformed gabbros. This suggests high differential stresses and strain rates during the deformation.

Shearing also occurred at presumably higher water/rock ratios and perhaps lower temperatures (see "Metamorphism and Alteration" section, this chapter) in the highly deformed upper 70 m of the hole (Fig. 7) and along steeply dipping amphibole veins and discrete shear zones in the rest of the core. The plagioclase and the brownish-green to green amphibole replacing the pyroxenes were kinked and recrystallized during this deformation.

Many of the high-strain zones cutting the gabbro show a large enrichment in iron-titanium oxides that sometimes exceed 10 or 20 vol%, with a sharp decrease at the boundary of the shear zone with undeformed gabbro (Figs. 10A and 10B). A common occurrence is a 1- or 2-cm-thick band of sheared or mylonitized, oxide-rich gabbro cutting an oxide-poor gabbro.

Overall, a strong association exists between deformation and ilmenite-magnetite enrichment throughout the section, with 0.2- to 10-cm-thick intervals of oxide-rich, plastically deformed metabasalt (1%–50% ilmenite and magnetite) occurring in lithologic Unit VI (below 400 mbsf; Fig. 7) and smaller zones occurring in Unit III (180–224 mbsf), interspersed with relatively undeformed and unaltered olivine gabbro zones. The paucity of oxides in the latter intervals is striking compared to the local enrichments in the adjacent metamorphosed and deformed gabbro. Although most of the plastically deformed zones in Hole 735B do not show such enrichment and much of the clearly magmatic ilmenite-magnetite gabbro in Unit IV (224–272 mbsf) is relatively undeformed, the zones of iron-oxide enrichment in Units III and VI commonly show a striking correlation among deformation, hydrothermal alteration of silicates to hornblende, and the presence of what appears to be secondary iron-titanium oxide. In these zones, the oxide is interstitial between deformed and recrystallized silicates. Local oxide-rich veins crosscut the primary igneous textures. In a number of cases, however, local shear zones a few centimeters thick show striking enrichment of iron-oxides, with little hydrothermal alteration of the silicates. This suggests that the passage of the fluids that precipitated the oxides through these shear zones took place at sufficiently low water pressure to preclude formation of the hydrous silicates (see discussion in “Metamorphism and Alteration” section, this chapter).

This association of intense plastic deformation with iron-titanium oxide enrichment might be due to localization of strain in previously formed oxide-rich zones, perhaps as a consequence of a rheological contrast between silicates and possibly more ductile oxides. Alternatively, it may be a result of channeling in the shear zones of hydrothermal fluids rich in dissolved oxides.

Brittle Deformation Structures

The numerous hydrothermal veins are typically about 1 mm wide, but range from hairline to more than 1 cm across. Multiple generations of jointing and fracturing are indicated by the presence of up to four different vein mineral assemblages in the core, sometimes with crosscutting relationships. Throughout the core there is a large population of very small, scarcely noticeable, subhorizontal white veins or open fractures that crosscut the higher-temperature amphibole veins. These appear to have developed very late, either because of unloading during uplift of the gabbro massif to its present elevation or to cracking that accompanied the drilling. By far the most prominent veins are monomineralic green amphibole veins that range from less than 100 μm to more than 1 cm thick and that occur throughout the core (495 of 687 veins measured for orientation). At about 85 mbsf (Fig. 7), plagioclase plus amphibole veins appear and persist to the bottom of the hole. These make up 12% of the veins measured. At about the same level, pale green veins (amphibole plus talc? or smectite) first appear and continue intermittently to the bottom of the hole. Deeper in the hole and adjacent to hydrothermally altered brecciated zones, vein assemblages include sphene and epidote in addition to amphibole and plagioclase. Diopside plus plagioclase veins appear below 300 mbsf. At several intervals, also adjacent to hydrothermally altered breccia zones, sparse carbonate veins crosscut the high-temperature silicate veins. These carbonate veins appear linked to highly localized oxidative alteration (see “Metamorphism and Alteration” section, this chapter).

Vein and fracture population statistics were collected from most of the cores in the upper one-half of Hole 735 and for a number of cores lower in the section. We found veins and fractures most abundant in the core between 0 and about 220 mbsf. In the upper mylonitic and gneissic zone (0–90 mbsf), we measured 332 veins and fractures in 42.5 m of recovered gabbro,

which gave a minimum fracture density of roughly eight veins per meter. Between 90 and 220 mbsf, we measured 333 veins and fractures in 62.2 m of core, which yielded a minimum of 5.3 veins and fractures per meter. The veins and fractures in this interval crosscut the gneissic foliation but are locally sheared. Below 220 mbsf, the number of veins and fractures in the core decreases precipitously to an average well below one vein per meter. At about 315 mbsf and down to about 350 mbsf, the density of veins and fractures increases slightly, in the vicinity of 1-m-thick zones of hydrothermally altered breccia. The veins crosscut the foliation and are generally undeformed, suggesting that they post-date the plastic deformation. However, the veins often do not cross zones of gneissic foliation or mylonite, which suggests that there they may have predated plastic deformation and were obliterated locally along zones of shear. It is also possible that the veins developed penecontemporaneously with this deformation because of brittle extension of the otherwise undeformed gabbro between the principal shear zones. Yet a third possible explanation is that the highly deformed gabbros were more resistant to brittle failure during the veining event than the surrounding poorly deformed gabbros. Locally, in the gneissic and mylonitic intervals, small amphibole veins orthogonal to the foliation crosscut stretched plagioclase augen; they represent extensional cracking and infilling penecontemporaneous with the plastic deformation. Numerous through-going amphibole veins in the same rocks are parallel to these cracks and are orthogonal to the foliation (Fig. 11), showing that cracking and vein filling related to the same basic regional stress field continued for some time after the end of the plastic deformation, possibly due to relaxation of the stored elastic strain.

Figure 12 is a histogram of the dips measured on 687 veins and fractures in 45 cores, mostly in the upper two-thirds of the hole. We excluded the set of subhorizontal white veins. Overall, most of the veins dip from 40° to 90°, with a strong peak between 60° and 65°, orthogonal to the prominent foliation, which averages 35° (Fig. 7). In general, conjugate vein sets are not visi-



Figure 11. Amphibole veins perpendicular to the foliation in a well-foliated to augen gneissic gabbro (118-735B-85R-4, 18–27, Piece 1C).

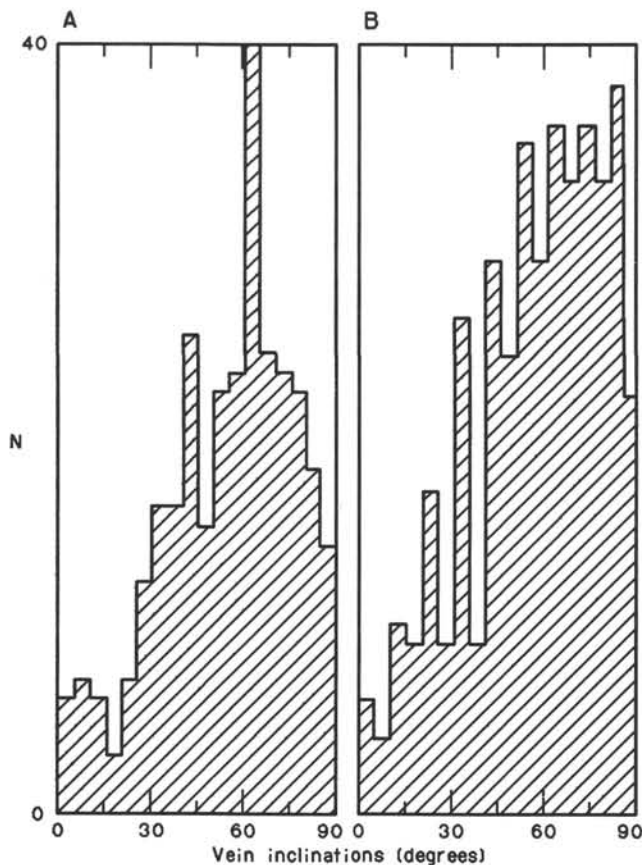


Figure 12. Histogram of the dips of the amphibole-bearing veins in Hole 735B. A. Cores 0–20. B. Cores 21–78.

ble in individual cores, and most veins, even those containing different mineral assemblages, all dip in the same direction. This suggests that the foliation suppressed the development of conjugate joints. Conjugate vein sets are evident in the more massive unfoliated gabbros.

Figure 12 clearly shows that the distribution of vein dips is skewed toward steeper inclinations. Interestingly, the peak distribution shifts to substantially steeper dips for veins measured below 90 mbsf (Core 118-735-21R), with the mean dip increasing as well. Unfortunately, foliations are poorly developed between 90 and 300 mbsf, which is the interval over which the majority of our vein data for the deeper section of the hole were obtained. However, the mean dip of the foliation decreases from about 35° in the upper part of the core, to about 30° below 250 mbsf (Fig. 7). This suggests that the stress field deeper in the hole was rotated with respect to that higher in the hole, and that the maximum principal stress was closer to vertical. Such a downward decrease in dip of foliation is also consistent with stacked listric normal faults, which flatten with depth as they pass downward into the underlying ductile zone.

Cataclastic Deformation

Three separate major zones of autoclastic metagabbro breccia were drilled at 176–181, 273–275.5, and 328.5–330 mbsf. The uppermost zone coincides with the contact between lithologic Units II and III; the second lies just below the base of the mylonite separating the Unit IV magnetite-ilmenite gabbro from the underlying Unit V olivine gabbro; whereas the third such zone appears to lie within Unit V. In the former two cases, faults or lithological contacts possibly may have localized hydrothermal alteration. The base of the mylonite at the bottom

of Unit IV shows the effects of the hydrothermal alteration, which is developed much more extensively in the brecciated gabbro below it. Thus, the hydrothermal alteration post-dates the plastic deformation in this zone. The breccia zones all appear structurally similar, although they contain somewhat different mineral assemblages. The lowermost zone is particularly well exposed in the core, beginning with an amphibole-rich vein that cuts upward into massive gabbro. Downward, the vein broadens to enclose angular fragments of the gabbro and its constituent minerals, which appear to be *in situ*. Hydrothermal epidote, quartz, and plagioclase occur in the cementing matrix. The vein disappears into disaggregated gabbro and mineral fragments that seem randomly arranged in a matrix of finer-grained fragments and hydrothermal minerals. The breccias show no evidence of plastic deformation, although considerable cataclasis and possibly crushing has occurred, which suggests that these breccias post-date the plastic deformation. These zones could represent hydrothermal upflow zones, perhaps the product of fluids hydrofracturing through the gabbro.

Intrusive Contacts

A single basalt dike crosscuts gabbro in Sections 118-735B-23R-4 and 118-735B-23R-5 (100 mbsf). It consists of chemically normal mid-ocean ridge basalt (see “Geochemistry” section, this chapter). Both dike contacts were recovered in the core and dip at 50°. The dike has well-developed, chilled margins that consist of fine-grained to cryptocrystalline glassy basalt containing olivine and plagioclase microphenocrysts. The interior of the dike is substantially more altered and coarser grained and consists of fine-grained basalt having a greenish cast in hand specimen. Unfortunately, the particular pieces containing the contacts are unveined and unfoliated; thus, we could not determine if the basalt was crosscutting the foliation or the vein sets. The dike appears to be undeformed and at least 70 cm thick. The dip of the contacts, however, is close to that for the mean of the veins, which suggests that it could have been intruded under the same stress regime as the veins.

Trondjemite veins composed largely of plagioclase and quartz were also found in the core. These veins crosscut gabbro having gneissic foliation in Cores 118-735B-53R and -54R (255 mbsf), where a small stockwork of trondjemite veins occurs. Locally, the veins appear to have a trellised structure, with some apparent digestion of the wall rock indicated by a grayish color in the trondjemite adjacent to the gabbro. The trondjemite veins strike parallel to the gneissic structure, but dip 85°, 38°, and 45° from the dip of the foliation. Trondjemites are generally believed to mark the last stage of magmatic evolution in ocean-ridge magma chambers. Given the evidence for local assimilation of the wall rock by the trondjemite, the wall rocks must have been very hot and near their solidus at the time of intrusion. Thus, it is evident that the gneissic foliation must have developed near the region of magmatic activity at the ridge axis. This hypothesis is consistent with the high-temperature mineral assemblage found in the gneisses (see “Metamorphism and Alteration” section, this chapter).

Igneous Lamination and Layering

Crystal layering is evident in a number of different forms throughout the section. The principal types include graded layering, phase layering, and modal layering. The most easily measured feature is an igneous lamination consisting of minerals that show a preferred tabular orientation, presumably as a result of crystal settling. The igneous lamination is marked by the shape fabric of euhedral plagioclase and clinopyroxene crystals. This lamination is well defined in the olivine gabbros and iron-titanium oxide gabbros of lithologic Units III and IV (see Fig. 6 and “Lithostratigraphy” section, this chapter). Lower in the

section, well-developed phase layering occurs but is more difficult to measure. Plastic deformation textures may overprint the igneous lamination. When this is the case, the plastic foliation commonly crosscuts the igneous lamination at a high angle (Figs. 10A and 10B).

Downhole Structural Evolution

Distribution of the Textural Types

The log of the plastic deformation textures indicated a rough qualitative estimate of the downhole strain distribution (with a nonlinear scale; Fig. 7). Textures are well foliated to mylonitic from 0 to 40 mbsf. Deformation is then constrained to narrow, well-foliated to mylonitic zones down to about 250 mbsf. From 250 mbsf to the second brecciated zone at 273 mbsf, a pervasively deformed interval containing augen gneissic and mylonitic bands occurs. The gabbro is undeformed down to 405 mbsf. From 405 to 500.7 mbsf, the gabbro ranges from undeformed to augen gneissic having mylonitic bands too thin to plot on the log.

Overall, there are three main zones of plastic deformation, which suggests three major ductile faults. At least one of these faults separates two distinct petrologic units (the magnetite-ilmenite gabbro of Unit IV and the olivine gabbro of Unit V). In addition, a 60-cm-thick zone of augen gneissic gabbro having mylonitic bands occurs at the bottom of Unit III at 224 mbsf (Fig. 7); this could also be a ductile fault.

Igneous laminations and occasional igneous graded or modal layering are consistently present from 170 mbsf to the brecciated zone at 273 mbsf (Fig. 7). The laminations decrease in dip downhole from 60° at 170 mbsf to 0°–5° at 240 mbsf. Below this depth, the dip stabilizes and remains subhorizontal down to 250 mbsf. The zone of intense shear (about 60 cm of mylonitic and gneissic gabbro) at the Unit III/Unit IV boundary (223 mbsf) cuts the igneous lamination (Fig. 10B) without deflecting or otherwise disturbing it. This indicates that, at least here, the deformation post-dated the total solidification of the gabbro (Fig. 7).

Dip of the Foliation

The foliation dips 0° to 60° and averages about 35° in the upper portion of the hole and about 20° near its bottom (Fig. 7). There are significant deviations from this overall pattern downhole. For example, foliations in the interval between 24 and 26 mbsf are subhorizontal, and in the interval at 400–435 mbsf the gabbros are cut by mylonitic shear zones a few centimeters thick that dip 50° to 70°. The lineations produced by mineral elongations, when visible in the cored section, are usually downdip, indicating normal or reverse faulting, rather than strike-slip motion. The steeper dipping shear zones below 400 mbsf have a sense of shear that suggests normal faults, which may post-date the low-angle fault planes associated with the general foliation.

PRIMARY PETROGRAPHY

A variety of igneous and meta-igneous rocks were recovered at Site 735. These include olivine-bearing and olivine gabbros, two-pyroxene gabbros, iron-titanium oxide-rich gabbros, troctolites, microgabbros, and rare basalts and trondjemites. The two-pyroxene gabbros appear principally as porphyroclastic rocks in lithologic Unit I, along with metamorphosed olivine gabbros. Olivine and olivine-bearing gabbros are the principal constituent of Units II, III, V, and VI. Iron-titanium oxide gabbros are the dominant lithology in Unit IV but also occur in thin intervals in Units II, III, and VI. Troctolites are most abundant in Unit VI, but are found rarely in Units II and V.

Porphyroclastic Gabbro

There are no igneous textures preserved in any of the porphyroclastic and mylonitic gabbros that make up Unit I from Holes 735A and 735B. Textures range from weakly foliated to mylonitic but are predominately porphyroclastic. Relict plagioclase, orthopyroxene, clinopyroxene, and iron-titanium oxides occur as porphyroclasts in a recrystallized matrix dominated by plagioclase. The plagioclase porphyroclasts are undulose, elongate augen, ranging from 4 to 10 mm in size. They make up from 5% to 30% of the rock; initial plagioclase abundances are estimated to have been 50% to 60%. Compositions are estimated optically to be between An_{40} and An_{60} . Clinopyroxene occurs as 1- to 4-mm-wide augen, which now make up 2% to 15% of the rock but originally composed 30% to 50%. Orthopyroxene augen are 6 to 7 mm in size and make up 0% to 4% of the samples studied; original orthopyroxene abundances are estimated to have been from 0% to 10%. The pyroxene augen are bent and sometimes fractured. The clinopyroxene grains commonly have small patches and rims of brown amphibole. Olivine grains, 0.1 to 5 mm in diameter, occur in samples from Cores 118-735B-2D and 118-735B-6D through 118-735B-11D in abundances from 0% to 4%. We believe that the olivine composed up to 12% of the original rock. Orthopyroxene and olivine are found together in Sample 118-735B-10D-1, 24–26 cm, Piece 6A, and are inferred to have coexisted in one or two other samples. Small grains of iron-titanium oxide make up 2% to 3% of some samples; in rare cases, it may be as much as 23%. We believe that some of this oxide is primary, particularly in the orthopyroxene-bearing samples; however, much of it may be secondary because it (1) fills fractures perpendicular to the foliation, (2) occurs preferentially in porous portions of the rock, and (3) is sometimes associated with post-deformational development of green amphibole.

The olivine-bearing porphyroclastic gabbros are more common than the orthopyroxene-bearing gabbros from Core 118-735B-7D downward, although orthopyroxene-bearing gabbros do occur in this interval. This increase in olivine is reflected in more magnesian bulk-rock compositions, and probably indicates the occurrence of at least two protoliths for the porphyroclastic gabbros: olivine-bearing gabbro such as that found in Unit II and two-pyroxene gabbro or noritic gabbro. The latter is most common in Cores 118-735B-1D to -6D, and the former is the principal protolith in Cores 118-735B-7D to -10D.

Olivine-Bearing and Olivine Gabbros

Olivine-bearing (<5% modal olivine) and olivine (>5% modal olivine) gabbros are the most abundant rock types recovered from Hole 735B. They are the main rock types in lithologic Units II, III, V, and VI. Their primary mineralogy, estimated by point counting—2000 points on 5 × 8 cm thin sections or 1000–1500 points on standard thin sections—consists of olivine (0%–25%), plagioclase (40%–70%), clinopyroxene (30%–50%), orthopyroxene (generally in trace amounts but up to 3%), and trace amounts of opaques, primary brown amphibole, and sulfides (see Table 3). Modal proportions in thin section vary considerably (Fig. 13), which partly reflects modal and phase layering within the intrusion(s) (see “Textural Variations” section, this chapter) and partly reflects the irregular distribution of crystals in coarse-grained rocks. The average grain size varies from fine (<1 mm) to very coarse (approximately 10 mm) and varies systematically within normally graded units (discussed in more detail in “Textural Variations” section, this chapter). Based on optical determinations, olivine compositions range from Fo_{65} to Fo_{85} , with an average of Fo_{80} , and plagioclase compositions range from An_{55} to An_{72} , with an average of An_{65} .

Table 3. Mineral modes determined by point counting.

Core/section: Interval (cm): Rock type ¹ :	118-735B-1D-1 78-82 1,9	118-735B-1D-1 117-120 1,9	118-735B-2D-2 116-120 2,9	118-735B-7D-1 74-76 2,9	118-735B-10D-2 18-20 2,9
<i>Primary minerals</i>					
Olivine			3.7		4.5
Plagioclase	30.9	23.0	55.1	8.6	19.8
Clinopyroxene	13.0	2.2	10.7	15.0	27.9
Low-Ca pyroxene					
Opaques		3.3			
<i>Secondary minerals</i>					
Clay minerals	10.1			tr	
Carbonate	tr			1.0	
Chlorite			1.4		tr
Brown amphibole	15.6	21.5	8.6	4.0	
Actinolite	5.9	8.6	0.6	21.8	10.3
Tremolite	11.3		3.2	10.4	2.1
Magnetite	4.4		0.8	0.5	1.3
Talc			1.7		
Plagioclase (neoblasts)	8.8	41.1	13.0	38.5	24.6
Clinopyroxene (neoblasts)			0.4		7.8
Orthopyroxene (exsolution)					0.4
Other			0.8	0.2	1.3

Modes are based on point counts of greater than 500 points.

¹ Key to rock types: (1) gabbro, (2) olivine gabbro, (3) Fe-Ti gabbro, (4) norite, (5) troctolite, (6) microgabbro, (7) basalt, (8) altered sample, (9) deformed and/or metamorphosed sample, (10) sample including a contact between two rock types or distinctive textures.

Table 3 (continued).

Core/section: Interval (cm): Rock Type ¹ :	118-735B-19R-3 73-75 2,8	118-735B-19R-5 47-50 1,9	118-735B-20R-2 54-56 2	118-735B-21R-2 53-56 2	118-735B-21R-2 57-63 1
<i>Primary minerals</i>					
Olivine	2.8		6.1	3.0	1.6
Plagioclase	40.0	10.0	61.2	51.9	64.5
Clinopyroxene	7.9	9.1	30.7	29.6	25.7
Low-Ca pyroxene		4.4			
Opaques					
<i>Secondary minerals</i>					
Clay minerals	3.0	3.0			
Carbonate					
Chlorite	0.2		0.1	0.4	
Brown amphibole		1.1	0.7		0.5
Actinolite	27.0	15.2	0.1	3.9	4.6
Tremolite	2.0		0.2	1.5	1.8
Magnetite	1.0	1.8	0.1	0.1	0.1
Talc	0.4		0.7	0.7	0.9
Plagioclase (neoblasts)	14.5	52.0		8.6	
Clinopyroxene (neoblasts)		3.4		0.3	
Orthopyroxene (exsolution)			0.1		
Other					

Typically, the gabbros and olivine gabbros are massive and have poorly defined layering and localized deformation structures. Near shear zones, porphyroclastic and mylonitic textures are common, and more than 50% of the rock has been recrystallized, thus obscuring primary grain sizes and shapes (see "Deformation and Structure" section, this chapter). In most of these rocks, however, the amount of recrystallization is limited to less than 5%, and the only evidence of strain is microscopic, including nearly ubiquitous kink banding in olivine and bent

and/or dislocated twin lamellae in plagioclase. The degree of alteration varies from negligible to almost 50% and generally decreases downhole (Table 3). The types of alteration are discussed in detail in the "Metamorphism and Alteration" section, this chapter.

On the basis of primary textures, the gabbros and olivine gabbros can be subdivided into three groups: (1) poikilitic gabbro (Fig. 14), characterized by clinopyroxene oikocrysts that enclose or partially enclose plagioclase and sometimes olivine; (2)

Table 3 (continued).

Core/section: Interval (cm): Rock Type ¹ :	118-735B-13R-2 55-58 2,9	118-735B-14R-4 22-25 2,9	118-735B-15R-3 92-96 1	118-735B-16R-5 47-51 6	118-735B-18R-2 143-146 2,8
<i>Primary minerals</i>					
Olivine	2.0	6.8	0.6	10.9	1.2
Plagioclase	41.0	11.8	23.5	52.5	52.2
Clinopyroxene	18.9	10.5	19.8	25.4	25.2
Low-Ca pyroxene					
Opaques					
<i>Secondary minerals</i>					
Clay minerals		2.2	1.3	2.0	
Carbonate				tr	0.2
Chlorite	2.4	0.8	0.1		4.6
Brown amphibole	0.2	2.5	6.5	1.8	
Actinolite	4.6	5.2	19.2	2.8	6.2
Tremolite	2.6	tr	2.1		6.2
Magnetite	0.1	1.2	2.4	0.1	2.6
Talc	0.3	2.0	1.1	4.3	1.6
Plagioclase (neoblasts)	27.3	51.3	22.9		
Clinopyroxene (neoblasts)	0.6	4.2			
Orthopyroxene (exsolution)		0.7		0.2	
Other					

Table 3 (continued).

Core/section: Interval (cm): Rock Type ¹ :	118-735B-22R-2 86-91 2	118-735B-22R-2 110-115 2,8	118-735B-22R-3 116-120 2,8	118-735B-23R-2 34-36 2	118-735B-23R-3 34-37 3
<i>Primary minerals</i>					
Olivine	17.8	0.3	0.4	3.7	
Plagioclase	32.6	52.6	40.0	53.2	20.0
Clinopyroxene	40.7	10.8	14.4	33.8	45.7
Low-Ca pyroxene					6.4
Opaques					15.0
<i>Secondary minerals</i>					
Clay minerals	0.3	1.7	3.0		
Carbonate				tr	
Chlorite	tr	1.7	2.0	1.2	tr
Brown amphibole	1.2	tr	tr		6.6
Actinolite	3.5	29.1	33.9	6.3	6.3
Tremolite	0.5	2.4	1.5	1.4	
Magnetite	1.5	0.5	1.0	0.2	
Talc	1.2	0.1		0.2	
Plagioclase (neoblasts)					
Clinopyroxene (neoblasts)					
Orthopyroxene (exsolution)	tr				
Other		0.1			

granular gabbro (Fig. 15), characterized by tabular or prismatic plagioclase, subhedral clinopyroxene, and anhedral to subhedral olivine; and (3) equigranular microgabbro, which is distinctly finer grained (0.5–1.5 mm) than the main gabbro units. Use of the term microgabbro follows that of MacKenzie et al. (1982), who applied it to the fine-grained marginal facies of the Skaergaard intrusion.

Poikilitic gabbro is the most common type. These rocks are medium- to coarse-grained and contain clinopyroxene oikocry-

sts ranging in size from 2 mm to 10 cm. In many places, the oikocrysts are elongated in a subvertical direction (see "Textural Variations" section, this chapter). The pyroxene oikocrysts enclose chadacrysts of euhedral plagioclase and olivine. In rare instances, chadacrysts of olivine and plagioclase are intergrown and surrounded by clinopyroxene, indicating that olivine and plagioclase crystallized together prior to the crystallization of clinopyroxene. Granular gabbros are also medium- to coarse-grained. They are characteristic of the bottom part of size-

Table 3 (continued).

Core/section: Interval (cm): Rock Type ¹ :	118-735B-23R-4 120-122 7	118-735B-24R-4 26-28 1	118-735B-25R-3 144-146 2	118-735B-26R-1 135-138 6,10	118-735B-26R-1 135-138 2,10
<i>Primary minerals</i>					
Olivine		1.1	9.4	3.7	8.0
Plagioclase	51.0	51.1	49.6	49.8	34.5
Clinopyroxene	24.1	18.9	26.4	14.8	30.9
Low-Ca pyroxene					tr
Opagues	3.3		tr		
<i>Secondary minerals</i>					
Clay minerals	16.0	3.0	0.3	0.3	0.8
Carbonate					
Chlorite		tr			
Brown amphibole		tr	tr	3.7	0.8
Actinolite		23.9	3.3	14.6	12.7
Tremolite		0.6	5.1	3.1	3.6
Magnetite		0.5	0.2	3.9	2.2
Talc	5.3	0.3	5.6	5.4	6.2
Plagioclase (neoblasts)					
Clinopyroxene (neoblasts)					
Orthopyroxene (exsolution)					
Other					

Table 3 (continued).

Core/section: Interval (cm): Rock Type ¹ :	118-735B-34R-4 8-12 3	118-735B-35R-1 29-31 2	118-735B-35R-4 43-46 2	118-735B-36R-3 28-34 1,10	118-735B-36R-3 28-34 2,10
<i>Primary minerals</i>					
Olivine	0.7	5.7	8.6		0.6
Plagioclase	42.3	56.0	49.0	52.4	59.3
Clinopyroxene	32.2	21.8	24.8	41.2	25.4
Low-Ca pyroxene					
Opagues	20.8		tr		
<i>Secondary minerals</i>					
Clay minerals	1.6		0.1		
Carbonate					
Chlorite	0.1	0.8	0.5		
Brown amphibole	0.2	0.1		1.5	2.6
Actinolite	0.6	9.2	9.0	4.8	8.2
Tremolite		6.2	6.7		0.5
Magnetite		0.1	0.7		2.5
Talc					
Plagioclase (neoblasts)					
Clinopyroxene (neoblasts)					
Orthopyroxene (exsolution)	1.2				
Other			0.6		

graded units and sometimes form 1- to 5-cm-thick monomineralic or biminerallitic layers (see "Textural Variations" section, this chapter). Olivine microgabbros occur sporadically as isolated pods or intrusive dikes or sills in Cores 118-735B-16R to 118-735B-40R (Fig. 16). Modal proportions determined in two microgabbros, one from Core 118-735B-16R and one from Core 118-735B-26R, are almost identical (Table 3): the average being 19% olivine, 53% plagioclase, and 28% clinopyroxene. Microgabbros of other lithologies, e.g., troctolite and iron-titanium oxide gabbro, occur elsewhere.

Crystals in the poikilitic and granular gabbros exhibit a variety of complex intergrowths. These include penetrative intergrowths between multiple clinopyroxene grains as well as between clinopy-

roxene and plagioclase grains. In extreme examples, blebby lamellae enclosed in one grain are optically continuous with an entire neighboring crystal. Another type of intergrowth is exhibited by vermicular (wormy) lamellae in clinopyroxene. These occur in pristine unaltered samples, sometimes appearing in only one side of a twinned crystal. They also occur in altered samples where clinopyroxene and amphibole form symplectic intergrowths at the margins of clinopyroxene grains. In the latter case, alteration of clinopyroxene appears to be controlled by crystal structure.

Textural relationships in thin sections and geochemical data (low abundances of incompatible elements, see "Geochemistry" section, this chapter) indicate that the olivine and olivine-

Table 3 (continued).

Core/section: Interval (cm): Rock Type ¹ :	118-735B-28R-3 63-69 4	118-735B-31R-2 40-45 2	118-735B-33R-3 85-89 1	118-735B-34R-1 103-105 2	118-735B-34R-2 18-22 2
<i>Primary minerals</i>					
Olivine	0.1	1.8	0.7	11.7	10.0
Plagioclase	58.4	53.3	67.0	47.6	61.7
Clinopyroxene	2.0	36.4	24.9	25.7	21.4
Low-Ca pyroxene	29.9				
Opagues	0.4			tr	0.1
<i>Secondary minerals</i>					
Clay minerals	0.4	0.2		1.6	0.5
Carbonate		tr		0.1	
Chlorite		0.3	1.4	0.3	0.9
Brown amphibole	2.8		tr	0.1	0.1
Actinolite	tr	4.2	4.5	2.8	0.5
Tremolite	5.1	3.2	1.4	3.8	2.4
Magnetite		0.1	0.1	1.0	
Talc		0.4		5.1	2.3
Plagioclase (neoblasts)					
Clinopyroxene (neoblasts)					
Orthopyroxene (exsolution)				0.2	0.1
Other	0.9				

Table 3 (continued).

Core/section: Interval (cm): Rock Type ² :	118-735B-37R-1 11-13 1	118-735B-38R-2 78-84 2	118-735B-40R-5 13-15 1	118-735B-41R-4 20-27 2	118-735B-42R-2 119-121 2
<i>Primary minerals</i>					
Olivine	0.9	22.6	3.1	3.4	8.1
Plagioclase	44.0	30.8	57.6	56.0	77.3
Clinopyroxene	23.4	37.2	35.2	27.8	8.5
Low-Ca pyroxene		tr		1.9	
Ilmenite		0.2	0.7	0.4	1.0
<i>Secondary minerals</i>					
Clay minerals	0.1		0.7	1.0	
Carbonate					
Chlorite	0.8	1.0		0.6	1.1
Brown amphibole	1.7		1.1	tr	tr
Actinolite	18.2	2.3	0.3	6.9	1.8
Tremolite	0.2	3.3		0.8	0.4
Magnetite	0.7	1.0	0.7	0.2	0.9
Talc					0.4
Plagioclase (neoblasts)	10.0				
Clinopyroxene (neoblasts)					
Orthopyroxene (exsolution)					tr
Other		1.6			

bearing gabbros are cumulates, i.e., they represent crystal concentrates formed during magmatic crystallization. They may form by *in-situ* crystallization on the walls, floor, or roof of a magma chamber, as well as by crystal sorting due to crystal/liquid density differences. Olivine, plagioclase, and clinopyroxene are the cumulus phases in the olivine gabbros. Intercumulus phases include overgrowths on cumulus phases, such as suggested by concentric, progressive extinction of plagioclase rims, and phases restricted to interstitial areas, such as iron-titanium oxides, sulfides, orthopyroxene, and primary brown amphibole. In some cases, the pore spaces between cumulus crystals are filled with symplectic intergrowths of orthopyroxene and iron-titanium oxide. Intercumulus phases represent the crystalliza-

tion products of liquid trapped in the pore space of accumulated crystals. Based on petrographic and geochemical data, the amount of crystallized trapped liquid in the olivine gabbros was 5% to 20%, which makes these gabbros adcumulates and mesocumulates.

Troctolites

The troctolites (olivine and plagioclase-rich gabbros) from Hole 735B fall into two categories: (1) medium-grained poikilitic and (2) fine-grained equigranular. The poikilitic variety is characterized by oikocrystic olivine enclosing plagioclase or by oikocrystic plagioclase enclosing olivine and contains on average 43% olivine (1-6 mm), 53% plagioclase (1-10 mm), 3% cli-

Table 3 (continued).

Core/section: Interval (cm): Rock Type ¹ :	118-735B-44R-3	118-735B-45R-1	118-735B-45R-1	118-735B-46R-4	118-735B-47R-4
	78-81	48-51	48-51	109-113	80-86
	2	2,10	3,10	3	2
<i>Primary minerals</i>					
Olivine	12.5	2.5			6.4
Plagioclase	54.4	60.5	39.4	53.6	46.1
Clinopyroxene	29.2	34.4	28.1	18.5	35.3
Low-Ca pyroxene	0.1		9.2		
Opagues		0.3	9.0	12.8	
<i>Secondary minerals</i>					
Clay minerals		tr		tr	0.7
Carbonate					
Chlorite	0.2			0.1	0.7
Brown amphibole	0.1	0.2	1.3	3.0	0.4
Actinolite		0.3	2.5	7.0	8.1
Tremolite	1.9				1.1
Magnetite		0.3			0.9
Talc					
Plagioclase (neoblasts)			10.1	2.0	
Clinopyroxene (neoblasts)					
Orthopyroxene (exsolution)		1.1			
Other	1.5				

Table 3 (continued).

Core/section: Interval (cm): Rock Type ¹ :	118-735B-52R-4	118-735B-54R-5	118-735B-58R-3	118-735B-59R-4	118-735B-61R-1
	88-94	117-119	107-114	29-35	85-87
	3	3	2	2	2
<i>Primary minerals</i>					
Olivine		0.5	9.8	6.9	5.6
Plagioclase	38.4	25.0	57.8	52.4	53.4
Clinopyroxene	24.9	44.7	30.6	39.6	37.4
Low-Ca pyroxene			0.5		
Opagues	11.2	9.7	0.2	0.1	
<i>Secondary minerals</i>					
Clay minerals	0.2	1.8	0.1	0.1	0.2
Carbonate	tr				
Chlorite	tr				
Brown amphibole	5.6	1.8		tr	0.7
Actinolite	14.9	5.4		0.2	1.3
Tremolite	0.5		0.5		
Magnetite			0.2	0.1	0.6
Talc				0.6	0.1
Plagioclase (neoblasts)	4.2	10.2			
Clinopyroxene (neoblasts)					
Orthopyroxene (exsolution)		0.5		tr	
Other			0.2		

nopyroxene (1-20 mm), up to 1% spinel, and trace amounts of sulfide. In contrast, the fine-grained equigranular variety contains on average 22% olivine (0.1-1.5 mm), 67% plagioclase (0.2-2 mm), 9% clinopyroxene (0.1-2 mm), 0.5% orthopyroxene, 1.5% brown amphibole, and trace amounts of spinel and sulfide. The different mineralogies probably indicate a difference in the proportion of cumulus to intercumulus phases, the coarse poikilitic variety having a greater proportion of cumulus olivine and the finer-grained variety having a greater proportion of trapped intercumulus liquid.

Troctolites or troctolitic gabbros were noted either in visual core descriptions or in thin section descriptions in Cores 118-735B-12R, -20R, -38R, and -79R to -87R (Fig. 16). Their fre-

quency and number increase toward the bottom of the hole. Furthermore, the coarser-grained olivine-rich variety appears to be restricted to Cores 118-735B-79R and -87R. This undoubtedly reflects both greater accumulation of olivine near the bottom of the hole and crystallization of more primitive (higher MgO) liquids. This is consistent with the geochemical data, which indicates higher bulk-rock Mg/(Mg + Fe) ratios in the last few cores.

Iron-Titanium Oxide Gabbro

Iron-titanium oxide gabbros generally contain more than 5% opaque minerals. The opaque minerals are mainly ilmenite and magnetite, but minor amounts of sulfides, such as pyrrhotite,

Table 3 (continued).

Core/section: Interval (cm): Rock Type ¹ :	118-735B-49R-1 42-46 3	118-735B-50R-2 43-47 3	118-735B-50R-4 87-89 3	118-735B-51R-1 102-104 3	118-735B-52R-4 69-71 3
<i>Primary minerals</i>					
Olivine	0.1	0.1			0.1
Plagioclase	49.5	36.6	58.7	58.3	30.6
Clinopyroxene	26.6	16.8	15.2	12.2	37.8
Low-Ca pyroxene					
Opaques	15.1	21.9	5.9	7.3	15.0
<i>Secondary minerals</i>					
Clay minerals	0.8	0.4			1.1
Carbonate	0.4				
Chlorite			0.5	0.5	
Brown amphibole	0.5	1.0	1.6	2.0	2.9
Actinolite	6.4	23.0	3.5	7.1	4.2
Tremolite	tr	0.2		0.3	0.9
Magnetite					tr
Talc		0.1			
Plagioclase (neoblasts)	0.6		14.2	11.8	7.0
Clinopyroxene (neoblasts)					
Orthopyroxene (exsolution)	0.1		0.1		
Other					

Table 3 (continued).

Core/section: Interval (cm): Rock Type ¹ :	118-735B-62R-1 91-94 2	118-735B-63R-5 126-130 2,9	118-735B-65R-3 54-58 2	118-735B-67R-3 74-78 1	118-735B-68R-2 16-21 2
<i>Primary minerals</i>					
Olivine	7.0	5.9	9.0	2.0	13.4
Plagioclase	58.9	59.0	54.6	65.3	64.0
Clinopyroxene	31.8	24.9	34.5	19.3	20.7
Low-Ca pyroxene					
Opaques	tr	tr	0.2		
<i>Secondary minerals</i>					
Clay minerals	tr	0.3	0.1	0.7	
Carbonate		tr			
Chlorite		0.6	0.2	0.6	1.0
Brown amphibole	0.3	3.9	tr	0.7	tr
Actinolite	1.2	3.3	tr	8.8	
Tremolite		tr	0.8	tr	0.4
Magnetite		0.5	0.1	0.2	0.3
Talc	0.3			1.9	
Plagioclase (neoblasts)					
Clinopyroxene (neoblasts)					
Orthopyroxene (exsolution)					0.2
Other		1.6	0.2		

chalcopyrite, and pyrite, are also present. Fresh iron-titanium oxide gabbro is gray and has dark gray specks of a metallic luster. When altered or metamorphosed, the rock becomes greenish. Iron-titanium oxide gabbro has the following general characteristics.

1. It contains calcium-poor pyroxenes (orthopyroxene and/or inverted pigeonite). Almost one-third of the iron-titanium oxide gabbros contain inverted pigeonite (Fig. 8), but this mineral is absent in other types of gabbro from Hole 735B.

2. Clinopyroxene usually has (001) exsolution lamellae, which are absent in other types of gabbro from Hole 735B.

3. Clinopyroxene commonly contains patches of orthopyroxene or inverted pigeonite, which show the same crystallographic orientation as exsolution in the host clinopyroxene.

4. Olivine is generally low in abundance (<2%) (Fig. 17), although a few olivine-rich iron-titanium oxide gabbros are present.

Iron-titanium oxide gabbros occur most abundantly from Sections 118-735B-46R-3 to 118-735B-56R-2 (Unit IV). Above lithologic Unit IV, there are some thin intervals (0.1-1 m) of iron-titanium oxide gabbro; these are in Sections 118-735B-23R-3, -24R-2, -24R-3, -28R-3, -28R-4, -32R-1, -34R-4, -37R-3, -38R-1, -38R-3, -38R-4, -44R-1, -44R-2, -44R-3, and -45R-1 (Fig. 8). At

Table 3 (continued).

Core/section: Interval (cm): Rock Type ¹ :	118-735B-69R-3 86-92 2	118-735B-70R-1 80-84 2	118-735B-71R-3 0-5 2	118-735B-72R-2 56-61 2	118-735B-73R-1 54-57 2
<i>Primary minerals</i>					
Olivine	3.5	2.1	6.1	8.2	4.0
Plagioclase	53.4	57.2	54.5	65.0	41.1
Clinopyroxene	35.8	32.6	35.0	26.0	39.6
Low-Ca pyroxene				0.1	
Opaques			0.2	0.2	0.2
<i>Secondary minerals</i>					
Clay minerals		0.6	tr		0.6
Carbonate					
Chlorite			0.2		
Brown amphibole		0.1	tr	0.1	11.4
Actinolite	3.9	5.2	2.0	0.4	1.9
Tremolite	2.5	1.5	1.5	tr	1.2
Magnetite	0.5	0.1		tr	
Talc	tr	tr			tr
Plagioclase (neoblasts)					
Clinopyroxene (neoblasts)					
Orthopyroxene (exsolution)					
Other				0.1	

Table 3 (continued).

Core/section: Interval (cm): Rock Type ¹ :	118-735B-79R-7 99-102 5	118-735B-80R-2 35-40 5	118-735B-80R-6 6-9 5	118-735B-81R-5 1-7 2	118-735B-84R-5 80-82 2
<i>Primary minerals</i>					
Olivine	19.8	19.5	11.5	7.3	10.2
Plagioclase	72.6	64.6	50.3	59.1	51.1
Clinopyroxene	5.7	15.4	35.1	31.3	33.9
Low-Ca pyroxene					
Opaques	0.2		tr	tr	0.4
<i>Secondary minerals</i>					
Clay minerals		0.1	0.5	0.1	
Carbonate					
Chlorite				tr	
Brown amphibole	1.7	0.3	1.7	0.2	0.8
Actinolite				0.3	1.4
Tremolite				0.5	1.5
Magnetite			0.3		0.3
Talc				tr	tr
Plagioclase (neoblasts)					
Clinopyroxene (neoblasts)					
Orthopyroxene (exsolution)					
Other			0.1		

the top of Unit IV, iron-titanium oxide gabbros are separated from olivine gabbros by a 60-cm-thick mylonite zone that cuts magmatic foliation developed in both the upper olivine gabbros and the lower iron-titanium oxide gabbros. The frequency of occurrence of iron-titanium oxide gabbros abruptly increases below Section 118-735B-46R-3 (Fig. 8). Similarly, the bottom of the unit is bounded by a mylonite zone about 6 m thick. Below this tectonic boundary, no iron-titanium oxide gabbro (except for minor opaque-rich zones) appears until a minor interval in Section 118-735B-73R-5 (Fig. 8). Within Unit IV, there are two intervals, 50–60 cm thick, where iron-titanium oxide-poor olivine gabbro occurs (Sections 118-735B-47R-3 and -48R-1). Con-

tacts between the olivine gabbros and surrounding iron-titanium oxide gabbros are very sharp, and the abundance of opaque minerals changes abruptly (Fig. 18). Below Section 118-735B-73R-5, there are some intervals that contain minor iron-titanium oxide gabbro, such as in Sections 118-735B-76R-1, -76R-3, -76R-4, and -79R-7 (Fig. 8). Below Section 118-735B-80R-6, iron-titanium oxide gabbro occurs intermittently with relatively abundant intervals in Sections 118-735B-80R-6, -80R-7, -81R-4, -82R-1, -82R-5, and -82R-6 (Fig. 8). It is nearly absent from the interval between Section 118-735B-83R-1 and Section 118-735B-85R-3, and ilmenite layers (less than 10 cm) appear only in Sections 118-735B-83R-5 and -84R-5. Below Section 118-735B-85R-4,

Table 3 (continued).

Core/section: Interval (cm): Rock Type ¹ :	118-735B-74R-6 41-43 6	118-735B-75R-5 27-30 1	118-735B-76R-3 93-97 2	118-735B-78R-1 132-136 2	118-735B-79R-6 90-95 5
<i>Primary minerals</i>					
Olivine		2.2	8.0	9.2	27.8
Plagioclase	57.0	57.7	63.8	51.3	68.0
Clinopyroxene	23.5	37.2	25.1	35.0	3.0
Low-Ca pyroxene	11.5				
Opaques	5.8	0.1	0.1		tr
Apatite	0.5				
<i>Secondary minerals</i>					
Clay minerals	tr		0.1	0.8	tr
Carbonate					
Chlorite			0.1	0.6	
Brown amphibole			tr	1.4	0.5
Actinolite	1.2	0.9	0.8	0.2	
Tremolite	0.5			0.1	
Magnetite		0.9	1.1	0.6	0.2
Talc			0.5	0.2	
Plagioclase (neoblasts)					
Clinopyroxene (neoblasts)					
Orthopyroxene (exsolution)					
Other		1.0			

Table 3 (continued).

Core/section: Interval (cm): Rock Type ¹ :	118-735B-85-7 17-19 5
<i>Primary minerals</i>	
Olivine	15.0
Plagioclase	65.0
Clinopyroxene	3.9
Low-Ca pyroxene	1.3
Opaques	tr
<i>Secondary minerals</i>	
Clay minerals	
Carbonate	
Chlorite	1.6
Brown amphibole	1.2
Actinolite	6.4
Tremolite	4.6
Magnetite	
Talc	tr
Plagioclase (neoblasts)	
Clinopyroxene (neoblasts)	
Orthopyroxene (exsolution)	
Other	

abundant iron-titanium oxide gabbro alternates on small scales (0.1–2 m) with iron-titanium oxide-free gabbro (olivine gabbro and troctolite) down to Section 118-735B-87R-6 (Fig. 8).

The primary minerals in iron-titanium oxide gabbros are plagioclase, clinopyroxene, iron-titanium oxide, ± olivine, and ± calcium-poor pyroxene (either orthopyroxene or inverted pigeonite). Minor amounts of reddish-brown hornblende, apatite, and sulfide are also present. The variation in abundance of iron-titanium oxide is wide ranging, from about 5% to 25%. Iron-titanium oxide gabbros having high concentrations of opaque minerals occur as layers ranging from 1 cm to 1 m thick. Iron-titanium oxides are ilmenite or magnetite with ilmenite exsolu-

tion lamellae. The volume ratio of ilmenite and magnetite varies from 1:2 to 2:1. Most of the iron-titanium oxide gabbros are poor in olivine and commonly contain less than 2% (Figs. 17 and 18). Some contain no olivine at all (e.g., Sample 118-735B-50R-4, 87–89 cm, Piece 1C). The modal abundance of calcium-poor pyroxene ranges from 0.5% to 3%. There are a few iron-titanium oxide gabbros that contain up to 10% olivine (e.g., Sample 118-735B-54R-3, 125–127 cm, Piece 3). These contain little calcium-poor pyroxene (as low as 0.1%). The reddish-brown hornblende (<1%) is probably primary, based on its high pleochroism and reddish tint. Primary sulfides include pyrrhotite, chalcopyrite, and pyrite. Their total modal abundance

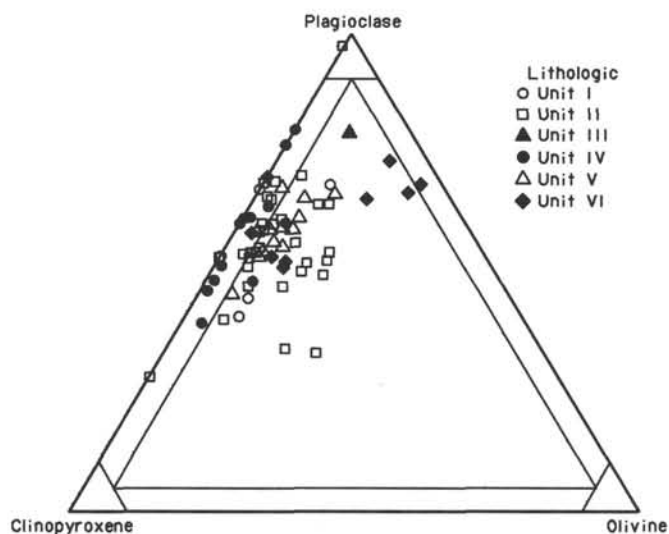


Figure 13. Modal proportions of plagioclase, clinopyroxene, and olivine. Proportions were determined by counting 2000 points at a spacing of 0.5 mm on 5- × 8-cm thin sections or 1000 to 1500 points at a spacing of 0.4 mm on standard thin sections.

ranges from trace amounts to 1%. Apatite (probably primary; see below) is present in some iron-titanium oxide gabbros (e.g., Samples 118-735B-54R-3, 125-127 cm, Piece 7, and 118-735B-55R-2, 50-55 cm, Piece 3A). Its mode is approximately 1%.

One peculiar gabbro containing 37.5% inverted pigeonite, 0.1% olivine, and 2.5% clinopyroxene was observed (Sample 118-735B-28R-3, 62-71 cm, Piece 4; Fig. 19). In thin section, this gabbro contains only 0.5% opaque minerals, but visual description of the core indicates higher concentrations of opaque minerals; thus, this pigeonite gabbro (or norite) may belong to the iron-titanium oxide gabbro suite. Another uncommon rock type that is probably related to the iron-titanium oxide gabbro is a coarse pyroxene layer, 1 cm thick, in olivine gabbro Sample 118-735B-35R-1, 45-47 cm, Piece 2E. Clinopyroxene and inverted pigeonite are the dominant minerals in this rock, with inverted pigeonite constituting approximately 10% of the layer. It is relatively rich in opaque minerals in thin section (2%). Thus, this layer can be treated as a pyroxene-rich layer of iron-titanium oxide gabbro.

Iron-titanium oxide gabbros are variably metamorphosed and altered. The abundance of secondary minerals as a result of metamorphism and alteration ranges from 2% to 25% and is commonly from 10% to 20%. The common secondary minerals are colorless amphibole and actinolite, which replace pyroxene or olivine; green to brown amphibole, which replaces clinopyroxene or red brown amphibole; yellowish-brown clay, which replaces olivine; carbonate, which replaces olivine or orthopyroxene; brown clay, which replaces iron-titanium oxide; and magnetite, which replaces olivine. Secondary pyrite (up to 1%) also occurs with green amphibole. Iron-titanium oxide gabbros also show varying degrees of deformation, with textures ranging from porphyroclastic to mylonitic.

Most of the iron-titanium oxide gabbros are partly deformed (Fig. 20) and metamorphosed, but igneous, undeformed textures are preserved in some specimens (Fig. 21). These specimens commonly show a magmatic foliation (Figs. 20 and 21) defined by elongated clinopyroxene and plagioclase crystals and aggregates of opaque minerals. The following description of primary igneous textures is based mainly on these fresh, relatively undeformed samples.

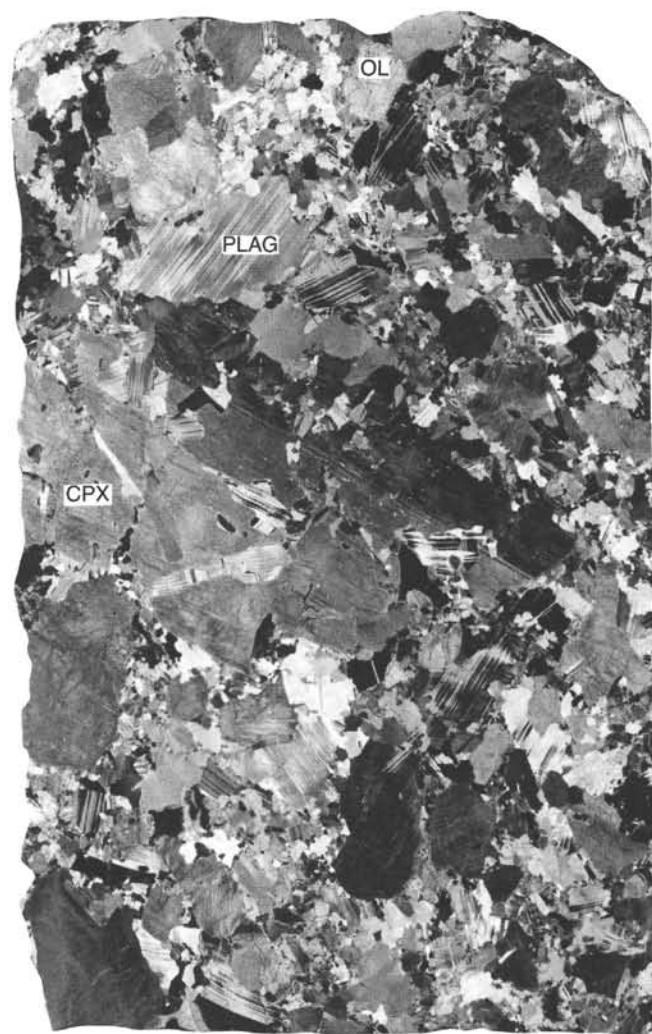


Figure 14. Polarized light photograph of 5- × 8-cm thin section showing a poikilitic gabbro (118-735B-27R-3, 73-81 cm, Piece 10). Note the 4-cm-wide clinopyroxene oikocryst in the center of the photograph. CPX = clinopyroxene; OL = olivine; PLAG = plagioclase.

Iron-titanium oxide gabbros from Hole 735B have average grain sizes that range from 0.3 mm for microgabbro to 30 mm for coarse-grained gabbro. The sizes of plagioclase, clinopyroxene, and opaque aggregates show concomitant variations.

Clinopyroxene is generally subhedral, rarely euhedral, and has an elongated shape. Oikocrysts of clinopyroxene are rare, compared with other types of gabbro from Hole 735B. In addition to (100) orthopyroxene exsolution lamellae, the clinopyroxene has (001) exsolution lamellae (orthopyroxene?), which are absent in clinopyroxenes in the olivine-bearing, iron-titanium oxide-poor gabbros. Even in porphyroclastic or mylonitic iron-titanium oxide gabbros, porphyroclasts of clinopyroxene have (001) exsolution lamellae. Large clinopyroxenes commonly contain patchy orthopyroxene or inverted pigeonite, which generally has the same crystallographic orientation as exsolution in the host clinopyroxene (Fig. 22). The patches of pigeonite are larger (0.5-1 mm) than those of orthopyroxene (0.1-0.3 mm) and occur in the cores of clinopyroxene crystals. These relationships indicate reaction between calcium-poor pyroxene and silicate melt to form calcium-rich pyroxene.

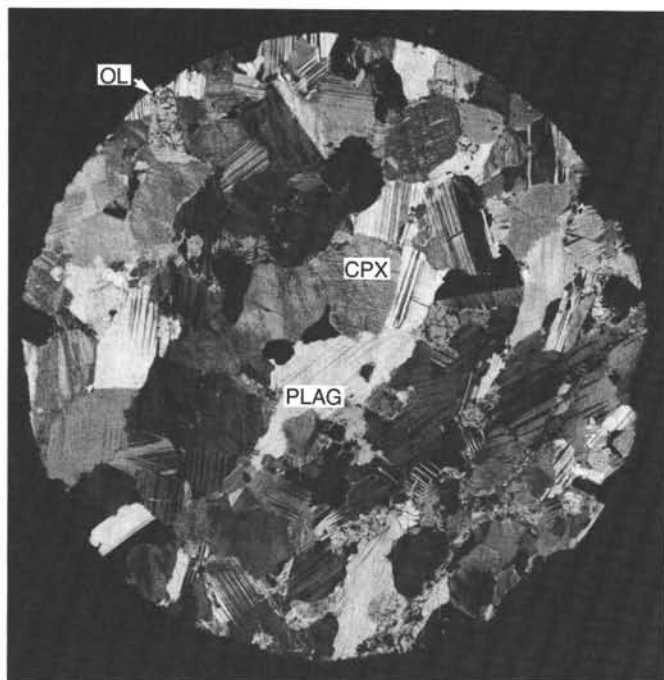


Figure 15. Polarized light photograph of thin section showing a granular gabbro (118-735B-36R-5, 131–133 cm, Piece 5E). The diameter of the round thin section is 2.5 cm. CPX = clinopyroxene; OL = olivine; PLAG = plagioclase.

Plagioclase is generally euhedral to subhedral, which suggests that it is a cumulus mineral (Fig. 23A). Euhedral plagioclase is enclosed in clinopyroxene or opaque minerals. It is commonly recrystallized into smaller grains by later deformation. Plagioclase compositions range from An_{30–45}, which are more sodic than those in the olivine gabbro and gabbro from Hole 735B.

When present, olivine is typically anhedral and occurs as thin films (0.1–0.3 mm) between opaque minerals and clinopyroxene (Fig. 23B). Olivine also occurs sandwiched between opaques and calcium-poor pyroxenes or plagioclase. These relationships suggest that pyroxenes were reacting with silicate liquid to produce iron-rich olivine and ilmenite. In iron-titanium oxide gabbros containing abundant olivine and rare calcium-poor pyroxene, olivine occurs as euhedral crystals. Olivine compositions range from Fo_{30–55}, which are more iron-rich than those in olivine gabbros and gabbros from Hole 735B.

Opaque minerals are generally anhedral and interfinger in a complex manner with clinopyroxene or plagioclase (Fig. 23A). These minerals also occur in plagioclase or clinopyroxene as euhedral inclusions. In two samples (Samples 118-735B-23R-3, 34–37 cm, Piece 2, and 118-735B-44R-2, 6–8 cm, Piece 1A), we found intergrowths of opaque minerals and orthopyroxene.

Calcium-poor pyroxenes are present as patches in clinopyroxene or as isolated grains generally in contact with, or enclosed in, clinopyroxene crystals. They are generally anhedral, but some are subhedral. Inverted pigeonite is euhedral. It has abundant clinopyroxene exsolution blebs, typically parallel to (001) from the pigeonite inversion. The host orthopyroxene also has thinner exsolved lamellae of clinopyroxene parallel to (100). Twinned crystals in pigeonite gabbro show a typical herringbone structure (Fig. 19B). The exsolution blebs are commonly irregular or parallel to (100). Clinopyroxene exsolution lamellae in calcium-poor pyroxenes have the same optical orientation as the surrounding large grains of clinopyroxene.

Reddish-brown hornblende commonly accompanies orthopyroxene patches in clinopyroxene or opaque minerals. Its grain size ranges from 0.1 to 0.3 mm. Apatite crystals from 0.1 to 0.5 mm long are present as euhedral to subhedral inclusions in opaque minerals or as polycrystalline aggregates interstitial to plagioclase and olivine. This suggests a primary origin for the apatite. See the “Oxide and Sulfide Mineralogy” section (this chapter) for textural characteristics of opaque minerals in iron-titanium oxide gabbros.

Basalt

A single basaltic dike having chilled contacts against gabbro was recovered between Section 118-735B-23R-4 at 66 cm and Section 118-735B-23R-5 at 25 cm. The contacts between basalt and gabbro are sharp and planar; crystals of plagioclase in the gabbro wall rock are abruptly truncated at the contact. Recovery of homogeneous basalt between these two contacts suggests a vertical thickness of approximately 1 m for the dike. The basalt is aphyric, fine-grained, and gray.

Grain size and texture within the basalt vary across the dike. At the dike margins one can see cryptocrystalline bands 1.0–1.5 mm wide that have subhedral plagioclase and olivine microphe-nocrysts aligned parallel to the contact. Inward, birefringent crystallites of clinopyroxene and/or olivine can be detected in the groundmass; the texture is incipiently intersertal, although groundmass crystals are less than 20 μm in size. Approximately 1 cm from the cryptocrystalline zones, the maximum microphe-nocryst size is only 0.4 mm. This is significantly smaller than the average microphe-nocryst size adjacent to the gabbro contact and may represent flow differentiation. The interior of the dike has a fine-grained intersertal texture and contains clinopyroxene crystals between 0.05 and 0.2 mm and plagioclase laths up to 1.2 mm in length. These textural variations are analogous to those described for planar dike margins from the sheeted dike complex of Hole 504B (Kempton, 1985). A single anhedral crystal of golden-brown chromium-spinel, 0.2 mm in diameter, was observed in the basalt and is probably a xenocryst.

Fine-grained, metamorphosed rocks that appear to intrude gabbros of Units I and II were observed in Sections 118-735B-6D-1 and 118-735B-19R-5. In Sample 118-735B-6D-1, 92–107 cm, Piece 18, a thin, apparently nonfoliated layer is enclosed within a porphyroclastic to mylonitic section. Petrographically, this sample was identified as an iron-titanium oxide-rich mylonite. In Section 118-735B-19R-5, greenish-gray, nonfoliated rocks sharply crosscut the surrounding coarse-grained, foliated metagabbro. This sample was identified petrographically as an amphibolitized, but relatively undeformed, microgabbro.

Felsic Rocks

Fragments of a trondjemite dike were recovered in Sample 118-735B-53R-5, 35–45 cm, Piece 3; possible effects of mixing between trondjemite and gabbro were observed in adjacent Sections 118-735B-53R-3, 118-735B-53R-4, and 118-735B-54R-2. The trondjemite is a medium-grained, leucocratic rock composed of approximately 75% plagioclase, 20% quartz, 2% biotite, 2% clinopyroxene, and 1% magnetite. Plagioclase occurs as blocky, subhedral crystals, which are relatively homogeneous in the cores but are strongly zoned over the outer 0.02 mm of the rims. Grain size averages about 0.5 mm, although a few crystals as large as 1.5 mm occur. Quartz generally occurs as an interstitial phase between plagioclase, but one large crystal, 1.5 mm in diameter, exhibits a euhedral outline while actually being composed of several subcrystals with independent undulose extinction. Clinopyroxene, now largely replaced by pale green actinolite, has an equant, euhedral to subhedral morphology and ranges from 0.2 to 0.5 mm in size. Biotite poikilitically encloses euhedral plagioclase crystals.

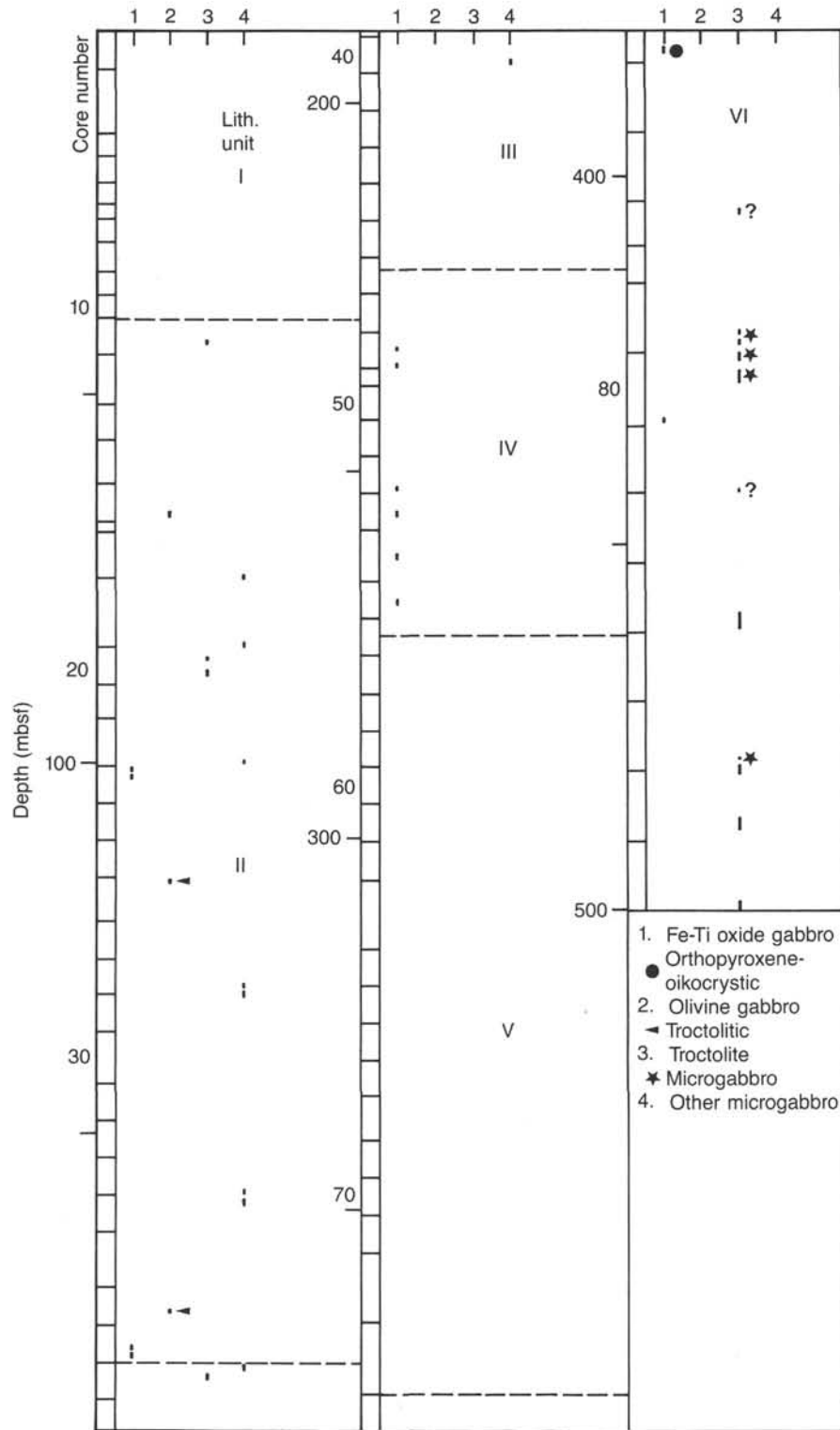


Figure 16. Downhole plot showing the location of troctolites and different types of microgabbros. Iron-titanium oxide microgabbros are plotted as small dots in column 1. Olivine microgabbros are plotted as small dots in column 2, with troctolitic varieties indicated by arrows. Troctolites are shown in column 3, with medium-grained varieties indicated by small dots and fine-grained varieties by stars. Metamorphosed microgabbros of questionable lithology are plotted in column 4.

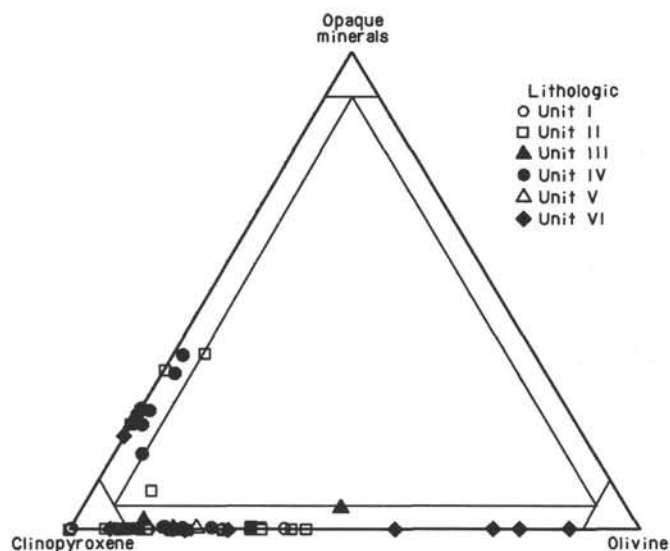


Figure 17. Ternary plot showing relative abundance of opaque minerals, clinopyroxene, and olivine. Iron-titanium oxide gabbros show distinct depletion of olivine.

The trondjemite intrudes iron-titanium gabbro of Unit III (see "Lithostratigraphy" section, this chapter). The contact between these two rock types is planar, and crystals in the gabbroic wall rock are truncated by the contact. In addition, feldspar adjacent to the contact has strongly zoned rims (0.1 mm wide) similar to plagioclase in the trondjemite.

The gabbroic wall rock adjacent to the trondjemite has been metasomatized as a result of the intrusion, as seen by the presence of abundant secondary mica along the contact. Ilmenite in the gabbro is surrounded by brown mica, possibly phlogopite. This brown mica is zoned to, or overgrown by, an unidentified green mica having high birefringence. Olivine is replaced by colorless amphibole and magnetite.

Intense mixing of felsic and gabbroic material was noted in several sections above and below the recovered trondjemite. In Section 118-735B-53R-4, the mixed material is described as broken, angular fragments of gabbro included in felsic material. Elsewhere, the mixing is more complete and the gabbroic fragments appear to be partially disaggregated and digested by the felsic material. Below the trondjemite in Section 118-735B-54R-2, felsic rocks are more strictly confined to veins approximately 1–2 cm wide. Traces of biotite were noted in a few pieces throughout this section.

Although not trondjemitic in composition, felsic veins free of amphibole were observed as high in the section as Section 118-735B-43R-4 and periodically thereafter. These veins are composed of subhedral to euhedral plagioclase, subhedral to euhedral clinopyroxene, epidote \pm sphene \pm chlorite \pm carbonate. We are not sure whether these veins are magmatic or hydrothermal, but we prefer a hydrothermal origin (see "Metamorphism and Alteration" section, this chapter). The abundance of these veins near the trondjemitic intrusion suggests that they may be genetically related.

Textural Variations

Some intervals in Hole 735B have distinct modal, phase, and size gradations. Variations in modal abundances and crystal size in individual samples of plutonic rocks have been documented in several samples dredged from fracture zones and rift valleys (e.g., Tiezzi and Scott, 1980; Engel and Fisher, 1975; Bloomer et al., 1985; Meyer et al., 1988). Such samples usually include only a single contact, either from one modal assemblage to an-

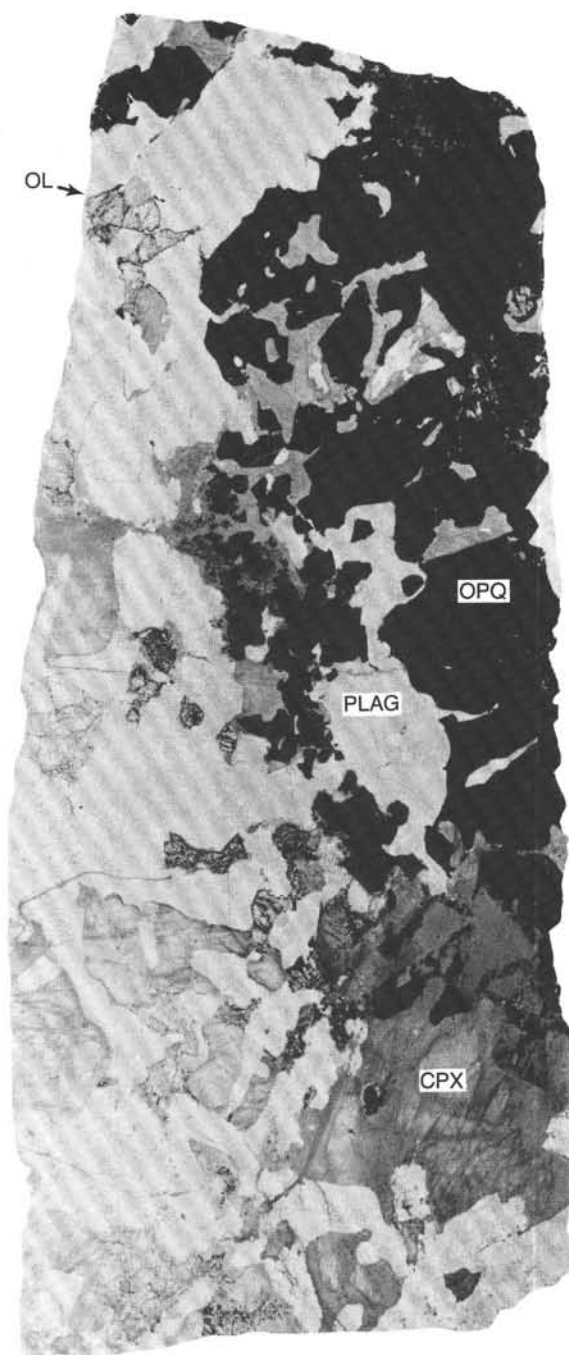
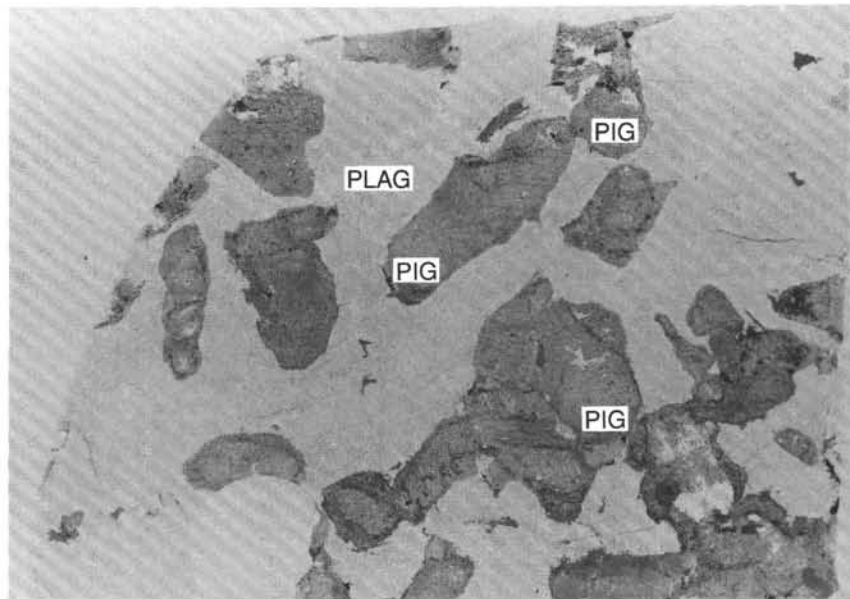


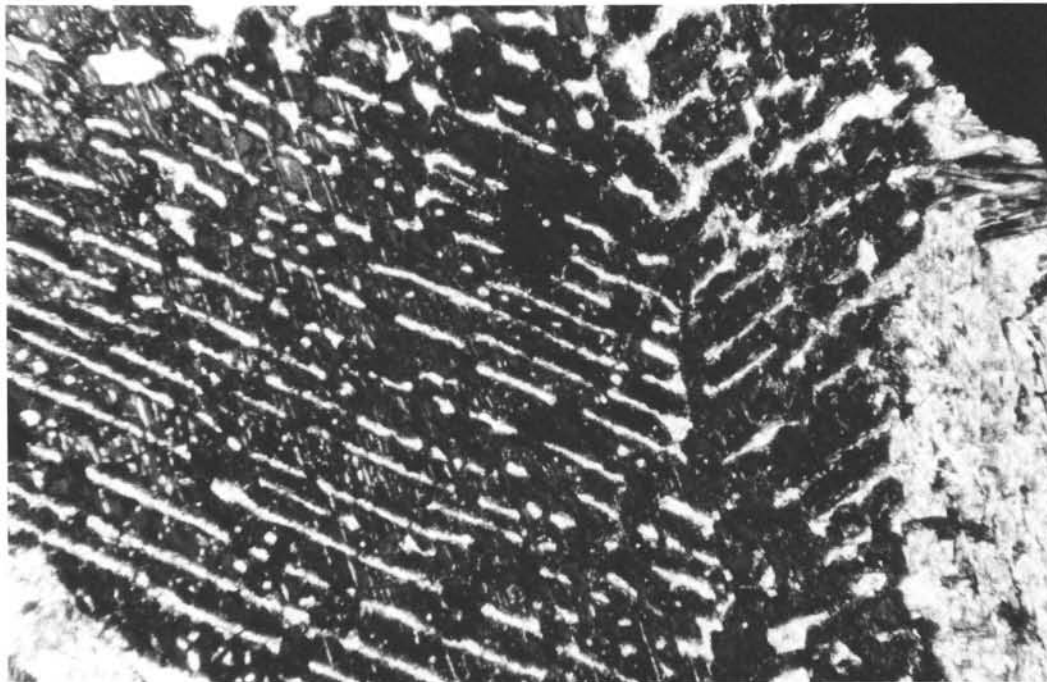
Figure 18. Polarized light photograph of thin section showing the contact between an olivine gabbro and an iron-titanium oxide gabbro (118-735B-44R-1, 113-120 cm, Piece 2I). CPX = clinopyroxene; OL = olivine; PLAG = plagioclase; OPQ = opaque minerals.

other or between two grain sizes, and it has not been possible to examine large-scale layering in mid-ocean ridge plutonic complexes. Here, we describe briefly the principal types of modal and textural variation seen in the gabbroic rocks from Hole 735B.

Although layering is well developed in the rocks from this hole, it is not the distinctive rhythmic phase layering so common in large basic intrusions like the Stillwater or Bushveld complexes, or even in the plutonic parts of many ophiolite complexes. The layering is locally, and often subtly, developed. Re-



A



B

Figure 19. A. Plane light photograph of 5- × 8-cm thin section showing pigeonite gabbro containing 40% euhedral inverted pigeonite (gray mineral in photograph; 118-735B-28R-3, 62-71 cm, Piece 4). B. Photomicrograph of inverted pigeonite in pigeonite gabbro, showing herringbone structure. Crossed nicols. Field of view is 2.5 mm. PIG = pigeonite; PLAG = plagioclase.

covery from Hole 735B, particularly in the deeper parts, was nearly continuous (Fig. 5) and provided a more detailed sampling than is generally available even from subaerial gabbroic complexes. The cored material was described centimeter by centimeter. Many of the size and textural variations identified from these descriptions are subtle and might not be recognized as layering if examined in the field. The preceding is not meant to diminish the importance of the textural variations in the gabbroic rocks from Hole 735B, but it is meant to alert the reader that

there are some important differences between this layering and that normally associated with layered basic intrusions.

Distinctly modal- or size-layered features were observed in about 25% to 28% of the sections in Units II, III, V, and VI and in about 40% of the sections in Unit IV. Intervals of 3 to 7 m of relatively massive gabbro, with little evidence of size or modal layering, are common in all of the lithologic units. In fact, massive gabbros are the most common textural type in the undeformed parts of the core. Many of the textural transitions are lo-



Figure 20. Plane light photograph of thin section showing slightly deformed iron-titanium oxide gabbro (118-735B-52R-4, 88-94 cm, Piece 4B). Elongated plagioclase (white) and pyroxene (gray) crystals define a primary igneous lamination cut by several microfaults. Redistribution of opaque minerals (black) along these microfaults clearly defines a foliation due to deformation.

cally developed, particularly the coarse- to fine-grain-size changes. In extreme cases, textures can change from very coarse- to fine-grained over 2 cm (Fig. 24). The type of layering observed in the core from Hole 735B is probably laterally discontinuous. The major mineralogical changes in the section occur between Units III and IV and Units IV and V. The latter is definitely a tectonic contact, and the former probably is as well. Unit V has some distinct troctolitic intervals, at least one of which (in Core 118-735B-83R) represents distinct phase layering. However, most of the troctolitic layers are fine-grained microgabbros that may be intrusive into the coarser-grained olivine gabbro.

Small-Scale Textures

The olivine gabbros are adcumulates and mesocumulates, with cumulus plagioclase and olivine and intergranular to ophitic clinopyroxene (Fig. 25). Moderately to weakly developed igneous lamination, defined principally by subparallel orientation of plagioclase laths, occurs locally (Fig. 26). Large oikocrysts of clinopyroxene (up to 10 cm in size) are common in the olivine gabbros. These large oikocrysts commonly are elongated perpendicular to the principal layering in the gabbros (Fig. 27). On a smaller scale, 1-cm oikocrysts of orthopyroxene in a microgabbro also exhibit a subvertical orientation. A similar vertical orientation of euhedral and subhedral plagioclase was noted in some cores and can be identified on a smaller scale in phase-layered gabbros (Fig. 28).

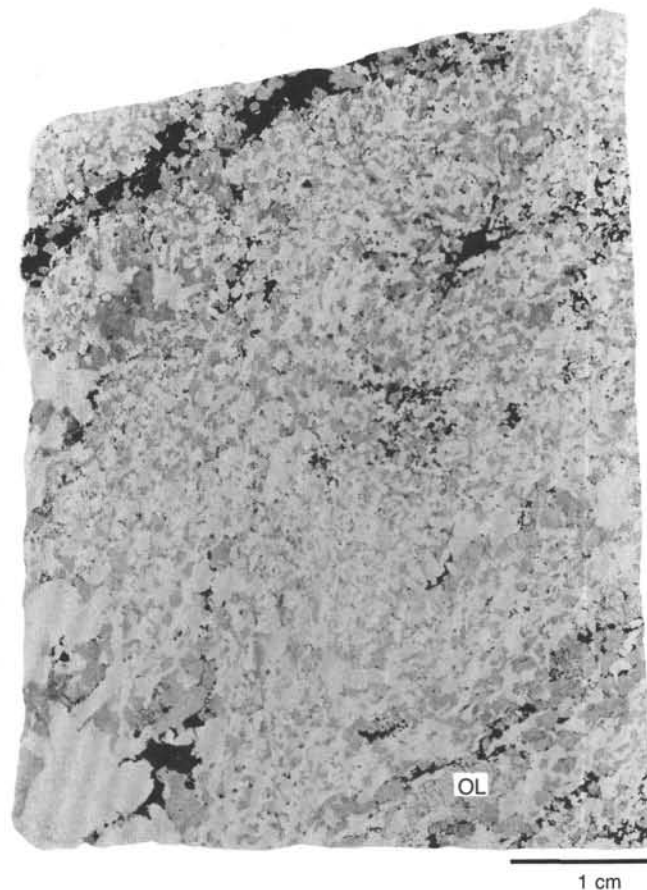


Figure 21. Plane light photograph of 5- × 8-cm thin section showing undeformed iron-titanium oxide gabbro with magmatic foliation (118-735B-46R-3, 121-128 cm, Piece 10). The foliation is defined by elongated euhedral laths of plagioclase (white) and thin opaque-rich layers (black). Gray grains are clinopyroxene and minor olivine. Large olivine (OL) is present at lower right corner, which is also elongated parallel to the foliation.

ered gabbros (Fig. 28). This type of crystal growth normal to the layering is reminiscent of the crescumulates seen in the Rhum Intrusion (Wager et al., 1960).

Granular textures occur in many samples; in some cases, subhedral clinopyroxene, as well as plagioclase, appears to have been a cumulus phase. These granular textures are most common in the iron-titanium oxide gabbros and in the coarse intervals in the olivine gabbros. In the iron-titanium oxide gabbros, the intergranular phases include a low-calcium pyroxene, olivine, and the oxide. The igneous lamination is more common in the oxide-bearing gabbros (Fig. 27).

Layering

Three principal types of layering can be identified in the gabbroic samples from Hole 735B. The first is modal layering, defined by variations in modal abundances of individual phases. Most common are layers rich in olivine (Fig. 29). These layers tend to be 1 to 5 cm thick, but may be up to 25 cm thick. They are repeated in single sections of core and are spaced at irregular intervals from 5 to 50 cm apart. Abundances of olivine may be from 5% to 30%, compared with abundances of 1% to 5% in the other layers. The olivine-rich zones do not correspond in any consistent way with coarse- or fine-grained intervals in the size-graded layers.

Phase layering, defined by abrupt and persistent appearance or disappearance of a phase, was not observed in these gabbros.



Figure 22. Polarized light photomicrograph of patchy orthopyroxene (OPX) in clinopyroxene (CPX). Field of view is 2.5 mm (118-735B-34R-4, 8–12 cm, Piece 2).

The nearest analogs are 1- to 5-cm-thick plagioclase- and pyroxene-rich layers, usually occurring in the coarser-grained parts of the size-graded intervals. In some cases, these layers approach pyroxenites or anorthosites in composition but have a limited vertical extent. In many cases, they are made up of only a one- or two-crystal-thick layer (Fig. 28).

The most common type of layering in these gabbros is defined by gradations in size. These graded units are coarse or very coarse layers fining upward to fine- and medium-grained layers (Fig. 30). These units are most commonly graded from crystal sizes of 10 to 20 mm to medium-grained intervals of 1 to 5 mm. The units vary in thickness from 10 to 100 cm; the transitions in grain size may be either gradational or quite sharp. Two to four graded intervals of various thicknesses may occur in a single section.

The third type of layering observed in the gabbros is defined by the contacts between gabbros and microgabbros. These microgabbros are fine-grained, equigranular units that occur in three distinct styles. The first style resembles rather large dike- or sill-like bodies, with sharp contacts against the host gabbros (Fig. 31). These often cut across the inferred layering orientation. The most common microgabbro occurrence is as small pods within a medium- or coarse-grained gabbro. These pods often are repeated within a short section, and their contacts define a foliation having an orientation similar to that inferred from graded sequences in other parts of the core (Fig. 31). The third style of microgabbro is as very small clots sandwiched between medium-grained gabbro (Fig. 31). The microgabbros as a group probably formed through a range of processes, including segregation of trapped liquids, intrusions of liquids into crystallizing gabbros, and rapid, localized changes in cooling rates.

OXIDE AND SULFIDE MINERALOGY

Introduction

Oxide and sulfide minerals are strikingly abundant in many Hole 735B gabbros. Their distribution in the cores reflects im-

portant aspects of the crystallization, deformation, and metamorphism experienced by the rocks.

The great diversity of gabbro types at Site 735 allows us to evaluate in more detail the oxide and sulfide mineralogy in an oceanic setting than may ever be possible using basalts. Not only are fairly extreme compositions, ranging from troctolites to trondjemites, present but most of the rocks are cumulates that have retained some fraction of intercumulus liquid, which eventually crystallized oxides and sulfides in intergranular spaces. In a few specimens, oxides and sulfides are primary cumulus phases. In addition, two-pyroxene gabbros and oxide-rich ferrogabbros, compositions representative of rather evolved basaltic parents, are common. With such rocks we may be able to study the sequence of crystallization of oxide and sulfide minerals in some detail and relate it to an appropriate stage of fractionation.

General Distribution of Oxides and Sulfides in Hole 735B

The abundance and to some extent the compositions and proportions of oxides and sulfides in Hole 735B reflect the rock compositions, their mechanical deformation, and their metamorphism under amphibolite facies conditions. The rocks cored are gabbroic, except for one basalt dike. The gabbros are primarily cumulates but are intensely deformed near the top and bottom of the hole and locally deformed inbetween (see "Metamorphism and Alteration" section, this chapter). The most important intermediate zone of deformation is above a fault at 272 mbsf, at the level of Core 118-735B-56R (Fig. 7).

Spinel

Chromian-spinel occurs in only one interval of troctolite, an olivine-plagioclase cumulate in Core 118-735B-83R. It is dark brown, almost opaque, up to 0.2 mm in diameter, and forms octahedral, sometimes skeletal crystals. The crystals are darker brown than either of the two grains of spinel observed in the basalt dike in Core 118-735B-23R. These grains have rounded, presumably resorbed outlines, and are zoned with very dark vermi-

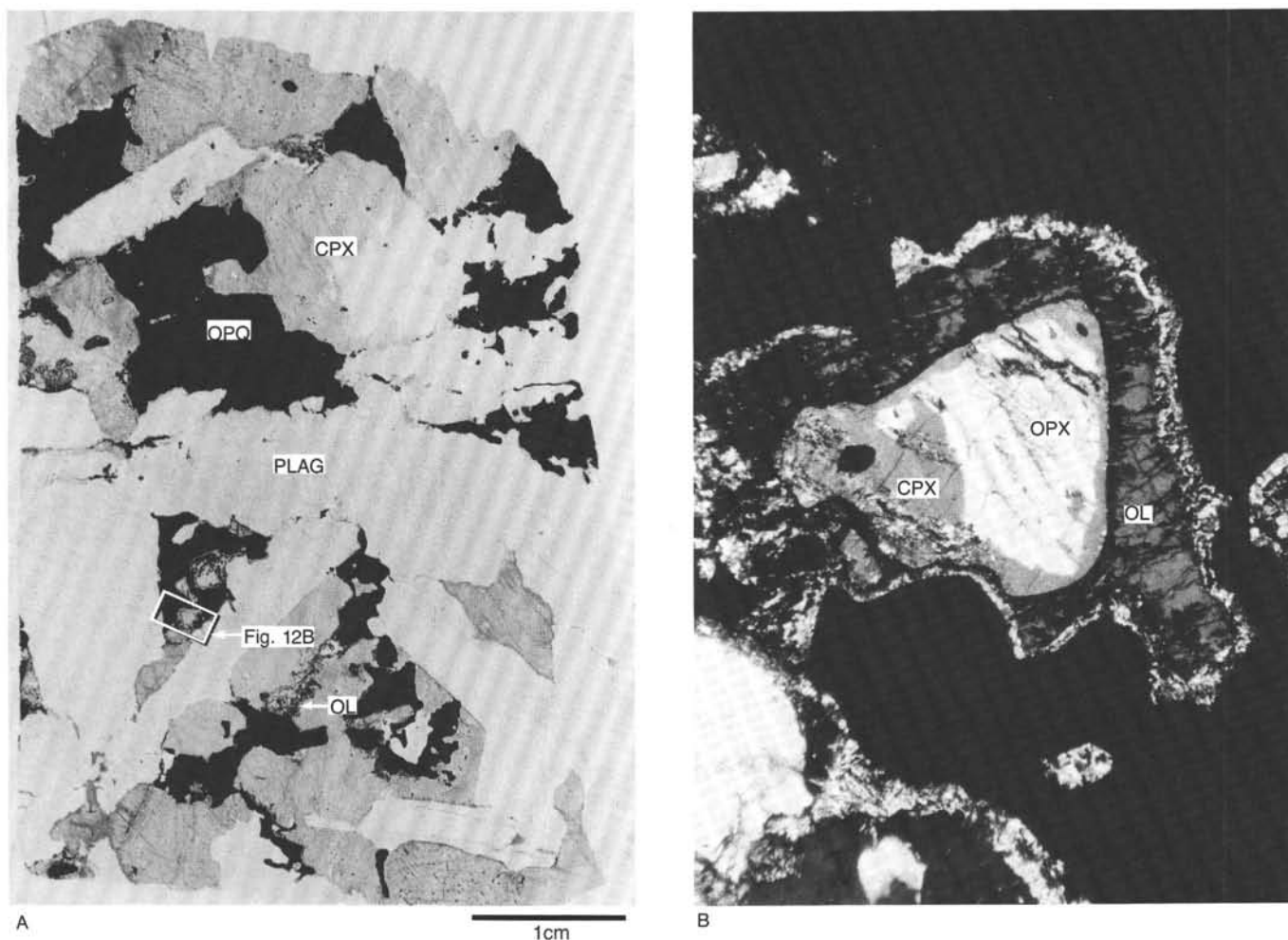


Figure 23. A. Plane light photograph of thin section showing undeformed iron-titanium oxide gabbro with interfingering relationships between opaque minerals (OPQ) and clinopyroxene (CPX) or plagioclase (PLAG); OL = olivine (118-735B-34R-4, 8–12 cm, Piece 2). Rectangle indicates view of photomicrograph. B. Photomicrograph of orthopyroxene (OPX) in clinopyroxene (CPX) rimmed by olivine (OL), which is further surrounded by opaque minerals. Crossed nicols. Field of view is 2.5 mm.

cular rims. A few grains in the troctolite enclose small, roughly cubic but rounded grains of a white mineral, distinctly anisotropic in cross-polarized light (pentlandite?). Other grains have pyrrhotite-chalcopyrite intergrowths at their edges similar to intergranular sulfides elsewhere in the section.

Iron-Titanium Oxides

Iron-titanium oxides are the most abundant opaque phases in most of the gabbros and correlate well with bulk-rock compositions as well as the lithology and petrography.

The abundances of iron-titanium oxides vary regularly within the lithologic units. These oxides are minor in Unit V and the top five cores of Unit VI; sporadically abundant in the more iron-rich parts of Units I, II, and the remainder of Unit VI; and very abundant in the ferrogabbros of Unit IV. In Units I and II, iron-titanium oxides vary from virtually 0% to as much as 10%. Thin sections containing more than 2% ilmenite and magnetite occur in Cores 118-735B-2R, -4R, -10R through -14R, -19R, -23R, -24R, -30R, -31R, -32R, and -34R, with highs of about 7% in a porphyroclastic metagabbro in Core 118-735B-4R (20 mbsf), and 10% in each of Cores 118-735B-32R (149 mbsf) and 118-735B-34R (165 mbsf). Similarly, in the iron-rich lower parts of Unit VI, thin sections containing more than 2% iron-titanium oxides occur in Cores 118-735B-82R, -86R, and -87R.

However, no slide has more than 5% of combined ilmenite and magnetite.

In the most iron-enriched gabbros of lithologic Units III and IV, several samples between Cores 118-735B-38R and 118-735B-44R have 2%–4% iron-titanium oxides. Many samples in Cores 118-735B-44R and -56R have at least 5% oxides, several have as much as 20%, and one sample, in Core 118-735B-47R (228 mbsf), has more than 50% combined ilmenite and magnetite.

Deformation greatly influences the distribution of these oxide minerals in Unit I and parts of Unit VI. In both units, coarsely porphyroclastic metagabbros have the greatest abundances (3%–7%), while finer-grained gneissic gabbros and mylonites typically have only 1%–2%. In ferrogabbros from Units III and IV, most specimens exhibit primary textural relations among oxides, sulfides, and silicates, but in some cases, the rocks also are sheared and granulated and have metamorphic fabrics. Gabbros from Unit V are rarely intensely deformed; thus, most oxides are simply intercumulus minerals in low abundance. The proportions of oxide minerals in the few mylonitized olivine gabbros are no greater than in the immediately surrounding undeformed rocks. Gabbros in the lower parts of Unit VI are not so deformed as those in the geochemically similar gabbros of Units I and II. Primary textures occur in some samples, metamorphic fabrics in others, and a few are only partly

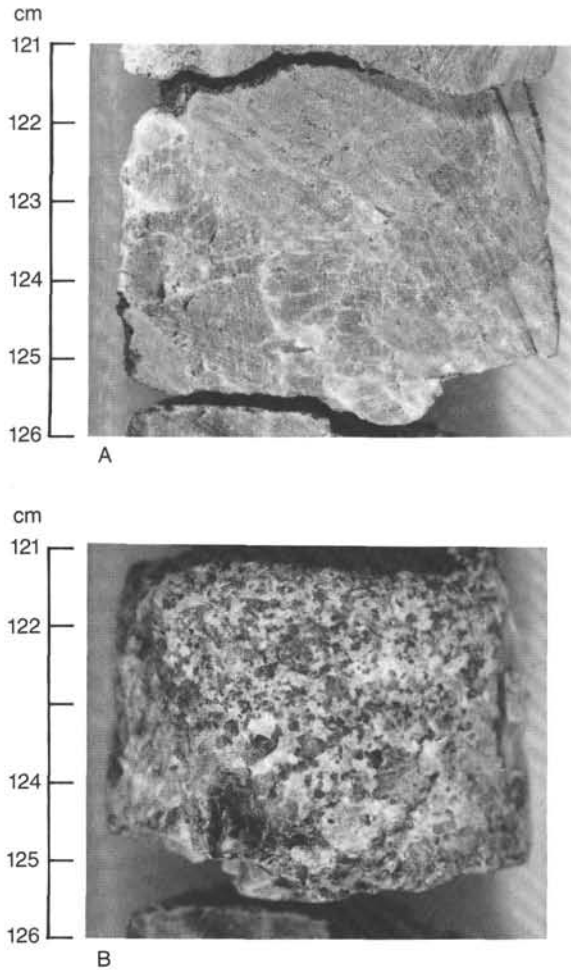


Figure 24. Grain-size variations between cut (A) and cored surface (B) of Section 118-735B-64R-1. Note the change from very coarse-grained (2-3 cm) on the cut surface to fine- or medium-grained on the cored surface.

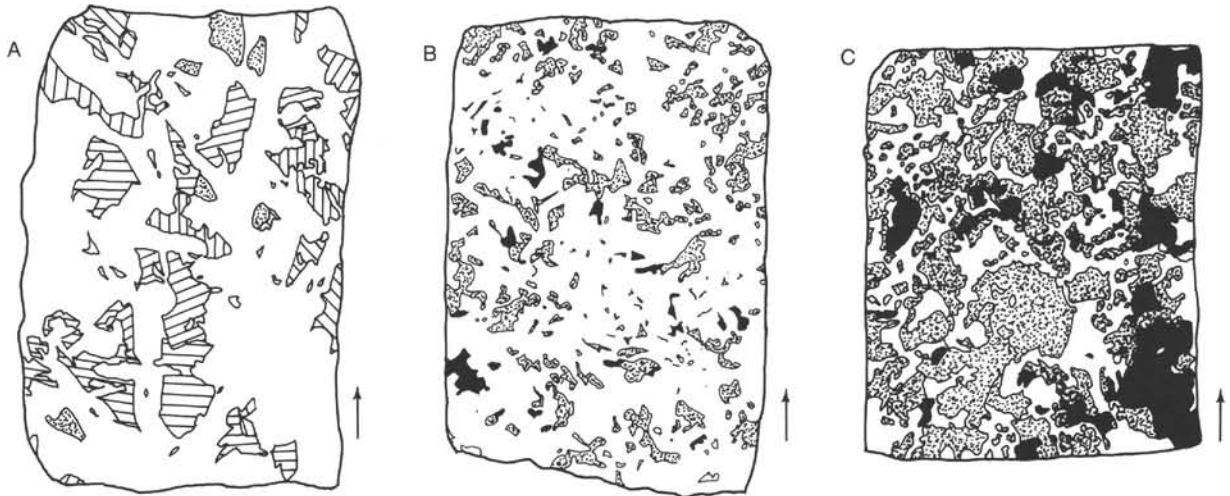


Figure 25. Grain tracing of individual pieces. Each slab is 5 cm wide. A. Clinopyroxene oikocrysts (lined) between cumulate plagioclase (white) and olivine (dotted) (118-735B-74R-5, 85-95 cm, Piece 3B). B. Skeletal clinopyroxene oikocrysts (black) in a plagioclase-rich troctolite (118-735B-79R-5, 81-90 cm, Piece 6A). Olivine is dotted and plagioclase is white. The clinopyroxene fragments in the center of the sketch are part of an optically continuous grain. C. Intergranular clinopyroxene (black) in an olivine-rich troctolite (118-735B-87R-5, 110-118 cm, Piece 11A). Olivine is dotted and plagioclase is white.

recrystallized, with both primary and metamorphic oxide-silicate relationships.

The proportion of ilmenite to magnetite in given samples is difficult to estimate, especially if the rocks are strongly mylonitized. In the deformed rocks, the iron-titanium oxides occur in veins or seams along the foliation. The two minerals are intergrown and, in some cases, magnetite has tiny exsolution lamellae of ilmenite. In the largest seams, the ilmenite is broken into plates many times larger than granulated plagioclases or clinopyroxenes in the same samples. The plates are bounded by curvilinear fractures, and each has a slightly different extinction direction. Because there is no alteration along the fractures, plates may have been produced simply by expansion of the minerals when they were brought to the sea surface. A few samples have ilmenite with hematite exsolution lamellae developed along similar fractures, which must have been produced *in situ*. These data suggest that ilmenite is by far more abundant than magnetite in these deformed rocks, perhaps in the ratios 2:1 to 3:1.

Where primary textural relationships can be ascertained, the proportions seem reversed. In undeformed olivine gabbros and troctolites of Unit V and the upper part of Unit VI, magnetite is more abundant than ilmenite, but the abundances of both are very low. Here, and in all other cases, ilmenite exsolved from magnetite is not considered primary, but is grouped with the magnetite to obtain the proportions of magmatic oxides.

The proportion of ilmenite to magnetite in ferrogabbros varies, with sometimes one, sometimes the other, predominating. In typical samples, the ratio of magnetite to ilmenite is perhaps 2:1. Also, ilmenite in the ferrogabbros began to crystallize before magnetite, which commonly encloses it subophitically. In some cases, the oxides grow into embayments in the silicate minerals, and in others, the silicates are poikilitically enclosed in oxides or vice versa. The high abundance of magnetite in gabbros with primary textures suggests that the TiO_2 was metasomatically increased in the metagabbros.

These intergrowths of generally coarse-grained ilmenite and magnetite are the most striking aspect of the opaque mineralogy of Hole 735B gabbros. In fact, the intergrowths in both undeformed and foliated rocks also typically include sulfide minerals, as described below. But there are other magnetites in the gabbros associated with minerals transformed during amphibol-



Figure 26. Polarized light photograph of 5- × 8-cm thin section showing igneous lamination in an olivine gabbro (118-735B-72R-2, 56-62 cm, Piece 1D). OL = olivine; CPX = clinopyroxene; PLAG = plagioclase.

lite-facies metamorphic conditions. These are typically much finer grained, are less reflective, have vermicular to skeletal morphologies, and occur with amphiboles, talc, and/or chlorite. They are particularly important to rock magnetic properties because they evidently carry the stable component of natural remanent magnetization in the rocks (see "Paleomagnetism" section, this chapter). The coarse magnetites in the magnetite-ilmenite-sulfide intergrowths give the rocks high magnetic intensities, but they are quite readily demagnetized.

A few specimens near the top of the hole and again at the very bottom contain minor iron oxyhydroxides that are sometimes fairly reflective and that are produced by transformation of ferromagnesian silicates during oxidative alteration. These are usually associated with clay minerals in the replacement of clinopyroxene and/or green amphibole in mylonites of Cores 118-735B-1D through -10D, and olivines in other parts of the core.

Sulfide Minerals in Undeformed Gabbros

The abundance of sulfide minerals in the gabbros is typically less than 1%, but both the abundances and proportions of sulfides follow the pattern of the iron-titanium oxides in the different rock types.

Sulfide minerals are least abundant in the olivine gabbros and troctolites of Unit V and the upper part of Unit VI, or in

similar rocks in the other units. Even so, they are more abundant than iron-titanium oxides in these rocks. Sulfides in the spinel-bearing troctolite in Core 118-735B-83R have already been described.

Sulfide minerals are more abundant in the noritic gabbros than in the olivine gabbros and are more abundant still in oxide-enriched ferrogabbros. In all these rocks, however, the proportion of iron-titanium oxides greatly exceeds that of sulfides.

Pyrrhotite and chalcopyrite are the principal phases in the olivine cumulates, with the former more abundant than the latter. The two appear to have precipitated together inasmuch as they are intergrown in globules and blebs, an indication of sulfide immiscibility in basaltic parental liquids.

Where ilmenite and magnetite are abundant, as in the more evolved gabbros of Units I, II, and VI, and the ferrogabbros of Units III and IV, the sulfides are closely associated with the oxide minerals. These minerals are sufficiently large so that chalcopyrite can be distinguished from pyrite in hand specimen. In these more evolved rocks, pyrite predominates but is usually intergrown with chalcopyrite, again in blebs and globules. Pyrrhotite occurs as well, but in minor abundances and most often forms as small sectors having linear, presumably facet-defined, edges within larger domains of pyrite. Three-phase aggregates of pyrrhotite, pyrite, and chalcopyrite are common. The optical anisotropy of both pyrrhotite and chalcopyrite is not as marked as it is in the olivine gabbros. These observations suggest changes in composition of these phases as temperatures decreased with increasing degree of fractionation (Mathez and Yeats, 1976).

The minor sulfide phases bornite, covellite, and sphalerite also occur in the oxide-rich ferrogabbros. The first two copper-bearing phases occur as rare intergrowths with the major sulfide minerals and are dispersed in the vicinity of major sulfide globules optically enclosed, for example, by clinopyroxene. In such cases, these are tiny crystals disseminated along cleavage planes in the host crystal away from the enclosed sulfide globule.

Sphalerite occurs only as complex intergrowths, with pyrite in fairly large globules. It is present only in a few samples, but is quite abundant in those; chalcopyrite does not occur in the intergrowths.

The primary sulfide minerals in Hole 735B gabbros appear to have crystallized in all lithologies cored and to range from troctolite to ferrogabbro. The sulfides shifted from a pyrrhotite-dominated assemblage at higher temperatures to a mainly pyrite-chalcopyrite assemblage at lower temperatures, then possibly to a pyrite-sphalerite assemblage in a few samples at even lower temperatures (Barton and Skinner, 1979). Optical properties suggest that changes also occurred in the compositions of individual phases, particularly those of pyrrhotite and chalcopyrite, as fractionation proceeded.

Sulfides in Metamorphosed Gabbros

Sulfide minerals also occur in close association with iron-titanium oxides in foliated metagabbros, notably in Units I, II, and VI. However, they are mostly pyrite rather than pyrrhotite. This indicates crystallization or recrystallization at slightly lower temperatures than in most of the igneous associations. This is especially the case in Unit VI, where some samples have coarse primary intergrowths of iron-titanium oxides and sulfides that are partly granulated and recrystallized at their edges. In more deformed samples, textural relations clearly show that the components of the sulfides were mobilized along with those of the oxide minerals and that they invaded the fabric of the metamorphosed gabbros as they were being recrystallized. In general, the recrystallized sulfides conform to shapes defined by neoblasts of clinopyroxene and plagioclase and fill fractures, areas near porphyroclasts, and other types of dilatant structures in the

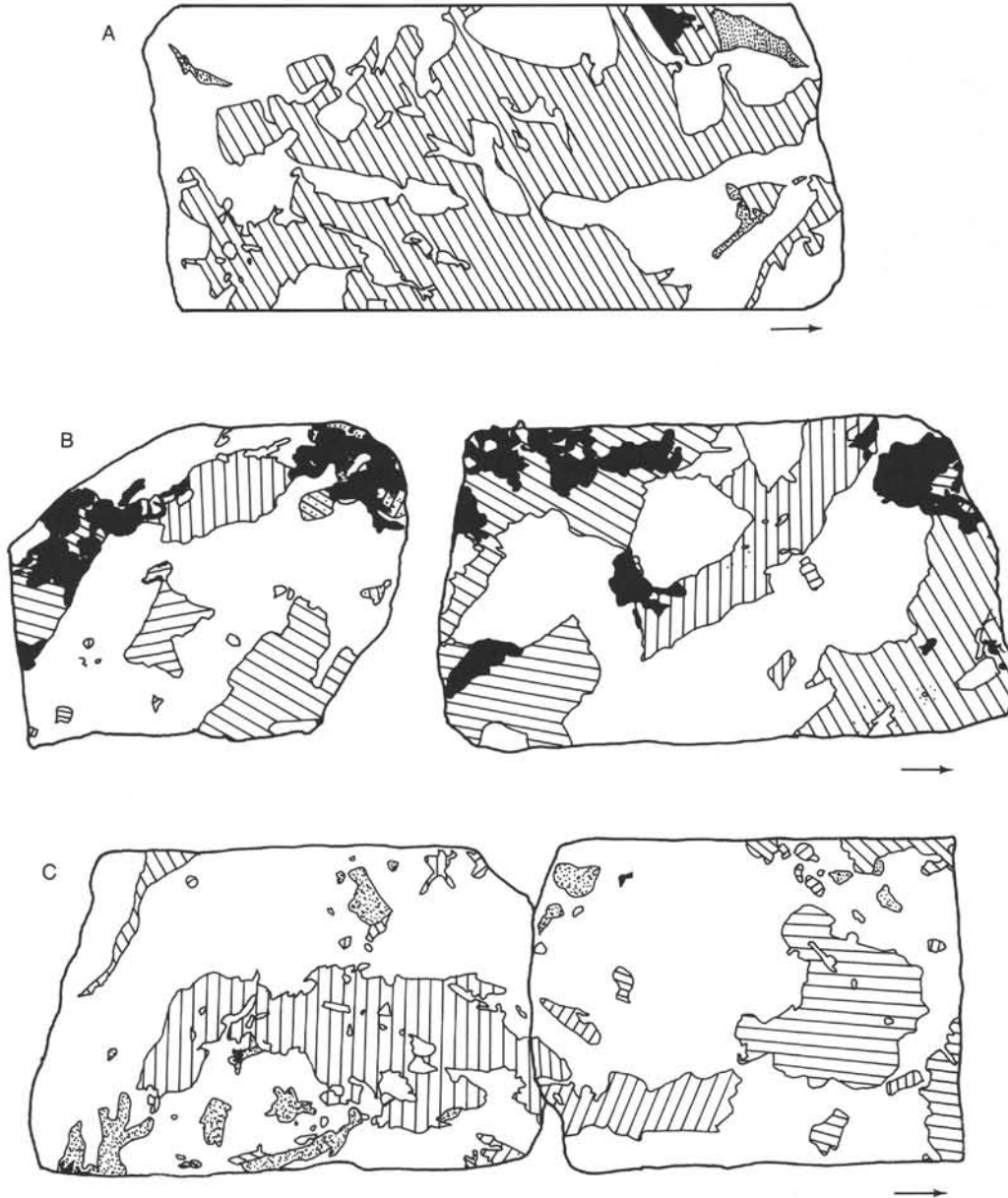


Figure 27. Grain-size tracings of individual pieces. Each slab is 5 cm wide. A. Large clinopyroxene oikocryst (lined) in an olivine gabbro (118-735B-74R-5, 71–85 cm, Piece 3A). Note vertical orientation of the grain. B. Steeply dipping lamination in a coarse-grained iron-titanium oxide gabbro (118-735B-47R-2, 11–41 cm, Pieces 2 and 3). Clinopyroxene is lined, oxides are black, and plagioclase is white. C. Intergranular clinopyroxene in an olivine gabbro (118-735B-87R-1, 10–30 cm, Pieces 3A and 3B). Note the vertical orientation of the large grain; the upper portion of this grain may be a chain of two or three pyroxenes. Clinopyroxene is lined, olivine is dotted, and plagioclase is white.

same manner as the oxide minerals. Contacts with iron-titanium oxides are along straight or curvilinear boundaries that conform to the pattern of ilmenite-magnetite intergrowths.

Relationships to Silicate Phases

In undeformed gabbros, both iron-titanium oxides and sulfide minerals have obvious primary igneous textures in relation to silicates. That is, they are intergranular in olivine gabbros and troctolites, but locally may be partly or completely enclosed by late-crystallizing ophitic pyroxenes or plagioclase. In ferro-

gabbros, the iron-titanium oxides are a dominant intercumulus assemblage, and they can both enclose and be enclosed by the magmatic silicates. In the most evolved ferrogabbros, iron-rich olivine occurs, and even this mineral may enclose, or partly enclose, oxide and sulfide phases.

A ubiquitous minor component of all comparatively fresh gabbros, and one closely associated with the oxide and sulfide minerals, is brown amphibole. This mineral is pale brown, pleochroic to clear in olivine gabbros, and darker reddish-brown in the ferrogabbros, where it is also more abundant. In completely

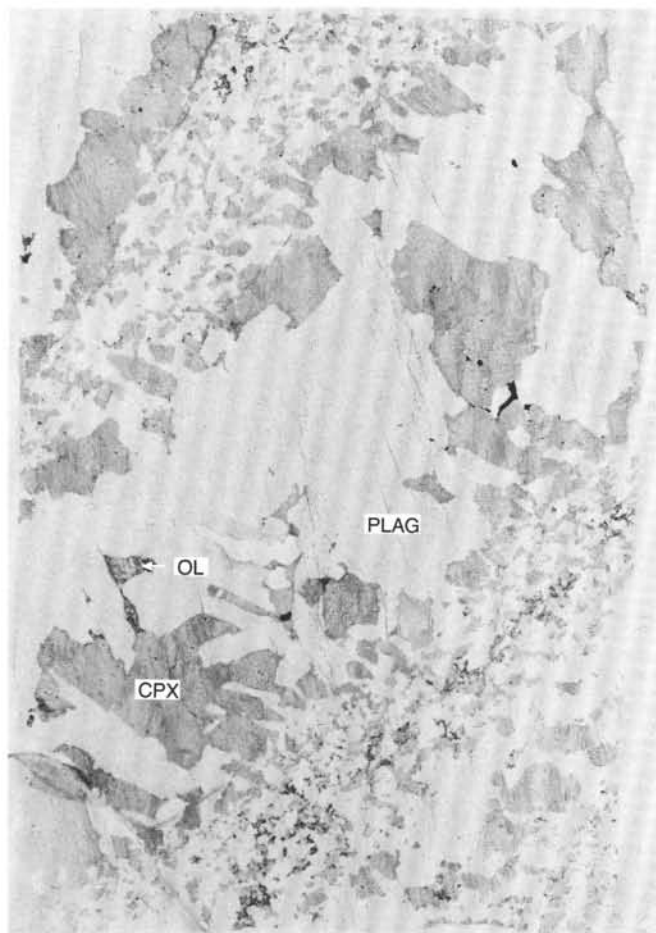


Figure 28. Plane light photograph of 5- × 8-cm thin section showing plagioclase-rich layer in a mixed gabbro-microgabbro interval. Note the orientation of the larger plagioclases and clinopyroxene approximately perpendicular to the layer boundary. Similar thin layers of plagioclase or clinopyroxene occur in some of the coarse-grained portions of size-graded intervals (118-735B-36R-3, 28-34 cm, Piece 1B). OL = olivine; PLAG = plagioclase; CPX = clinopyroxene.

undeformed rocks, it clearly represents late-stage crystallization from intergranular, volatile-rich fluids. These evidently became highly concentrated in the very evolved magmas from which the ferrogabbroic cumulus minerals precipitated.

Brown amphibole of similar appearance occurs in almost every foliated metagabbro, where it is also closely associated with iron-titanium oxides and sulfides. This amphibole crystallized during deformation and recrystallization of the gabbros (see "Metamorphism and Alteration" section, this chapter). In many metagabbros, such amphibole occurs in granulated zones among clinopyroxene neoblasts. It is present without associated iron-titanium oxides in such zones, in rare mylonitized olivine gabbros of Unit V, and with oxide minerals in the more evolved gneissic/porphyroclastic gabbros of Units I, II, and VI.

Where iron-titanium oxides are particularly abundant in shear zones, neoblasts and surrounded porphyroclasts of clinopyroxene and olivine are well preserved, even in specimens where these minerals otherwise were completely replaced by amphibole formed later. Such later amphibole is usually green and is readily distinguished from the brown amphiboles that formed in association with the oxide minerals during deformation. Thus, the oxide minerals evidently formed a nearly impermeable seal, protecting the silicates from later metamorphic transformation to

amphibole. In Cores 118-735B-1D through -7D, the only pyroxenes that can be found in some amphibolitized samples occur in the deformation zones, encased in iron-titanium oxides. In one sample, crosscutting fractures are lined with later-formed green amphibole, but these are diverted laterally along the foliation at the main ilmenite-magnetite seam in the rock.

The textural relationships among oxide minerals, neoblasts, porphyroclasts, and brown amphiboles in these highly deformed rocks leaves no doubt about the mobility of iron and titanium during metamorphism. The oxides and associated sulfides tend to fill almost any zone of potential dilatancy that developed in the deforming rocks. They invaded pressure shadows on either side of porphyroclasts; in many zones they filled all space between granular to mylonitic neoblasts; they entered boudinage-type vertical fractures in plagioclase bands in gneissic gabbros; they penetrated partings and cleavage spaces in clinopyroxenes; and they filled temporary fractures formed during deformation that locally crossed the main foliation obliquely, only to become isolated and deformed in turn by later contortions of the plastic rock mass. In no case, however, did the oxide minerals or sulfides replace any porphyroclastic or neoblastic olivine, clinopyroxene, or plagioclase, nor did the interstitial brown amphibole (although a reddish-brown amphibole did form in spaces created during the recrystallization of some clinopyroxene porphyroclasts).

This mobility of components of oxide-sulfide intergrowths, particularly that of titanium, did *not* occur during the later stages of metamorphism experienced by the rocks. Although many rocks were amphibolitized by subsequent metamorphic events, the ilmenite-magnetite intergrowths remained intact, even where isolated grains in a mylonitic matrix could presumably have been readily attacked. In some samples, near fractures where later hydrothermal fluids transformed the rocks to alkali feldspar-epidote-amphibole assemblages, ilmenite is partly or completely converted to sphene, but such occurrences are rare and restricted to narrow brecciated zones. Where later oxidative alteration has occurred, magnetite is altered and largely replaced by clay minerals and iron oxyhydroxides, but ilmenite exsolution lamellae remain.

Only the sulfide minerals were truly susceptible to later metamorphism and alteration. In most samples, they have pitted surfaces, indicating minor selective dissolution. In some rocks, however, sulfides are absent even though ilmenite and some magnetite remain. These rocks are almost wholly transformed to amphibole, and apparently, the reactive fluids involved in the transformation systematically removed sulfides from affected rocks. Occasionally in such rocks, traces of sulfide persist in least-altered cores of clinopyroxene porphyroclasts. But wherever there is pervasive green amphibole, the sulfide minerals are gone. In a few partially amphibolitized rocks, the migration of sulfide components occurred on a restricted scale. In these rocks, tiny pyrite veins can be seen in thin section, sometimes outlining the shapes of granulated neoblasts or partly filling networks of cracks in clinopyroxenes. More prominent secondary pyrite occurs in larger veins that are described in the core logs.

Finally, it is important to note the presence and variable abundance of magnetite in amphibole/talc reaction zones formed during high-temperature static metamorphism of the rocks. The reaction zones can be mere thin borders surrounding olivines and orthopyroxenes, or they can form along cracks within olivines. In a few cases, mafic phases are entirely replaced by clear or pale blue-green amphibole and/or talc. In all these cases, magnetite forms either very tiny or quite substantial crystals, some with vermicular or skeletal outlines. The metamorphism producing these reaction-zone intergrowths affected large parts of the rock, but to variable degrees. This was the principal episode

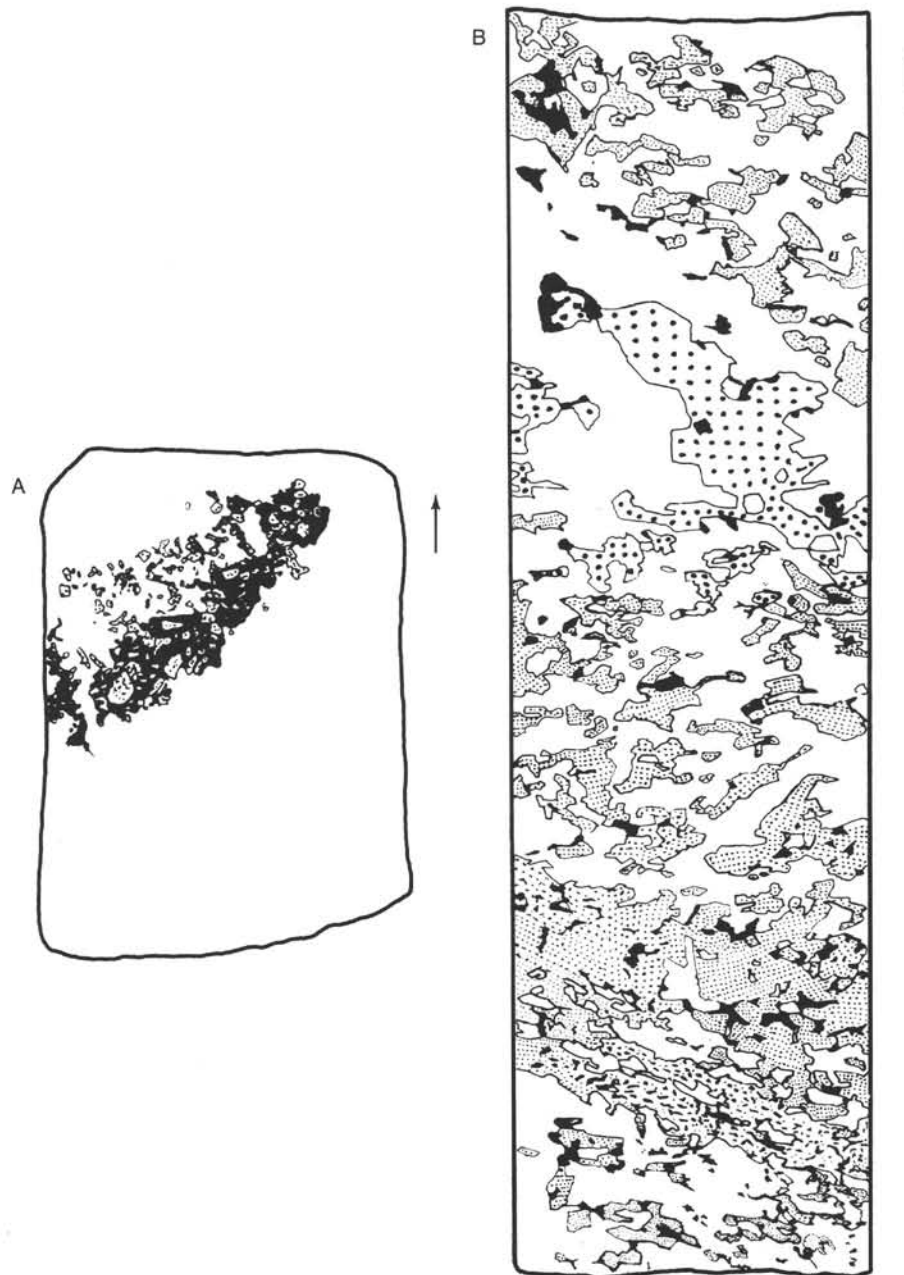


Figure 29. Phase layering in gabbros. Each slab is 5 cm wide. A. Olivine-rich layer (dotted) with poikilitic clinopyroxene (black) in an olivine-bearing, fine- to medium-grained gabbro (white; 118-735B-85R-6, 125-132 cm, Piece 4D). B. Modal layering in an olivine gabbro defined by 1- to 2-cm-thick accumulations of olivine, about 10 cm apart (118-735B-52R-4, 95-125 cm, Piece 4C). Olivine is in large dots, clinopyroxene in fine dots, oxides in black, and plagioclase is white.

of static metamorphism at high temperature that followed the deformation of the rocks. Later, localized hydrothermal alteration caused this magnetite to be removed from some of the rocks, along with their sulfide minerals.

Summary

From petrographic study, general conclusions are listed as follows.

1. Primary iron-titanium oxides and sulfide minerals are late-crystallizing phases in all undeformed gabbros. Principal minerals are ilmenite, magnetite, pyrrhotite, pyrite, and chalcopyrite.

2. Both iron-titanium oxides and sulfides are more abundant in evolved gabbros than in troctolites and olivine gabbros.

3. Phase proportions of sulfides, and probably their compositions, changed during the course of differentiation as a result of decreasing temperatures. Assemblages shifted from pyrrhotite-dominated to pyrite-dominated as differentiation proceeded.

4. The proportion of total iron-titanium oxides in the gabbros increased with fractionation, from less than that of sulfides to much greater, even though abundances of both oxide minerals and sulfides increased overall.

5. Iron-titanium oxides, sulfides, and brown amphibole are a ubiquitous intergranular and intercumulus mineral assem-



Figure 30. Size grading in an olivine gabbro (118-735B-45R-4, 93-104 cm, Piece 5A) width of slab is 5 cm. Clinopyroxene is lined, olivine is dotted, oxides are black, and plagioclase is white.

blage in undeformed gabbros and in many foliated metagabbros, provided the rocks have not experienced amphibolite-facies metamorphism and hydrothermal alteration. Such metamorphism and alteration stripped sulfides and most magnetite from the affected rocks.

6. The components of the primary opaque mineral assemblage were mobile during the high-temperature plastic deformation that produced the metagabbros and found pathways to migrate along evident porosity structure in a solid-fluid medium.

7. Subsequent static and cataclastic metamorphism produced green-brown, green, pale green, and colorless amphiboles in the gabbros and did not mobilize titanium or greatly modify the ilmenite-magnetite-sulfide intergrowths in either foliated or undeformed gabbros.

8. Fine-grained magnetite formed in reaction zones during a pervasive amphibolite-facies metamorphic event that influenced all the rocks. These are probably the minerals carrying the most stable component of magnetization in the gabbros and metagabbros.

9. Petrographic features suggest that the mobilization of iron-titanium oxides and sulfides took place at high temperatures, probably near the solidus because little apparent difference exists between the oxide-sulfide mineral associations that crystallized during the final stages of consolidation of the gabbros and those in the least-amphibolitized foliated metagabbros. A lower constraint for the temperatures attending deformation is suggested by the occurrence of ilmenite exsolution lamellae in magnetites and of hematite lamellae in ilmenites, as well as the transformation of some ilmenite to sphene. These occurrences all took place at or above 600°C (E. Kikawa, pers. comm., 1987; Miyashiro, 1973) and correspond to the highest-temperature static amphibolite-facies metamorphism that affected most of the rocks. The sulfide plus two-oxide mineral assemblages also indicate that conditions of extreme reduction existed.

METAMORPHISM AND ALTERATION

Introduction

Drilling at Site 735 recovered 434.91 m of gabbro and diabase, which were subjected to variable degrees of dynamothermal metamorphism (plastic deformation), followed by nonpermeable brecciation and static alteration associated with brittle deformation and the formation of late vein networks, respectively. The final event was an oxidative alteration that involved the formation of calcite, iron oxyhydroxide, and smectite in discrete horizons. In this section, we summarize the major episodes of metamorphism and alteration, as inferred from recrystallization and replacement of primary mineral assemblages observed in a hand sample to microscopic scale. A summary of deformation events observed on a stratigraphic scale is included in the "Structure and Deformation" section (this chapter).

Dynamothermal Metamorphism

The gabbroic rocks recovered from Hole 735B have been deformed and recrystallized to variable degrees. The textures observed in the gabbroic rocks grade from medium- to coarse-grained granoblastic to medium- to fine-grained porphyroclastic and mylonitic. To standardize the visual core descriptions and the nomenclature used, the Shipboard Scientific Party subdivided the deformed rocks into five groups that represent increasing intensity of deformation: (1) poorly foliated gabbro, (2) foliated gabbro, (3) porphyroclastic gabbro, (4) augen gneissic gabbro, and (5) mylonitic gabbro.

Textures of Deformed Gabbros

The poorly foliated gabbros show little recrystallization of the primary phases. Many of these gabbros retain their primary igneous textures (cumulus textures or hypidiomorphic granular and tabular granular, e.g., Samples 118-735B-8D-1, 45-48 cm, Piece 7; 118-735B-18R-3, 29-31 cm, Piece 3; 118-735B-18R-3, 37-40 cm, Piece 4; 118-735B-19R-2, 98-100 cm, Piece 12; 118-735B-29R-4, 19-24 cm, Piece 1B) even though some plagioclase porphyroclasts, granoblasts (crushed crystals), and neoblasts

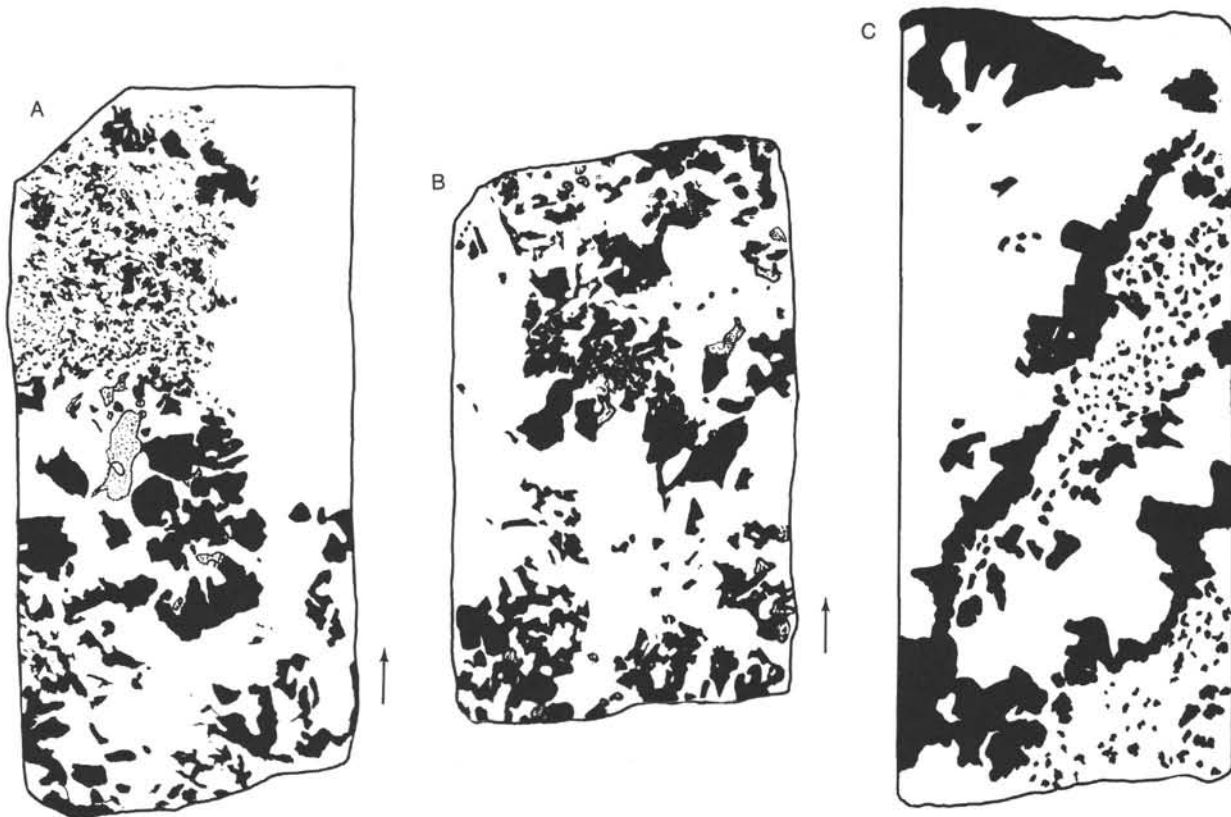


Figure 31. Textural variations in microgabbro. Width of slab is 5 cm. Clinopyroxene in black, olivine is dotted, and plagioclase is white. A. Small, fine-grained layer that may be intrusive (118-735B-45R-3, 55–72 cm, Piece 2A). The large, white area on the right side of the sample is a sheared, amphibolitized zone. B. Small, sandwiched pod of microgabbro (118-735B-76R-3, 74–83 cm, Piece 2F). C. Small, repeated lens of microgabbro (118-735B-36R-3, 28–34 cm, Piece 1B).

(recrystallized crystals) are developed (Fig. 32). The development of layers of continuous foliation distinguishes foliated from poorly foliated textures. A faint foliation results from preferred orientation of the plagioclase and pyroxene crystals. Increasing deformation results in coarse- to fine-grained porphyroclastic textures (e.g., Samples 118-735B-3D-1, 58–60 cm, Piece 11; 118-735B-9D-1, 14–17 cm, Piece 3; 118-735B-20R-2, 10–13 cm, Piece 1C; 118-735B-30R-3, 137–139 cm, Piece 6B).

Examples of poorly foliated, porphyroclastic, augen gneissic, and mylonitic gabbros are provided in Figures 32, 33, 34, and 35, respectively. These are found as isolated bands in poorly foliated to undeformed gabbros (middle section of the hole) as well as within relatively thick sequences of deformed gabbro (upper 40 m of the hole, e.g., Samples 118-735B-2D-1, 113–115 cm, Piece 2; 118-735B-4D-1, 64–68 cm, Piece 10; 118-735B-11D, 1–6 cm, Piece 1). There is a general overall grain-size reduction with increasing intensity of deformation. Grain-size reduction also depends on original texture and grain size of the rocks. The porphyroclasts can be several centimeters wide (1–4 cm) in foliated and porphyroclastic gabbros, but are generally less than 0.5 mm wide in gneissic and mylonitic gabbros. The groundmass surrounding the porphyroclasts ranges from medium- to coarse-grained (0.5–10 mm) in foliated and porphyroclastic gabbros, to fine-grained (<0.5 mm) in mylonitic gabbros. Plagioclase and pyroxene may be segregated into metamorphic bands (Figs. 35 and 36). The banding is rarely well developed in foliated gabbros, but is characteristic of some porphyroclastic gabbros and of most of the gneissic and mylonitic gabbros (Fig. 37). In mylonitic gabbros the foliation is defined by very fine alternating layers (0.4–1 mm thick) of plagioclase and mafic minerals with secondary pyroxene or actinolitic hornblende (e.g., Sample 118-735B-5D-1, 10–13 cm, Piece 3).

Several deformation features related to stress and strain constraints are well developed in the recrystallized textures of the gabbros. The primary phases were deformed at high temperatures under plastic conditions. Olivine shows kink planes, dislocation walls, and subgrain boundaries (e.g., Sample 118-735B-7D-2, 1–5 cm, Piece 1). In mylonitic gabbros, olivine is elongated and up to 6 mm long (e.g., Samples 118-735B-10D-1, 24–26 cm, Piece 6A; 118-735B-10D-2, 18–20 cm, Piece 2; 118-735B-13R-2, 55–58 cm, Piece 4B). Clinopyroxene is deformed and recrystallized into neoblasts (e.g., Samples 118-735B-1D-1, 78–82 cm, Piece 12; 118-735B-8D-1, 45–48 cm, Piece 7; 118-735B-22R-2, 41–43 cm, Piece 1C). The clinopyroxene porphyroclasts are kinked, bent, and elongated, particularly in gneissic and mylonitic gabbros. The augen-type porphyroclasts generally have symmetrical tails of granulated and recrystallized grains produced during grain-reducing mylonitization. They are partially pseudomorphically replaced by brown, yellow-brown, or brownish-green amphiboles (e.g., Samples 118-735B-9D-1, 14–17 cm, Piece 3; 118-735B-22R-2, 41–43 cm, Piece 1C). The pseudomorphic replacement gives a “leopard” texture that results from close intergrowths of amphibole and still fresh or reequilibrated clinopyroxene. The amphibole pseudomorphs are sometimes kinked, which indicates that they are at least partially pre-deformational or syndeformational. The clinopyroxene neoblasts are intergrown (not replaced) with brown or reddish-brown amphibole, which indicates contemporaneous deformation of the two (Fig. 38). The neoblasts of clinopyroxene and amphibole show a polygonal arrangement with straight crystal boundaries and triple junction contacts (e.g., Sample 118-735B-24R-3, 50–52 cm, Piece 3A). Seams of secondary magnetite or ilmenite frequently form on the neoblast boundaries. In mylonitic gabbros, concentrations of neoblasts form flattened lenses

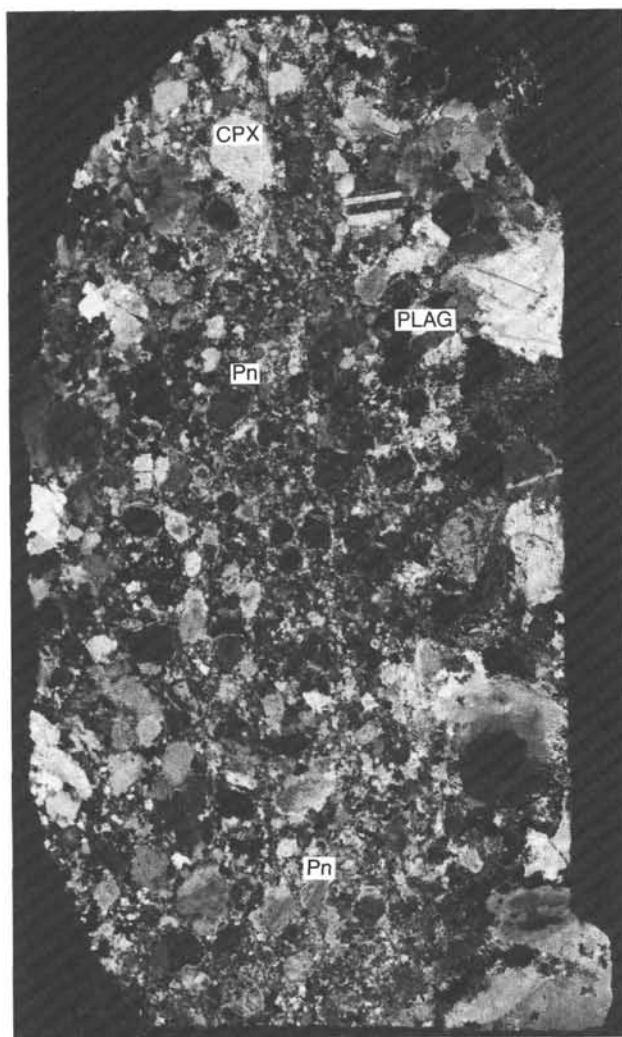


Figure 32. Photograph of whole thin section of a poorly foliated gabbro. Plagioclase (PLAG) is already partially recrystallized into neoblasts (Pn). Clinopyroxene (CPX) is only slightly deformed (118-735B-27R-1, 23-25 cm, Piece 5). Scale bar is 1 cm long.

or layers parallel to the foliation. Orthopyroxene occurs as porphyroclasts and augen, more rarely as neoblasts (e.g., Samples 118-735B-3D-1, 46-49 cm, Piece 9; 118-735B-20R-1, 76-80 cm, Piece 14). Orthopyroxene can also be found as exsolution lamellae in clinopyroxene in some mylonitic gabbros (e.g., Sample 118-735B-6D-1, 71-74 cm, Piece 13). Recrystallization of plagioclase is highly variable in all samples. Plagioclase porphyroclasts are strained and show mechanical twin deformation and undulose extinction (Fig. 39). They contain tiny chains of neoblasts running through the crystals (e.g., Sample 118-735B-13R-1, 102-105 cm, Piece 11B). Plagioclase neoblasts are polygonal or irregular in shape and have straight or wavy grain boundaries (Fig. 39). Granoblasts or neoblasts of plagioclase and clinopyroxene form a mosaic groundmass that includes brown amphibole and various amounts of ilmenite and magnetite. Triple-junction contacts were frequently observed (e.g., Samples 118-735B-1D-1, 90-92 cm, Piece 14; 118-735B-24R-3, 50-52 cm, Piece 3A). Ilmenite grains also are deformed and transposed into the foliation. Mechanisms of ilmenite transformation are described at the end of this section.

Brown amphibole occurs in different settings and its significance is discussed in the "Metamorphism" section, Site 733

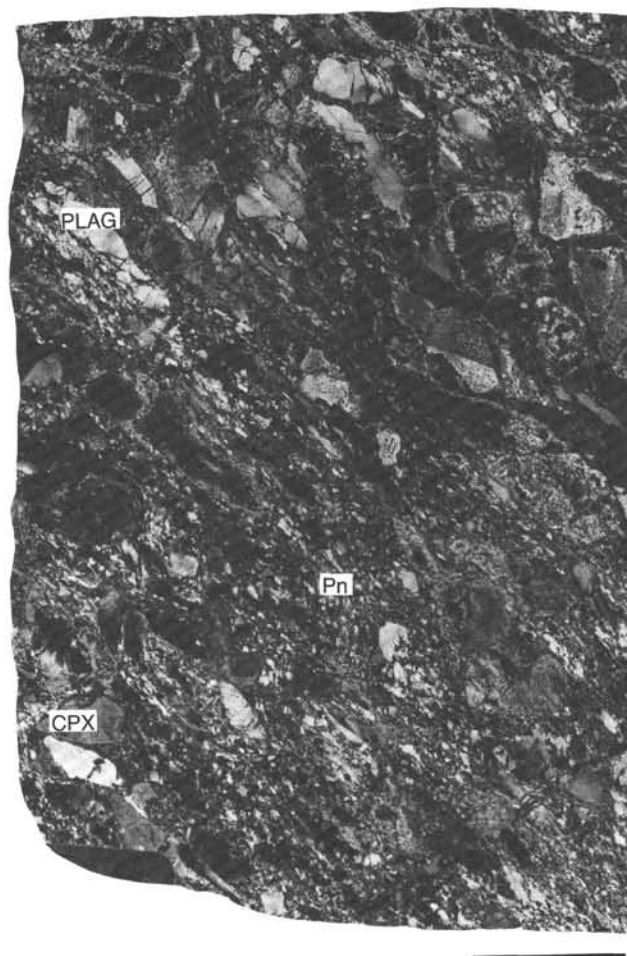


Figure 33. Photograph of whole thin section of a porphyroclastic gabbro showing a strong foliation defined by stretching of plagioclase and clinopyroxene. Plagioclase is highly recrystallized into neoblasts. Same legend as in Figure 32 (118-735B-4D-2, 10-16 cm, Piece 1). Scale bar is 1 cm long.

chapter (this volume). Brown amphibole is always associated with clinopyroxene or occluded ilmenite as patches within the clinopyroxene crystals or at their outermost margins. This type of brown amphibole is strongly pleochroic and limpid under plane light. It may be of primary origin. Brown amphibole of probable secondary origin is preferentially crystallized in micro-shear zones, cracks, or along cleavages of clinopyroxene. The correlation between the quantity of brown amphibole and the extent of deformation of the gabbro also suggests that the amphibole is secondary. Most of the brown amphibole occurs as granoblasts associated with mosaic groundmass pyroxene and plagioclase neoblasts (e.g., Sample 118-735B-30R-3, 137-139 cm, Piece 6B). Amphibole granoblasts are associated with deformed ilmenite grains in porphyroclastic, gneissic, and mylonitic gabbros. These observations suggest that the brown amphibole is pre-deformational or syndeformational. The association of brown amphibole and deformed, partially replaced pyroxene indicates a maximum temperature of 1050°C (Boyd, 1959; Holloway, 1973) and a minimum temperature of 770°C, according to Spear (1981).

The textural relationships between brown amphibole, clinopyroxene, and ilmenite indicate that crystallization of potential magmatic amphibole occurs near the solidus at a temperature near 900°C, which is consistent with Spear's (1981) experimen-

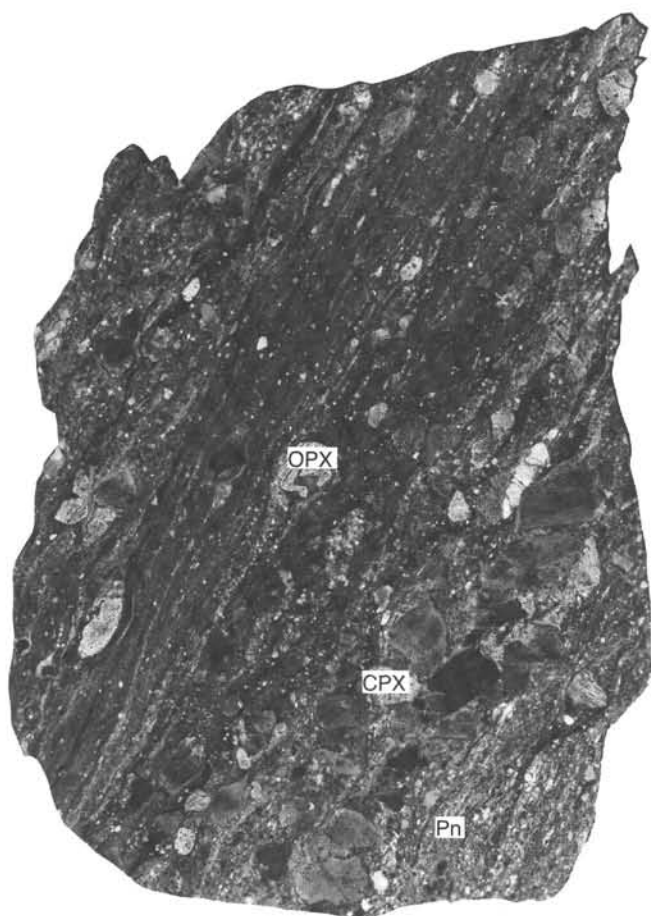


Figure 34. Photograph of whole thin section showing poorly banded augen gneissic gabbro in sharp contact with a very fine-grained mylonitic band. The foliation is enhanced by alternating fine- and coarse-grained bands. Orthopyroxene (OPX) is a coexisting phase. Same legend as Figure 32 (118-735B-1D-2, 80–90 cm, Piece 13). Scale bar is 1 cm long.

tal results and phase relations in the hydrous basaltic system. In addition, the sparse unambiguously igneous brown amphibole and the metamorphic hornblende that increases in quantity with deformation are optically indistinguishable. This, and their association with pyroxene neoblasts, suggest that the formation of the latter may have begun at temperatures over 800°C (Spear, 1981) as the fluids penetrated the gabbroic rocks along grain boundaries. Subsequent amphibole formation probably represents a continuum in compositions associated with declining temperatures and increasing hydration.

These temperatures might be lower, depending on the actual composition of amphibole, a_{H_2O} of the metamorphic fluid, total pressure, and presence of a vapor phase (Spear, 1981; Gilbert et al., 1982). Of these variables, lower a_{H_2O} and fugacity of H_2O are the most critical that might lower the upper stability limit of amphibole by 30° to 100°C.

The high-temperature stage of deformation and metamorphism is overprinted by a second stage of amphibolitization. The amphibole pseudomorphs are partially retrograded into light brown to green hornblende and fibrous green actinolite (e.g., Samples 118-735B-7D-2, 9–11 cm, Piece 1; 118-735B-13R-1, 102–105 cm, Piece 11B; 118-735B-18R-3, 29–31 cm, Piece 3; 118-735B-33R-1, 60–62 cm, Piece 11B) and some chlorite (e.g., Sample 118-735B-15R-1, 90–93 cm, Piece 7B). These late phases are locally deformed in the direction of former foliation or small

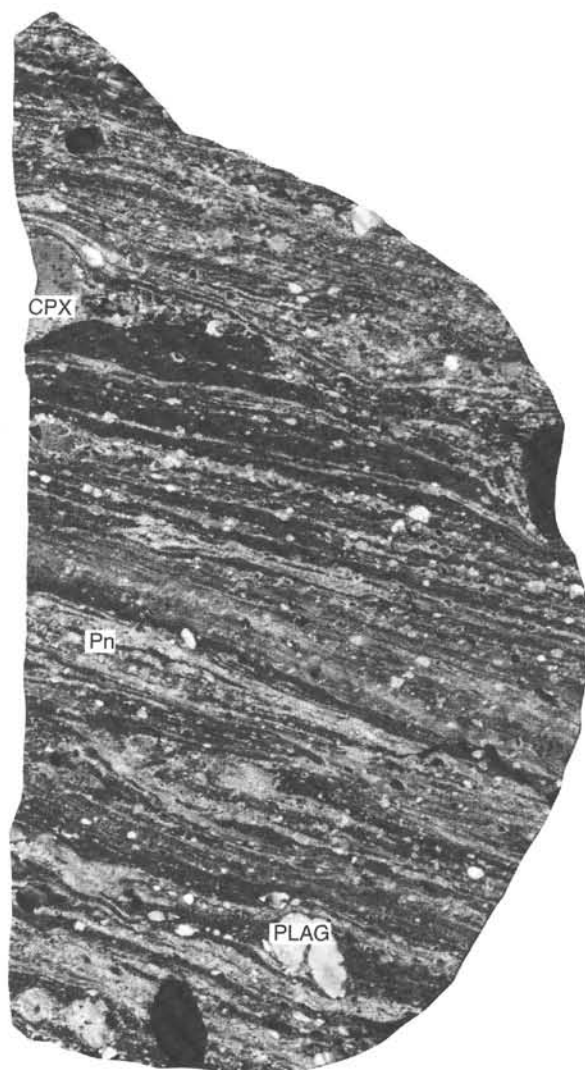


Figure 35. Photograph of a whole thin section of a mylonitic gabbro with well-defined fine-scale banding. Grain size is greatly reduced. Same legend as in Figure 32 (118-735B-3D-1, 44–49 cm, Piece 9). Scale bar is 1 cm long.

oblique shear zones. The deformation of medium-grade amphibole is related to a tectonic reactivation of foliation during minor compression-shearing events.

Ilmenite-Magnetite Concentrations in Deformed Gabbros

Several core intervals contain moderate to high concentrations of ilmenite and magnetite (e.g., Cores 118-735B-44R, -46R, -47R, etc., down to 212 mbsf, particularly in lithologic Units III and IV, see "Lithostratigraphy" section and for detailed descriptions of occurrences, see "Petrography" section, this chapter). These concentrations are layerlike, lens-shaped, or disseminated around silicates. The oxides occur in both massive gabbro and variously deformed olivine-bearing and olivine-free gabbro (e.g., Samples 118-735B-44R-2, 6–8 cm, Piece 1A; 118-735B-24R-2, 95–97 cm, Piece 5; 118-735B-53R-3, 15–17 cm, Piece 1B). In massive (undeformed) gabbros, the oxides are large grains that fill intergranular spaces between silicates. They contain small amounts of sulfide minerals. In deformed gabbros, ilmenite and magnetite are granular, recrystallized inter-

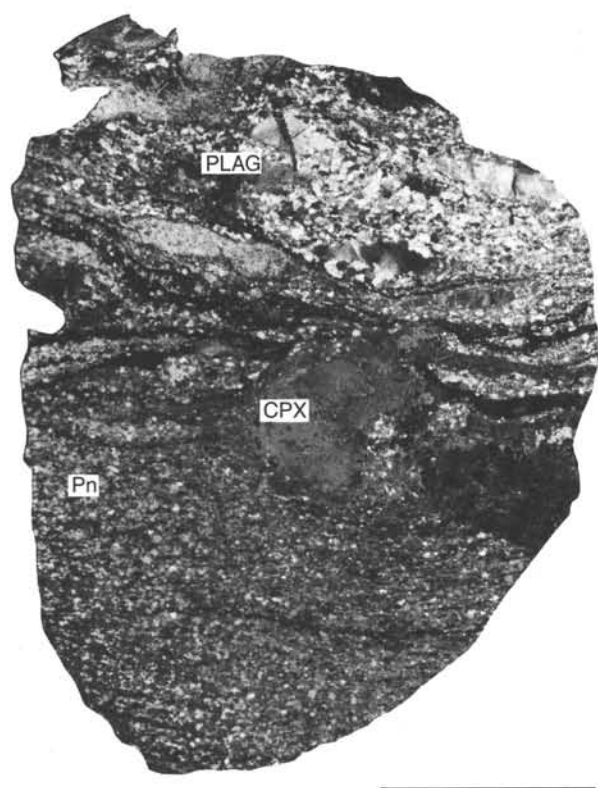


Figure 36. Photograph of whole thin section of an augen gneissic gabbro showing wavy plagioclase- and pyroxene-rich alternating bands. Clinopyroxene porphyroclasts are rotated into the foliation. Same legend as in Figure 32 (118-735B-1D-1, 26–30 cm, Piece 4). Scale bar is 1 cm long.

growths distributed in the foliation and in open fractures. These oxides are associated with iron-copper and iron sulfides closely mixed with the oxide grains or disseminated into intergranular silicate spaces.

Ilmenite-Magnetite Characteristics During Stages of Gabbro Deformation

Oxide occurrences in undeformed gabbros thought to reflect primary magmatic processes are typified by Samples 118-735B-23R-3, 34–37 cm, Piece 2; 118-735B-32R-1, 64–66 cm, Piece 1F; 118-735B-44R-4, 6–8 cm, Piece 1A; 118-735B-47R-4, 82–84 cm, Piece 6; and 118-735B-49R-2, 89–91 cm, Piece 1F. In thin sections, primary grain boundary contacts were observed between large undeformed ilmenite grains and clinopyroxene, orthopyroxene, and plagioclase (Fig. 40). Ilmenite is a post-cumulus or late-magmatic phase that poikilitically encloses the silicate minerals. In some cases, spectacular symplectite intergrowths of ilmenite and orthopyroxene were observed. The textural intergrowths are graphic and lamellar (see Fig. 40). Linear inclusions of ilmenite and occasionally rutile as an alteration product of ilmenite, were observed under reflected light (see “Relationship of Sulfides and Oxides to Metamorphism” subsection). In addition, abundant, strongly pleochroic, brown amphibole is intergrown with the ilmenite grains (in the clinopyroxene crystals and the groundmass).

Even though these gabbros are undeformed, the primary phases are partially replaced by metamorphic assemblages (e.g., secondary clinopyroxene and amphibole) and ilmenite shows signs of destabilization. There are coronas of colorless to grass green, fibrous actinolite surrounding ilmenite and clinopyroxene (Fig. 41). Phlogopite also was observed in contact with il-

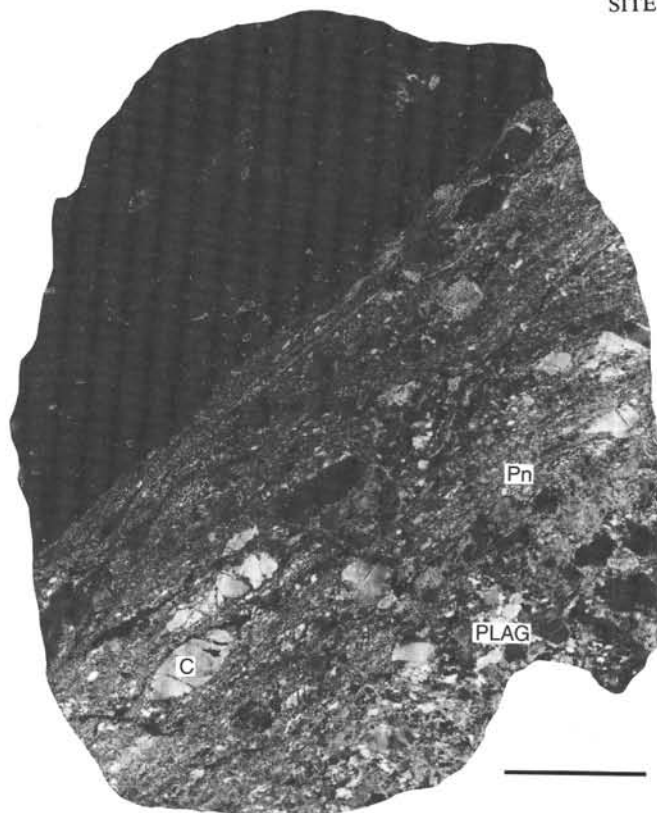


Figure 37. Photograph of a whole thin section of fine-grained porphyroclastic gabbro in sharp contact with a mylonitic band. Clinopyroxene is strongly elongated and plagioclase is present almost solely as neoblasts. Same legend as in Figure 32 (118-735B-4D-2, 24–29 cm, Piece 3). Scale bar is 1 cm long.

menite grains (e.g., Section 118-735B-62R-2, 302 mbsf). Irregular granules of magnetite form a discontinuous seam at the very margin of ilmenite within the actinolite coronas and are part of the reaction rim. In turn, primary brown amphibole and actinolite are rimmed by blue-green amphibole. Ilmenite was observed in cracks, along with blue-green amphibole and magnetite assemblages, which suggests remobilization during metamorphism. Vermicular pink sphene, also a metamorphic phase, is spatially associated with the ilmenite grain and was interpreted as a replacement of this phase. Ilmenite mobilization is accentuated where the gabbro is sheared (Fig. 42) or actinolite replacement more advanced. Magnetite is similarly concentrated along the planes of shearing. In crushed areas, there are broken pieces of blue-green and brown amphibole that do not have new metamorphic phases (e.g., Sample 118-735B-22R-1, 78–80 cm, Piece 9).

A second group of samples represents more advanced ilmenite mobility that increases with deformation and metamorphism (e.g., Samples 118-735B-28R-2, 57–60 cm, Piece 6; 118-735B-27R-1, 23–25 cm, Piece 5; 118-735B-48R-4, 82–84 cm, Piece 6; 118-735B-51R-4, 102–104 cm, Piece 1C; 118-735B-52R-4, 69–71 cm, Piece 4B). The host gabbro is deformed and has a porphyroclastic texture. The cores of the clinopyroxene porphyroclasts are fresh and are surrounded by granoblasts of clinopyroxene, brown amphibole, ilmenite, and magnetite. The clinopyroxene neoblasts are inclusion-free and intergrown with neoblasts of both ilmenite and brown amphibole. Granular ilmenite and magnetite are injected into the planes of deformation. The oxides are associated with brown amphibole in all stages of deformation and recrystallization. Where present, cracks are preferentially filled with ilmenite and brown amphibole, along with magnetite granules. Epidote, pink sphene, and actinolite can also be found in open fractures. In this case, ilmenite has been

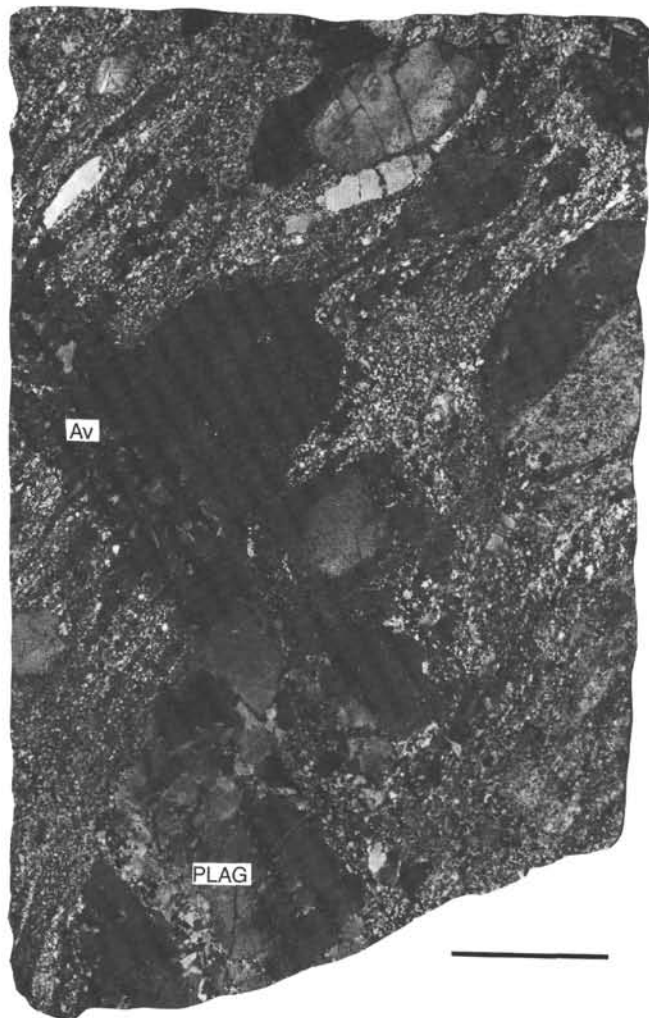


Figure 38. Photograph of whole thin section of a fine-grained porphyroclastic gabbro showing elongation of pyroxene and plagioclase porphyroclasts and plagioclase neoblasts. An amphibole vein (Av) cuts the porphyroclasts. Same legend as in Figure 32 (118-735B-14R-3, 31–35 cm, Piece 2A). Scale bar is 1 cm long.

remobilized during actinolite growth in already hydrated rocks at high temperature. The deformation plays an important role in increasing the surface area of grains (recrystallization, crushing) and in creating favorable structures for deposition for mobilized oxides. The metamorphic recrystallization of the igneous clinopyroxene is also a process that may contribute ilmenite to the rock by exclusion of ilmenite inclusions and loss of titanium and iron from enriched clinopyroxene margins or hosted orthopyroxene lamellae.

The third stage of ilmenite destabilization is characterized by development of a strong foliation in the host rock (e.g., Sample 118-735B-53R-3, 15–17 cm, Piece 1B). Like the brown amphibole, ilmenite and magnetite are largely disseminated along the foliation. Intergrowths of ilmenite and brown amphiboles (primary?) were observed in less deformed areas. These assemblages may represent high-temperature igneous assemblages (~900°C). Growth of grass-green amphibole occurred contemporaneously with replacement of igneous calcic plagioclase by sodic plagioclase. Other types of replacement are similar to those in less deformed rocks.

We observed intense transposition of ilmenite-magnetite intergrowths in porphyroclastic gabbros (e.g., Samples 118-735B-

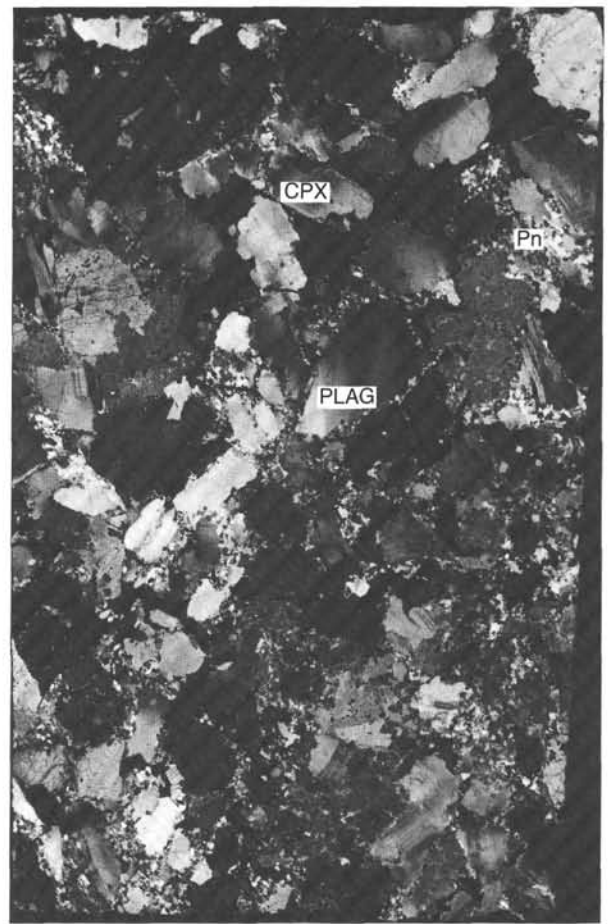


Figure 39. Photograph of whole thin section of a foliated gabbro showing more extensive recrystallization of plagioclase into neoblasts. There is a weak preferred orientation of clinopyroxene and plagioclase. Same legend as in Figure 32 (118-735B-55R-2, 101–105 cm, Piece 4). Scale bar is 1 cm long.

24R-2, 95–97 cm, Piece 5; 118-735B-24R-3, 50–52 cm, Piece 3A). The distribution of ilmenite is largely controlled by the well-defined foliation. Again, interstitial granular oxides can be seen in close association with brown amphibole. Both are deformed and recrystallized into granoblasts, forming a mosaic of polygonal grains. We observed plagioclase neoblasts having irregular contacts and rare triple junctions, which indicate a non-equilibrium state. We are not sure whether ilmenite-magnetite intergrowths are *in-situ* recrystallized grains or if they are precipitated phases from hydrothermal fluids. However, the invariable association of oxides with hydrous phases favors the second hypothesis, particularly for the deformed gabbros and for samples where no primary oxide-silicate contacts are preserved.

Summary

Relationship of Sulfides and Oxides to Metamorphism

Remobilization of ilmenite and magnetite is clearly related to hydration of the gabbroic rocks. The ilmenite first begins to break down at the stage of high-temperature brown amphibole formation. Further breaking down of the oxides during development of green and blue-green amphibole was related to the late vein network (see "Static Alteration in Undeformed Gabbros" section, this chapter) and fluid circulation along the foliation. Clearly, under dynamothermal metamorphism, ilmenite is more extensively altered and remobilized. This remobilization is

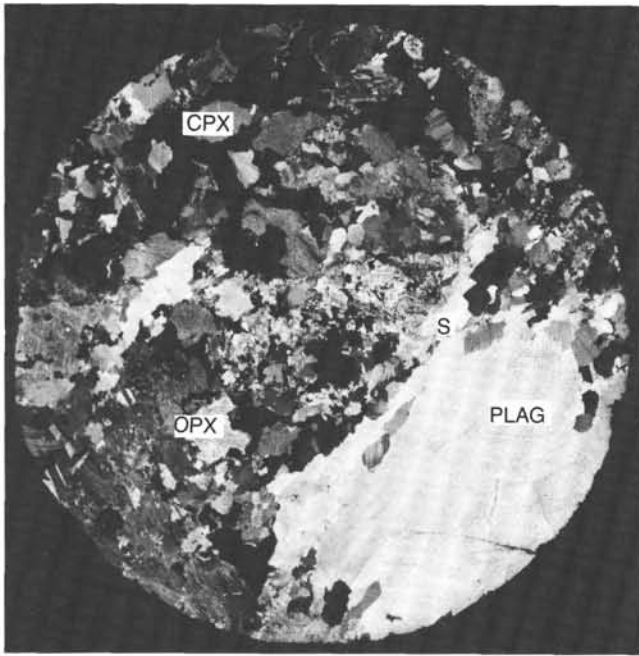


Figure 40. Photograph of whole thin section of primary ilmenite (black) in a poorly foliated orthopyroxene-bearing gabbro. Symplectite relationship between ilmenite and orthopyroxene is visible (S). Ilmenite is a post-cumulus phase. Same legend as in Figure 34 (118-735B-44R-2, 6-8 cm, Piece 1A). Scale bar is 1 cm long.

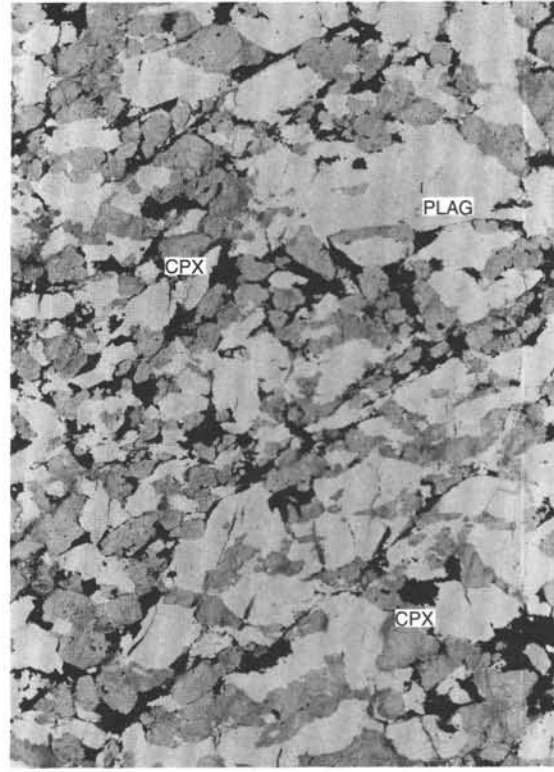


Figure 42. Photograph of whole thin section of a foliated gabbro showing important remobilization of ilmenite-magnetite intergrowths along the foliation and into oblique cracks in plagioclase. Brown amphibole (light gray) is intimately associated with iron oxides. Same legend as in Figure 32 (118-735B-52R-4, 88-94 cm, Piece 4B). Scale bar is 1 cm long.

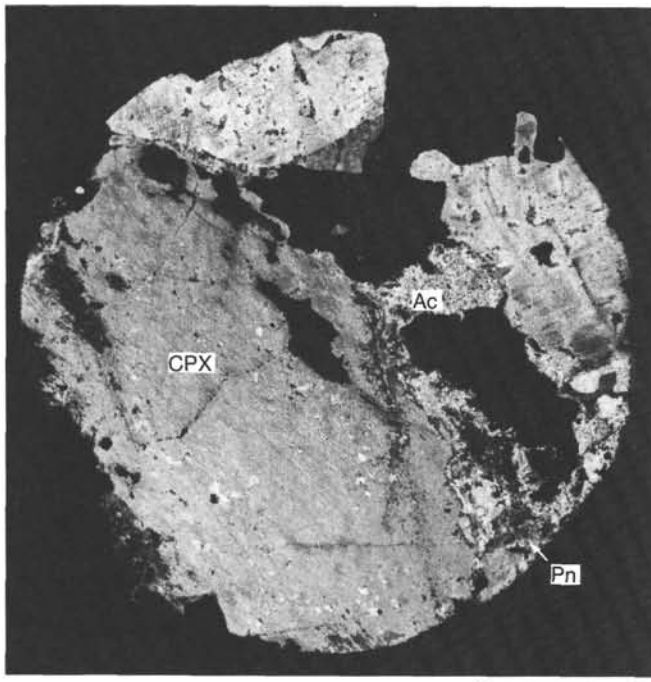


Figure 41. Photograph of whole thin section of a massive ilmenite gabbro showing partial replacement of ilmenite surrounded by coronitic actinolite (Ac). Same legend as in Figure 32 (118-735B-32R-1, 64-66 cm, Piece 1F). Scale bar is 1 cm long.

then amplified in the later hydration stages of medium- to low-grade metamorphism. However, under static metamorphism, the oxides are only partially recrystallized, even at the final stages of hydration. Higher concentrations of iron-copper and iron-sulfides in deformed rocks are consistent with this interpretation. The combined effects of high-temperature deformation (plastic deformation) and hydration (formation of amphibole, micas) are responsible for major alteration of oxides. In addition, recrystallization of clinopyroxene might liberate excess ilmenite. This would add to the quantity of optically identical primary magmatic ilmenite, similar to what was observed for red-brown amphibole under comparable conditions. Ilmenite production may also be mobilized by hydrous fluids at temperatures that prevent the formation of abundant hydrous phases even though PH_2O is elevated. Thus, we wish to stress that under hydrothermal conditions titanium-iron oxides can be considered relatively mobile and capable of being transported in hydrous fluids and deposited in favorable deformation structures. Still unresolved is the question of how far the iron-titanium oxides can be hydrothermally transported. Primary iron-titanium oxide-rich gabbros are known to occur on the ocean floor; generally, these are evolved ferrogabbros (Fox and Stroup, 1981). However, in Hole 735B, the oxide-rich gabbros are often olivine-bearing (e.g., Sample 118-735B-44R-4, 6-8 cm, Piece 1A), which indicates that they originated from a more primitive liquid. The presence of large amounts of iron-titanium oxide in olivine-bearing gabbros suggests a metasomatic origin for the ox-

ides, particularly in the deformed rocks. The assemblage olivine plus abundant ilmenite is very unusual in oceanic crustal rocks.

Alteration Associated with Cataclastic Deformation

Brittle deformation of the gabbros resulted in formation of predominantly hornblende-bearing veins 0.5 to 2 cm wide. These veins bear a fixed relationship to the orientation of the foliation in the plastically deformed rocks and probably result from the same stress conditions. Secondary alteration associated with crosscutting veins occupies from 1% to 30% of the rock, with an average of about 5%–10%. The vein network provided pathways for fluids to penetrate the gabbros at temperatures low enough to permit the formation of hydrous secondary phases. All alteration that occurred after plastic deformation was related to fractures of variable sizes. Even the smallest percentage of secondary alteration can be related to proximity to microcracks. Movement along some of these fractures is manifested in sheared mineral assemblages within the veins. In addition, zones of brecciation were identified at depths of 180, 260, 270–285, 315, 330, 345, and 500 mbsf. Highly altered pieces of shattered gabbro were recovered from these zones. Mirolitic vein mineralization suggests the existence of open fractures during alteration in these zones. Oxidized halos on pieces of rubble and the replacement of the metamorphic assemblage by carbonate and carbonate veins within these brecciated zones reflect a later lower-temperature alteration under more oxidizing conditions than was observed in nonbrecciated sections of the core.

Within the upper 50 m of the section (Cores 118-735B-1D through 118-735B-14R), the only minerals within the cracks and veins are hornblende and sodic plagioclase. The thin (<0.5 mm) white veins that we observed are submillimeter cracks along which fluids have induced sodium metasomatism. Replacement of the calcic plagioclase by sodic plagioclase is ubiquitous wherever microcracks penetrate the rock. This process is most intense near the fracture systems and almost complete within the brecciated zones. This results in anastomosing networks of milky white sodic plagioclase as rims or complete replacements of the original calcic plagioclase. Clinopyroxene adjacent to these cracks is replaced by dark green hornblende, some of which has euhedral crystal faces projecting into the fracture. In slightly larger veins, hornblende has formed within the fracture as euhedral green laths or fine needles, distinct from the albitized and amphibolitized vein margins. Where shearing has occurred along fractures, the distinction between metasomatic replacement and direct precipitation is difficult to determine. Fragments of sodic plagioclase within such microshears have a crosshatched extinction pattern. We believe this results from almost complete albitization of shattered plagioclase crystals. Only the largest hornblende-sodic plagioclase veins contain blocky grains of untwinned sodic plagioclase that appear to have precipitated directly from metamorphic fluids, rather than forming as a replacement of a preexisting calcic plagioclase. The best example of euhedral metamorphic sodic plagioclase is in the mirolitic veins in the cataclastic breccia (e.g., Sample 118-735B-81R-6, 87–90 cm, Piece 5).

Amphibole veins up to 1.5 cm wide crisscross the foliated metagabbros (Fig. 36), both in the upper part of the section (e.g., Section 118-735B-1D-2, upper 6 m) and in the lowermost foliated gabbros (e.g., Section 118-735B-85R-4 at 475 mbsf). In the upper, intensely foliated section, the green hornblende veins are usually coarsely crystalline. Some are deformed by stretching along the plane of foliation and must predate the last episode of deformation. Most of the hornblende veins in the upper foliated metagabbros, however, and all the veins below the shallow deformation zone (about 75 mbsf) postdate all episodes of plastic deformation. However, these may represent a part of the

same deformation event as a late brittle rupturing. In these rocks, as well as in the undeformed units, the vein amphibole occurs as fine-grained laths or needles that may have grown into open cavities as euhedral prisms. The vein hornblende is either green, green-to-brown pleochroic, or, less commonly, brown. Some of the larger veins contain hornblende that is spectacularly zoned from outer green rims to deep brown interiors (Sample 118-735B-12R-1, 65–68 cm, Piece 5B). These veins also contain lesser quantities of green hornblende that is pleochroic to shades of blue-green or turquoise.

The vein amphibole is optically different from the red-brown amphibole that forms neoblasts and intergrowths in the foliated rocks. Where late hornblende veins crosscut foliated metagabbros or mylonites, the clinopyroxene and red-brown hornblende neoblasts are replaced by green-to-brown hornblende of the vein assemblage (Sample 118-735B-7D-1, 63–67 cm, Piece 9). Similarly, clinopyroxene porphyroclasts are replaced by coarse aggregates of green amphibole associated with the late veins (Fig. 43). Some of the clinopyroxene porphyroclasts are replaced by a pale brown hornblende unlike the vein minerals. These latter porphyroclasts sometimes contain relict clinopyroxene cleavage and may have margins replaced by smaller aggregates of green hornblende. This pale brown hornblende may be a syndeformational or pre-(plastic) deformational phase. Extensive amphibolitization and sodium metasomatism are exemplified by Sample 118-735-1D-1, 117–120 cm, Piece 19. In this sample, porphyroclasts



Figure 43. Photograph of a whole thin section of a weakly deformed metagabbro cut by numerous veins of bright green amphibole. Clinopyroxene is partially replaced by the same green amphibole as in the veins. Olivine is replaced by talc plus tremolite plus magnetite with a reaction corona of chlorite extending into the plagioclase (118-735B-15R-3, 92–96 cm, Piece 8). Scale bar is 1 cm long.

of clinopyroxene are pervasively replaced by coarse aggregates of pleochroic brown hornblende. Some of the hornblende crystals are deformed, and the aggregate is rimmed by green hornblende at the boundary with plagioclase. Sodic plagioclase forms an anastomosing network throughout the plagioclase. Only a few neoblasts of clinopyroxene remain; presumably most of them have been replaced by green hornblende.

More extensive alteration of the deformational assemblages (clinopyroxene-plagioclase-orthopyroxene-ilmenite-olivine-red hornblende) results in complex replacement coronas identical to those in the undeformed gabbros. Examples are Samples 118-735B-7D-1, 10–16 cm, Piece 2A; 118-735B-35R-7, 14–17 cm, Piece 2; and 118-735B-37R-1, 11–13 cm, Piece 2A, in which elongate porphyroclasts of orthopyroxene or olivine are replaced by either talc plus acicular amphibole plus magnetite or hematite plus calcite assemblages (Fig. 44). The cummingtonite or anthophyllite in the porphyroclast cores occurs as colorless blades

having a fringe of green actinolite. Relict cracks through the porphyroclasts are lined with cummingtonite and opaque grains. The porphyroclasts are surrounded by neoblasts of red-brown hornblende and ilmenite. The red-brown hornblende is partially replaced by actinolite-tremolite. The outermost corona and boundary with plagioclase is composed of pale green pargasite, sometimes intergrown with phlogopite, that extends into the adjacent mosaic of plagioclase (Fig. 45). These samples are crosscut by late veins of green or blue-green hornblende that merge into green amphibole pseudomorphs of clinopyroxene. In foliated samples that have discrete layers of ilmenite, reaction coronas of green hornblende and pleochroic green phlogopite line the boundary between plagioclase and ilmenite (e.g., Sample 118-735B-1D-2, 86–90 cm, Piece 13). Replacement of primary clinopyroxene by amphibole in Cores 118-735B-1D through 118-735B-57R varies from 2%–20%. This *in-situ* replacement, combined with the hornblende within veins (from 0%–30%), brings the total amphibole replacement of gabbro to 10% to 15%.

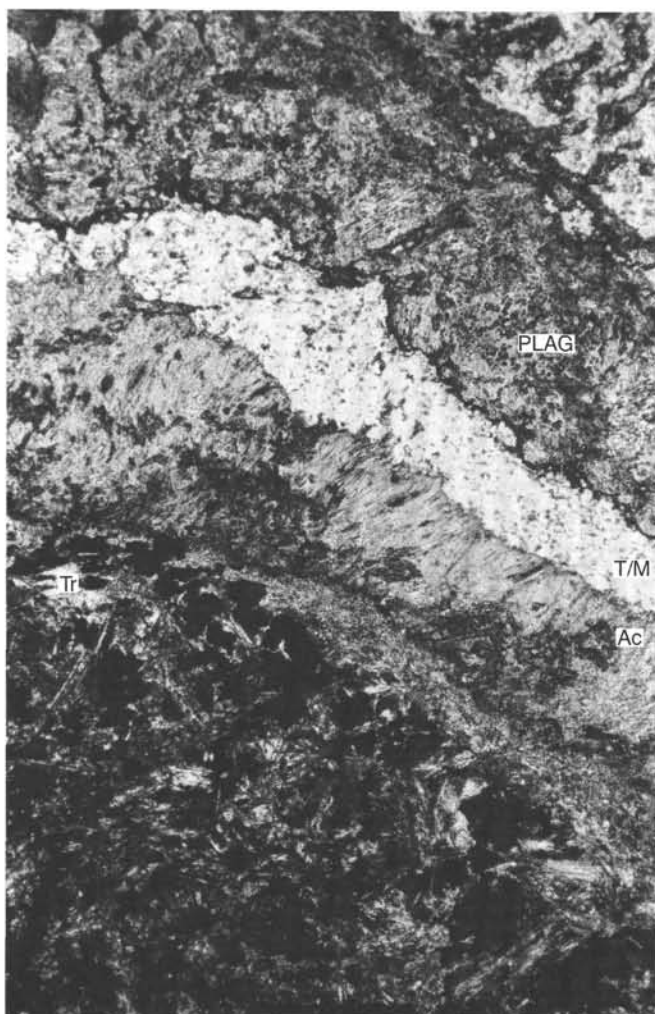


Figure 44. Microphotograph of an olivine pseudomorph with a reaction corona from interval 118-735B-7D-1, 10–16 cm, Piece 2A. The core is replaced by tremolite and talc, with opaque grains of magnetite. The assemblage is itself partially replaced by hematite and calcite. The corona around olivine is (from olivine outward) colorless tremolite (Tr), a skirt of green actinolite, and finally a green talc or mica (T/M) that protrudes into plagioclase. Scale bar is 0.1 mm long. Same legend as in Figures 32 and 41. Plane light.

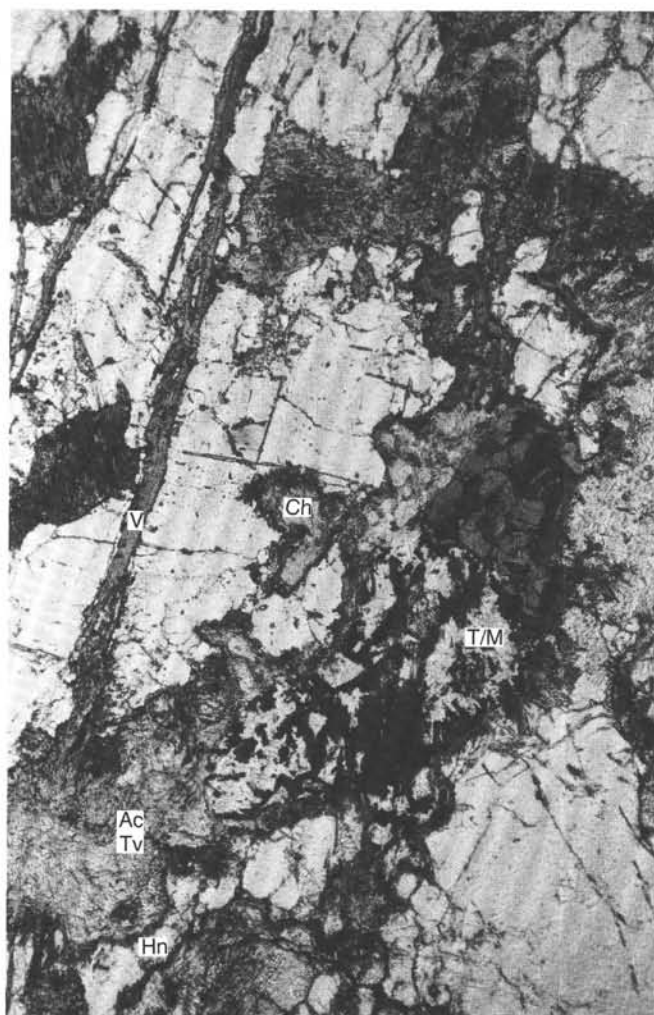


Figure 45. Microphotograph of reaction coronas in Sample 118-735B-37R-1, 11–13 cm, Piece 2A. Veins (V) contain green hornblende. Clinopyroxene is replaced by a core of colorless tremolite rimmed with green actinolite. Where the actinolite extends into plagioclase, it is mixed with dark chlorite (Ch). Olivine is replaced by talc plus magnetite. A relict brown hornblende neoblast (HN) is unaltered. The vein is 1 mm wide. Same legend as in Figures 41 and 44. Plane light.

Hydrothermal-Plagiogranite Veins

Small quantities of unusual veins were observed in Cores 118-735B-35R, -43R, -44R, -46R, -64R, and -77R and may be of magmatic or hydrothermal origin. A deformed vein in Sample 118-735B-35R-2, 105–106 cm, Piece 4G, contains hornblende, sodic plagioclase, quartz, diopside, phlogopite, and clinzoisite. The hydrothermal vein assemblages are unique and contain either euhedral diopside or hornblende, large (>1 mm) pink, euhedral sphene, yellow rutile, clinzoisite, pistacite, and sodic plagioclase (e.g., Samples 118-735B-68R-3, 62–64 cm, Piece 5 and 118-735B-43R-4, 135–139 cm, Piece 8B), and occasionally carbonate (e.g., Sample 118-735B-77R-1, 33–35 cm, Piece 2C). Similar assemblages replace wall rocks adjacent to these veins (e.g., Sample 118-735B-76R-5, 62–64 cm, Piece 1F). Analcite containing actinolite fibers was observed in veins (Sample 118-735B-19R-2, 98–100 cm, Piece 12) and as rims on plagioclase (Sample 118-735B-45R-4, 136–140 cm, Piece 7). Apatite and euhedral sulfides also were observed in this latter example. In addition, segregated diopside-sodic plagioclase veins up to 1.5 cm wide were observed in cores at about 300 mbsf. Clinzoisite was frequently observed in and below Core 118-735B-18R (below about 70 mbsf). Assemblages observed in altered wall rock below 300 mbsf (e.g., Samples 118-735B-64R-4, 73–76 cm, Piece 1H, and 118-735B-70R-2, 8–10 cm, Piece 2) include green diopside, andesine, clinzoisite, actinolite, sphene, or rutile. Pistacitic epidote and chlorite are abundant only in the largest veins near brecciated zones. Prehnite was optically identified only in a few thin sections, where it combines with tremolite in reaction coronas.

Static Alteration in Undeformed Gabbros

Alteration in the undeformed gabbros produced reaction coronas around and pseudomorphs of primary igneous minerals. The most abundant hydrous phase is green amphibole, but other secondary minerals include tremolite, talc, clinzoisite, magnetite, chlorite, cummingtonite, pargasite, pinkish sphene, yellow rutile, epidote, and sparse flakes of phlogopite. The quantity and identity of the alteration assemblages were determined by (1) the original permeability that allowed the influx of water, (2) the primary modal abundances, (3) the composition of the primary minerals, and (4) the ambient temperatures existing during the alteration. Olivine and orthopyroxene are preferentially replaced by talc-magnetite \pm tremolite \pm cummingtonite. The replacement of olivine by talc and magnetite is ubiquitous and apparently occurred at high temperatures with minute quantities of fluid. For example, in one sample, a thin, healed fracture left a subtle alteration scar (where a minute amount of water diffused into the rock) across an otherwise pristine olivine gabbro. Along the fracture, the plagioclase twins are discontinuous, brown hornblende appears as inclusions in clinopyroxene, and a seam of talc and magnetite cuts across a grain of olivine. The proportion of talc increases downhole with the increase of modal olivine, from trace quantities mixed with amphibole to volumes of up to 20% (e.g., Samples 118-735B-16R-5, 24–26 cm, Piece 1B, and 118-735B-20R-1, 29–33 cm, Piece 2B).

Magnesian amphibole (tremolite, anthophyllite, or cummingtonite) also increases in volume with depth, although not as dramatically as talc, because tremolite and actinolite also replace pyroxene throughout the hole. These latter pseudomorphs typically consist of colorless blades of magnesian amphibole at the center with a fringe of bright green actinolite along the boundary with plagioclase. In some of the foliated metagabbros, both porphyroclasts and neoblasts of clinopyroxene, as well as the earlier green to brown hornblende, are replaced by actinolite, which results in layers that completely mask the deformed mafic phases. These layers consist of fine-grained colorless tremolite

and green actinolite that extends into the adjacent mosaic of plagioclase.

Plagioclase is replaced along microfractures by sodic plagioclase or by small patches of acicular green amphibole. Plagioclase-olivine boundaries typically are replaced by actinolite (foliated rocks) or by a second outer corona within the plagioclase that consists of pale radial aggregates of pargasite at shallow depths or chlorite at greater depths. Chlorite appears in trace amounts in Core 118-735B-16R and in larger quantities within Core 118-735B-18R, but it is never abundant except locally in veins (e.g., Sample 118-735B-87R-7, 12–15 cm, Piece 1C, a vein in a troctolite). Epidote also appears as a replacement of plagioclase (e.g., Sample 118-725B-18R-3, 29–31 cm, Piece 3), most commonly near veins or brecciated zones.

The spherulitic chlorite that replaces plagioclase along the boundaries with olivine is so dark that in thin section the anomalous blue extinction was difficult to discern. We believe that this reflects a highly magnesian composition. In contrast, chlorite observed along ilmenite-plagioclase boundaries in the oxide-rich gabbros is a very clear green, which probably reflects a high iron content. Small amounts of highly pleochroic, iron-rich, phlogopitic mica were observed as a replacement of ilmenite within the chloritic coronas. In Sample 118-735B-45R-4, 136–140 cm, Piece 7, iron-poor zoisite is joined by a second, more pistacitic, epidote within an iron-titanium oxide-rich zone. The amphibole in the oxide gabbros is similarly bright green and highly pleochroic, which reflects iron-rich compositions. We believe that these iron-rich phases result from the iron-rich protolith (the oxide-rich gabbros), rather than any substantial change in metamorphic conditions.

Alteration Assemblages in the Cataclastic Zones

Within the cataclastic zones, brecciation of the gabbroic rocks resulted in greater permeability, lower ambient temperatures of alteration, and a greater percentage of replacement by secondary minerals. The high-temperature zoisite or clinzoisite was joined by a true pistacitic green epidote. The dominant amphibole is actinolite, rather than hornblende. Chlorite appears in greatest abundance at these zones, and large pink crystals of sphene replace ilmenite. Extensive albitization of the plagioclase was enhanced by the crushing of plagioclase grains. Silicic clots within these crush zones contain small amounts of quartz.

The distribution of vein assemblages suggests that the predominantly amphibolite to granulite grade conditions that existed for the gabbro declined through a transitional zone to true greenschist grade within the breccia zones. Epidote and chlorite are abundant only within these zones, but prehnite was not observed as a vein mineral. Experimental studies of mineral paragenesis of low-grade metamorphism of basaltic composition (Liou et al., 1985) show that iron-poor epidote and tremolite-actinolite (present in veins outside the breccia zones) are the stable assemblage (over chlorite and prehnite) at temperatures above 400°C at 1 kb. The appearance of green epidote and chlorite in the breccia zones suggests minimum temperatures between 350° to 400°C.

Oxidative Alteration

One of the unexpected features of Hole 735B was the appearance of oxidized zones, even at substantial depth within the drill hole. It is important to characterize the location and relative timing of oxidative alteration because this may point to zones of permeability through which cold, oxygenated seawater might circulate. The oxidation, as observed in thin section, produces carbonate-hematite pseudomorphs after olivine and orthopyroxene. Mixtures of smectite and hematite were observed to replace chlorite, plagioclase, or olivine. Some oxidation (<10% clay and hematite replacing orthopyroxene) was observed in the

top 26 m of the hole (Cores 118-735B-1D through -6D), but Cores 118-735B-9D and -10D (33–39 mbsf) make up the first major oxidized zone. The surface oxidation declines in Core 118-735B-7D, and the characteristic smectite-carbonate pseudomorphs are replaced by talc-tremolite and small percentages of clinozoisite. The oxidation was interpreted as a late overprint.

The gabbro breccia zones show evidence of significant oxidation, including iron staining and increased abundance of smectite or carbonate. In Core 118-735B-10D, no amphibole veins occur, decreasing albitization is noted, and the late fractures are filled with calcite. Assemblages and textures characteristic of the higher-temperature plastic deformation are sometimes apparent, but more commonly, the brecciated fragments have suffered less plastic deformation. In the brecciated zones at 180, 275, and 330 mbsf, the recovered core consists of shattered fragments coated with orange-brown iron oxide. Here, the orthopyroxene is completely replaced by clots of smectite and hematite and the albite is stained (e.g., Sample 118-735B-9D-1, 120–123 cm, Piece 23). Proximity of the breccia zones to mylonitic zones or magmatic boundaries, (see “Structure and Deformation” section, this chapter) combined with the increased alteration within the zones, suggests that they represent major hydrothermal conduits. In addition, the associated oxidation suggests that permeability may have persisted to allow penetration of lower-temperature fluids.

Summary

Metamorphism within the rocks from Hole 735B includes dynamothermal, cataclastic, and static alteration. There is no conspicuous variation of metamorphic grade with depth, except perhaps for the appearance of diopside in place of hornblende. Rather, the change in metamorphic grade relates to the distribution of deformation zones and penetration of seawater into cracks and brecciated layers. Dynamothermal alteration occurred at temperatures equivalent to upper amphibolite to granulite grade and produced foliated metagabbros and mylonitic zones. Post-plastic deformation alteration resulted from the penetration of cracks into the gabbros and the development of permeable breccia zones. We are not sure what determines the location of the breccia zones. At 278 mbsf, the breccia zone is adjacent to an impermeable mylonite layer, which suggests a rheological control. At other depths, there may be a geochemical discontinuity, which suggests hydrothermal cracking from diachronous magmatic events. Metamorphism associated with the vertical cracks produced hornblende-sodic plagioclase assemblages at temperatures estimated at 400° to 600°C (Spear, 1980, 1981). Increased circulation within the breccia zones produced lower temperatures of alteration, although the minimum temperature was approximately 350°C (Liou et al., 1985). A late oxidative overprint occurs sporadically throughout the drill hole and is most intense in brecciated zones. Large carbonate veins are associated with these brecciated zones. We believe that this results from renewed circulation of cold oxygenated seawater.

GEOCHEMISTRY

A total of 97 whole-rock samples from Hole 735B was analyzed using X-ray fluorescence (XRF) for major oxide compositions and abundances of the trace elements vanadium, chromium, nickel, copper, zinc, rubidium, strontium, yttrium, zirconium, and niobium. Sample preparation techniques and analytical procedures are outlined in the “Introduction and Explanatory Notes” (this volume).

The main objective of the sampling strategy was to establish a chemical stratigraphy of the recovered gabbro section. Therefore, care was taken to select from each core at least one sample that was representative of the major part of the drilled sequence. In addition, intervals of macroscopically significantly

different lithologies were sampled whenever we thought it necessary. As a rule, the freshest possible material was selected to reduce the effects of alteration on the chemical data. In a few cases, strongly altered samples were taken adjacent to the fresher intervals to gain a first estimate of the effects of chemical redistribution processes.

To minimize the problem of representative sampling of plutonic rocks, most of the chemical analyses were performed on medium- to fine-grained core intervals. Samples were prepared either from slabs used for large thin sections or from minicores used for measuring paleomagnetic and physical properties. Sample sizes generally ranged from 35 to 55 g. All samples were ground in an agate mill.

In most cases, totals of shipboard XRF major elemental oxides were between 99.2% and 100.8%. The deviations from 100% result essentially from counting statistics and from weighing errors that affect all components to the same extent. The analysis of duplicate glass beads showed that a few anomalously large deviations (98%–103%) might be attributed to weighing problems in the shipboard environment. To overcome these weighing problems, all measured values were normalized to a sum of 100%.

The loss-on-ignition (LOI) values provide only limited information on the amount of bound water (and/or CO₂) in the rocks because the loss of weight from removing volatiles is counterbalanced by oxidation of the ferrous iron. Actually, many of the iron-rich rocks analyzed have positive LOI values because of this effect.

Shipboard data for major elements were supplemented with post-cruise data for H₂O and CO₂ contents and for ferrous/ferric iron ratios. The analyses were performed on powdered samples prepared on board the ship and were conducted at Giessen and Leuven Universities using standard analytical methods. The major element data are listed in Table 4. All components are normalized to a sum of 100%. Shipboard XRF analyses of ignited samples were recast to actual rock compositions using the shore-based FeO, H₂O, and CO₂ data.

The obtained trace-element abundances were determined from pressed powder pellets prepared from dried, i.e., not ignited, material (Table 4). Except for rubidium and niobium, the observed abundances are well above the respective detection limits, so that the analytical errors summarized in the “Introduction and Explanatory Notes” (this volume) apply. The measured contents of rubidium and niobium in many cases are below the detection limits of 0.8 and 0.5 ppm, respectively. Values close to the detection limits should be used with care because they are affected by relative large errors (on the order of 50% relative).

In addition to the standard sample designations (core, section, section interval in centimeters, piece number), each sample was tagged by the nominal depth in meters below seafloor (mbsf) and given a rock type code. The latter was used to provide concise information about petrography, metamorphism, and deformation of the rocks. The type abbreviations are explained in a footnote to Table 4.

According to this simplified classification scheme, the spectrum of analyzed rocks covers:

- 42 olivine gabbros (olivine content > 5 vol%),
- 14 olivine-bearing gabbros (4 of them foliated and metamorphosed),
- 5 gabbros,
- 15 metagabbros (14 of them deformed),
- 2 gabbroites (1 deformed),
- 3 microgabbros,
- 8 iron-titanium oxide gabbros (5 of them olivine-bearing),
- 4 troctolites,
- 1 basalt dike, and
- 1 trondjemite (small dike).

Table 4. Chemical composition of rock samples from Hole 735B.

Core/section: Interval (cm): Piece: Mbsf ¹ :	ID-1 90-98 14 0.9	ID-1 117-120 19 1.2	ID-2 91-94 14 2.4	2D-1 76-80 14 7.3	2D-2 116-120 19B 9.2	3D-1 46-49 9 15.0	4D-2 10-16 1 19.1	6D-1 71-74 13 24.7	7D-1 63-67 9 26.6	7D-2 1-5 1 27.5	10D-1 46-49 8 36.7	12R-1 118-123 11 40.6	13R-1 102-105 11B 45.5	14R-3 136-141 10 55.1	15R-1 90-93 7B 57.1	15R-3 92-96 8 60.1	16R-1 139-141 3H 63.2	17R-1 22-27 5 67.2	18R-2 143-146 17 71.4
Unit ² : Type ³ :	I MGD	I MGD	I MGD	I MGD	I MGD	I MGD	I GND	I MGD	I MGD	I MGD	I MGD	II GO	II GOD	II GO	II MGD	II G	II MGD	II GO	II MGD
SiO ₂	51.66	54.21	51.87	51.35	51.17	53.93	52.69	49.97	49.28	49.28	52.64	50.73	50.34	51.71	51.40	50.25	51.56	50.74	50.58
TiO ₂	0.85	0.56	0.84	0.42	0.37	0.55	0.33	1.78	0.26	0.25	0.62	0.23	0.32	0.38	0.60	0.44	1.13	0.56	0.37
Al ₂ O ₃	14.90	20.93	15.01	16.93	19.24	15.64	16.30	14.65	14.92	15.13	14.97	20.49	16.04	17.20	16.39	14.06	16.56	15.34	13.65
Fe ₂ O ₃	2.05	1.15	1.91	1.85	2.71	1.64	2.96	2.15	2.53	1.91	2.19	0.57	1.34	1.10	1.44	1.55	1.37	1.23	0.97
FeO	6.64	3.80	6.74	6.52	4.34	5.96	5.51	7.06	3.88	4.52	6.19	3.74	4.89	4.42	6.12	6.27	5.85	5.91	4.61
MnO	0.17	0.10	0.16	0.17	0.13	0.16	0.20	0.19	0.13	0.12	0.19	0.11	0.12	0.11	0.12	0.13	0.10	0.13	0.10
MgO	6.98	3.82	6.89	8.39	6.78	8.05	8.03	7.56	12.92	12.30	7.80	6.42	10.57	7.95	8.54	10.94	7.67	10.37	12.20
CaO	11.98	9.64	11.99	9.66	10.41	11.07	8.15	11.61	12.65	12.41	11.13	13.53	12.90	13.04	10.93	12.58	10.86	11.76	14.36
Na ₂ O	3.40	5.19	3.46	3.30	3.62	3.53	4.00	3.48	2.03	2.39	3.14	2.98	2.49	2.99	3.37	2.44	3.73	2.64	1.69
K ₂ O	0.16	0.09	0.16	0.25	0.12	0.16	0.13	0.11	0.12	0.14	0.12	0.07	0.04	0.04	0.07	0.07	0.07	0.08	0.05
P ₂ O ₅	0.02	0.02	0.03	0.04	0.07	0.07	0.13	0.54	0.00	0.02	0.01	0.00	0.01	0.01	0.04	0.02	0.20	0.04	0.01
H ₂ O	1.17	0.43	0.94	1.13	0.79	1.24	1.27	0.80	1.21	1.24	1.04	1.08	0.71	0.75	0.98	1.09	0.93	1.22	1.48
CO ₂	0.07	0.09	nd	nd	0.24	nd	0.34	nd	nd	0.28	nd	0.07	0.26	0.31	nd	0.19	nd	nd	nd
⁴ LOI	1.01	0.29	0.73	0.72	1.11	1.05	1.25	0.71	1.63	1.00	0.76	1.11	0.77	0.73	0.88	0.79	0.86	1.08	1.70
V	243	152	254	128	90	165	88	210	127	124	238	94	131	171	179	173	169	122	182
Cr	9	1	8	8	8	18	4	168	605	328	35	441	360	76	72	308	36	854	795
Ni	32	16	30	53	48	51	89	82	165	172	50	71	121	59	68	122	76	179	211
Cu	42	9	42	25	22	22	18	61	35	20	68	16	39	18	12	12	9	55	12
Zn	60	35	62	56	42	56	45	52	28	35	58	35	38	27	31	27	17	40	26
Rb	3.3	<0.8	3.2	3.0	0.8	1.8	1.4	1.1	<0.8	<0.8	1.5	<0.8	1.0	<0.8	<0.8	<0.8	<0.8	<0.8	<0.8
Sr	157	259	158	176	220	157	199	162	141	125	170	194	159	175	163	134	187	153	111
Y	19	11	21	12	7	36	28	51	9	12	17	8	12	14	28	14	41	31	12
Zr	26	17	27	26	15	37	969	136	8.3	24	39	12.1	25.2	18.7	110	23.9	187	89	15.9
Nb	0.7	<0.5	0.5	0.6	0.6	2.4	1.3	3.9	<0.5	<0.5	<0.5	<0.5	0.6	<0.5	1.2	<0.5	2.1	1.8	<0.5
⁵ Mg#	0.63	0.62	0.63	0.68	0.68	0.69	0.67	0.63	0.81	0.80	0.66	0.87	0.78	0.75	0.71	0.75	0.69	0.75	0.82
MgO/Al ₂ O ₃	0.47	0.18	0.46	0.50	0.35	0.51	0.49	0.52	0.87	0.81	0.52	0.31	0.66	0.46	0.52	0.78	0.46	0.68	0.89
CaO/Al ₂ O ₃	0.80	0.47	0.80	0.57	0.54	0.71	0.50	0.79	0.85	0.82	0.74	0.66	0.80	0.76	0.67	0.89	0.66	0.77	1.05
CaO/Na ₂ O	3.52	1.86	3.46	2.93	2.88	3.14	2.04	3.19	6.22	5.19	3.55	4.54	5.18	4.36	3.24	5.16	2.91	4.46	8.48

¹ Mbsf = meters below seafloor.² Unit = lithologic unit.³ G = gabbro; GN = gabbro; OG = olivine gabbro; GO = gabbro, olivine-bearing; FG = Fe-Ti-oxide gabbro; FGO = Fe-Ti-oxide gabbro, olivine-bearing; MIG = microgabbro; MG = metagabbro; MGO = metagabbro, olivine-bearing; TR = troctolite; TJ = trondhjemite; BD = basalt dike; D at the end = deformed (e.g., MGD = deformed metagabbro).⁴ LOI = weight loss on ignition: values preceded with + sign denote gain in weight on ignition.⁵ Mg# = molar ratio (Mg/Mg+0.86Fe_(tot)).⁶ nd = not determined.

Table 4 (continued).

Core/section: Interval (cm): Piece: Mbsf ¹ :	18R-3 37-40 4 71.9	19R-3 73-75 6A 78.3	20R-2 23-27 2 85.8	21R-2 53-56 1B 90.7	22R-2 86-91 3B 96.4	23R-2 42-48 1C 101.6	23R-2 66-73 1D 101.8	23R-4 83-86 5 104.8	24R-4 1-6 1A 109.8	25R-1 21-25 5 110.7	25R-3 43-48 2B 113.7	25R-3 144-146 3B 114.7	26R-1 131-134 6A 116.8	26R-4 91-92 5 120.9	27R-3 73-81 1D 125.2	28R-3 63-69 4 130.1	29R-3 124-130 14C 135.6	30R-1 135-138 18 137.9	30R-5 110-115 7 143.5
Unit ² : Type ³ :	II MIG	II GO	II GOD	II OG	II OG	II MIG	II OG	II BD	II G	II MG	II OG	II OG	II OG	II G	II OG	II GN	II OG	II MGO	II GO
SiO ₂	48.00	51.07	41.03	52.06	49.23	46.44	50.71	49.71	50.60	49.97	50.48	48.30	49.82	51.74	50.27	51.88	49.93	51.67	53.13
TiO ₂	0.19	0.32	0.39	0.31	0.52	4.84	0.31	1.67	0.24	0.93	0.26	0.21	0.27	0.25	0.40	1.13	0.26	0.48	0.49
Al ₂ O ₃	17.32	18.47	5.01	19.60	9.26	12.96	18.81	15.17	19.08	14.08	17.86	16.01	15.70	22.90	14.08	11.66	17.78	15.78	17.22
Fe ₂ O ₃	1.42	0.83	5.45	3.77	0.64	2.13	0.80	2.61	0.52	2.31	0.43	0.80	0.59	0.14	0.59	3.00	0.93	1.41	1.09
FeO	4.86	3.52	19.62	0.00	6.91	11.13	4.07	7.29	4.21	7.91	3.97	4.93	4.18	2.67	4.83	11.19	4.00	6.28	6.47
MnO	0.09	0.09	0.41	0.08	0.16	0.19	0.09	0.19	0.09	0.11	0.09	0.12	0.11	0.06	0.12	0.33	0.10	0.14	0.15
MgO	11.71	8.46	22.01	7.03	16.98	8.05	8.80	7.96	9.19	9.54	10.22	13.85	11.90	4.92	12.14	9.88	10.04	8.47	6.55
CaO	11.34	13.26	4.50	14.19	14.26	9.78	12.71	10.91	12.51	11.18	13.65	12.67	14.22	13.14	14.92	7.14	13.32	10.84	10.30
Na ₂ O	2.46	2.82	0.71	2.94	1.21	3.25	2.73	2.53	2.87	2.91	2.37	2.11	1.91	3.36	1.98	2.91	2.47	3.43	4.01
K ₂ O	0.18	0.03	0.12	0.03	0.02	0.19	0.06	0.05	0.06	0.11	0.02	0.07	0.04	0.04	0.02	0.05	0.05	0.03	0.07
P ₂ O ₅	0.01	0.01	0.01	0.01	0.01	0.00	0.01	0.17	0.06	0.01	0.00	0.00	0.01	0.01	0.00	0.05	0.00	0.00	0.04
H ₂ O	2.25	1.12	0.74	0.00	0.82	0.91	0.94	1.76	0.64	0.94	0.54	1.01	1.26	0.63	0.53	0.78	1.12	1.48	0.51
CO ₂	0.19	nd	nd	nd	nd	0.15	nd	nd	nd	nd	0.11	nd	nd	0.15	0.13	nd	nd	nd	nd
⁴ LOI	2.25	1.00	+0.11	0.97	0.27	0.10	0.78	1.71	0.52	1.02	0.35	0.89	0.51	0.56	0.60	0.20	1.35	1.57	0.23
V	76	117	102	124	219	842	118	273	88	541	122	92	130	81	185	165	116	224	155
Cr	327	148	96	165	324	24	134	212	251	221	368	383	459	180	633	2	327	49	24
Ni	233	92	318	79	172	82	97	99	113	128	125	220	171	62	145	34	117	47	52
Cu	5.0	12	93	10	63	32	10	61	15	9	21	103	43	9	70	44	11	9.0	79
Zn	17	21	128	18	48	52	24	84	22	17	23	35	29	17	32	117	25	30	47
Rb	<0.8	<0.8	2.2	<0.8	<0.8	<0.8	<0.8	0.9	<0.8	<0.8	<0.8	<0.8	<0.8	<0.8	<0.8	<0.8	<0.8	<0.8	<0.8
Sr	157	177	47	185	84	120	176	152	172	134	162	145	135	214	125	153	159	168	204
Y	5	8	11	8	15	34	8	34	7	18	6	6	7	6	12	19	8	13	17
Zr	11.8	18.6	18.3	15.5	27.1	29.1	11.6	131	13.2	19.8	6.5	4.5	9.7	9.2	14.5	27.8	7.3	12.9	41.9
Nb	<0.5	<0.5	2.8	<0.5	<0.5	2.3	<0.5	3.4	0.5	1.1	<0.5	<0.5	<0.5	<0.5	<0.5	1.2	<0.5	<0.5	<0.5
⁵ Mg#	0.80	0.80	0.65	0.81	0.83	0.56	0.79	0.63	0.80	0.66	0.83	0.84	0.84	0.79	0.82	0.60	0.81	0.70	0.65
MgO/Al ₂ O ₃	0.68	0.46	4.39	0.36	1.83	0.62	0.47	0.52	0.48	0.68	0.57	0.87	0.76	0.21	0.86	0.85	0.56	0.54	0.38
CaO/Al ₂ O ₃	0.65	0.72	0.90	0.72	1.54	0.75	0.68	0.72	0.66	0.79	0.76	0.79	0.91	0.57	1.06	0.61	0.75	0.69	0.60
CaO/Na ₂ O	4.61	4.70	6.34	4.83	11.79	3.01	4.66	4.32	4.37	3.85	5.76	6.00	7.42	3.91	7.55	2.45	5.39	3.16	2.57

Table 4 (continued).

Core/section: Interval (cm): Piece: Mbsf ¹ :	31R-2 40-45 2B 145.4	31R-2 77-81 3C 145.8	32R-3 54-60 1E 151.7	32R-4 43-49 1E 152.5	33R-3 85-89 7 157.3	33R-4 27-29 2B 158.1	34R-2 18-22 1C 160.0	35R-4 43-46 2A 168.3	36R-2 98-102 1E 173.5	36R-4 30-33 1B 175.1	37R-3 80-82 4 179.6	38R-2 78-84 4B 183.3	39R-1 145-147 3B 187.5	40R-4 1-5 1A 194.4	41R-4 22-27 1A 200.4	42R-3 9-14 1B 204.0	43R-1 22-29 1B 206.2	44R-2 6-8 1A 212.3	44R-3 78-81 5D 214.4
Unit ² : Type ³ :	II OG	II MGD	II OG	II OG	II GO	II GOD	II OG	II OG	II GO	II G	II G	III OG	III OG	III MIG	III OG	III GO	III GO	III FG	III OG
SiO ₂	51.47	48.91	53.00	51.35	51.56	53.90	49.96	49.53	49.91	52.49	49.85	50.92	51.04	52.48	52.26	51.66	52.69	35.05	49.63
TiO ₂	0.31	2.70	0.18	0.30	0.23	0.37	0.24	0.23	0.20	0.41	2.24	0.65	0.43	0.43	0.47	0.83	0.51	7.86	0.26
Al ₂ O ₃	16.19	15.73	18.88	15.30	21.19	17.54	18.62	16.41	21.29	15.66	12.45	12.95	16.68	16.07	15.85	17.04	15.74	10.92	17.89
Fe ₂ O ₃	0.54	1.78	0.30	0.61	0.27	1.35	0.41	0.85	0.65	1.51	3.64	1.63	1.27	0.97	1.73	2.84	1.33	14.43	0.76
FeO	4.32	8.07	3.79	4.11	2.82	4.71	3.37	4.05	2.92	6.17	9.14	8.66	7.88	6.32	6.26	5.53	5.98	15.78	3.55
MnO	0.11	0.17	0.08	0.11	0.07	0.12	0.08	0.10	0.07	0.16	0.24	0.22	0.17	0.16	0.16	0.16	0.17	0.32	0.09
MgO	10.38	7.22	8.54	10.69	6.24	6.60	9.99	12.60	8.41	8.55	8.01	10.14	8.89	8.18	8.23	6.93	7.91	5.43	11.04
CaO	13.15	10.91	9.84	14.10	13.66	10.44	14.32	13.33	13.00	11.20	10.62	11.28	9.48	11.54	11.29	10.38	11.76	6.81	13.88
Na ₂ O	2.50	3.37	3.98	2.28	3.10	4.19	2.22	2.17	2.80	3.26	2.90	2.76	3.49	3.34	3.21	3.48	3.22	2.56	2.07
K ₂ O	0.09	0.06	0.08	0.05	0.05	0.05	0.02	0.04	0.04	0.03	0.05	0.07	0.04	0.03	0.03	0.05	0.03	0.06	0.03
P ₂ O ₅	0.01	0.03	0.00	0.00	0.00	0.00	0.01	0.00	0.01	0.00	0.00	0.01	0.00	0.00	0.00	0.01	0.00	0.08	0.00
H ₂ O	0.93	0.95	1.24	0.98	0.83	0.74	0.76	0.68	0.56	0.46	0.85	0.71	0.62	0.48	0.43	0.59	0.38	0.69	0.68
CO ₂	nd	0.10	0.12	0.13	nd	nd	nd	0.01	0.14	0.11	nd	nd	nd	nd	0.10	0.50	0.30	nd	0.11
⁴ LOI	0.87	0.84	1.49	1.01	0.86	0.56	0.78	0.64	0.74	0.18	0.28	0.42	+0.15	0.23	0.18	0.92	0.09	+0.71	0.76
V	131	388	68	159	87	145	104	107	69	178	509	216	108	174	178	216	193	1594	144
Cr	323	79	147	384	240	12	633	464	320	29	27	43	7	7	15	3	8	79	885
Ni	131	132	118	132	64	31	181	239	125	43	39	49	39	33	41	31	35	60	161
Cu	34	157	9.0	23	9.0	15	74	47	35	66	51	36	35	39	67	27	67	199	39
Zn	29	36	19	21	15	29	21	25	21	42	80	61	54	40	41	45	43	189	26
Rb	<0.8	<0.8	<0.8	<0.8	<0.8	<0.8	0.9	<0.8	<0.8	<0.8	0.9	1.2	<0.8	<0.8	<0.8	<0.8	<0.8	<0.8	<0.8
Sr	147	169	182	138	193	202	170	152	198	184	145	153	196	184	175	209	175	128	163
Y	14	30	24	16	6	16	6	8	5	11	18	16	10	12	11	10	14	14	7
Zr	25.3	34.7	53.8	16.5	7.2	14.0	7.1	8.7	17.3	11.0	23.9	25.5	13.2	11.9	12.1	14.8	15.2	56	8.5
Nb	<0.5	2.0	1.1	<0.5	<0.5	0.7	<0.5	<0.5	<0.5	<0.5	1.5	0.6	<0.5	<0.5	0.6	<0.5	<0.5	4.7	<0.5
⁵ Mg#	0.82	0.61	0.81	0.83	0.81	0.70	0.85	0.84	0.83	0.70	0.57	0.68	0.67	0.70	0.69	0.64	0.70	0.29	0.84
MgO/Al ₂ O ₃	0.64	0.46	0.45	0.70	0.29	0.38	0.54	0.77	0.39	0.55	0.64	0.78	0.53	0.10	0.52	0.41	0.50	0.50	0.62
CaO/Al ₂ O ₃	0.81	0.69	0.52	0.92	0.64	0.59	0.77	0.81	0.61	0.72	0.85	0.87	0.57	0.72	0.71	0.61	0.75	0.62	0.78
CaO/Na ₂ O	5.26	3.23	2.47	6.17	4.26	2.49	6.45	6.13	4.66	3.43	3.66	4.09	2.72	3.46	3.52	2.98	3.65	2.66	6.44

Table 4 (continued).

Core/section:	45R-1	46R-3	46R-4	47R-4	48R-2	50R-2	52R-4	53R-1	53R-5	54R-1	55R-2	58R-3	59R-4	60R-1	61R-1	62R-1	63R-5	65R-3	67R-3
Interval (cm):	48-54	121-129	109-113	80-86	109-113	43-47	88-94	47-54	40-43	131-136	101-105	107-114	29-35	80-83	81-85	91-94	126-130	54-58	74-78
Piece:	1F	10	11	5	9	1B	4B	2C	3	8B	4	1F	1C	1E	3A	3	5A	1D	1H
Mbsf ¹ :	216.5	225.1	226.5	231.2	233.4	239.5	252.9	253.5	258.5	259.3	267.5	284.3	289.6	291.3	296.3	301.4	312.2	323.1	333.6
Unit ² :	III	IV	IV	IV	IV	IV	IV	IV	IV	IV	IV	V	V	V	V	V	V	V	V
Type ³ :	GO	FGO	FG	OG	FGO	FG	FG	FGO	TJ	FGO	FGO	OG	OG	OG	OG	OG	OG	OG	OG
SiO ₂	52.45	47.53	45.62	49.82	45.41	38.89	42.53	44.66	70.82	44.86	41.69	50.26	51.02	51.85	49.74	50.06	51.05	49.83	50.91
TiO ₂	0.90	2.58	6.10	0.29	3.73	9.08	6.89	6.34	0.22	2.33	7.23	0.37	0.49	0.36	0.34	0.35	0.28	0.33	0.32
Al ₂ O ₃	14.49	13.30	14.92	14.65	12.13	9.89	10.93	11.41	17.28	12.02	10.66	16.37	15.43	18.04	16.53	14.83	17.45	16.39	17.74
Fe ₂ O ₃	1.61	4.02	5.55	0.27	5.51	8.32	7.34	5.15	1.24	5.35	7.33	1.39	1.28	0.41	1.04	1.28	0.53	0.67	0.96
FeO	7.55	11.02	10.27	4.46	12.76	15.29	14.06	13.51	0.00	17.69	15.13	5.46	4.84	3.57	5.62	5.82	4.41	4.78	3.05
MnO	0.20	0.23	0.20	0.11	0.25	0.28	0.30	0.28	0.02	0.42	0.30	0.13	0.13	0.10	0.13	0.14	0.10	0.11	0.09
MgO	8.03	7.48	4.27	13.24	7.36	6.30	5.50	5.48	0.17	5.03	5.29	10.32	10.08	7.61	10.66	11.33	9.53	11.41	8.95
CaO	11.11	10.08	8.74	14.66	9.37	8.85	9.21	9.52	1.93	6.72	9.15	12.51	14.03	14.72	12.93	13.62	13.10	13.72	14.84
Na ₂ O	3.18	3.03	3.68	1.66	2.72	2.25	2.70	3.02	6.95	3.47	2.59	2.76	2.34	2.75	2.37	2.03	2.68	2.05	2.25
K ₂ O	0.05	0.05	0.05	0.00	0.04	0.04	0.04	0.04	1.48	0.17	0.05	0.04	0.02	0.03	0.01	0.01	0.03	0.02	0.01
P ₂ O ₅	0.02	0.00	0.01	0.03	0.00	0.00	0.00	0.00	0.01	1.20	0.03	0.00	0.00	0.00	0.01	0.00	0.00	0.00	0.00
H ₂ O	0.41	0.69	0.60	0.81	0.58	0.81	0.52	0.61	nd	0.75	0.55	0.39	0.25	0.59	0.65	0.53	0.84	0.71	0.78
CO ₂	nd	nd	nd	nd	0.13	nd	nd	nd	nd	nd	nd	0.01	0.09	nd	nd	nd	nd	nd	0.09
⁴ LOI	0.25	0.01	+0.05	0.72	+0.31	+0.58	+0.27	+0.33	0.40	+0.79	+0.44	0.40	0.01	0.76	0.16	0.09	0.72	0.47	0.88
V	243	587	777	149	712	1173	634	542	—	70	628	128	175	139	126	152	120	123	146
Cr	10	20	5	822	110	<1	6	3	—	<1	11	212	382	397	305	404	433	584	504
Ni	31	30	31	206	39	29	10	8	—	10	19	115	108	70	139	125	123	196	114
Cu	67	59	71	40	84	106	73	62	—	57	86	37	94	50	95	122	20	91	20
Zn	54	76	82	24	94	123	120	109	—	170	133	38	30	22	35	37	31	30	21
Rb	<0.8	0.9	0.9	<0.8	<0.8	<0.8	<0.8	<0.8	—	<0.8	0.80	<0.8	<0.8	<0.8	<0.8	<0.8	<0.8	<0.8	<0.8
Sr	172	178	200	134	155	125	161	153	—	193	155	172	162	180	159	148	165	153	164
Y	18	15	13	7	16	19	24	23	—	69	32	8	11	10	8	10	22	8	8
Zr	26.9	18.0	45	7.2	21	52.5	48	48.6	—	59.2	104	11.0	16.4	13.5	11.6	9.8	17.5	12.7	10.8
Nb	0.8	1.6	2.8	0.8	1.8	5.0	4.1	4.0	—	5.6	6.5	<0.5	<0.5	<0.5	<0.5	<0.5	0.8	<0.5	<0.5
⁵ Mg#	0.65	0.51	0.37	0.85	0.46	0.36	0.36	0.38	0.00	0.32	0.34	0.76	0.78	0.80	0.77	0.77	0.80	0.82	0.83
MgO/Al ₂ O ₃	0.55	0.56	0.29	0.90	0.61	0.64	0.50	0.48	0.01	0.48	0.50	0.63	0.65	0.42	0.64	0.76	0.55	0.70	0.50
CaO/Al ₂ O ₃	0.77	0.76	0.59	1.00	0.77	0.89	0.84	0.83	0.11	0.56	0.86	0.76	0.91	0.82	0.78	0.92	0.75	0.84	0.84
CaO/Na ₂ O	3.49	3.33	2.35	8.81	3.44	3.92	3.41	3.16	0.28	1.94	3.54	4.53	5.98	5.34	5.46	6.70	4.89	6.70	6.60

Table 4 (continued).

Core/section:	68R-2	69R-3	70R-1	70R-2	71R-3	72R-2	73R-1	74R-6	75R-5	76R-3	77R-2
Interval (cm):	16-21	86-92	80-84	129-131	0-5	56-62	54-57	115-119	27-30	93-97	4-7
Piece:	1B	5C	3A	3C	1A	1D	3B	5B	1A	2H	1A
Mbsf ¹ :	336.7	344.5	346.8	353.6	353.9	358.1	366.0	383.5	390.3	397.5	405.0
Unit ² :	V	V	V	V	V	V	V	V	V	V	VI
Type ³ :	OG	OG	OG	OG	OG	OG	OG	OG	OG	OG	OG
SiO ₂	47.40	50.30	50.69	48.29	50.43	49.89	50.46	50.70	51.00	49.49	54.00
TiO ₂	0.23	0.34	0.32	0.28	0.32	0.38	0.34	0.27	0.29	0.25	0.49
Al ₂ O ₃	14.87	16.80	17.51	19.26	17.59	17.56	15.13	18.00	16.48	17.56	16.56
Fe ₂ O ₃	0.59	1.23	0.32	0.73	0.94	1.05	0.83	0.69	0.43	0.94	0.92
FeO	7.29	3.80	4.10	3.44	3.80	4.45	4.14	3.27	3.74	4.53	5.95
MnO	0.14	0.10	0.10	0.12	0.10	0.11	0.11	0.09	0.10	0.10	0.16
MgO	15.98	10.52	9.68	7.92	9.96	10.45	11.53	9.37	10.10	11.41	7.02
CaO	10.97	14.17	14.29	12.58	14.03	13.43	15.14	14.64	15.33	13.04	10.19
Na ₂ O	1.84	2.17	2.29	3.21	2.29	2.25	1.81	2.33	2.00	2.13	3.90
K ₂ O	0.01	0.02	0.02	0.02	0.02	0.02	0.01	0.01	0.01	0.00	0.06
P ₂ O ₅	0.00	0.00	0.00	0.00	0.00	0.01	0.00	0.00	0.00	0.00	0.06
H ₂ O	0.68	0.45	0.68	4.24	0.42	0.32	0.37	0.43	0.51	0.46	0.62
CO ₂	nd	0.10	nd	nd	0.09	0.11	0.13	0.11	nd	0.08	nd
⁴ LOI	0.14	0.29	0.38	0.38	0.50	+0.09	0.39	0.61	0.33	0.60	1.22
V	88	134	133	88	112	116	166	119	139	108	173
Cr	353	519	542	317	496	315	544	375	441	335	10
Ni	260	149	124	109	134	124	165	114	126	137	24
Cu	117	56	41	22	88	60	117	76	100	108	29
Zn	45	25	25	37	27	31	26	21	21	29	43
Rb	<0.8	<0.8	<0.8	<0.8	<0.8	<0.8	<0.8	<0.8	<0.8	<0.8	<0.8
Sr	146	161	163	235	164	164	132	167	152	161	203
Y	6	9	8	17	8	9	9	8	8	6	10
Zr	8.3	12.9	11.7	59	11.3	15.1	11.0	9.3	8.4	7.5	13.7
Nb	<0.5	<0.5	<0.5	1.4	<0.5	<0.5	<0.5	<0.5	<0.5	<0.5	<0.5
⁵ Mg#	0.81	0.82	0.82	0.78	0.82	0.80	0.83	0.83	0.84	0.81	0.68
MgO/Al ₂ O ₃	1.07	0.63	0.55	0.41	0.57	0.59	0.76	0.52	0.61	0.65	0.42
CaO/Al ₂ O ₃	0.74	0.84	0.82	0.65	0.80	0.76	1.00	0.81	0.93	0.74	0.62
CaO/Na ₂ O	5.96	6.54	6.23	3.92	6.12	5.96	8.37	6.30	7.67	6.12	2.60

Table 4 (continued).

Core/section: Interval (cm): Piece: Mbsf ¹ :	78R-1 132-136 5B 410.8	79R-6 90-95 3 422.7	80R-2 35-40 4 425.8	80R-6 6-9 1 431.4	81R-5 1-7 1 439.2	82R-1 49-54 3 443.5	83R-7 77-81 4D 462.0	84R-5 80-82 9 468.5	85R-7 79-85 5 480.7	87R-7 51-55 6 499.7
Unit ² : Type ³ :	VI OG	VI TR	VI TR	VI OG	VI OG	VI OG	VI TR	VI OG	VI OG	VI TR
SiO ₂	50.00	48.33	46.28	50.66	50.81	49.36	42.35	50.86	50.23	44.87
TiO ₂	0.29	0.20	0.20	0.38	0.24	0.20	0.17	0.46	0.30	0.14
Al ₂ O ₃	16.84	17.62	21.52	15.04	18.17	19.04	11.99	15.09	15.85	17.42
Fe ₂ O ₃	0.33	1.21	-0.01	0.21	0.22	0.00	1.31	0.61	0.59	1.38
FeO	4.54	4.44	4.74	5.03	4.02	4.88	6.69	4.87	3.16	5.96
MnO	0.10	0.11	0.08	0.12	0.09	0.09	0.14	0.12	0.09	0.12
MgO	11.07	13.34	12.96	11.54	9.83	13.07	24.99	10.40	10.62	17.69
CaO	14.30	12.25	11.58	14.28	13.65	12.99	8.05	14.69	16.34	8.64
Na ₂ O	2.02	1.94	1.84	2.18	2.41	1.62	0.80	2.20	2.01	1.95
K ₂ O	0.01	0.02	0.01	0.01	0.02	0.08	0.02		0.02	0.06
P ₂ O ₅	0.00	0.00	0.00	0.00	0.00	0.01	0.00	0.02	0.01	0.00
H ₂ O	0.53	0.56	0.80	0.57	0.54	0.73	3.10	0.68	0.80	1.76
CO ₂	nd	nd	nd	nd	nd	nd	nd	nd	nd	nd
⁴ LOI	0.45	0.32	0.42	0.35	0.37	0.85	2.37	0.53	0.68	1.44
V	124	69	42	159	92	80	68	184	162	20
Cr	753	1570	222	227	410	402	3668	318	2857	52
Ni	159	285	392	135	145	234	741	102	190	386
Cu	48	51	33	47	90	74	55	83	19	67
Zn	27	26	28	28	24	35	53	31	18	43
Rb	<0.8	<0.8	<0.8	<0.8	<0.8	<0.8	0.9	<0.8	<0.8	<0.8
Sr	145	144	136	129	146	147	80	152	124	143
Y	7	5	5	10	9	8	4	13	9	2
Zr	8.8	12.7	13.2	14.0	11.8	31.9	5.3	22.7	11.4	2.7
Nb	<0.5	<0.5	<0.5	<0.5	<0.5	0.60	<0.5	0.7	<0.5	0.6
⁵ Mg#	0.83	0.83	0.85	0.82	0.83	0.85	0.87	0.80	0.86	0.84
MgO/Al ₂ O ₃	0.66	0.76	0.60	0.77	0.54	0.69	2.08	0.69	0.67	1.02
CaO/Al ₂ O ₃	0.85	0.70	0.54	0.95	0.75	0.68	0.67	0.97	1.03	0.50
CaO/Na ₂ O	7.08	6.32	6.28	6.55	5.67	2.03	10.00	6.68	8.12	4.44

Olivine Gabbros

Most of the analyzed samples from Hole 735B are olivine gabbros that are essentially composed of plagioclase (around 60 vol%), clinopyroxene (around 30 vol%), and olivine (5 to 15 vol%). These rocks constitute major portions of lithologic Units II, V, and VI (see "Lithostratigraphy" section, this chapter) and also occur subordinately in Units III and IV. A description of their petrographical and mineralogical characteristics is given in the "Petrography" section (this chapter), which also provides quantitative information on the modal compositions of many of the chemically investigated samples (Table 4).

Table 5 summarizes the average chemical composition of the olivine gabbros within each of the various units and gives the respective range of variation (expressed as ± 1 s in wt%). A close scrutiny of this table reveals that the olivine gabbros from Units II, V, and VI vary within relatively restricted chemical limits and display almost identical average values. This means that according to shipboard data, the olivine gabbros selected from these three major lithologic units exhibit the same overall chemical composition and that no significant chemical differences exist between Units V and VI. Most of the analyzed samples have major oxide compositions in the following ranges (in weight percent):

SiO ₂	49.5–51.5
TiO ₂	0.27–0.37
Al ₂ O ₃	15.5–17.5
Fe ₂ O ₃	5.0–6.5
MnO	0.9–12.0
MgO	0.08–0.22
CaO	12.5–14.5
Na ₂ O	1.7–2.8
K ₂ O	0.01–0.05

The magnesium numbers are between 0.78 and 0.85, indicating that these rocks crystallized from very primitive basaltic liquids.

Typical concentration ranges (in parts per million) of the trace elements determined are as follows:

V	100–180
Cr	300–600
Ni	100–200
Cu	20–100
Zn	20–50
Rb	< 1
Sr	120–180
Y	5–15
Zr	7–18
Nb	< 1

Three olivine gabbros analyzed from lithologic Unit III (Samples 118-735B-38R-2, 78–84 cm, Piece 4B; 118-735B-39R-1, 145–147 cm, Piece 3B; and 118-735B-41R-4, 22–27 cm, Piece 1A) form a chemically distinct rock group, which clearly is distinguished from all other olivine gabbros recovered from Hole 735B. Their magnesium numbers of 0.67 to 0.69 indicate crystallization from relatively evolved basaltic liquids. Correspondingly, they show significantly higher contents of SiO₂, TiO₂, Fe₂O₃, MnO, and Na₂O and lower contents of CaO (Table 5). The evolved chemical character of these rocks is also reflected in their low abundances of chromium and nickel, which are in the range of 5–45 ppm and 40–50 ppm, respectively.

Troctolites

The four troctolite samples selected from the depth interval 422.7 to 500 mbsf (Unit VI) are distinguished by specific chemi-

Table 5. Average concentrations (wt%) and variation (± 1 s) of the olivine gabbros of the various lithologic units of Hole 735B.

Lith. unit: Number of samples:	II	IIIA	IIIB	IV	V	VI
	13	3	1	1	17	7
SiO ₂	50.69 ± 1.37	51.29 ± 0.76	49.83	49.98	50.31 ± 1.02	50.47 ± 1.38
TiO ₂	0.30 ± 0.09	0.52 ± 0.12	0.26	0.29	0.34 ± 0.05	0.32 ± 0.09
Al ₂ O ₃	16.46 ± 2.84	15.13 ± 1.95	17.96	14.70	16.83 ± 1.42	16.88 ± 1.34
Fe ₂ O ₃	5.42 ± 1.15	9.97 ± 1.28	4.72	5.24	5.98 ± 1.31	5.40 ± 1.06
MnO	0.11 ± 0.02	0.18 ± 0.03	0.09	0.11	0.11 ± 0.02	0.11 ± 0.02
MgO	11.13 ± 2.65	9.07 ± 0.96	11.08	13.28	10.42 ± 1.89	10.47 ± 1.56
CaO	13.48 ± 1.32	10.66 ± 1.04	13.94	14.71	13.65 ± 1.06	13.48 ± 1.56
Na ₂ O	2.39 ± 0.68	3.14 ± 0.37	2.08	1.67	2.35 ± 0.40	2.28 ± 0.61
Mg #	0.83 ± 0.02	0.68 ± 0.01	0.84	0.85	0.80 ± 0.02	0.82 ± 0.05

All data anhydrous basis and normalized to sum + 100%; Fe₂O₃ = total iron expressed as ferric iron.

cal features and differ significantly from the olivine gabbros. The high olivine abundance is reflected in high to very high MgO contents, which vary from 13.0 to 25.6 wt%. The magnesium numbers range from 0.83 to 0.87 and are the highest of all rocks analyzed. The average major oxide composition of the troctolites and the variation (± 1 s) is as follows:

SiO ₂	45.88 \pm 2.08
TiO ₂	0.18 \pm 0.03
Al ₂ O ₃	17.28 \pm 3.82
Fe ₂ O ₃	7.12 \pm 1.70
MnO	0.11 \pm 0.03
MgO	17.46 \pm 5.86
CaO	10.21 \pm 2.02
Na ₂ O	1.65 \pm 0.55

These rocks are extremely low in K₂O (<0.02 wt%), rubidium, and niobium (close to or below the detection limits of 0.8 and 0.5 ppm, respectively). The zirconium contents are between 2 and 14 ppm, and yttrium varies from 2 to 5 ppm. The troctolites contain up to 3668 ppm chromium and 747 ppm nickel.

Iron-Titanium Oxide Gabbros

The iron-titanium enriched and ilmenite- and/or magnetite-bearing gabbros make up large sections of lithologic Unit IV and also occur at specific intervals in Units II, V, and VI. They define a chemically distinct group of plutonic rocks drilled at Hole 735B. In general, they are characterized by unusually high concentrations of iron (up to 30 wt% Fe₂O₃) and titanium (up to 9.0 wt% TiO₂). The eight analyzed samples selected at different levels (between 225 and 268 mbsf) from Unit IV have the following average major element composition and variation (± 1 s):

SiO ₂	43.52 \pm 2.76
TiO ₂	5.49 \pm 2.38
Al ₂ O ₃	11.81 \pm 1.61
Fe ₂ O ₃	21.12 \pm 3.48
MnO	0.28 \pm 0.06
MgO	5.79 \pm 1.12
CaO	7.69 \pm 2.10
Na ₂ O	2.91 \pm 0.47
K ₂ O	0.06 \pm 0.04

Except for Sample 118-735B-54R-1, 131–136 cm, Piece 8B, which shows considerable phosphorus enrichment (1.19 wt% P_2O_5), the P_2O_5 contents are below 0.03 wt%. Because of the very high iron concentrations, the magnesium-numbers of these rocks are the lowest of all samples analyzed and vary between 0.32 and 0.51.

The trace-element chemistry of the iron-titanium oxide gabbros is characterized by significant vanadium enrichment (up to 1173 ppm), low contents of chromium and nickel (mostly <20 and <32 ppm, respectively), and significant, though somewhat erratic, enhancement of zirconium (up to 105 ppm), yttrium (up to 69 ppm), and niobium (up to 6 ppm) concentrations.

Trondjemite

Sample 118-735B-53R-5, 40–43 cm, Piece 3, was recovered from a dikelet (about 4 cm wide) of fine-grained, leucocratic, plagioclase-quartz rock, which according to its macroscopic appearance and mineralogical composition was termed trondjemite ("plagiogranite"). Our assumption that this felsic vein represents a highly differentiated, late-stage, "granitelike" melt was corroborated by its major oxide composition. The extremely high contents of the alkali elements, sodium and potassium, and of silicon (70.8 wt% SiO_2) and the low contents of magnesium, iron, titanium, and calcium define a whole-rock chemistry that corresponds to that of a granitic melt having a very high albite component. Because of the limited amount of rock material available, this sample was not analyzed for trace elements.

Basalt Dike

A basaltic dike having well-developed chilled margins against the gabbro cuts the plutonic sequence in Core 118-735B-23R (see "Petrography" section, this chapter). Sample 118-735B-23R-4, 83–86 cm, Piece 5, was selected from the aphyric part of this aphyric to sparsely olivine-phyric dike rock. Chemically, this basalt closely resembles the basalts recovered at Site 732 (see "Geochemistry" section, Site 732 chapter, this volume), and according to its high zirconium/niobium (38) and yttrium/niobium (10) ratios can be assigned to the group of depleted normal-type mid-ocean ridge basalts.

Among the gabbroic rocks analyzed are four additional samples that definitely lie outside the chemical spectrum defined by the various types of gabbros and that, according to their higher zirconium, yttrium, and niobium contents, may represent liquid rather than cumulate compositions. The samples belong to the deformed series of lithologic Unit I (Sample 118-735B-6D-1, 71–74 cm, Piece 13, a mylonitic gabbro) and to a deformed interval of Unit II (Samples 118-735B-15R-1, 90–93 cm, Piece 7B, a porphyroclastic metagabbro; and 118-735B-16R-1, 139–141 cm, Piece 3H, described as a gneissic metagabbro). A fourth zirconium- and yttrium-enriched sample (118-735B-17R-1, 22–27 cm, Piece 5) is an undeformed olivine-bearing gabbro. Trace-element ratios in these rocks are similar to those of depleted normal mid-ocean ridge basalts. These observations suggest that the four zirconium- and yttrium-enriched samples are either gabbros containing an unusually high amount of trapped basaltic liquid, or deformed and recrystallized basaltic dikes.

Chemical Stratigraphy

Figure 46 presents the downhole distribution of the major oxides (in weight percent) SiO_2 , Al_2O_3 , CaO, Na_2O , MgO, total iron as Fe_2O_3 , TiO_2 , and the trace elements, nickel and chromium (in parts per million). In addition, plotted as a function of depth (mbsf) are the magnesium-numbers of the samples (calculated as the molar ratio, $Mg/(Mg + 0.86 Fe_{tot})$) and their MgO/Al_2O_3 ratios, which provide some information about the degree of chemical evolution of the rocks. Figure 47 shows the downhole variation of the MgO/Al_2O_3 ratio, a measure of the

proportion of mafic minerals to plagioclase, of Fe-Ox (ratio of actual Fe_2O_3 content to total iron, expressed as Fe_2O_3), a measure of the degree of iron oxidation, of wt% H_2O , and of concentrations (in parts per million) of the trace elements, copper, zinc, strontium, yttrium, and zirconium.

A preliminary evaluation of these figures shows that despite a certain scatter of the data, significant downhole variations in rock composition exist and that several zones having distinct chemical features can be recognized. Outstanding is the depth interval at about 250 mbsf, which is characterized by locally extreme iron and titanium enrichments. Rocks of this zone show the lowest overall concentrations in SiO_2 , Al_2O_3 , CaO, and MgO and have the lowest magnesium-numbers; i.e., they represent the most evolved lithologies. In keeping with this are the very low abundances of nickel and chromium. The lower boundary of this zone is defined by a pronounced chemical discontinuity between Cores 118-735B-56R and 118-735B-58R, i.e., at a depth of about 280 mbsf. This boundary coincides with the boundary of lithologic Units IV and V. The upper boundary of this iron-titanium-rich chemical zone is marked by a change in the downhole gradients of SiO_2 , MgO, Fe_2O_3 , TiO_2 , and the magnesium-numbers. This boundary can be placed at a depth of about 220 mbsf (i.e., between Sections 118-735B-45R-1 and 118-735B-46R-3). There is excellent agreement with the lithostratigraphic subdivision, which places the boundary between Units III and IV at 224 mbsf.

Farther up, the next obvious chemical change occurs at about 180 mbsf (between Sections 118-735B-36R-2 and 118-735B-36R-4) and is well defined by a discontinuity in the nickel and chromium contents, as well as in the magnesium-numbers. This boundary closely matches the transition between lithologic Units II and III.

Sample density and possible small-scale variations in lithology do not yet allow us to draw reliable chemical boundaries in the higher parts of the recovered gabbro section. However, the data available suggest that there is a chemical change at a depth of about 40 mbsf, which coincides with the boundary of the uppermost deformed gabbro suite and the underlying massive gabbro sequence.

A further chemical boundary corresponding to the transition of lithologic Units V and VI can be found at 400 mbsf (between Cores 118-735B-76R and 118-735B-77R).

Trace-Element Variations

The strongly compatible trace elements nickel and chromium show clear-cut differences in concentration among the various lithologic units (Fig. 47). Abundances of nickel and chromium in Units I, III, and IV are low, which agrees with the lower magnesium-numbers. In particular, the transition between Units II and III is marked by a sharp decrease in concentrations of nickel and chromium. The scattered nickel and chromium contents in lithologic Unit II are somewhat larger than in Units V and VI (aside from the troctolites) and mirror the larger scatter of the magnesium-numbers in Unit II.

Vanadium (when above the detection limit of 0.5 ppm) correlates with TiO_2 and shows a pronounced enrichment in the iron-titanium oxide gabbros. Unit IV is also enriched in zinc and to lesser extent, so is Unit I. Copper contents vary erratically. Because the precision of XRF determinations of copper and zinc is similar, the larger scatter of copper suggests control by minor sulfide phases.

The abundances of strontium appear to be determined largely by the proportions of strontium-rich plagioclase. Hence, strontium contents inversely correlate with MgO/Al_2O_3 ratios (Fig. 48).

In most samples, rubidium contents are below the detection limit of 0.8 ppm. Values above the detection limit are generally

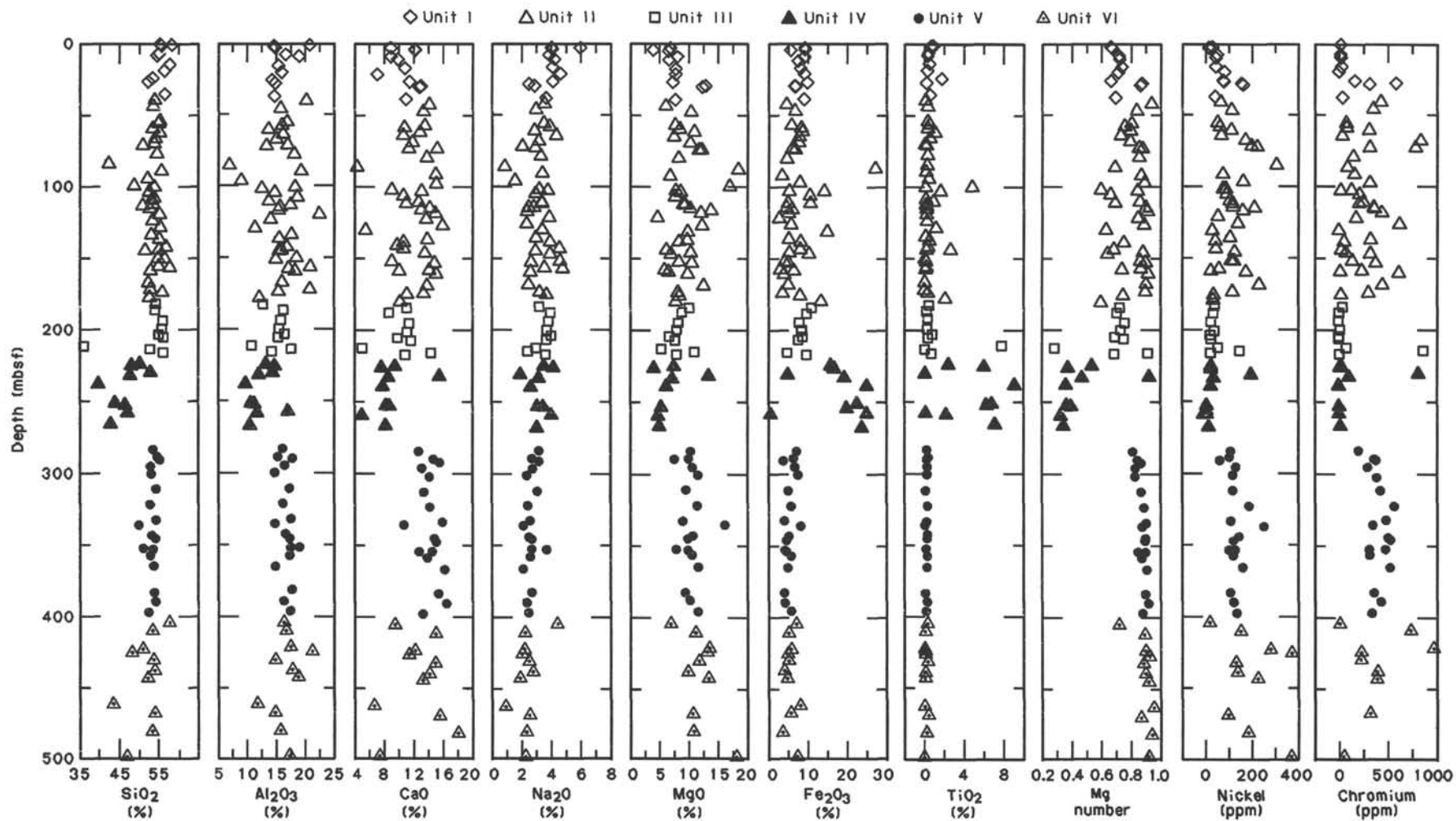


Figure 46. Downhole variation in chemical composition of Hole 735B samples. The six different symbols represent the six different lithologic units.

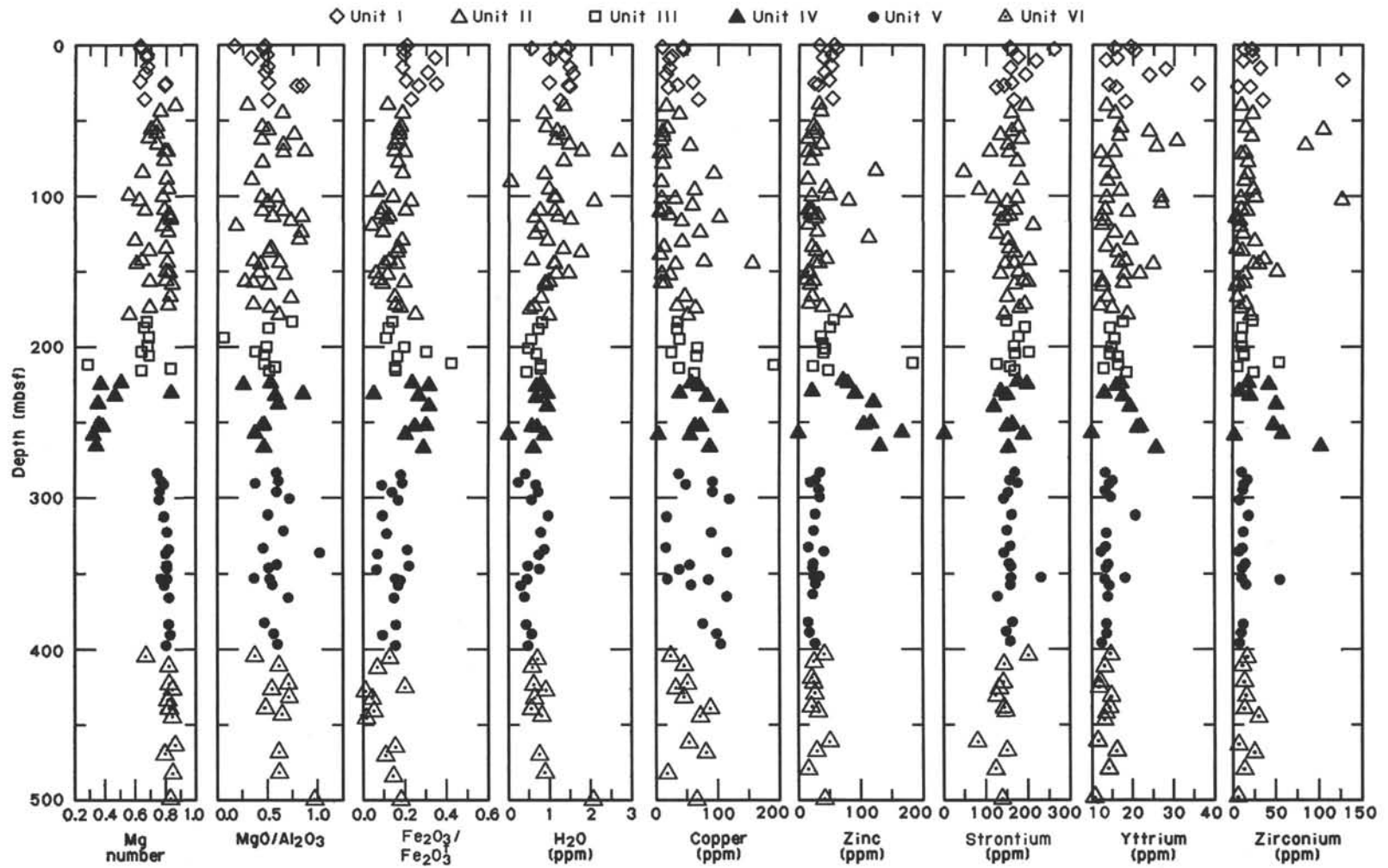


Figure 47. Downhole variation in chemical composition of Hole 735B samples. Symbols as in Figure 46.

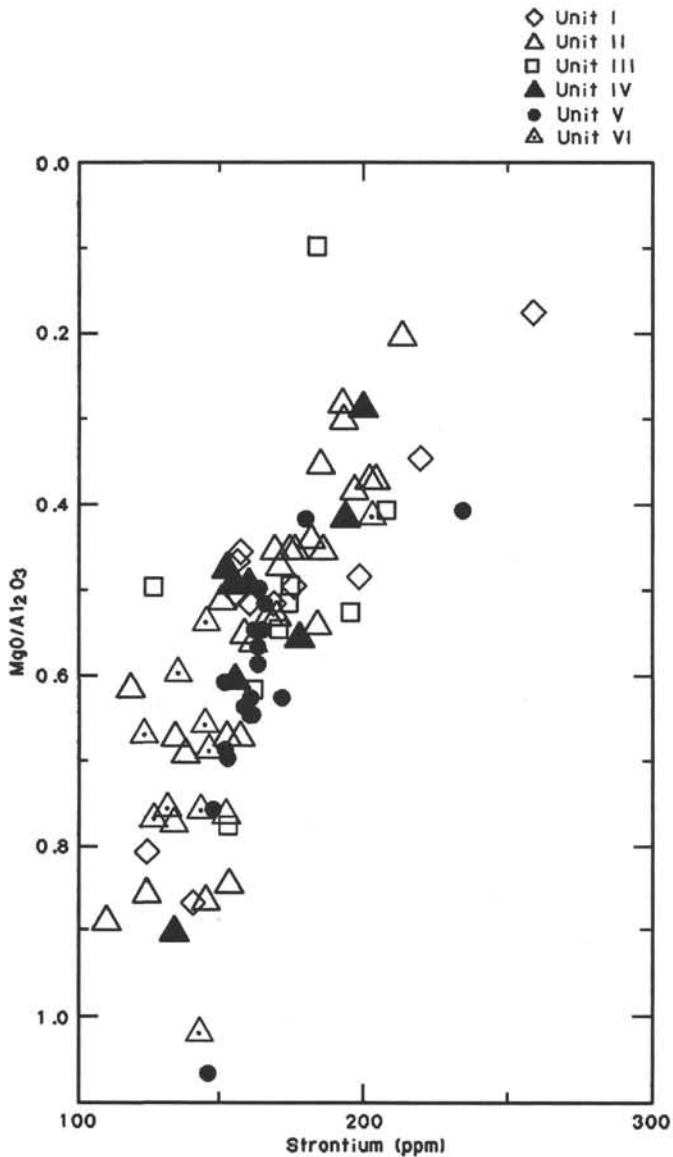


Figure 48. Strontium vs. MgO/Al₂O₃ ratio of Hole 735B samples. Symbols as in Figure 46.

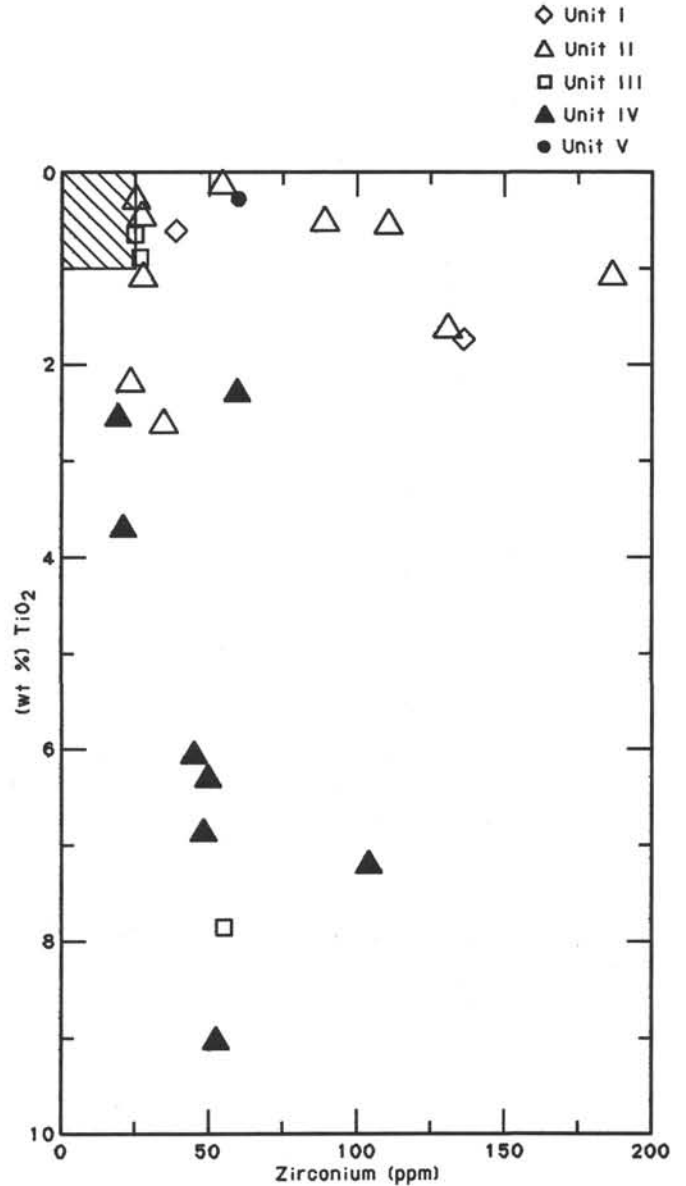


Figure 49. Zirconium vs. TiO₂ of Hole 735B samples. Symbols as in Figure 46. Most samples lie within hatched box area.

accompanied by higher potassium contents. The higher values in Unit I most likely reflect uptake from seawater during low-temperature alteration. Zirconium and yttrium show limited variation in the various gabbro types. There is slight zirconium enrichment in the iron-titanium oxide gabbros (Fig. 49). Samples having high zirconium values (>80 ppm) include the basalt dike and the four anomalous gabbros mentioned previously. The samples that are part of the high zirconium/titanium trend also show significant enrichment of yttrium. Otherwise, yttrium abundances appear to be determined largely by the proportion of clinopyroxene and, as opposed to strontium, are positively correlated with MgO/Al₂O₃ ratios.

PALEOMAGNETICS

Introduction

The Vine-Matthews (1963) model of linear marine magnetic anomalies is central to our understanding of plate tectonics and has been widely applied in the study of marine geological and geophysical processes. Identification of the source layer for

these anomalies has been attempted using inversion of marine magnetic anomaly field data and direct measurements of samples acquired by dredging, by DSDP drilling, and by sampling ophiolites. Although some of these studies suggest that the upper extrusive layer can account for the magnetic anomaly observed at the sea surface (Atwater and Mudie, 1973; Klitgord et al., 1975; Macdonald, 1977; Johnson, 1979; Swift and Johnson, 1984), other studies indicate that the magnetic structure of oceanic crust is very complex and that a contribution from the lower, intrusive layers is required (Fox and Opdyke, 1973; Kent et al., 1978; Harrison, 1981; Banerjee, 1984). To date, however, sampling of *in-situ* lower oceanic crust has been restricted to the sheeted dike complex sampled at DSDP Hole 504B (Smith and Banerjee, 1986) and to unoriented dredge samples (Kent et al., 1978).

Hole 735B penetrated 500.7 m into gabbro, with nearly 87% recovery, thus providing the first continuous, vertically oriented suite of plutonic rocks from the oceanic crust. A shipboard paleomagnetic study was conducted on recovered samples (1) to

examine their contribution to an overlying marine magnetic anomaly, (2) to characterize their magnetic properties as a function of lithology and alteration, and (3) to provide a "ground truth" for downhole magnetic logging data acquired in this hole.

Experimental Methods

Minicores 2.5 cm in diameter and about 2.5 cm long were drilled from vertically oriented sections of the recovered drill core. A total of 135 samples was taken for an average sample interval of 4 m. Paleomagnetic measurements were performed using a spinner magnetometer, and stepwise alternating-field demagnetization (AFD) was conducted with a single-axis demagnetizer (see "Introduction and Explanatory Notes" chapter, this volume). Most samples were demagnetized until less than 15% of the natural remanent magnetization (NRM) remained. Two samples were not demagnetized because their original remanence was near the noise level of the spinner (Samples 118-735B-23R-4, 26–28 cm, Piece 1B, and 118-735B-38R-2, 15–17 cm, Piece 1B). Four samples were progressively thermally demagnetized (Samples 118-735B-3D-1, 60–62 cm, Piece 11; 118-735B-19R-3, 73–75 cm, Piece 6A; 118-735B-38R, 28–30 cm, Piece 1C; and 118-735B-54R-5, 117–119 cm, Piece 5; see "Introduction and Explanatory Notes" chapter, this volume). Magnetic susceptibility was measured with an induction-type sensor, and Koenigsberger ratios were calculated assuming a value of 0.38 Oe for Site 735 (Merrill and McElhinny, 1983). The above described parameters are displayed in Table 6.

Zijderveld diagrams were plotted from demagnetization data, and stable inclinations and declinations were determined using a least-squares approximation. Although ODP hard-rock cores are only oriented vertically, further shore-based studies will attempt azimuthal orientation using *in-situ* magnetic data acquired with a gyroscopically oriented magnetometer (see "Magnetometer Logs" section, this chapter). Table 7 contains natural remanent inclinations, stable inclinations, and uncorrected stable declinations.

Results

Intensity of Remanent Magnetization (J_0)

J_0 values are displayed in Figure 50. The most salient feature of this plot is the extremely large range of observed J_0 values. In comparison, gabbros dredged from the Kane Fracture Zone have an average value that falls within this range (820×10^{-6} emu/cm³, Fox and Opdyke, 1973). Many of the gabbros from Site 735 are of a similar order of magnitude but have dramatically higher values. In fact, two of the measured samples (Samples 118-735B-32R-1, 64–66 cm, Piece 1F, and 118-735B-44R-2, 6–8 cm, Piece 1A) over-ranged the magnetometer and thus must have values greater than 2.5 emu/cm^3 . The high J_0 values are most commonly from gabbros containing extremely large amounts of iron-titanium oxide minerals (see "Oxide and Sulfide Mineralogy" section, this chapter). Such gabbros were recovered throughout much of the drilled section and are the dominant lithology from 224 to 272 mbsf. Further shore-based studies will be conducted in an effort to correlate the variation in magnetization with deformation, alteration, and lithology.

Magnetic Susceptibility (X_0)

X_0 values are plotted in Figure 51. Although a large range of values can be seen, there is much less scatter than is observed in J_0 , and most samples have values less than 1000×10^{-6} cgs. The values from Hole 735B fall within the range of values observed from dredged gabbros by both Fox and Opdyke (1973) and Kent et al. (1978). The highest X_0 values from Hole 735B were observed in the magnetite-ilmenite-rich gabbros. Many of

Table 6. Results of paleomagnetic measurements of samples from Hole 735B.

Core/section (cm)	Depth (mbsf)	J_0	X_0	MDF	Q
118-735B-1D-1, 19	0.19	381	526	235	1.9
1D-1, 141	1.41	379	248	230	4.0
2D-1, 113	7.63	438	300	70	3.8
2D-1, 139	7.89	418	408	178	2.7
2D-2, 99	8.99	334	250	140	3.5
3D-1, 60	15.10	586	199	-100	7.8
4D-2, 7	19.07	2,443	1455	100	4.4
6D-1, 111	25.11	205	136	170	4.0
7D-1, 74	26.74	637	374	150	4.5
7D-2, 9	27.39	671	499	75	3.5
8D-1, 45	29.65	562	112	235	13.2
9D-1, 120	34.40	311	322	130	2.5
10D-1, 24	36.44	231	227	300	2.7
11D-1, 6	39.26	98,970	-100	-100	-100.0
12R-1, 32	39.72	4,767	3410	90	3.7
12R-2, 36	41.26	624	1710	155	1.0
12R-3, 8	42.48	295	993	63	0.8
12R-3, 83	43.23	1,327	194	330	18.0
13R-1, 102	45.02	1,223	640	230	5.0
13R-2, 55	46.55	97	278	475	0.9
14R-1, 35	51.55	2,148	1900	97	3.0
14R-2, 22	52.92	544	377	185	3.8
14R-4, 22	55.92	2,579	896	105	7.6
15R-2, 128	58.98	4,119	1680	30	6.5
16R-1, 139	63.19	91	79	410	3.0
16R-4, 77	67.07	270	53	420	13.4
16R-5, 24	67.30	937	324	25	7.6
18R-3, 29	71.79	23	43	255	1.4
19R-3, 73	78.43	1,202	595	-100	5.3
19R-5, 126	81.54	323	673	20	1.3
20R-2, 54	86.24	1,550	550	350	7.4
21R-2, 49	91.19	1,481	541	240	7.2
22R-2, 41	95.91	139	620	410	0.6
22R-3, 118	98.18	1,369	614	60	5.9
23R-2, 34	102.34	686	310	185	5.8
23R-4, 120	106.20	5	56	-100	0.2
24R-2, 95	107.95	37,586	-100	38	-100.0
24R-3, 50	109.00	10,944	-100	225	-100.0
24R-4, 26	110.23	6,801	383	40	46.7
25R-2, 5	112.05	180	62	260	7.7
25R-3, 137	114.87	678	481	185	3.7
26R-1, 62	116.22	2,997	2035	60	3.9
27R-1, 84	122.34	1,270	564	200	5.9
27R-3, 32	124.82	602	434	150	3.6
28R-2, 12	127.96	7,242	2515	60	7.6
28R-2, 114	128.98	929	298	215	8.2
29R-2, 46	133.46	576	384	600	3.9
29R-4, 19	135.85	181	90	450	5.3
30R-3, 137	140.87	28,023	-100	25	-100.0
30R-4, 14	141.14	1,958	1144	15	4.5
30R-5, 91	143.21	2,370	2065	45	3.0
31R-2, 120	146.20	1,130	644	20	4.6
31R-4, 118	148.98	1,737	608	15	7.5
32R-1, 64	149.14	2,500,000	-100	-100	-100.0
32R-3, 14	151.64	973	161	370	15.9
33R-4, 27	158.27	3,254	5725	20	1.5
33R-4, 129	159.29	552	630	30	2.3
34R-1, 103	159.53	565	240	675	6.2
34R-4, 30	162.76	44	305	-100	0.4
35R-1, 29	163.79	601	224	500	7.1
35R-5, 131	170.81	245	194	20	3.3
36R-2, 11	172.61	922	1102	300	2.2
36R-3, 36	174.36	2,552	1148	200	5.8
37R-1, 11	176.11	1,034	1061	320	2.6
37R-3, 80	179.80	5,541	4469	20	3.3
38R-2, 15	182.65	3	48	-100	-100.0
38R-4, 28	185.78	1,525	1800	-100	-100.0
39R-1, 145	187.45	1,206	1169	310	2.7
39R-3, 21	189.21	2,213	389	380	15.0
40R-2, 62	193.12	1,144	290	210	10.4
40R-5, 13	196.05	1,040	749	600	3.7
41R-4, 68	200.86	1,078	1070	440	2.7
42R-2, 119	203.69	2,573	1405	20	4.8
42R-4, 62	206.12	2,683	1248	240	5.7
43R-1, 126	207.26	1,204	1003	365	3.2
43R-4, 64	211.14	7,424	3152	25	6.2
44R-2, 6	212.56	2,500,000	-100	-100	-100.0

Table 6 (continued).

Core/section (cm)	Depth (mbsf)	J_0	X_0	MDF	Q
118-735B-44R-2, 131	213.81	4,236	1868	20	6.0
(Cont.) 45R-2, 15	217.65	118	105	30	3.0
46R-2, 21	222.71	645	773	680	2.2
46R-2, 128	223.78	599	400	35	3.9
47R-3, 50	229.50	3,808	1852	35	5.4
48R-4, 82	236.32	34,618	-100	40	-100.0
49R-2, 89	238.39	13,117	-100	30	-100.0
50R-4, 87	243.37	8,881	4996	35	4.7
51R-1, 102	244.02	24,618	-100	30	-100.0
52R-4, 69	253.19	35,704	-100	40	-100.0
53R-3, 15	256.15	30,586	-100	40	-100.0
54R-3, 125	262.25	33,961	-100	40	-100.0
54R-5, 117	265.17	21,004	-100	-100	-100.0
55R-3, 130	269.30	56,689	-100	40	-100.0
56R-2, 11	271.61	8,951	4213	40	5.6
56R-2, 144	272.94	41	177	600	0.6
57R-2, 135	277.85	1,150	1085	700	2.8
58R-2, 33	282.33	2,751	852	340	8.5
59R-3, 70	289.20	2,230	475	900	12.4
60R-1, 18	290.68	1,860	389	900	12.6
61R-1, 81	296.31	993	645	550	4.0
62R-3, 104	304.54	5,269	871	410	15.9
63R-3, 80	309.30	1,550	510	360	8.0
63R-6, 28	313.28	517	794	575	1.7
64R-2, 54	317.04	910	1089	380	2.2
65R-2, 67	322.17	3,137	487	310	17.0
66R-2, 86	327.36	6,777	364	260	49.0
66R-3, 134	329.34	253	34	-100	19.6
68R-3, 15	338.15	831	716	20	3.1
69R-4, 138	346.88	556	304	460	4.8
70R-1, 105	347.05	215	67	280	8.5
71R-2, 82	353.32	148	440	800	0.9
72R-3, 36	359.36	174	77	900	5.9
72R-6, 106	364.56	298	265	650	3.0
73R-3, 73	369.23	191	70	460	7.2
74R-2, 38	376.88	537	150	800	9.4
74R-6, 41	382.91	9,013	5606	50	4.2
75R-3, 48	387.98	260	246	270	2.8
75R-6, 75	392.75	126	120	30	2.8
76R-3, 50	397.50	9,139	3649	30	6.6
77R-4, 70	408.70	3,540	2092	30	4.5
78R-4, 65	414.65	293	126	30	6.1
79R-2, 65	416.65	8,037	4520	25	4.8
79R-7, 99	424.49	103	131	25	2.1
80R-1, 131	425.31	1,090	965	40	3.0
80R-7, 23	433.23	7,493	4093	40	4.9
81R-2, 54	435.54	230	223	20	2.7
81R-7, 64	442.84	145	126	165	3.0
82R-2, 13	444.63	223	176	30	3.3
82R-6, 11	450.61	34,064	-100	40	-100.0
83R-4, 95	457.95	248	178	30	3.7
83R-7, 104	462.54	289	330	35	2.3
84R-2, 67	464.17	1,329	508	20	6.9
84R-3, 14	465.14	596	885	350	1.8
85R-4, 9	476.09	1,475	1016	20	3.8
85R-7, 17	480.67	1,108	535	20	5.5
86R-6, 143	489.93	12,205	-100	40	-100.0
87R-5, 20	496.70	16,529	-100	60	-100.0

Depth is in meters below seafloor, J_0 is the intensity of natural remanent magnetization in 10^{-6} emu/cm³, X_0 is magnetic susceptibility in 10^{-6} cgs units, MDF is the median demagnetizing field in Oersteds, and Q is the Koenigsberger ratio. Values of -100 indicate a parameter that could not be obtained for a particular sample. Note that the two samples that over-ranged the magnetometer were given values of $2,500,000 \times 10^{-6}$ emu/cm³, which is the maximum value that the magnetometer can measure.

these samples over-ranged the susceptibility meter and thus must have values greater than $10,000 \times 10^{-6}$ cgs. Because susceptibility is directly related to grain size and concentration of magnetic minerals and because the magnetite gabbros were observed to have both high contents of magnetite and large grain sizes, the high susceptibility values are not surprising.

Table 7. Magnetic directions of samples from Hole 735B.

Core/section (cm)	Depth (mbsf)	I_{nrm}	I_s	Dec
118-735B-1D-1, 19	0.19	68.7	72	333
1D-1, 141	1.41	71.8	70	135
2D-1, 113	7.63	62.1	57	137
2D-1, 139	7.89	78.4	69	320
2D-2, 99	8.99	69.0	73	315
3D-1, 60	15.10	76.1	74	61
4D-2, 7	19.07	57.2	51	250
6D-1, 111	25.11	67.7	68	190
7D-1, 74	26.74	74.9	74	0
7D-2, 9	27.39	86.0	87	330
8D-1, 45	29.65	75.0	75	250
9D-1, 120	34.40	78.5	76	159
10D-1, 24	36.44	86.4	84	231
11D-1, 6	39.26	76.4	-100	-100
12R-1, 32	39.72	53.6	54	53
12R-2, 36	41.26	36.8	80	208
12R-3, 8	42.48	13.7	68	61
12R-3, 83	43.23	18.3	18	126
13R-1, 102	45.02	66.5	67	52
13R-2, 55	46.55	78.5	75	153
14R-1, 35	51.55	66.0	69	126
14R-2, 22	52.92	83.6	78	199
14R-4, 22	55.92	69.1	69	24
15R-2, 128	58.98	-70.3	45	261
16R-1, 139	63.19	-19.0	31	152
16R-4, 77	67.07	86.8	83	194
16R-5, 24	67.30	-74.5	63	61
18R-3, 29	71.79	81.3	79	247
19R-3, 73	78.43	89.6	81	215
19R-5, 126	81.54	-58.5	79	139
20R-2, 54	86.24	73.3	52	48
21R-2, 49	91.19	60.1	71	339
22R-2, 41	95.91	69.1	64	70
22R-3, 118	98.18	80.1	75	214
23R-2, 34	102.34	73.7	64	175
23R-4, 120	106.20	53.5	-100	-100
24R-2, 95	107.95	58.4	51	295
24R-3, 50	109.00	75.8	78	325
24R-4, 26	110.23	80.1	75	112
25R-2, 5	112.05	62.6	70	19
25R-3, 137	114.87	73.3	73	147
26R-1, 62	116.22	79.2	73	248
27R-1, 84	122.34	29.5	31	316
27R-3, 32	124.82	74.7	80	358
28R-2, 12	127.96	68.0	72	42
28R-2, 114	128.98	84.1	77	72
29R-2, 46	133.46	51.8	83	53
29R-4, 19	135.85	59.6	65	212
30R-3, 137	140.87	-55.4	44	316
30R-4, 14	141.14	-64.4	69	44
30R-5, 91	143.21	-72.2	67	181
31R-2, 120	146.20	-74.8	44	232
31R-4, 118	148.98	-75.8	68	196
32R-1, 64	149.14	-70.8	-100	-100
32R-3, 14	151.64	66.0	67	66
33R-4, 27	158.27	-77.7	67	20
33R-4, 129	159.29	-69.4	75	135
34R-1, 103	159.53	5.4	78	48
34R-4, 30	162.76	-74.8	-100	-100
35R-1, 29	163.79	71.2	69	195
35R-5, 131	170.81	-70.7	68	159
36R-2, 11	172.61	-73.6	79	189
36R-3, 36	174.36	74.5	83	94
37R-1, 11	176.11	-30.7	80	140
37R-3, 80	179.80	-67.4	75	152
38R-2, 15	182.65	-60.7	-100	-100
38R-4, 28	185.78	47.9	-64	238
39R-1, 145	187.45	-49.0	68	120
39R-3, 21	189.21	66.8	75	130
40R-2, 62	193.12	83.5	80	163
40R-5, 13	196.05	15.8	68	107
41R-4, 68	200.86	64.5	62	210
42R-2, 119	203.69	-49.7	76	24
42R-4, 62	206.12	-40.0	70	353
43R-1, 126	207.26	32.4	69	125
43R-4, 64	211.14	-75.0	62	141

Table 7 (continued).

Core/section (cm)	Depth (mbsf)	I_{nrm}	I_s	Dec
118-735B-44R-2, 6	212.56	-81.1	-100	-100
(Cont.) 44R-2, 131	213.81	-77.7	59	194
45R-2, 15	217.65	-66.1	31	262
46R-2, 21	222.71	-2.2	59	108
46R-2, 128	223.78	-70.5	51	352
47R-3, 50	229.50	-76.1	61	288
48R-4, 82	236.32	-73.2	40	117
49R-2, 89	238.39	-60.9	60	94
50R-4, 87	243.37	-58.4	63	120
51R-1, 102	244.02	-72.9	85	170
52R-4, 69	253.19	-63.1	42	354
53R-3, 15	256.15	-60.2	17	3
54R-3, 125	262.25	-74.5	54	138
54R-5, 117	265.17	-58.0	-100	-100
55R-3, 130	269.30	-77.5	39	171
56R-2, 11	271.61	-67.0	52	315
56R-2, 144	272.94	1.9	47	243
57R-2, 135	277.85	5.0	76	224
58R-2, 33	282.33	-59.3	-68	5
59R-3, 70	289.20	63.0	76	28
60R-1, 18	290.68	80.9	74	218
61R-1, 81	296.31	26.2	52	67
62R-3, 104	304.54	71.8	80	324
63R-3, 80	309.30	71.0	68	133
63R-6, 28	313.28	-51.7	66	321
64R-2, 54	317.04	-37.7	76	230
65R-2, 67	322.17	63.4	72	12
66R-2, 86	327.36	56.5	52	331
66R-3, 134	329.34	-63.0	-100	-100
68R-3, 15	338.15	-55.5	71	38
69R-4, 138	346.88	22.3	68	30
70R-1, 105	347.05	53.5	62	312
71R-2, 82	353.32	-27.9	75	133
72R-3, 36	359.36	77.5	72	217
72R-6, 106	364.56	-43.9	68	48
73R-3, 73	369.23	66.7	67	235
74R-2, 38	376.88	47.4	58	191
74R-6, 41	382.91	-71.2	42	15
75R-3, 48	387.98	-16.0	79	323
75R-6, 75	392.75	-79.2	57	185
76R-3, 50	397.50	-72.1	65	170
77R-4, 70	408.70	-66.3	51	82
78R-4, 65	414.65	-71.4	59	120
79R-2, 65	416.65	-84.6	43	146
79R-7, 99	424.49	-59.8	54	231
80R-1, 131	425.31	-74.8	57	211
80R-7, 23	433.23	-64.6	52	338
81R-2, 54	435.54	-68.1	71	239
81R-7, 64	442.84	-71.0	-100	-100
82R-2, 13	444.63	-72.2	53	211
82R-6, 11	450.61	-70.4	33	233
83R-4, 95	457.95	-57.1	49	126
83R-7, 104	462.54	-54.5	63	48
84R-2, 67	464.17	-71.7	78	198
84R-3, 14	465.14	-45.6	72	183
85R-4, 9	476.09	-67.8	80	128
85R-7, 17	480.67	-74.1	73	224
86R-6, 143	489.93	-63.9	69	189
87R-5, 20	496.70	-78.7	70	188

Depth is in meters below seafloor, I_{nrm} is the natural remanent inclination in degrees, I_s is the stable inclination in degrees, and Dec is the uncorrected, stable declination in degrees. Values of -100 indicate a directional parameter that could not be obtained for that particular sample.

With the exception of the magnetite-ilmenite gabbros, the X_0 values measured in recovered samples agree well with those measured in the borehole with the USGS susceptibility tool (see "Magnetometer Logs" section, this chapter). Although both measurements indicate an increase in magnetic susceptibility within the magnetite-ilmenite-rich gabbros, the values measured *in situ* are substantially lower than those estimated by the over-ranged susceptibility meter. The nature of this discrepancy will be examined more closely during shore-based studies.

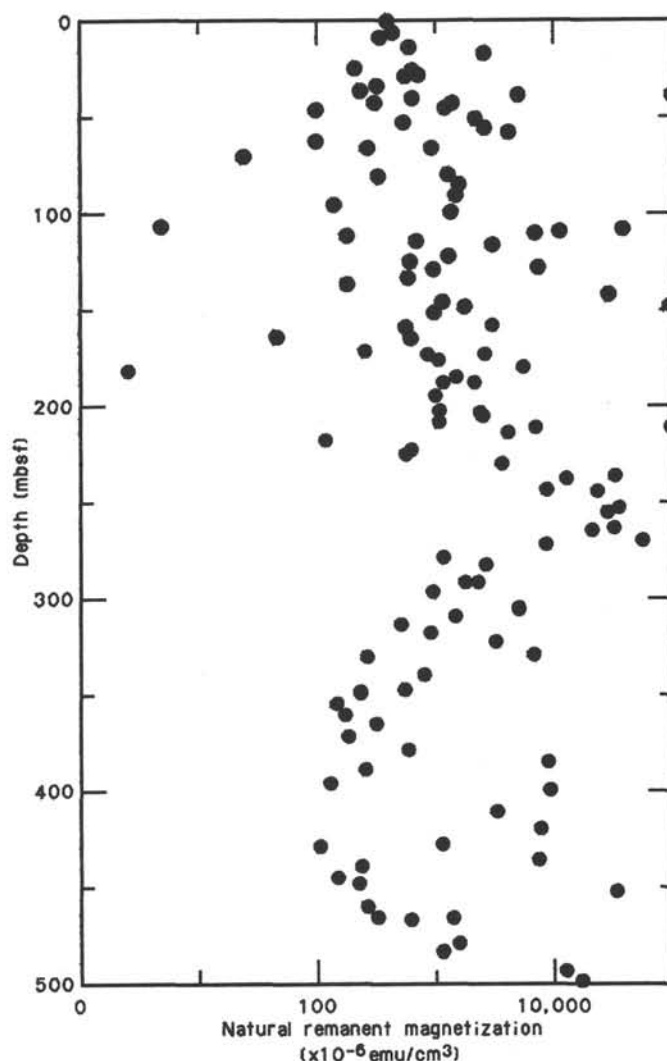


Figure 50. Intensity of natural remanent magnetization (NRM) plotted vs. depth in Hole 735B.

Koenigsberger Ratio (Q)

The Koenigsberger ratio is an estimate of the relative contributions of remanent and induced magnetization within a given rock. It is commonly used to determine whether *in-situ* magnetization is dominated by remanent magnetization ($Q > 1$) or an induced component parallel to the current field ($Q < 1$). Q values are displayed in Figure 52 and show little scatter. Most samples have Q ratios between 1 and 10, which indicates that the *in-situ* magnetization is indeed dominated by a remanent magnetization. Gabbros from both the Troodos ophiolite and the Kane Fracture Zone also show Q ratios ranging between 1 and 10 (Pariso and Johnson, in press; Fox and Opdyke, 1973) and thus agree well with the values observed in Hole 735B gabbros.

Alternating Field Demagnetization

Demagnetization curves were plotted for all samples that were subjected to AFD. From these curves, the peak alternating field required to remove one-half the initial magnetization was determined. This is commonly referred to as the median demagnetizing field (MDF), and these data are displayed in Figure 53. The majority of the samples have high, although scattered, MDF values. However, a large number of samples have very low

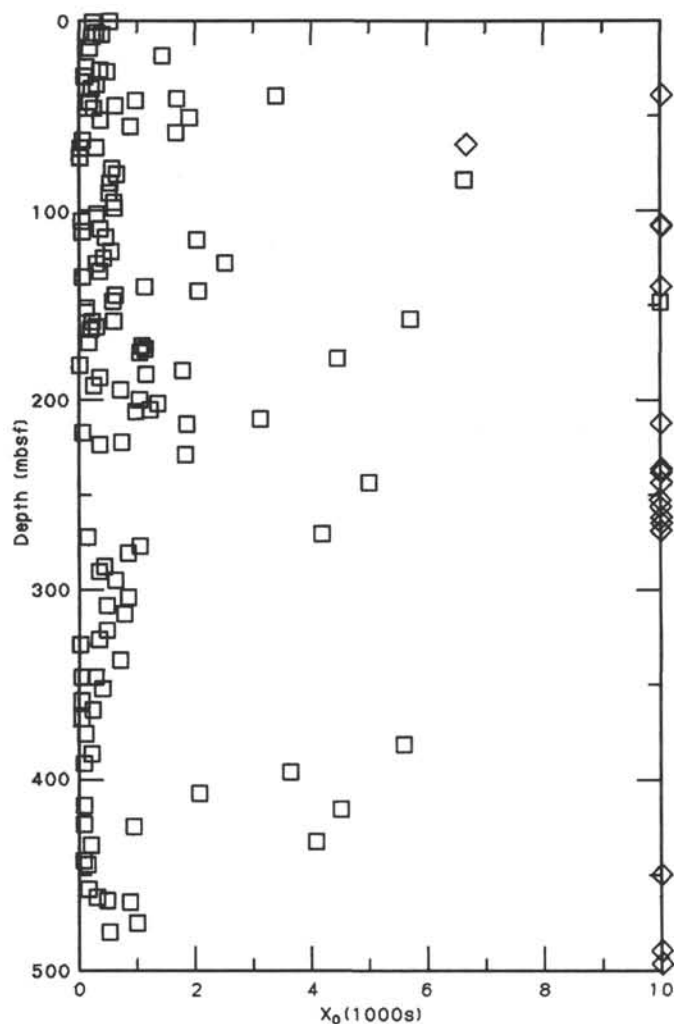


Figure 51. Magnetic susceptibility plotted vs. depth in Hole 735B. Units are 10^{-6} cgs. Samples that over-ranged the susceptibility meter are plotted with a diamond symbol and were given a value of $10,000 \times 10^{-6}$ cgs, which represents the minimum possible value.

(<50 Oe) MDF values. The low MDF samples are most often associated with the magnetite- and ilmenite-rich samples.

The demagnetization curves plotted for individual samples commonly fall into one of three shape-based categories. The most frequently observed shape is similar to that displayed in Figure 54 and indicates the gradual removal of a single, stable magnetic vector. In contrast, a large number of samples, particularly those in the magnetite-ilmenite gabbros, exhibit curves similar to that in Figure 55. This type of demagnetization is characterized by the removal of an extremely large component at very low peak fields. The Zijderveld diagram in Figure 55 shows the change in direction of the removed vector, and in such cases, it is always in the direction opposite the stable magnetization. Finally, a significant portion of samples have curves similar to those in Figures 56 and 57. This type of curve is characterized by the easy removal of a small secondary component. Examination of the corresponding Zijderveld diagram shows that this component is usually in the direction opposite the stable magnetization, and thus its removal results in a small, but abrupt, increase in total field magnetization.

Thermal Demagnetization

Stable inclinations were determined in three of the four samples that were thermally demagnetized. Although heating and

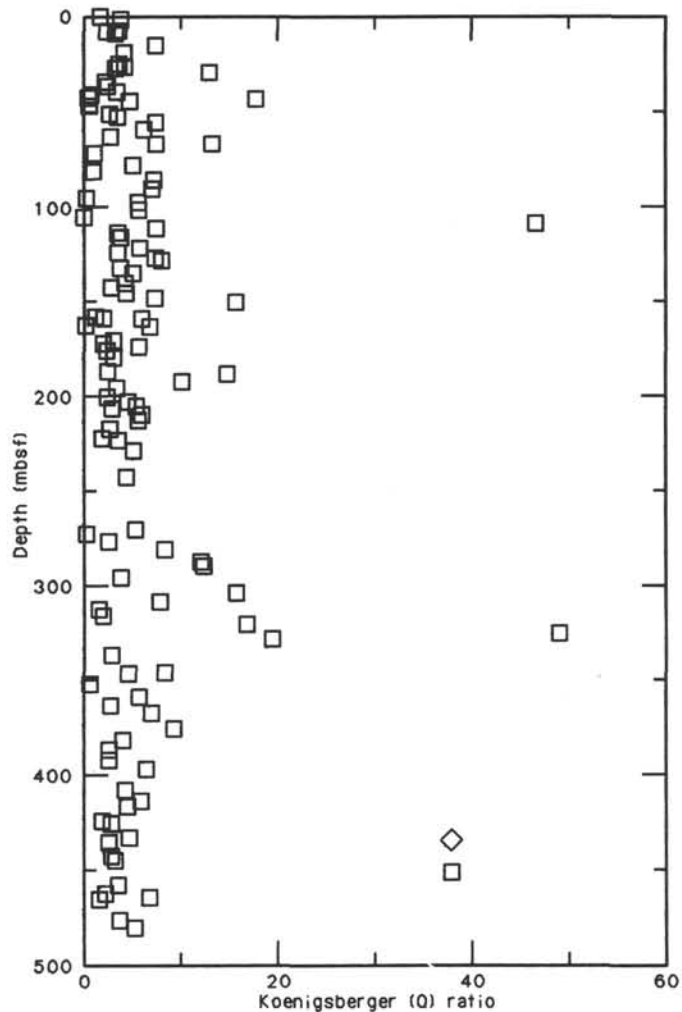


Figure 52. The Koenigsberger (Q) ratio plotted vs. depth in Hole 735B using a value of 0.38 Oe for the magnetic field intensity at Site 735.

cooling cycles were performed in air, a short time (a 20-min heating cycle and a 10-min cooling cycle) was spent at elevated temperatures to minimize oxidation. The demagnetization data for two samples are plotted in Figures 58 and 59. Figure 58 shows a three-component system composed of (1) a stable component carried by magnetite, (2) another component probably associated with titanium-poor titanomagnetite, and (3) a weak, viscous component. The remanence of this sample is clearly dominated by a stable component. Figure 59 shows a two-component system having a well-defined stable remanence carried by magnetite and another component roughly opposite to that of the stable component. The secondary and unstable component may be caused by a mineral having a low blocking temperature, such as pyrrhotite or a titanium-rich titanomagnetite.

Magnetic Inclinations

Natural remanent inclinations are plotted vs. depth in Figure 60. The data clearly fall into two groups: one having steep positive inclinations and one having steep negative inclinations. Stable inclinations are plotted vs. depth in Figure 61 and, with the exception of two negative values, are all steep and positive. The two samples having negative stable inclinations were not identified until the working halves of the cores were stored and must be examined further at a later date to explore the possibility that they were misoriented. Average inclination was calculated as 65°

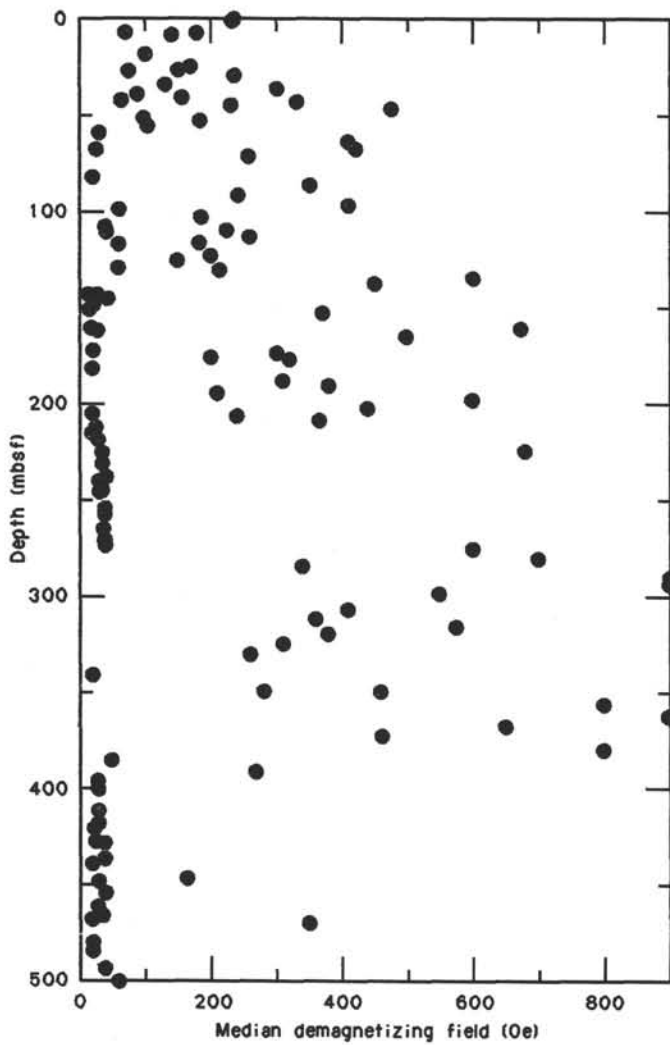


Figure 53. Median demagnetizing field plotted vs. depth in Hole 735B. Units are Oersteds.

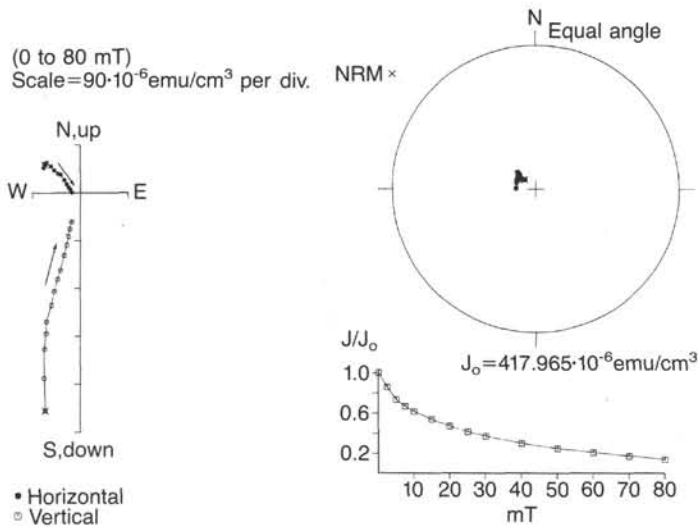


Figure 54. Demagnetization data plotted in three diagrams for interval 118-735B-2D-1, 139-141 cm, Piece 24. The Zijderveld diagram on the left shows no change in magnetic direction during demagnetization, as does the stereographic projection of the total intensity vector on the upper right. The diagram on the lower right is the decay of normalized intensity with increasing peak alternating fields.

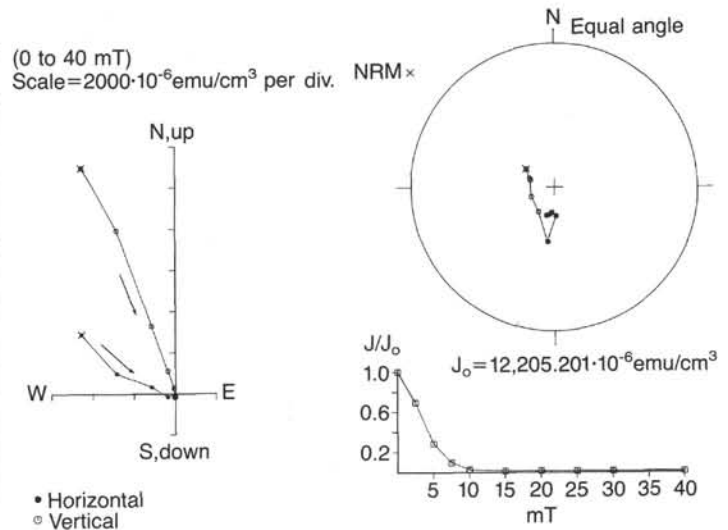


Figure 55. Alternating field demagnetization data plotted in three diagrams for interval 118-735B-86R-6, 14-16 cm, Piece 19. Although the Zijderveld diagram on the left shows only a large, secondary component of magnetization, the change in direction is obvious on the stereographic projection of the total intensity vector on the upper right. In the diagram on the lower right, an abrupt decay in normalized intensity is observed to occur at very low peak alternating fields.

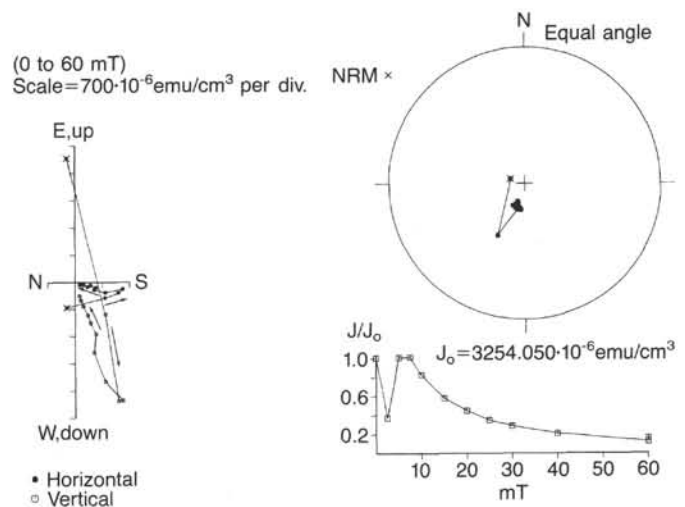


Figure 56. Alternating field demagnetization data plotted in three diagrams for interval 118-735B-33R-4, 27-29 cm, Piece 2B. Two components of almost opposite polarity are observed on the Zijderveld diagram on the left and also on the stereographic projection on the upper right. The figure on the lower right shows an abrupt increase in normalized intensity after removal of the secondary magnetization. This type of curve results in a low MDF, although the coercivity of the stable magnetization appears to be high.

$\pm 7^\circ$, using McFaddin and Reid's method (1982). Based upon a geocentric axial dipole, the theoretical inclination for latitude 33°S is -52° and thus the average of the observed inclination is not only reversed but is slightly steeper than expected. Note that logging of the drill hole indicated that it deviates 4° to 6° north from vertical. If this is the case, one might expect a slight shallowing of the true inclination. To clarify this point, further examination of the logging data will be essential. In addition, preliminary examination of the magnetic logging data indicates that all the *in-situ* crustal rocks are of one magnetic polarity. This suggests that the observed negative NRM inclinations may result from a drilling-induced remanence. Again, further exami-

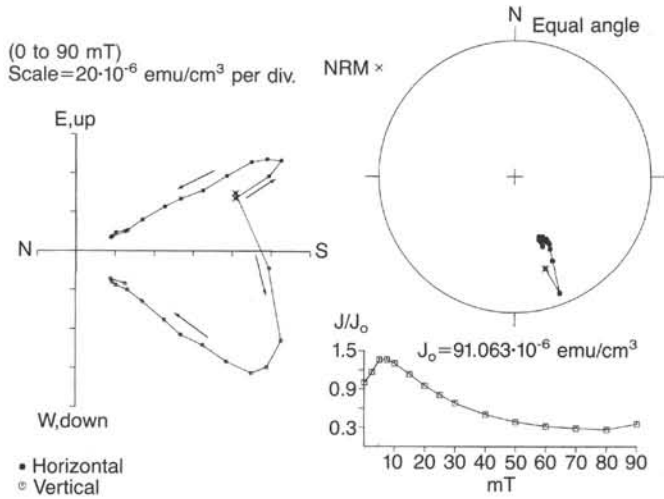


Figure 57. Alternating field demagnetization data plotted in three diagrams for interval 118-735B-16R-1, 139-141 cm, Piece 3H. Two components of almost opposite polarity are observed on the Zijderveld plot on the left and the stereographic projection on the upper right. The curve on the lower right shows an abrupt increase in normalized intensity after removal of the secondary component. This type of curve results in a very high MDF, which therefore is not a good indicator of the coercivity of the primary magnetization.

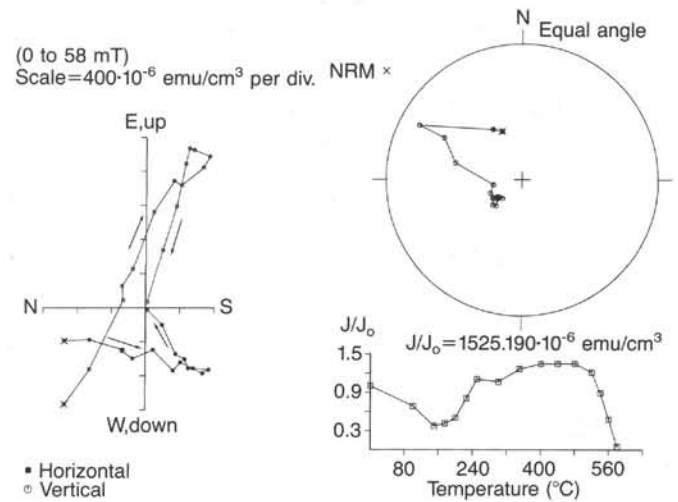


Figure 59. Thermal demagnetization data plotted in three diagrams for Sample 118-735B-38R-4, 28-30 cm, Piece 1C. Two well-defined components of almost opposite polarity appear on both the Zijderveld plot on the left and the stereographic projection on the upper right. The curve on the lower right shows that the removal of the secondary magnetization results in an increase in total intensity.

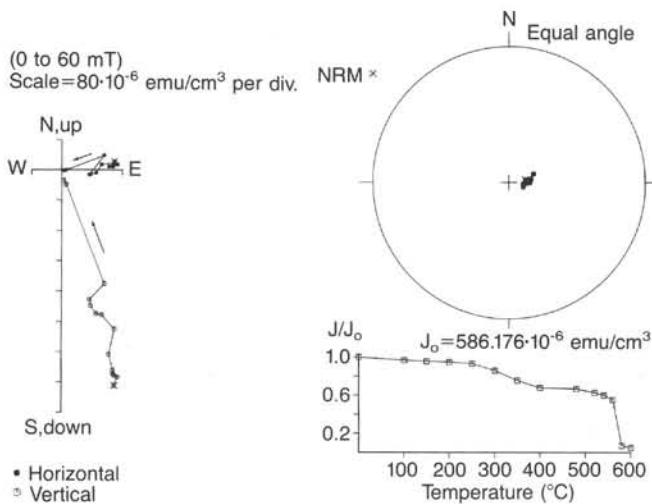


Figure 58. Thermal demagnetization data plotted in three diagrams for Sample 118-735B-3D-1, 60-62 cm, Piece 11. Three weakly defined components appear on the Zijderveld plot on the left, although the stereographic projection on the upper right shows that the total intensity vector changes direction very little. The curve on the lower right also shows three very weakly defined trends from 0° to 250°C, from 250° to 560°C, and from 560° to 580°C.

nation of both the logging and the discrete-sample data will be important for clarifying this point.

Conclusions

The samples studied vary widely in magnetic properties, but clearly can be divided into two major populations: (1) those having high J_0 , low MDF, high X_0 values, and negative NRM inclinations and (2) those having low J_0 , high MDF, low Q values, and steep, positive NRM inclinations. Samples of Group 1 clearly possess a very strong but unstable secondary magnetization directed parallel to the present geomagnetic field. The in-

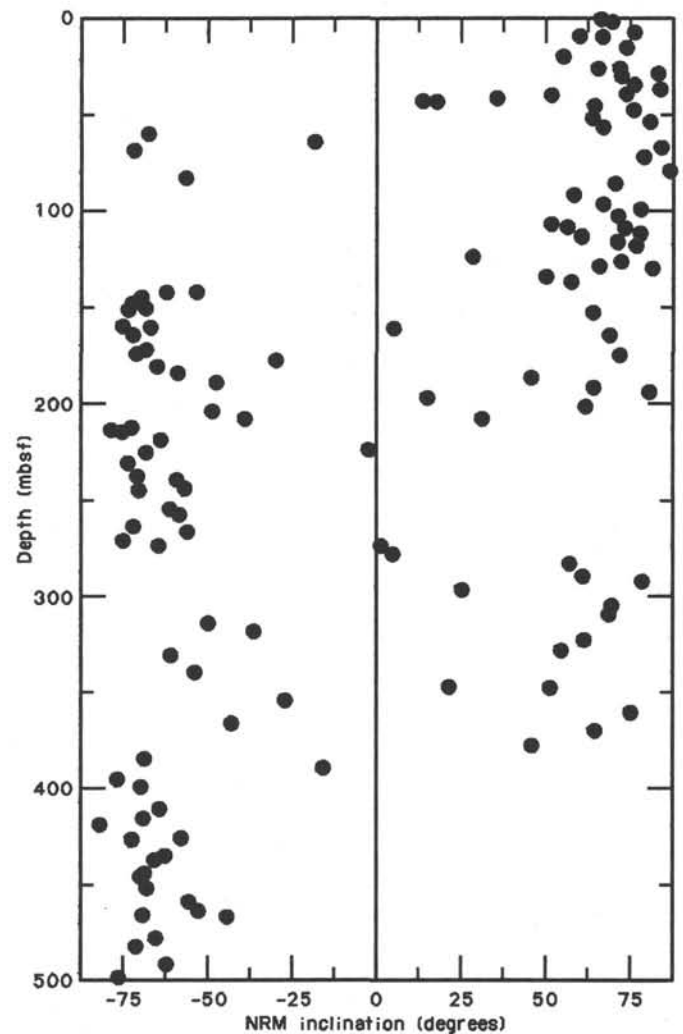


Figure 60. Natural remanent inclinations plotted vs. depth for Hole 735B.

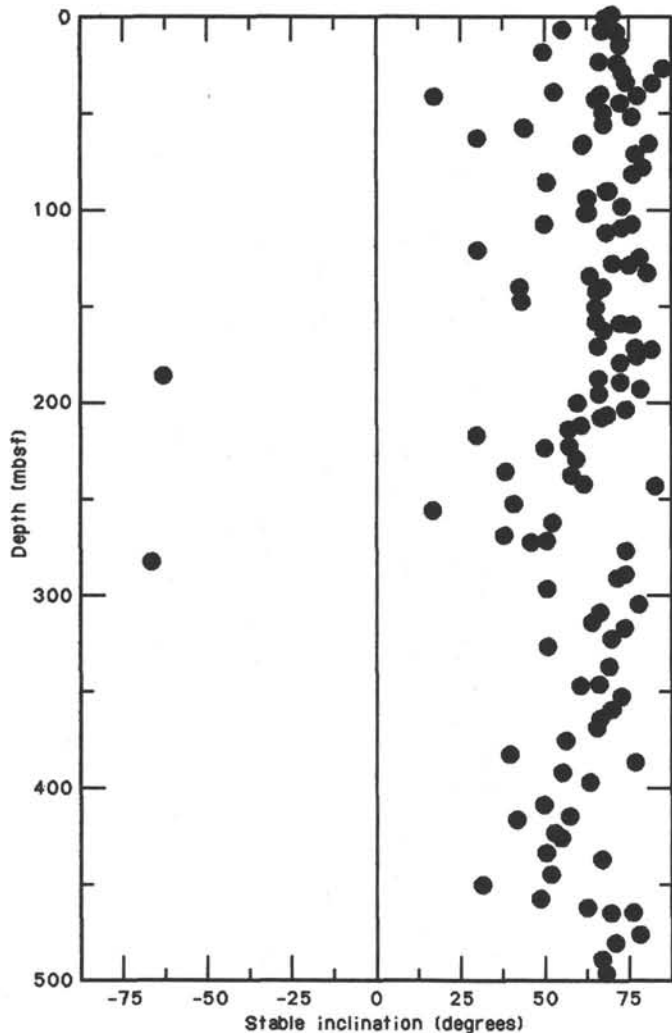


Figure 61. Stable inclinations plotted vs. depth for Hole 735B.

tensity of this magnetization is anomalously high and is clearly associated with the very large concentrations of iron-titanium oxides within these rocks. We are not sure of the source of the secondary magnetization but likely possibilities include (1) a magnetization acquired as a result of the drilling process, such as piezo-remnant magnetization or isothermal remnant magnetization; or (2) viscous remnant magnetization acquired over time in the current field; or (3) magnetization due to secondary alteration (partial thermal remnant magnetization or chemical remnant magnetization). Preliminary analysis of the downhole magnetic logs indicates that the most likely cause is related to drilling.

Although two normal (negative) stable inclinations were observed, the section as a whole clearly has a stable reversed magnetization. A marine magnetic anomaly survey suggests an age of about 12 Ma (anomaly 5A) for the study area (Dick et al., unpublished data). Therefore, the reversed magnetization obtained from this crustal section may be correlated to one of the reversed polarity chrons observed near anomaly 5A. Moreover, because both metamorphosed and unmetamorphosed gabbros of various types have stable positive (reversed) inclinations, a relatively short time interval probably occurred between the initial cooling and metamorphism of these rocks. The remnant intensities are considered large enough to contribute to the marine magnetic anomaly. However, the presence of different magnetic polarities in the vertical section should result in a lower ef-

fective intensity. Because the reversals result from a secondary magnetization (as mentioned above), it is important to constrain the source of this magnetization. Further shore-based studies will concentrate on this problem.

Finally, the value of the stable inclination is slightly steeper than expected. If the samples are corrected for inclination of the drill hole (approximately 5°), an even steeper anomalous inclination would result. Although paleosecular variation may have resulted in steeper than expected inclinations, we believe that given the long time required to cool the crustal section, tectonic rotation is a more likely cause for the observed stable inclinations.

PHYSICAL PROPERTIES

Compressional-wave velocities and index properties were measured for about 180 samples selected as representative of the core obtained at Hole 735B. These data are summarized in Tables 8 through 10. The velocity-density, velocity-porosity and velocity-depth relationships are plotted in Figures 62A, 62B, 63, and 64, and are coded according to rock type. Compressional-wave velocities reflect the component mineral properties and proportions, porosity (especially fracture porosity), and possibly rock texture. Also, V_p can vary with direction in rocks that are layered or that have preferred orientations of cracks or mineral grains, which are themselves anisotropic. All these factors are involved in the suite of rocks studied (Figs. 62A and 62B). Several features of this data set are noteworthy and important and are discussed in detail in the following paragraphs.

1. These crystalline rocks have high seismic velocities (up to 7.28 km/s) and densities (most are greater than 2.9 Mg/m³). Peridotite is the only common rock type having velocities and densities this high. The high velocities and densities occur because these gabbros were variably altered by retrograde metamorphic hydration reactions. A key reason for this is that amphibole is the most abundant alteration mineral. Amphibole ($V_p = 6.8\text{--}7.0$ km/s, density = 3.0–3.2 Mg/m³; Christensen, 1982; Johnson and Olhoeft, 1984) has properties similar to the minerals it replaces, such as clinopyroxene. This contrasts with the low-grade alteration assemblages that include phyllosilicates (such as talc, serpentine, and the micas, with V_p under 6.3 km/s and densities between 2.7 and 2.8 Mg/m³).

2. Metagabbros have the same range of velocities and densities as their igneous gabbroic protoliths (Fig. 62A). In general, this dynamic metamorphism has not changed the mineral assemblages or proportions but has changed grain sizes, grain-grain articulation (grain interrelationships), and mineral crystallographic orientations, none of which was expected to change the average compressional-wave velocities. The observed velocities and densities can be rationalized easily, starting with a basic two-mineral gabbro that consists of plagioclase feldspar (composition = An₅₈, $V_p = 6.7$ km/s, and density = 2.68 Mg/m³) and an augitic clinopyroxene ($V_p = 7.22$ km/s and density = 3.32 Mg/m³) at a ratio of approximately 60:40. Adding olivine, the most common mineral component ($V_p = 8.42$ km/s and density = 3.31 Mg/m³), raises both V_p and density of the gabbros, whereas ilmenite, the most typical oxide component ($V_p = 6$ km/s and density = 4.79 Mg/m³), greatly lowers V_p and raises density. Most of the oxide-bearing gabbros and their metagabbro derivatives clearly are displaced to the high-density/low-velocity direction of the velocity-density plot in Figure 62A. The maximum observed velocity is 7.27 km/s, which suggests a maximum olivine content of 23%, consistent with that observed in this section (See "Primary Petrography" section, this chapter).

3. The foliated and/or mylonitized gabbros and metagabbros display varying degrees of V_p anisotropy, depending on the type of foliation developed. Foliated gabbros collected from in-

Table 8. Index properties of the crystalline rocks recovered from Site 735.

Core/section interval (cm)	DIR	Depth (mbsf)	Velocity (km/s)
118-735B-1D-1, 19-21	C	0.19	5.53
1D-1, 141-143	C	1.41	6.40
2D-1, 113-115	C	7.63	5.94
2D-1, 139-141	C	7.89	6.38
2D-1, 142-145	A	7.92	6.30
2D-1, 142-145	B	7.92	6.76
2D-1, 142-145	C	7.92	6.69
2D-2, 99-101	C	8.99	6.08
4D-2, 7-9	C	19.07	6.40
6D-1, 111-113	C	25.11	6.66
7D-1, 74-76	C	26.74	6.90
7D-2, 9-11	C	27.59	7.01
8D-1, 45-48	C	29.65	6.75
9D-1, 120-122	C	34.40	6.82
10D-1, 24-26	C	36.44	6.74
11D-1, 6-8	C	39.26	6.52
12R-1, 36-41	A	39.76	6.27
12R-1, 36-41	C	39.76	6.74
12R-1, 55-62	A	39.95	5.55
12R-1, 55-62	C	39.95	6.06
12R-2, 32-34	A	41.22	6.58
12R-2, 32-34	B	41.22	6.70
12R-2, 32-34	C	41.22	6.24
12R-2, 36-38	C	41.26	6.73
12R-3, 8-10	C	42.48	6.90
12R-3, 77-84	A	43.17	7.39
12R-3, 77-84	C	43.17	6.99
12R-3, 83-85	C	43.23	7.19
13R-1, 91-94	A	45.41	6.86
13R-1, 91-94	B	45.41	6.94
13R-1, 91-94	C	45.41	6.94
13R-1, 102-105	C	45.52	7.27
13R-2, 55-58	C	46.05	7.19
13R-2, 109-112	A	47.09	6.48
13R-2, 109-112	B	47.09	6.34
13R-2, 109-112	C	47.09	6.62
13R-3, 121-127	A	47.21	5.75
13R-3, 121-127	B	47.21	6.74
14R-1, 20-26	A	51.40	6.58
14R-1, 35-38	C	51.55	7.04
14R-2, 22-25	C	52.92	7.19
14R-3, 122-128	A	55.44	6.52
14R-4, 22-25	C	55.92	7.20
15R-2, 128-130	C	58.98	6.62
16R-1, 80-86	A	62.60	5.70
16R-1, 139-141	C	63.19	6.69
16R-4, 34-36	A	66.64	6.07
16R-4, 34-36	B	66.64	6.64
16R-4, 34-36	C	66.64	6.53
16R-4, 77-79	C	67.07	6.84
16R-5, 24-26	C	68.04	6.70
18R-3, 29-31	C	71.79	6.87
19R-1, 138-145	A	76.08	6.06
19R-3, 126-133	A	78.96	6.53
19R-5, 126-128	C	80.96	7.14
20R-1, 17-20	A	84.37	6.82
20R-1, 17-20	B	84.37	6.66
20R-1, 17-20	C	84.37	6.82
20R-2, 54-56	C	86.24	7.22
21R-1, 47-50	A	89.67	5.87
21R-1, 47-50	B	89.67	6.44
21R-1, 47-50	C	89.67	6.52
21R-2, 49-51	C	91.19	5.90
22R-2, 41-43	C	95.91	7.14
22R-3, 118-120	C	98.18	7.15
23R-2, 34-36	C	102.34	7.22
23R-3, 33-41	A	103.83	5.68
23R-4, 120-122	C	105.20	6.45
24R-2, 95-97	C	107.95	6.78
24R-3, 50-52	C	109.00	6.69
24R-4, 26-28	C	110.26	6.95

Table 8 (continued).

Core/section interval (cm)	DIR	Depth (mbsf)	Velocity (km/s)
118-735B-25R-2, 5-7	C	112.05	6.61
(Cont.) 25R-3, 42-49	A	113.92	6.11
25R-3, 137-139	C	114.87	7.26
26R-1, 62-64	C	116.12	6.92
26R-3, 64-66	C	119.14	6.91
26R-3, 64-66	B	119.14	6.86
26R-3, 64-66	A	119.14	6.78
27R-1, 84-86	C	122.34	7.21
27R-3, 21-29	A	123.71	6.80
27R-3, 32-34	C	123.82	7.11
28R-1, 22-24	A	126.72	5.61
28R-1, 22-24	B	126.72	6.26
28R-1, 22-24	C	126.72	6.10
28R-2, 12-14	C	128.12	6.96
28R-2, 105-113	A	129.05	6.72
28R-2, 114-116	C	129.14	7.17
29R-2, 46-48	C	133.46	7.16
29R-4, 19-21	C	136.19	6.85
30R-3, 137-139	C	140.87	6.18
30R-4, 14-16	C	141.14	6.80
30R-5, 91-93	C	143.41	6.72
31R-2, 120-122	C	146.20	7.03
31R-4, 118-120	C	148.18	6.56
32R-1, 64-66	C	149.14	6.71
32R-3, 14-16	C	151.64	7.05
33R-1, 93-100	A	154.43	7.11
33R-4, 27-29	C	158.27	6.79
33R-4, 129-131	C	159.29	6.57
34R-1, 103-105	C	159.53	6.64
34R-4, 30-32	C	163.30	6.13
35R-1, 29-31	C	163.79	7.21
35R-2, 11-14	A	165.11	6.75
35R-2, 11-14	B	165.11	6.90
35R-2, 11-14	C	165.11	6.89
35R-5, 131-133	C	170.31	7.15
35R-6, 71-74	A	171.71	6.67
35R-6, 71-74	B	171.71	6.73
35R-6, 71-74	C	171.71	7.05
36R-2, 11-13	C	172.61	7.16
36R-3, 36-38	C	174.36	7.12
37R-1, 11-13	C	176.11	6.86
37R-1, 77-83	A	176.77	6.61
37R-3, 80-82	C	179.80	6.86
38R-2, 15-17	C	182.65	7.03
39R-1, 138-141	A	187.38	7.10
39R-1, 138-141	B	187.38	7.25
39R-1, 138-141	A	187.38	7.09
39R-1, 145-147	C	187.45	6.99
39R-3, 21-23	C	189.21	6.11
40R-2, 62-64	C	193.12	6.08
40R-5, 13-15	C	197.13	6.86
41R-4, 68-70	C	201.18	6.90
42R-2, 119-122	C	203.69	7.00
42R-2, 123-130	A	203.73	6.96
42R-4, 62-65	C	206.12	6.90
43R-1, 126-128	C	207.26	6.75
43R-4, 58-61	A	211.08	6.96
43R-4, 58-61	B	211.08	6.90
43R-4, 58-61	C	211.08	7.01
43R-4, 64-66	C	211.14	6.92
44R-2, 131-133	C	213.81	6.71
44R-4, 102-110	A	216.52	6.74
45R-2, 15-17	C	217.65	7.16
46R-1, 14-17	A	221.14	7.04
46R-1, 14-17	B	221.14	6.94
46R-1, 14-17	C	221.14	6.99
46R-2, 21-23	C	222.71	6.90
46R-2, 120-123	A	223.70	6.42
46R-2, 120-123	B	223.70	6.76
46R-2, 120-123	C	223.70	6.77
46R-2, 128-130	C	223.78	6.67
47R-1, 34-41	A	226.34	6.19

Table 8 (continued).

Core/section interval (cm)	DIR	Depth (mbsf)	Velocity (km/s)
118-735B-47R-3, 50-52	C	229.50	7.01
(Cont.) 48R-4, 82-84	C	235.32	6.64
49R-1, 53-61	A	236.53	6.23
49R-2, 89-91	C	238.39	6.81
50R-4, 87-89	C	243.37	6.62
51R-1, 52-60	A	243.52	6.29
51R-1, 102-104	C	244.02	6.62
52R-4, 69-71	C	253.19	6.82
53R-2, 15-17	C	254.65	6.74
53R-2, 79-82	A	255.29	6.47
53R-2, 79-82	B	255.29	6.56
53R-2, 79-82	C	255.29	6.68
53R-3, 107-110	A	257.07	6.23
53R-3, 107-110	B	257.07	6.49
53R-3, 107-110	C	257.07	6.39
54R-3, 125-127	C	262.25	6.75
55R-2, 45-55	A	266.95	6.19
55R-3, 130-133	C	270.30	6.77
56R-2, 11-14	C	271.61	6.62
56R-2, 22-25	B	271.72	6.76
56R-2, 22-25	C	271.72	6.75
56R-2, 144-146	C	272.94	6.34
57R-2, 135-137	C	277.85	6.90
57R-3, 23-30	A	278.23	6.65
58R-2, 33-35	C	282.33	6.95
59R-3, 70-72	C	289.20	6.91
59R-3, 126-134	A	289.76	6.39
60R-1, 18-20	C	290.68	7.10
61R-1, 81-83	C	296.31	7.10
62R-3, 104-106	C	304.54	7.03
62R-4, 32-39	A	305.32	6.62
63R-3, 80-82	C	308.80	7.02
63R-6, 28-30	C	312.78	6.99
64R-1, 18-24	A	315.18	6.51
64R-2, 54-56	C	317.04	7.06
65R-2, 67-69	C	322.17	7.07
66R-2, 86-88	C	327.36	6.79
66R-3, 134-138	C	329.34	5.95
67R-3, 79-87	A	333.79	6.76
68R-3, 15-17	C	338.15	6.99
69R-4, 138-140	C	346.88	7.15
70R-1, 105-107	C	347.05	6.13
71R-2, 50-57	A	353.00	6.78
71R-2, 82-84	C	353.32	7.13
72R-2, 90-98	A	358.40	6.86
72R-3, 36-38	C	359.36	7.25
72R-6, 106-108	C	364.56	7.09
73R-3, 73-75	C	369.23	7.17
73R-5, 120-126	A	372.70	5.55
74R-6, 41-43	C	382.91	6.47
75R-3, 48-50	C	387.98	7.15
75R-5, 31-38	A	390.81	7.01
75R-6, 75-77	C	392.75	7.20
76R-3, 50-52	C	397.50	6.87
76R-6, 21-28	A	401.71	6.83
77R-2, 91-100	A	405.91	6.52
77R-3, 52-55	A	407.05	6.49
77R-3, 52-55	B	407.05	6.83
77R-3, 52-55	C	407.05	6.83
77R-4, 70-72	C	408.70	6.91
78R-4, 65-67	C	414.65	7.22
79R-2, 64-67	C	416.64	6.97
79R-7, 99-102	C	423.49	7.27
80R-1, 131-133	C	425.31	6.74
80R-7, 23-25	C	432.23	6.79
81R-2, 54-56	C	435.54	7.09
81R-3, 142-150	A	437.92	6.61
81R-7, 64-66	C	442.14	7.17
82R-2, 13-15	C	444.63	7.07
82R-6, 11-13	C	450.61	6.72
83R-4, 95-97	C	457.95	7.09
83R-7, 104-106	C	461.54	6.94
84R-2, 67-69	C	464.17	5.73
84R-3, 14-16	C	465.14	7.06
85R-4, 9-11	C	476.09	6.34
85R-5, 15-17	A	477.65	5.99

Table 8 (continued).

Core/section interval (cm)	DIR	Depth (mbsf)	Velocity (km/s)
118-735B-85R-5, 15-17	B	477.65	6.56
(Cont.) 85R-5, 15-17	C	477.65	6.53
85R-7, 17-19	C	479.67	6.85
86R-4, 24-34	A	485.74	6.60
86R-6, 143-145	C	489.93	6.60
87R-5, 15-17	A	496.65	5.99
87R-5, 15-17	B	496.65	6.56
87R-5, 15-17	C	496.65	6.53
87R-5, 20-23	C	496.70	6.34

DIR = propagation and vibration directions of P -wave where A = Direction normal to foliation; B = direction parallel to lineation; C = direction perpendicular to lineation and parallel to foliation. Aluminum standard used for calibration purposes at the end of velocity measurements (standard velocity 6295 m/s).

tervals having igneous textures tend to be isotropic (Table 10), whereas metagabbros having porphyroclastic or mylonitic textures can transmit P waves as much as 11.4% faster in the lineation direction, compared to that perpendicular to foliation. Both plagioclase feldspar and clinopyroxene display marked V_p anisotropy ($V_p(\max)/V_p(\min) = 1.26$ and 1.23 , respectively; Christensen, 1982), and thus a relatively modest preferred orientation can lead to significant velocity anisotropy. Evidently, magmatic processes do not produce significant preferred orientations. This interpretation may be tested using universal-stage techniques.

Velocities in the metagabbro tectonites of Hole 735B are very directional and have an average velocity of 6.3 km/s and anisotropy ranging from 1.8% to 11.4%. Velocity is always slowest perpendicular to foliation and generally fastest in the direction of lineation. This anisotropy probably stems from the mineral-orienting mechanisms that operate during *in-situ* inelastic deformation. Preliminary inspection of thin sections of some of the tectonite samples confirms the presence of plagioclase and clinopyroxene having preferred orientations. Some of the porphyroclastic metagabbros are banded and have elongated pyroxene porphyroclasts enclosed in a matrix of fine granular plagioclase feldspar. Such banding can also cause velocity anisotropy (see review by Crampin, 1981). Those sources of velocity anisotropy should be investigated during future work using these samples.

A number of altered rocks have velocities that are significantly lower than those expected for plagioclase feldspar plus clinopyroxene \pm olivine \pm oxide assemblages. Nearly all of these are altered gabbroic rocks or vein fillings having high porosities (Fig. 63). A few rocks have a high proportion of phyllosilicates, which should lower their velocities. Most of the low V_p rocks have high porosities, presumably because of networks of interconnected microfractures. Porosity markedly lowers V_p in rocks (Christensen, 1982), which appears to be the principal reason why some of the rocks from Hole 735B have low V_p . This hypothesis can be tested by measuring velocity at pressure, which closes up fracture porosity and raises V_p to values nearer the component mineral grain velocities.

One of our objectives was to compare the compressional-wave velocities in the core with the sonic and vertical seismic profile (VSP) logs in the borehole. Figure 64 is a plot of V_p vs. depth for Hole 735B, based on our measurements. This portrayal of V_p with depth is presently inadequate for a number of reasons. First, even though the sampling density was unprece-

Table 9. Index properties of the crystalline rocks recovered from Site 735.

Core/section interval (cm)	Bulk density (Mg/m ³)	Porosity (%)	Water content (%)	Grain density (Mg/m ³)	Void ratio	Dry-bulk density (Mg/m ³)
118-735B-1D-1, 19-21	2.938	2.9	1.0	2.940	0.03	2.909
1D-1, 141-143	2.945	1.5	0.5	2.920	0.02	2.930
2D-1, 113-115	3.103	4.1	1.4	3.102	0.04	3.061
2D-1, 139-141	2.924	2.0	0.7	2.918	0.02	2.904
2D-2, 99-101	2.947	1.2	0.4	2.920	0.01	2.934
4D-2, 7-9	2.876	1.2	0.4	2.876	0.01	2.864
6D-1, 111-113	2.900	0.9	0.3	2.891	0.01	2.890
7D-1, 74-76	2.961	0.4	0.1	2.956	0.00	2.957
7D-2, 9-11	3.001	0.2	0.1	3.017	0.00	2.998
8D-1, 45-48	2.891	0.7	0.3	2.884	0.01	2.883
9D-1, 120-122	2.969	0.9	0.3	2.971	0.01	2.960
10D-1, 24-26	3.019	0.4	0.1	3.035	0.00	3.015
11D-1, 6-8	3.173	0.7	0.2	3.195	0.01	3.166
12R-2, 36-38	2.959	0.6	0.2	2.954	0.01	2.952
12R-3, 8-10	2.905	0.2	0.1	2.886	0.00	2.903
12R-3, 83-85	2.996	0.3	0.1	2.973	0.00	2.993
13R-1, 102-105	2.966	0.1	0.1	2.959	0.00	2.965
13R-2, 55-58	2.889	0.2	0.1	2.897	0.00	2.887
14R-1, 35-38	3.010	0.5	0.2	3.024	0.00	3.005
14R-2, 22-25	3.027	-0.2	-0.1	3.007	0.00	3.029
14R-4, 22-25	2.956	0.2	0.1	2.991	0.00	2.954
15R-2, 128-130	2.878	0.4	0.1	2.856	0.00	2.873
16R-1, 139-141	2.920	0.8	0.3	2.911	0.01	2.912
16R-4, 77-79	2.926	1.0	0.4	2.929	0.01	2.916
16R-5, 24-26	2.922	0.0	0.0	2.916	0.00	2.921
18R-3, 29-31	2.927	0.3	0.1	2.925	0.00	2.924
19R-5, 126-128	2.859	-0.1	0.0	2.866	0.00	2.860
20R-2, 54-56	2.949	0.3	0.1	2.950	0.00	2.946
21R-2, 49-51	2.821	4.5	1.6	2.809	0.05	2.775
22R-2, 41-43	2.953	0.4	0.2	2.943	0.00	2.948
22R-3, 118-120	2.912	0.7	0.2	2.910	0.01	2.905
23R-2, 34-36	2.945	0.5	0.2	2.937	0.00	2.940
23R-4, 120-122	2.955	1.7	0.6	2.930	0.02	2.938
24R-2, 95-97	3.350	1.0	0.3	3.392	0.01	3.339
24R-3, 50-52	3.132	1.1	0.3	3.110	0.01	3.121
24R-4, 26-28	2.975	0.7	0.2	2.991	0.01	2.968
25R-2, 5-7	2.928	1.6	0.6	2.920	0.02	2.912
25R-3, 137-139	2.967	0.0	0.0	2.964	0.00	2.967
26R-1, 62-64	2.925	0.2	0.1	2.928	0.00	2.923
27R-1, 84-86	3.005	0.6	0.2	3.009	0.01	3.000
27R-3, 32-34	2.893	0.4	0.2	2.894	0.00	2.889
28R-2, 12-14	3.033	0.6	0.2	3.013	0.01	3.026
28R-2, 114-116	2.974	0.5	0.2	2.986	0.00	2.970
29R-2, 46-48	2.952	0.3	0.1	2.945	0.00	2.948
29R-4, 19-21	2.928	1.0	0.3	2.919	0.01	2.918
30R-3, 137-139	3.271	2.3	0.7	3.274	0.02	3.247
30R-4, 14-16	2.876	0.5	0.2	2.882	0.01	2.871
30R-5, 91-93	2.917	0.4	0.2	2.879	0.00	2.912
31R-2, 120-122	2.942	0.4	0.2	2.930	0.00	2.937
31R-4, 118-120	2.890	2.4	0.8	2.872	0.02	2.866
32R-1, 64-66	4.083	0.9	0.2	4.061	0.01	4.074
32R-3, 14-16	2.894	0.4	0.2	2.903	0.00	2.889
33R-4, 27-29	2.870	0.5	0.2	2.866	0.00	2.865
33R-4, 129-131	2.930	0.3	0.1	2.897	0.00	2.927
34R-1, 103-105	2.969	0.2	0.1	2.963	0.00	2.967
34R-4, 30-32	2.991	2.4	0.8	3.018	0.02	2.966
35R-1, 29-31	2.972	0.1	0.0	2.949	0.00	2.971
35R-5, 131-133	2.989	0.0	0.0	2.979	0.00	2.989
36R-2, 11-13	2.913	0.1	0.0	2.907	0.00	2.912
36R-3, 36-38	2.935	0.4	0.1	2.937	0.00	2.930
37R-1, 11-13	2.927	0.6	0.2	2.931	0.01	2.921
37R-3, 82-84	3.065	0.9	0.3	3.041	0.01	3.055
38R-2, 15-17	2.962	0.6	0.2	2.952	0.01	2.956
38R-4, 28-30	2.981	0.4	0.1	3.087	0.00	2.977
39R-1, 145-147	2.958	0.5	0.2	2.968	0.00	2.953
39R-3, 21-23	2.871	2.1	0.8	2.819	0.02	2.849
40R-2, 62-64	2.895	2.4	0.9	2.881	0.03	2.870

dented for a 0.5-km hard-rock hole (averaging 1 sample every 3-5 m), the rich variation of lithologies with depth makes this sampling inadequate. The clear relationships between mineralogy and porosity on one side and velocity and density on the other, as described above, will allow us eventually to construct a synthetic velocity profile when the detailed lithologic log is finished. A second limitation is that the pressure increases to ap-

proximately 22 MPa at the bottom of the hole, including the pressure of the water column. This will increase V_p for the lower porosity rocks by closing porosity, especially fracture porosity. This will be corrected during shore-based studies by measuring V_p at elevated pressure. Third, our samples are a maximum 70 mm long and do not contain macroscopic fractures. Large-scale *in-situ* fractures may substantially lower *in-situ* V_p . Com-

Table 9 (continued).

Core/section interval (cm)	Bulk density (Mg/m ³)	Porosity (%)	Water content (%)	Grain density (Mg/m ³)	Void ratio	Dry-bulk density (Mg/m ³)
118-735B-40R-5, 13-15	2.915	0.6	0.2	2.928	0.01	2.909
(Cont.) 41R-4, 68-70	2.930	0.5	0.2	2.919	0.00	2.925
42R-2, 119-122	2.930	0.5	0.2	2.946	0.01	2.925
42R-4, 62-65	2.947	0.6	0.2	2.923	0.01	2.940
43R-1, 126-128	2.981	0.4	0.1	2.983	0.00	2.977
43R-4, 64-66	3.033	1.0	0.3	3.024	0.01	3.023
44R-2, 131-133	2.978	1.2	0.4	2.948	0.01	2.965
45R-2, 15-17	2.942	0.8	0.3	2.925	0.01	2.934
46R-2, 21-23	2.996	0.9	0.3	2.987	0.01	2.986
46R-2, 128-130	2.952	1.4	0.5	2.921	0.01	2.938
47R-3, 50-52	2.998	0.5	0.2	3.004	0.01	2.993
48R-4, 82-84	3.255	0.8	0.3	3.265	0.01	3.247
49R-2, 89-91	3.298	0.4	0.1	3.272	0.00	3.294
50R-4, 87-89	2.957	0.7	0.3	2.931	0.01	2.949
51R-1, 102-104	3.083	0.7	0.2	3.058	0.01	3.075
52R-4, 69-71	3.164	0.6	0.2	3.168	0.01	3.159
53R-3, 15-17	3.144	0.7	0.2	3.139	0.01	3.136
54R-3, 125-127	3.283	0.6	0.2	3.288	0.01	3.277
54R-5, 117-119	3.171	0.5	0.1	3.179	0.00	3.166
55R-3, 130-133	3.257	0.2	0.1	3.240	0.00	3.254
56R-1, 11-14	3.155	0.1	0.0	3.150	0.00	3.154
56R-2, 144-146	3.189	0.8	0.3	3.169	0.01	3.181
57R-2, 135-138	2.921	0.3	0.1	2.900	0.00	2.918
58R-2, 33-35	2.864	0.1	0.0	2.841	0.00	2.862
59R-3, 70-72	3.013	0.2	0.1	3.014	0.00	3.011
60R-1, 18-20	2.990	0.2	0.1	2.986	0.00	2.988
61R-1, 81-83	2.990	0.2	0.1	2.974	0.00	2.988
62R-3, 104-106	3.000	0.2	0.1	3.013	0.00	2.998
63R-3, 80-82	2.925	0.4	0.1	2.897	0.00	2.921
63R-6, 28-30	2.930	0.3	0.1	2.917	0.00	2.927
64R-2, 54-56	3.017	0.3	0.1	3.010	0.00	3.013
65R-2, 67-69	3.022	0.6	0.2	2.960	0.01	3.016
66R-2, 86-88	2.923	0.9	0.3	2.981	0.01	2.914
66R-3, 134-138	2.931	4.9	1.7	2.961	0.05	2.882
68R-3, 15-17	2.937	0.3	0.1	2.936	0.00	2.934
69R-4, 138-140	2.985	0.2	0.1	2.970	0.00	2.983
70R-1, 105-107	2.776	2.4	0.9	2.765	0.02	2.752
71R-2, 82-84	2.929	0.1	0.0	2.936	0.00	2.928
72R-3, 36-38	2.987	0.1	0.0	2.997	0.00	2.986
72R-6, 106-108	2.968	0.2	0.1	2.981	0.00	2.966
73R-3, 73-75	3.021	0.1	0.0	3.021	0.00	3.021
74R-6, 41-43	3.054	0.4	0.1	2.927	0.00	3.050
75R-3, 48-50	2.995	0.3	0.1	2.994	0.00	2.992
75R-6, 75-77	2.948	0.1	0.0	2.937	0.00	2.947
76R-3, 50-52	2.988	0.6	0.2	2.981	0.01	2.982
77R-4, 70-72	2.990	0.3	0.1	2.999	0.00	2.987
78R-4, 65-67	3.004	0.2	0.1	2.962	0.00	3.002
79R-2, 64-67	3.108	0.2	0.1	3.106	0.00	3.106
79R-7, 99-102	2.932	0.2	0.1	2.937	0.00	2.930
80R-1, 131-133	3.046	0.4	0.1	3.049	0.00	3.042
80R-7, 23-25	3.222	0.3	0.1	3.213	0.00	3.220
81R-2, 54-56	2.959	0.2	0.1	2.960	0.00	2.957
81R-7, 64-66	2.971	0.2	0.1	2.978	0.00	2.970
82R-2, 13-15	2.906	0.1	0.0	2.905	0.00	2.905
82R-6, 11-13	3.201	0.5	0.2	3.193	0.00	3.196
83R-4, 95-97	2.995	0.2	0.1	2.981	0.00	2.993
83R-7, 104-106	3.121	0.4	0.1	3.103	0.00	3.117
84R-2, 67-69	2.816	1.6	0.6	2.818	0.02	2.800
84R-3, 14-16	2.963	0.1	0.0	2.947	0.00	2.963
85R-4, 9-11	2.929	0.6	0.2	2.932	0.01	2.922
85R-7, 17-19	2.864	0.0	0.0	2.879	0.00	2.864
86R-6, 143-145	2.917	0.5	0.2	2.917	0.01	2.911
87R-5, 20-22	3.148	1.2	0.4	3.124	0.01	3.135

Bulk density = wet weight/wet volume, grain density = dry weight/dry volume, void ratio = pore space/volume sample (including salt content), dry bulk density = dry weight/wet volume.

parison of the velocity logs with our core-based profile should help guide us concerning the distribution and widths of open fractures around the borehole (see also "Borehole Televiewer" section, this chapter). Many of the fractures observed in the core were filled, typically with amphiboles. As indicated in the section above, amphiboles have high velocities, and such frac-

ture filling probably will diminish the effect of fractures for reducing V_p .

Despite the above limitations of the raw velocity profile of Figure 64, some gross features stand out. First, the rapid increase in velocities from the seafloor to about 40 mbsf correlates well with the greater degree of alteration and higher fracture po-

Table 10. Directional compressional-wave velocities measured using cube samples.

Core/section interval (cm)	Velocity ¹ (km/s)			Anisot. ² index, %	Rock type
	A	B	C		
118-735B-2D-1, 142-145	6.29	6.76	6.69	7.5	Mylonitic metagabbro
12R-2, 32-34	6.58	6.70	6.24	1.8	Porphyroclastic metagabbro
13R-1, 91-94	6.86	6.94	6.94	1.2	Foliated gabbro
13R-2, 109-112	6.47	6.34	6.62	0.0	Foliated gabbro
16R-4, 34-36	6.06	6.64	6.53	9.6	Mylonitic metagabbro
20R-1, 17-20	6.81	6.66	6.82	-2.2	Foliated olivine gabbro
21R-1, 47-50	5.87	6.64	6.52	9.7	Foliated metagabbro
26R-3, 64-66	6.91	6.86	6.78	-0.7	Foliated olivine gabbro
28R-1, 22-24	5.61	6.26	6.09	11.4	Mylonitic metagabbro
35R-2, 11-14	6.75	6.90	6.89	2.2	Porphyroclastic oliv. gabbro
35R-6, 7-74	6.67	6.73	7.05	0.9	Porphyroclastic metagabbro
39R-1, 138-141	7.10	7.25	7.09	2.1	Foliated gabbro
43R-4, 58-61	6.96	6.90	7.01	-0.9	Foliated olivine gabbro
46R-1, 14-17	7.04	6.93	6.99	-1.6	Foliated gabbro
46R-2, 120-123	6.42	6.76	6.77	5.3	Porphyroclastic metagabbro
53R-2, 79-82	6.47	6.56	6.78	1.4	Foliated oxide gabbro
53R-3, 107-110	6.23	6.49	6.39	4.2	Foliated oxide gabbro
56R-2, 22-25	6.56	6.76	6.75	3.0	Mylonitic oxide metagabbro
77R-3, 52-55	6.49	6.83	6.83	5.2	Mylonitic metagabbro
85R-5, 15-17	5.99	6.55	6.53	9.3	Mylonitic metagabbro

¹ A = direction normal to foliation; B = direction parallel to lineation; C = direction perpendicular to lineation and parallel to foliation.
² Anisotropy index = $(V_A - V_B)/V_A$.

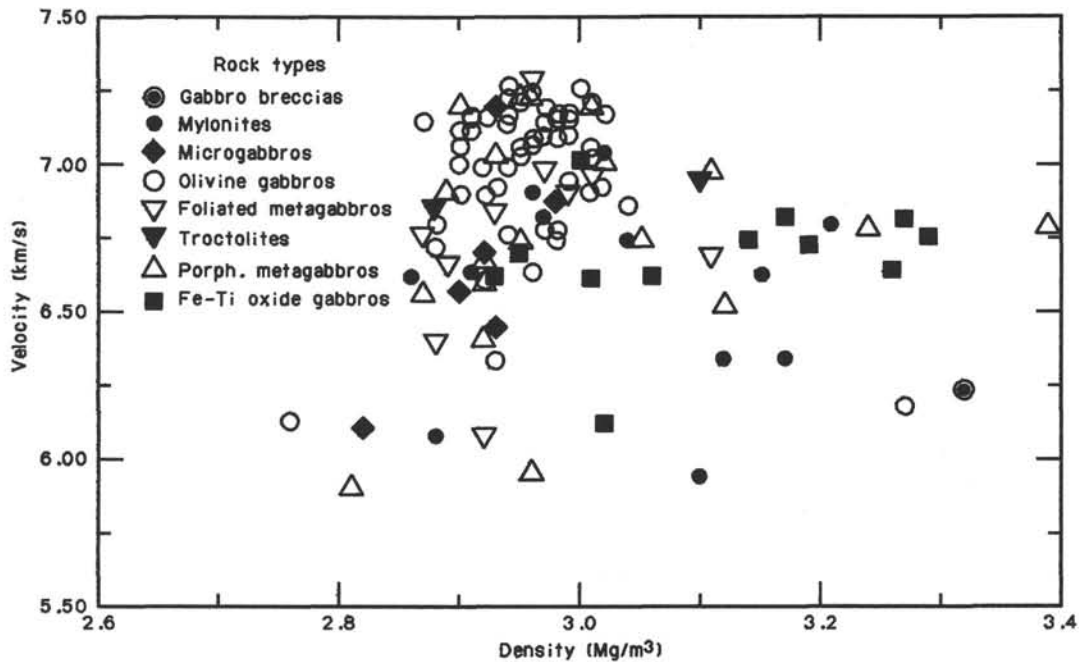


Figure 62. Velocity-density relationships for the rocks of Hole 735B, coded according to rock type. Nominally fresh rocks. Note the clustering of data at $V_p = 7.0$ km/s and density = 2.95 Mg/m^3 for olivine gabbros and metagabbros, which is consistent with the mineral proportions and properties.

rosities in the rocks of lithologic Unit I, and with the lower apparent V_p evident from the traveltime curves in the VSP study (see “Vertical Seismic Profiling” section, this chapter). Second, the oxide-rich gabbros and metagabbros of lithologic Unit IV (see “Lithostratigraphy” section, this chapter) clearly produce a dip in velocity and a sharp increase in density (Table 9). This lithologic unit also correlates well with a marked increase in the NRM (see “Paleomagnetism” section, this chapter) and reduction in electrical resistivity (see “Schlumberger Logs” section, this chapter). Third, the velocities indicated in Figure 64 include 34 measurements of V_p along the original vertical direction in

half-core samples, averaging 6.5 km/s compared with 7.0 km/s for measurements having horizontal propagation directions. The VSP experiments indicate that the hole-averaged vertical $V_p = 6.55 \pm 0.15$ km/s, which corresponds well with the hole-averaged vertical V_p measurements cited above. Inversions of marine seismic-refraction traveltime data indicate that V_p for layer 3 is 6.8 ± 0.2 km/s for near-horizontal propagation directions (Fox and Stroup, 1981), which compares well with our hole-averaged horizontal V_p measurements from core samples. This vertical vs. horizontal V_p anisotropy is significant and parallels *in-situ* VSP and seismic-refraction observations. Other fine struc-

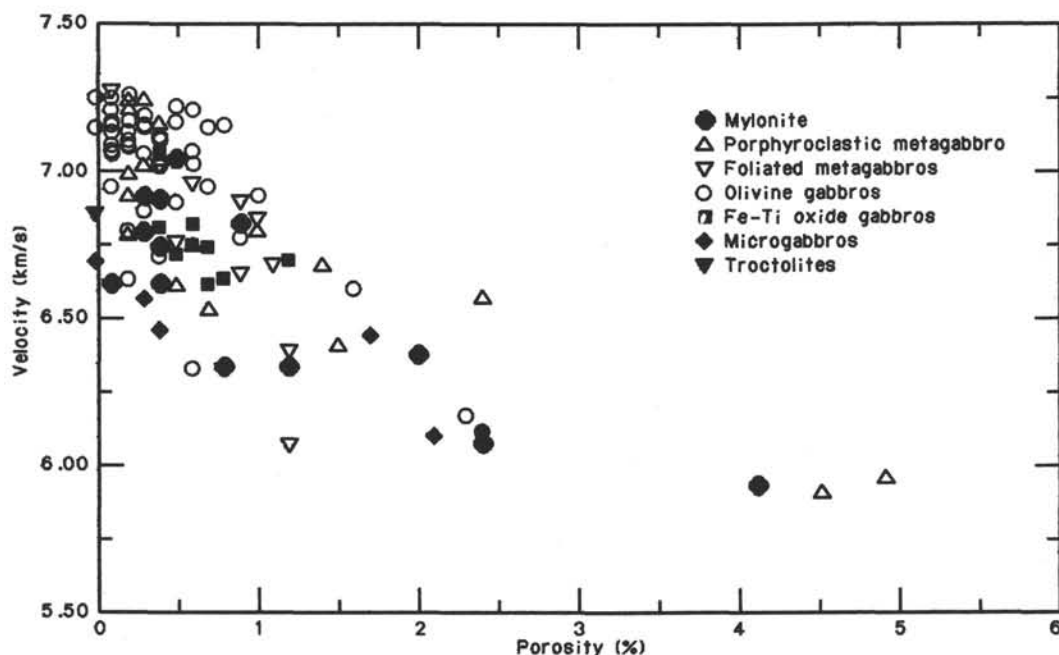


Figure 63. Velocity vs. porosity, using the same rock-type symbols as in Figure 62. Note the systematically lower V_p values for the higher-porosity rocks of a given rock type.

ture of the data may emerge when combined with the lithostratigraphic log to produce velocity and density logs.

The observed V_p anisotropy of oriented cubes cut from the core has interesting implications concerning remote sensing of fault zones in the lower oceanic crust using seismic-reflection techniques. Although the sheared rocks represent a minority (25%) of those recovered from Hole 735B, they might still be detected by modern seismic-refraction techniques. Azimuthal variation in V_p in the oceanic crust may originate from foliation development in the lower crust, rather than that caused by fracturing in the upper crustal basalts (see references in the review by Kirby and Kronenberg, 1987). The marked V_p anisotropy among the mylonitic metagabbros (averaging 8%) might also be detected from reflections of elastic waves at the mylonite-host rock boundaries, which are often very sharply defined. Maximum elastic impedance should obtain for normal-incidence P waves. The full elastic wave energy partitioning between incident, reflected, and refracted waves in an anisotropic setting should be investigated from this standpoint.

These results have important implications about the nature of the Moho discontinuity in the deep ocean basins. It has been suggested that the uppermost mantle might be extensively serpentinized. If the rocks recovered from Hole 735B are typical of the lower oceanic crust, then the low V_p of serpentine (6.3 km/s) implies that no more than 30% serpentinization might be present for a significant discontinuity (say, 0.4 km/s) to occur between gabbroic rocks of the lower crust and partially serpentinized peridotite of the uppermost mantle.

THERMAL CONDUCTIVITY

Introduction

Core samples from Hole 735B were measured nondestructively for thermal conductivity in the shipboard laboratory. Measurements were performed for about 5 to 6 min with a heated needle probe sandwiched between the sample and a slab of low-conducting material (Vacquier, 1985). This method is most convenient for hard-rock cores, which are cut in the form of a half-round cylinder as this shape is easily adapted for the apparatus.

The theory of the method closely approximates the heating of a line source in a plane separating half-spaces of the sample material and a thermal insulator, which in turn is a relatively straightforward extension of the heating of a uniform complete-space method by a line source (Jaeger, 1956; Von Herzen and Maxwell, 1959). If the substrate on which the sample is placed were a perfect thermal insulator, the rise in temperature with time at the needle probe would be exactly twice that experienced by the probe in an infinite medium having the same thermal conductivity as the sample. In practice, the low-conducting substrate absorbs a fraction of the heat during measurement, which depends on the ratio of sample to substrate conductivity. For most of the rock samples measured at this site, this ratio is large enough (>15–20) for the adjustment from the simple theory to require a relatively small correction. This correction is determined by careful measurements using materials of known conductivity that have values near those measured for the samples.

Measuring rock thermal conductivities using this technique was sporadic during previous ODP legs. Measurements for nine basalt samples were reported from Leg 109, Site 648, as well as some from Leg 111, Site 504 (K. Becker, pers. comm., 1987). These studies indicated that the multiplication factors for converting the conductivity value calculated from the full-space theory to the actual value represented by the samples ranged from about 2.1 to 2.7, apparently depending on the time period used after beginning the transient experiment. These factors were obtained by comparing values for standard materials determined over the same time periods in the same apparatus. The following discussion presents some reasons why such unexpectedly large and variable correction factors were determined, and some suggestions for improving the measurements.

Measuring Techniques

Calibration Standards

To improve the accuracy of the data obtained, two new calibration standards were used for Leg 118. One is a plate of fused silica glass, about 10.3 cm square by 2.5 cm thick, with uniform and well-established conductivity (1.38 W/m/K; Clark, 1966).

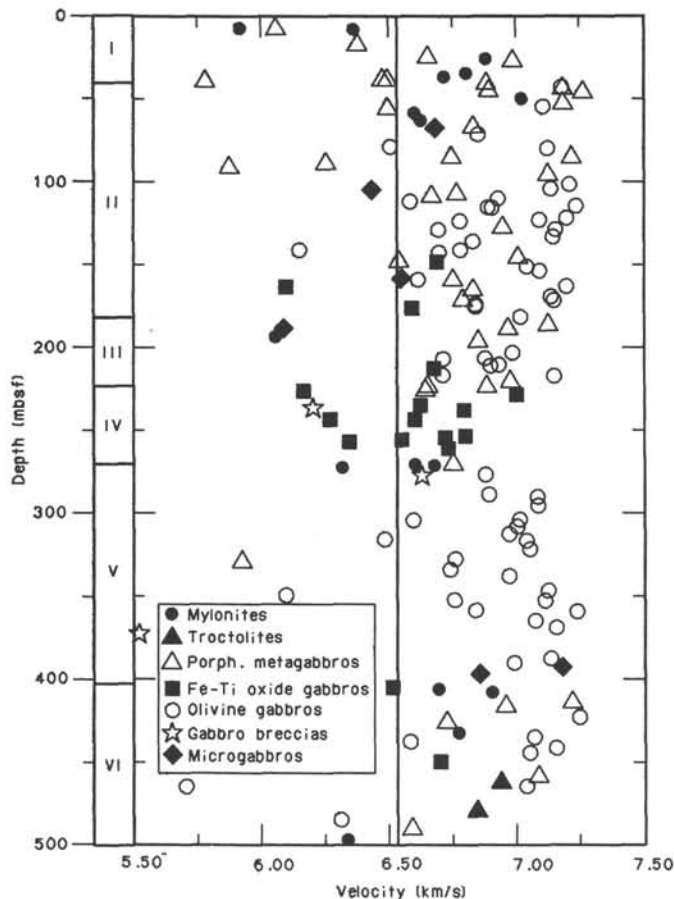


Figure 64. Velocity-depth data for Hole 735B, using the same symbols as in Figure 62. The lower velocities of the shallow rocks reflect their generally higher porosities and locally higher proportion of low-grade alteration minerals. The lower velocities associated with the oxide-rich gabbros at about 250 mbsf are also evident. Also shown lines are the boundaries of the lithologic units described in the "Lithostratigraphy" section (this chapter). The vertical line indicates the average V_p determined from the VSP experiments ("Vertical Seismic Profiling" section, this chapter).

This plate was used in place of the thin (0.6-cm-thick) plate available previously, which gave confusing results during previous legs for any measurements lasting more than 1 to 2 min (see below). The other new standard is a slab of synthetic material designated as "Macor," having a conductivity reported as 1.68 W/m/K by the manufacturer, which is near those values expected for igneous rocks of the oceanic crust. This material was obtained in the form of a short cylinder about 10.3 cm in diameter by 8 cm long, which was cut in half along the axis to give it the same shape (although somewhat larger) as the half-round core sample sections.

Calibration Tests

Before and while measuring the samples obtained from this hole, several measurements were performed using both of the above calibration standards. These measurements were run over a transient needle-probe heating duration of 6 min to determine the best period during which data should be obtained. Almost all the measurements produced the same heating pattern: an initially steep slope of temperature vs. \ln time over the first 60 to 90 s, gradually decreasing to a more uniform slope, sometimes trailing off to a slightly reduced slope over the last minute (Fig.

65). Most measurements of core samples from this hole showed the same characteristics. To reduce the effects of any external temperature changes, all calibration runs were conducted when the temperature of the standard in the bath was changing at a rate less than 0.01 °C/min. The data reduction program will remove a linear temperature change, but inaccuracies occur if the change is too rapid or nonlinear.

Measurements from the calibration standards were analyzed for two different time periods of data acquisition: one during the early (30–66 s) period of rapid, quasilinear change of temperature vs. \ln time, and the other during the later (60–90 s to 5–6 min) period with a nearly linear relationship (Fig. 66). Results show that the "F" factors (i.e., the factors necessary to multiply the result to obtain the standard value, assuming that the needle probe was measuring in an infinite medium of the calibration material) are separated into two groups, depending on the time interval of the data. For the early transient period, the "F" factors range widely from about 2.2 to 2.8, significantly greater than expected theoretically (Vacquier, 1985), whereas for the later linear period of the data, the "F" factors cluster around a value of 2.0 (Fig. 66).

These results suggest that more accurate and uniform values would be obtained by using the data during the measuring period from about 1 to 6 min. The more scattered results during the early time period with anomalously high "F" factors may be explained by several effects. Probably, most important is that the needle probe is not mounted exactly symmetrically between the low-conductivity substrate of the experimental apparatus and the sample (or standard); rather, it is flush with the surface of the substrate, so that the initial heating period will be affected more strongly by its low conductivity, which explains the systematically higher slopes and higher "F" factors. The scatter of the early time results may also result from the variability in surface roughness of the sample, or in the amount of grease used to improve thermal contact between the substrate and the sample or calibration standard. For convenience, a relatively low-conducting silicon grease was used; a higher-conductivity grease might alleviate this problem to some extent. However, although use of a higher-conducting grease might reduce some of the scatter in the results, it seems unlikely to eliminate the anomalous systematic differences between the early and late time measurements described above.

Note that the mean "F" factor for the silica glass standard is 1.94, whereas for the Macor standard it is 2.01, using the standard values given above. The former is near that expected (1.95) when using the empirical relationship proposed by Vacquier (1985, Eq. 5), whereas a factor of 2.0 could only be approached (not exceeded) for a large sample-to-substrate conductivity ratio. We surmise that the conductivity of the Macor standard is somewhat lower than the value quoted. Assuming that the average "F" factor for Macor should be about 1.96 because it has significantly higher conductivity than silica glass, we estimate the conductivity of this standard as 1.64 W/m/K.

Results

A total of 56 measurements was performed on 38 rock core samples from Hole 735B (Table 11) using the techniques described above. All data were carefully edited to remove the early nonlinear transient heating, and only the linear portions of the temperature vs. \ln time relationships were used, usually between about 1 and 5 min after initiating the heating. The time period during which data were used varied from a minimum of 30 to 120 s, to a maximum of 4 to 6 min. The variability of this time range between measurements probably indicates differences in the details of placing the sample in the measurement apparatus, with consequent variability in boundary conditions near the

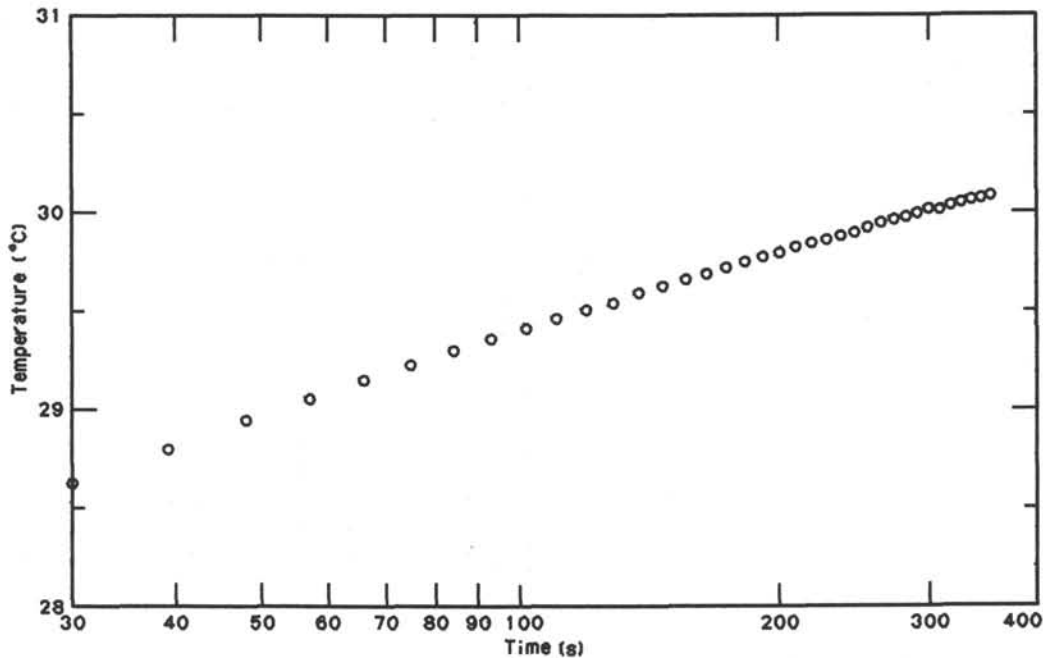


Figure 65. Plot of the data for a typical thermal conductivity measurement of a rock sample using the needle probe and the half-space method. Note that the slope of the temperature vs. \ln time relationship is steeper over the first few data points and tends to a linear relationship after 60 to 90 s.

needle probe. A constant “ F ” factor of 1.97 was used to multiply the value calculated as if a full-space of the sample were being measured to obtain the actual value, based on tests with calibration standards. This value is slightly larger than that determined with the silica glass standard (see above) to account for the systematically higher conductivity of the rock samples. Consistency of the values and results of repeat measurements show that the values have uncertainties on the order of 5%, although no formal error analysis was conducted.

The variability of values between samples is significantly greater than the experimental uncertainty, which reflects real differences in conductivity. Measurements were repeated for about half of the samples with the needle probe aligned in orthogonal directions, usually parallel or perpendicular to the core axis, to determine any anisotropy. In most cases, foliation in the samples is subhorizontal (see “Petrography” section, this chapter), although the needle probe measures a combination of the conductivity in two orthogonal directions as a result of its radial geometry. Most of the samples showed slightly greater conductivity with the needle aligned parallel to the core axis (Fig. 67), although the differences are generally small, of the order of the experimental uncertainty.

Generally, the thermal conductivity values do not indicate any large variation with depth in the hole, although the mineralogy varies throughout the section and probably accounts for much of the variability observed. There may be significantly higher conductivity between depths of about 100 to 240 mbsf (Fig. 67), although we cannot be sure because of the local variability. The somewhat lower conductivity values between 250 and 300 mbsf may correspond to the iron-titanium oxide-rich gabbros found in this depth interval (see “Primary Petrography” section, this chapter). The mean of all the values determined is 2.21 W/m/K, with a standard deviation of 0.22 W/m/K, which is within the variability of the values for gabbro reported by Clark (1966, Tables 21-4 and 21-5).

TEMPERATURE MEASUREMENTS

Introduction

Temperatures were measured in Hole 735B and in the ocean above it with a high-resolution probe provided by the U. S. Geological Survey (USGS). Two runs were conducted that were separated by a time period of 38 hr to obtain data for estimating an equilibrium conductive temperature profile for the borehole (Becker et al., 1983).

Temperature Logging Equipment

The sensor of the USGS probe is a Sostman platinum wire resistance element (type PT-139X) having the following characteristics.

Element length	1.57 cm
Element diameter	0.26 cm
Time constant	2.3 s
Resistance at 0°C	100.020 ohms
Resistance at 100°C	139.229 ohms
Temperature coefficient	0.00392 ohms/ohm/degree ($\pm 0.1\%$ at 0°C)

The sensing element is attached to the bottom of a weighted, high-pressure probe housing, where it is protected by a metal cage that allows the fluid in the borehole to flow over and around it as the probe is lowered or raised in the hole. The probe is 5.3 m long, 6.35 cm in diameter, and weighs approximately 120 kg in air.

Prior to Leg 118, temperature calibration data for the sensor were obtained from the Yellow Springs Instrument Co., Yellow Springs, Ohio. A third-degree polynomial was fitted to the calibration data in the range 0–200°C, with a standard error of 0.004°C. This equation was incorporated in the computer program used to acquire data.

During logging, the resistance of the sensing element was measured in a four-point, current-potential system by an HP-

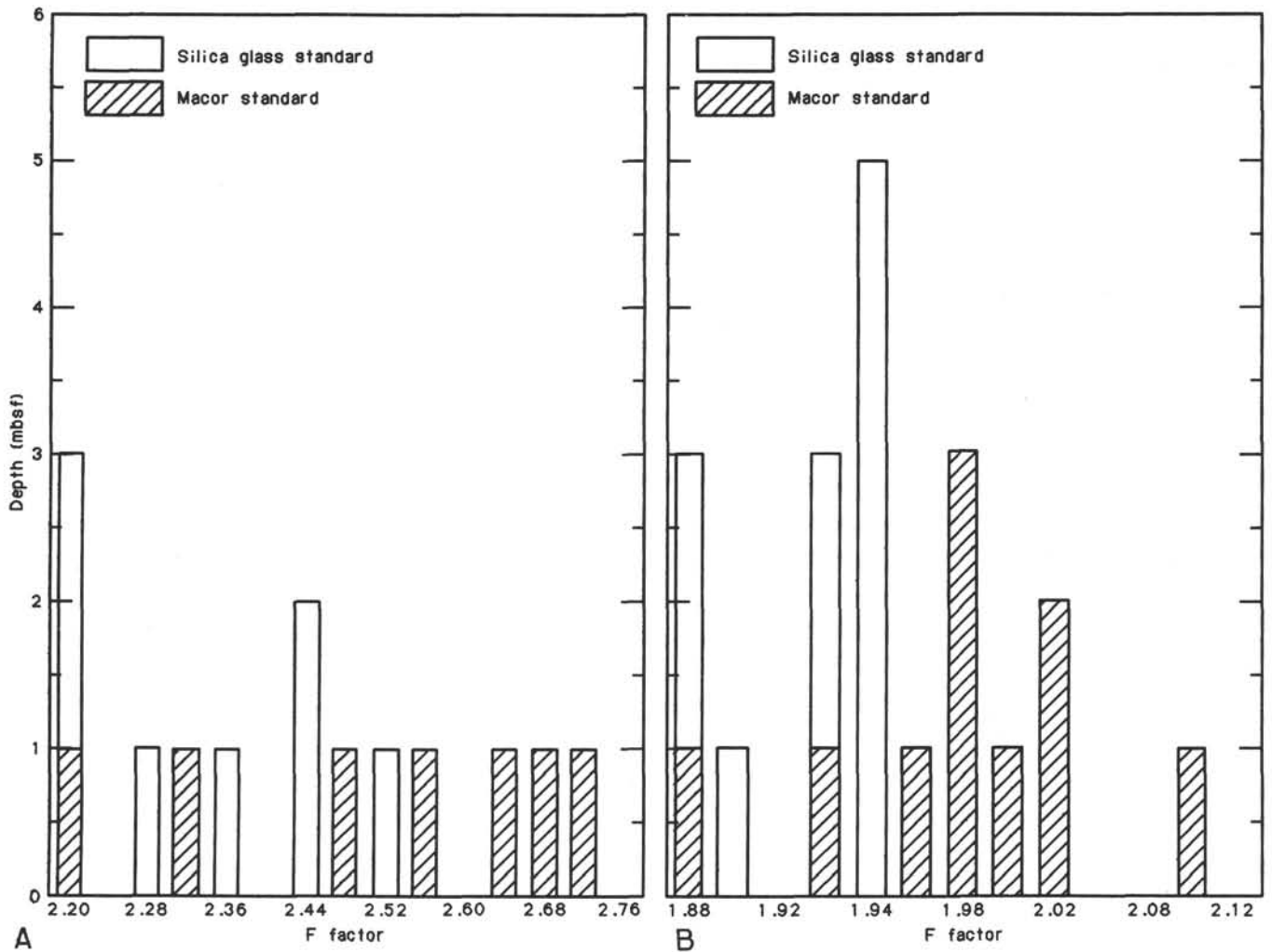


Figure 66. Histograms of the "F" factors (see text) calculated for measurements of thermal conductivity standards over different periods of time after the probe first heats. A. Early data (30 to 66 s). B. Late data (1/1.5 to 5/6 min). Note that the horizontal scale divisions for the early data are twice those of the later data. Values for standards assumed as 1.38 W/m/K for silica glass and 1.68 W/m/K for "Macor."

3455A DVM having a readout resolution of 5.5 digits. The digital resistance readings were transferred to the data acquisition computer (HP-9845B) via an HP-IB interface cable, where they were converted to temperature by the third-degree calibration equation. The depth of the probe was obtained from the depth register of the ship's wireline winch system, which was read continually by the MassComp computer in the Downhole Measurements Laboratory and sent to the HP-9845B computer via an RS-232 cable link. Depths and temperature readings were recorded on digital magnetic tape by an HP-9875A tape deck. A block diagram of the temperature measurement system is shown in Figure 68.

Pre-logging temperature bath tests (0° - 60°C) aboard the *Resolution* indicated that the temperatures measured by the sensor-DVM-computer system were accurate to 0.1°C , and that changes as small as 0.01°C were detectable by the system. When test measurements were conducted using a short cable connecting the probe to the DVM, the system noise was less than 0.01°C . But when measurements were performed through the logging cable, the noise increased to $\pm 0.04^{\circ}\text{C}$.

Logging Data

We started the first logging run at 1330 hr on 6 December 1987, recording temperatures every 0.2 m as we lowered the probe through the pipe to the seafloor at a speed of 12 m/min.

Because the water inside the pipe had not been disturbed significantly since the navidrill was pulled out of the hole at 2400 hr on 4 December, the temperature inside the pipe was nearly in equilibrium with that of the seawater. The temperature profile in this interval showed a normal decrease from about 20°C at the surface of the ocean to 10° at the seafloor (Fig. 69).

As the probe approached the seafloor and entered Hole 735B at 1442 hr, we reduced the logging speed to 7 m/min and held it constant, recording temperatures every 0.2 m to a depth of 1226 mbrf (494.7 mbsf), which allowed a margin of safety of 6 m to the bottom of the hole at 1232 mbrf (500.7 mbsf). After the probe entered the top of the hole, the temperature increased rapidly from 10°C at the seafloor to nearly 13°C at a depth of 770 mbrf (39 mbsf), and then gradually decreased to about 11°C near the bottom of the hole. The temperature profile recorded for Run 1 is shown in Figure 69, together with the computed temperature gradient. The gradient was computed by subtracting the average temperature in the 10-m interval above the plotting depth from the average temperature in the 10-m interval below this depth and then dividing this difference by the 10-m spacing between the centers of the averaged intervals. Thus, the gradient plotted in Figure 69 is based on a 10-m differential temperature with 10-m boxcar smoothing.

A second temperature log was run in Hole 735B about 38 hr after the first run, using the same equipment, techniques, and

Table 11. Summary of thermal conductivity data, Hole 735B.

Core/section	Interval (cm)	Depth (mbsf)	Thermal Conductivity (W/m/K)	
			Parallel ¹	Perpendicular ²
118-735B-12R-1	36-41	39.8	2.30	2.35
12R-1	55-62	40.0	2.19	—
14R-1	20-26	51.4	2.20	—
14R-3	122-130	55.2	2.06	—
16R-1	80-86	62.6	1.94	1.90
19R-1	138-145	76.1	2.15	1.94
19R-3	126-133	79.0	2.07	—
23R-3	33-41	103.8	2.82	2.57
25R-3	42-49	114.0	2.11	2.27
27R-3	21-29	124.8	2.32	2.46
28R-2	105-113	128.1	2.51	2.41
33R-1	93-100	154.5	2.48	2.37
37R-1	77-83	176.8	2.29	2.27
42R-2	123-130	203.8	2.32	2.07
44R-1	102-110	207.1	2.48	2.34
47R-1	34-41	226.4	2.27	2.16
49R-1	53-61	236.6	2.34	2.01
51R-1	52-60	243.6	1.96	1.71
53R-2	81-86	255.3	2.21	2.07
55R-2	45-55	267.0	1.78	1.82
56R-2	76-85	272.3	2.16	2.16
57R-3	23-30	278.3	2.01	—
59R-3	126-134	289.8	2.28	—
62R-4	32-39	305.4	2.24	—
64R-1	18-24	315.2	2.29	—
65R-1	34-43	320.4	2.12	—
67R-3	79-87	333.8	2.22	—
71R-2	50-57	353.0	2.30	—
72R-2	90-98	358.4	2.09	—
75R-5	31-38	390.9	2.55	—
76R-6	21-28	401.7	2.29	—
77R-2	37-46	405.4	2.04	1.92
79R-3	127-136	418.8	2.31	—
80R-7	56-64	433.6	2.10	—
81R-3	142-150	438.0	2.34	—
85R-6	134-145	480.4	2.02	—
86R-4	24-34	485.8	2.63	—
87R-3	72-78	494.2	2.30	—

¹ Conductivity measured with needle probe parallel to core axis.
² Conductivity measured with needle probe perpendicular to core axis.

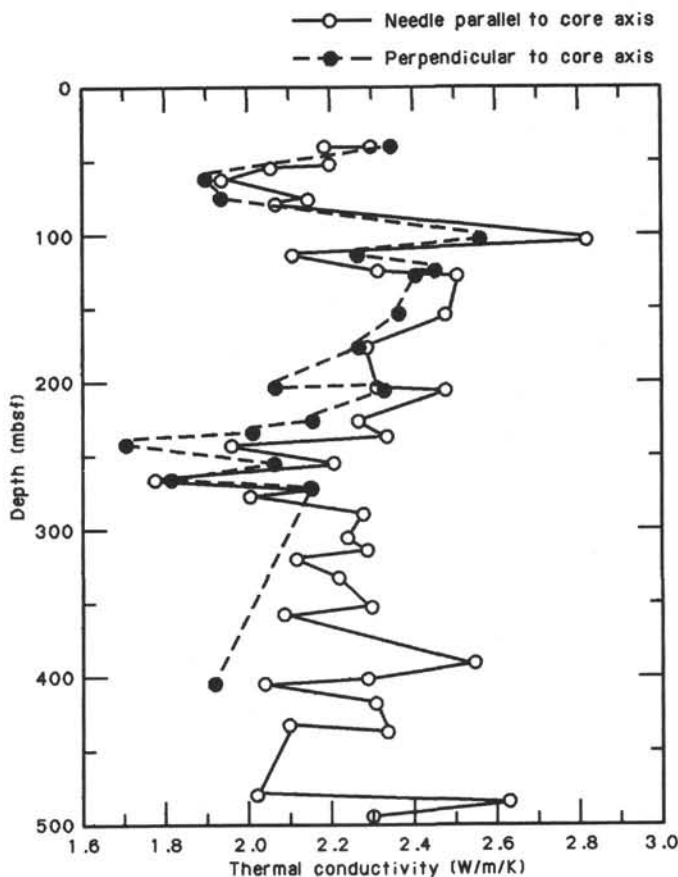


Figure 67. Thermal conductivity vs. depth below seafloor for Hole 735B. Data plotted are those found in Table 11.

logging speeds. The probe entered the hole below the seafloor for Run 2 at 0445 hr on 8 December. Results shown in Figure 70 indicate that most of the hole cooled an average of about 1.5°C during the 38-hr interval between runs, with somewhat greater cooling near the bottom of the hole than at the top. However, the general shape and character of Run 2 closely matches that of Run 1, including two small positive anomalies at depths of approximately 920 mbrf (190 mbsf) and 990 mbrf (260 mbsf). These anomalies may reflect changes in thermal properties or fracturing and hydrology in the vicinity of the mineralized sections of the hole, where concentrations of magnetite and ilmenite occur in the gabbro.

Data from the two temperature runs and the drilling records were used to estimate the equilibrium temperature profile that we expected to find in the borehole when the thermal disturbance from drilling had completely dissipated. The technique, described by Becker et al. (1983), is based on the following equation for calculating the time-decay curve of the temperature disturbance caused by drilling.

$$T = \frac{Q \log}{4\pi K} (1 + t_D/t), \quad (1)$$

where Q = thermal disturbing source (Bullard, 1947),

K = thermal conductivity of crust,
 t_D = time duration of drilling and circulation,
 t = time after drilling and circulation ceased until measurement.

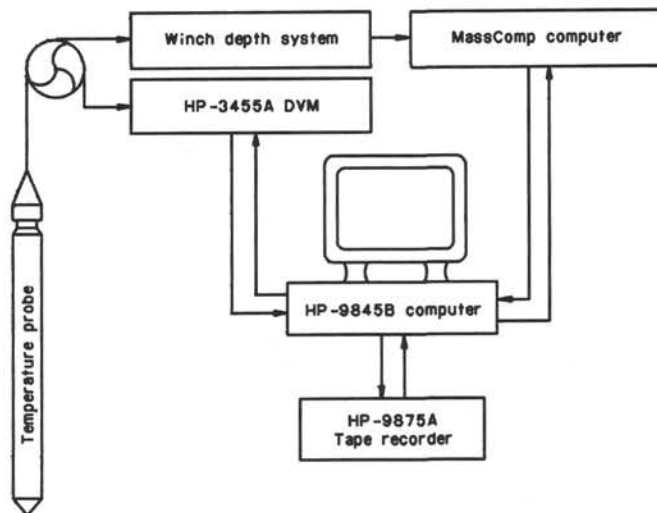


Figure 68. Block diagram of the USGS downhole temperature-measuring system used to log Hole 735B.

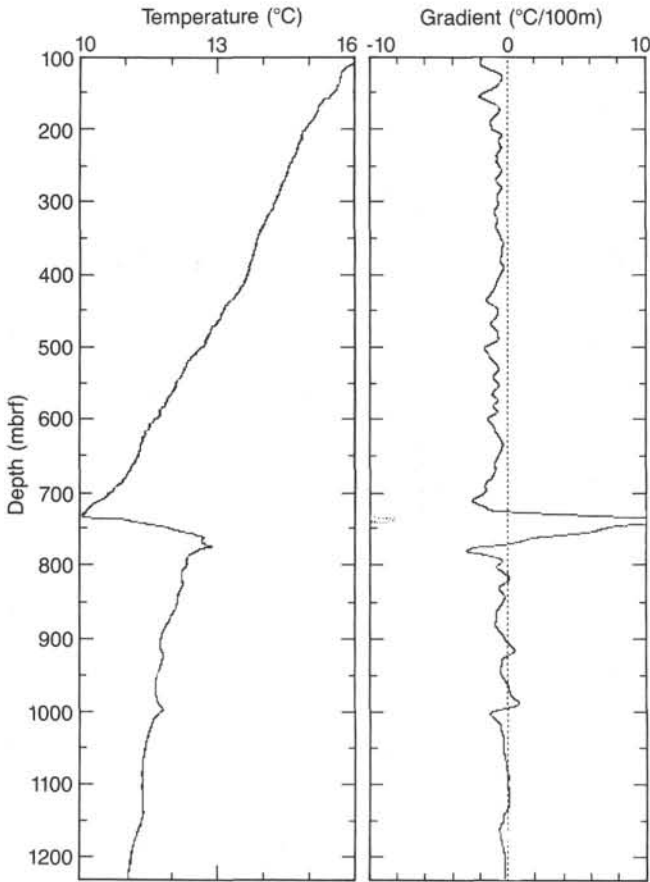


Figure 69. Temperature Run 1, Hole 735B, with observed temperature at 0.2-m vertical intervals and temperature gradient smoothed over 10-m intervals (see text) plotted vs. depth below rig floor (m). Temperature was logged traveling down the hole at 7 m/min. Entry time into the borehole was 1442 hr, 6 December 1987.

If we replace the temperature disturbance, T , in Equation 1 with $T_1(z) - T_e(z)$ for logging Run 1, and $T_2(z) - T_e(z)$ for Run 2, where $T_1(z)$ and $T_2(z)$ are the temperatures measured during the two runs, and $T_e(z)$ is the unknown equilibrium temperature profile of the borehole, we obtain Equations 2 and 3:

$$T_1(z) - T_e(z) = \frac{Q \log}{4\pi K} [1 + t_D(z)/t_1(z)] \quad (2)$$

and

$$T_2(z) - T_e(z) = \frac{Q \log}{4\pi K} [1 + t_D(z)/t_2(z)]. \quad (3)$$

If we then take the ratio of these two equations and solve for $T_e(z)$, the factor $Q/4\pi K$ disappears and we obtain:

$$T_e(z) = \frac{R(z) T_2(z) - T_1(z)}{R(z) - 1} \quad (4)$$

where

$$R(z) = \frac{\log [1 + t_D(z)/t_1(z)]}{\log [1 + t_D(z)/t_2(z)]}$$

The equilibrium temperature log computed using Equation 4 is shown in Figure 71. The decrease in temperature with time indicates that the hole was heated during drilling by the circulation of relatively warm water from the surface of the ocean. The negative temperature gradient with depth in the upper part of

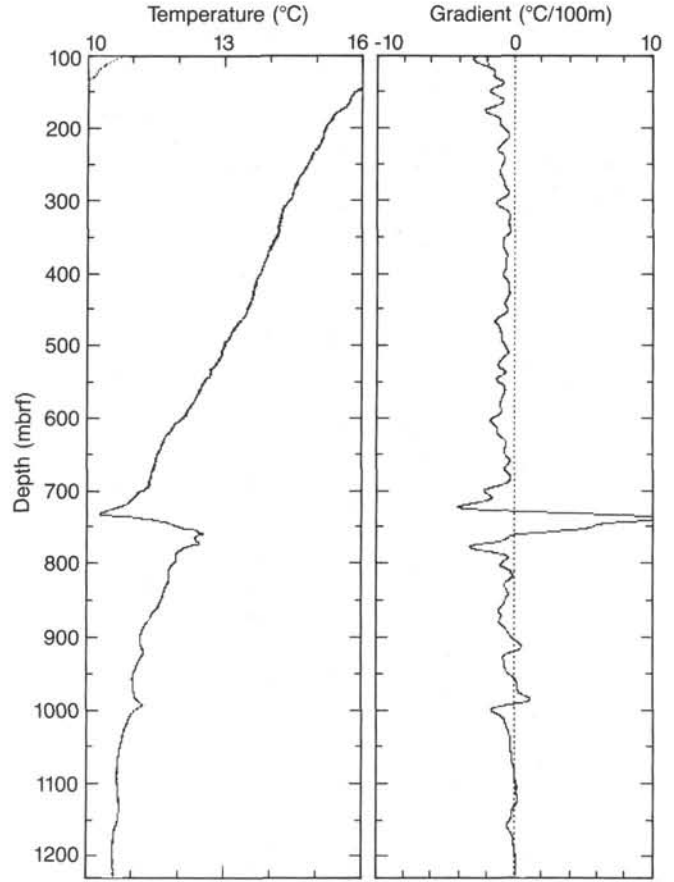


Figure 70. Temperature Run 2, Hole 735B, with the same parameters as for run 1 (Fig. 71), except that entry time into the borehole was 0445 hr, 8 December 1987.

the hole is unexpected and may reflect advection of seawater through permeable rock. We hope to develop a model that will explain these somewhat unusual observations by incorporating the results of the packer permeability measurements and laboratory measurements of thermal conductivity of core with the temperature data.

SCHLUMBERGER LOGS

Introduction

A series of Schlumberger tools were the first well logs run in Hole 735B. Four tool combinations were used, including resistivity, geochemical, sonic, and physical-property measurements.

The borehole was flushed with seawater before logging measurements. Two bit sizes were used for drilling—a 10.5-in. bit to 28.4 mbsf and a 9.875-in. bit to a depth of 500.0 mbsf. Following drilling, borehole conditions were considered ideal for logging, thus the side-wall entry sub was not used. The data presented here were digitized with a 0.152-cm digitization interval.

Run 1 (Dual Induction-Sonic-Caliper-Natural Gamma)

The first run consisted of a combination of induction resistivity, full waveform sonic, caliper, and gamma-ray logs. An electrical short in the cable head (probably from seawater that entered the head) caused poor quality logs. The full waveform sonic results are discussed in the "Multichannel Sonic Log" section (this chapter). Owing to the low amplitude of the P -waves, the Schlumberger software was unable to pick reliable arrival times, and thus no sonic velocity log is available.

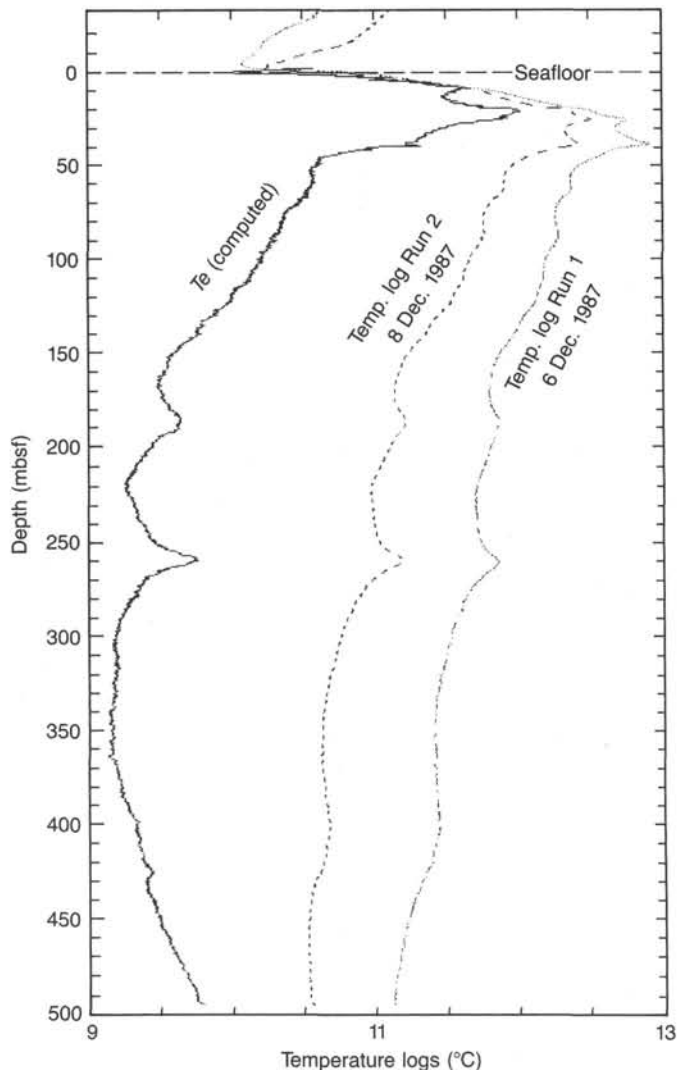


Figure 71. Temperature logging Runs 1 and 2 and calculated borehole temperature equilibrium profile (T_e).

Run 2 (Litho-Density)

The second tool string lowered into Hole 735B was the litho-density probe. The output logs include natural gamma, epithermal and thermal neutron porosity, density, and photoelectric factor. A tool module that provided a three-component magnetometer used to measure borehole azimuth, deviation, and temperature logs was also included in this run. No logging problems were encountered, and all data are of good quality. The logs are presented in Figures 72, 73, and 74.

Run 3 (Geochemical Combination)

The third run consisted of a combination of tools which together measure the concentration of the elements hydrogen, chlorine, silicon, calcium, iron, sulfur, aluminum, potassium, uranium, and thorium. The tool determines elemental concentrations by measuring both the natural and excitation gamma-ray emission spectra from the rock. (Refer to the ODP Wireline Logging Manual, 1987, or Serra, 1985.)

Two complete passes of the geochemical tool were recorded to improve its statistical measurements. Results from Run 1 are presented in Figures 75, 76, and 77. The results of both runs were good, but a few minor problems occurred in the data.

First, the tool voltage decreased for a short period of time in the first run, causing a small section of poor data between 161 and 165 mbsf.

The second, and unavoidable, problem occurred in the data from Run 2. After the first pass of the tool, the rock was bombarded by a californium source and high-energy neutrons from the minitron tube. The effects of this excitation dominated the second pass measurement of natural spectral radiation, from which potassium, uranium, and thorium are determined. Thus, the elemental concentrations of the preceding three elements should be ignored in the data from the second run.

Run 4 (Induction Resistivity-Caliper)

The failure of the cable head during Run 1 required a second pass of the induction resistivity and caliper tools. No problems were encountered during this second pass. The output of the tool includes resistivity measurements at shallow, medium, and deep penetration into the rock (ILM, ILD; Fig. 78) and that of borehole diameter (in inches) from the three-arm caliper tool (CALI, in Fig. 72).

Run 5 (Dual Laterolog Resistivity)

The final Schlumberger run was logged with the dual laterolog resistivity tool. The results include two log curves, corresponding to various depths of penetration (LLS, shallow, and LLD, deep). The laterolog data are presented in Figure 78.

Log Data Observations

Borehole Conditions

The caliper log (Fig. 72) from Hole 735B clearly indicates the change in bit size at 28 mbsf. The log also indicates that the borehole varies up to 1.6 in. in diameter below the level of the bit change. There is a minor correlation of lithology with borehole size, with massive zones showing less variation in diameter. Further discussion of the borehole shape is provided in the "Borehole Televiewer" section (this chapter). The Schlumberger logs have been suitably corrected for changes in borehole size.

The borehole at Hole 735B is not vertical, as indicated from the deviation log (Fig. 72). The average tilt of the borehole is 5.9° from vertical; it becomes more vertical with depth. The azimuth from this deviation (Fig. 72) varies predominantly between 0° and 40° .

The temperature in the borehole was also determined during the Schlumberger geochemical run; the bottom-hole temperature was 11.7°C (Fig. 73). Further analyses of the temperature profile are presented in the "Temperature Measurements" section (this chapter). The Schlumberger temperature profile is similar to the USGS temperature results.

The three components of the Schlumberger magnetometer, results of which correlate well with the USGS results, also are presented in Figure 73. This tool is not oriented in azimuth, as is the USGS tool. Comparison of the USGS results discussed in the "Magnetometer Logs" section (this chapter) with the Schlumberger logs indicates a high degree of similarity in the data obtained with both tools.

Physical-Properties Measurements

The thermal and epithermal neutron porosity logs measure the concentration of hydrogen in the rock (Fig. 74). In sedimentary environments, the thermal neutron porosity log is used to determine total hydrogen concentration, whereas the difference between the neutron logs is interpreted as bound water. This interpretation model may not stand up at Hole 735B because the distribution of water does not fit the clay-filled matrix porosity model.

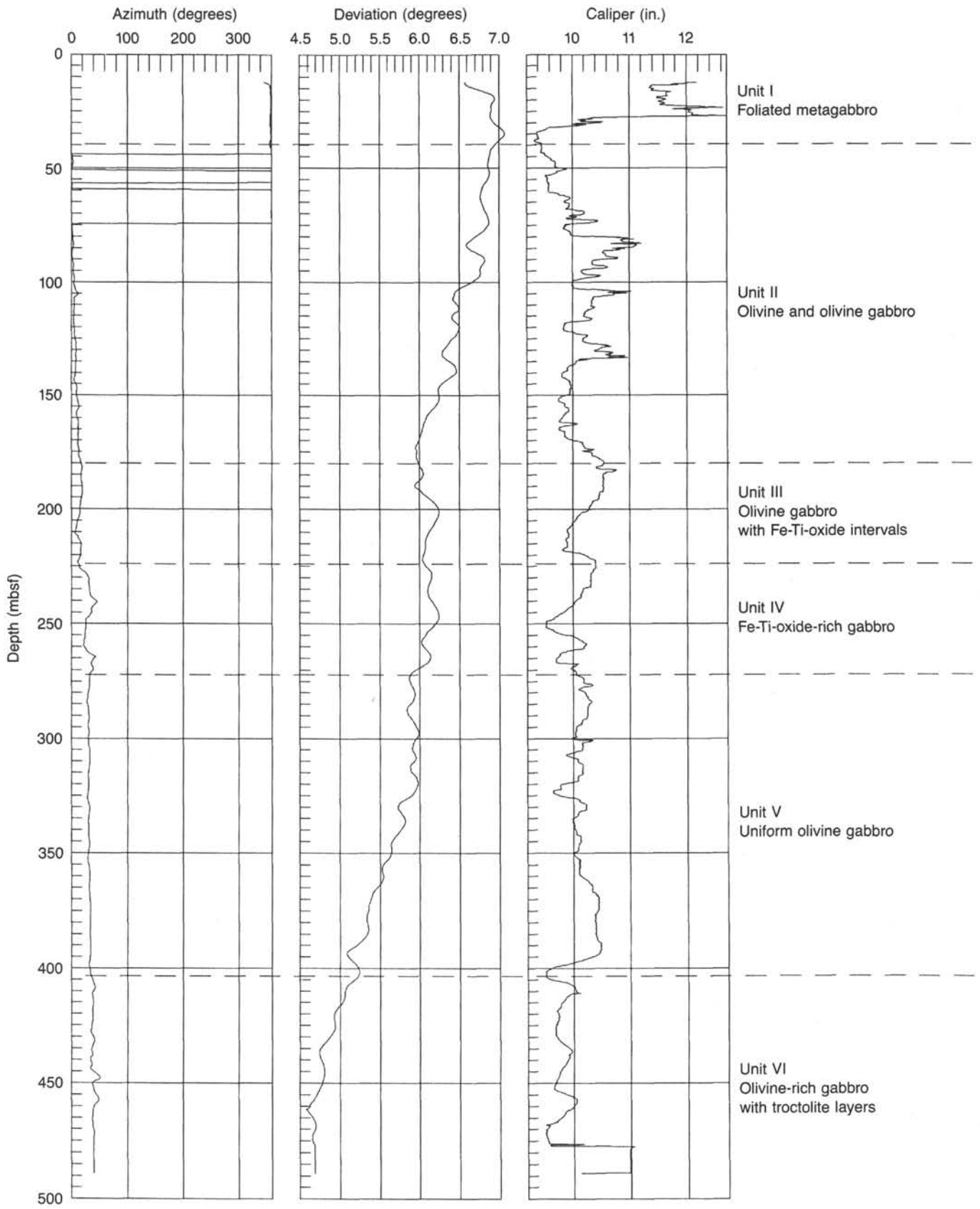


Figure 72. Azimuth, deviation, and caliper logs, with lithologic intervals (see "Lithostratigraphy" section, this chapter).

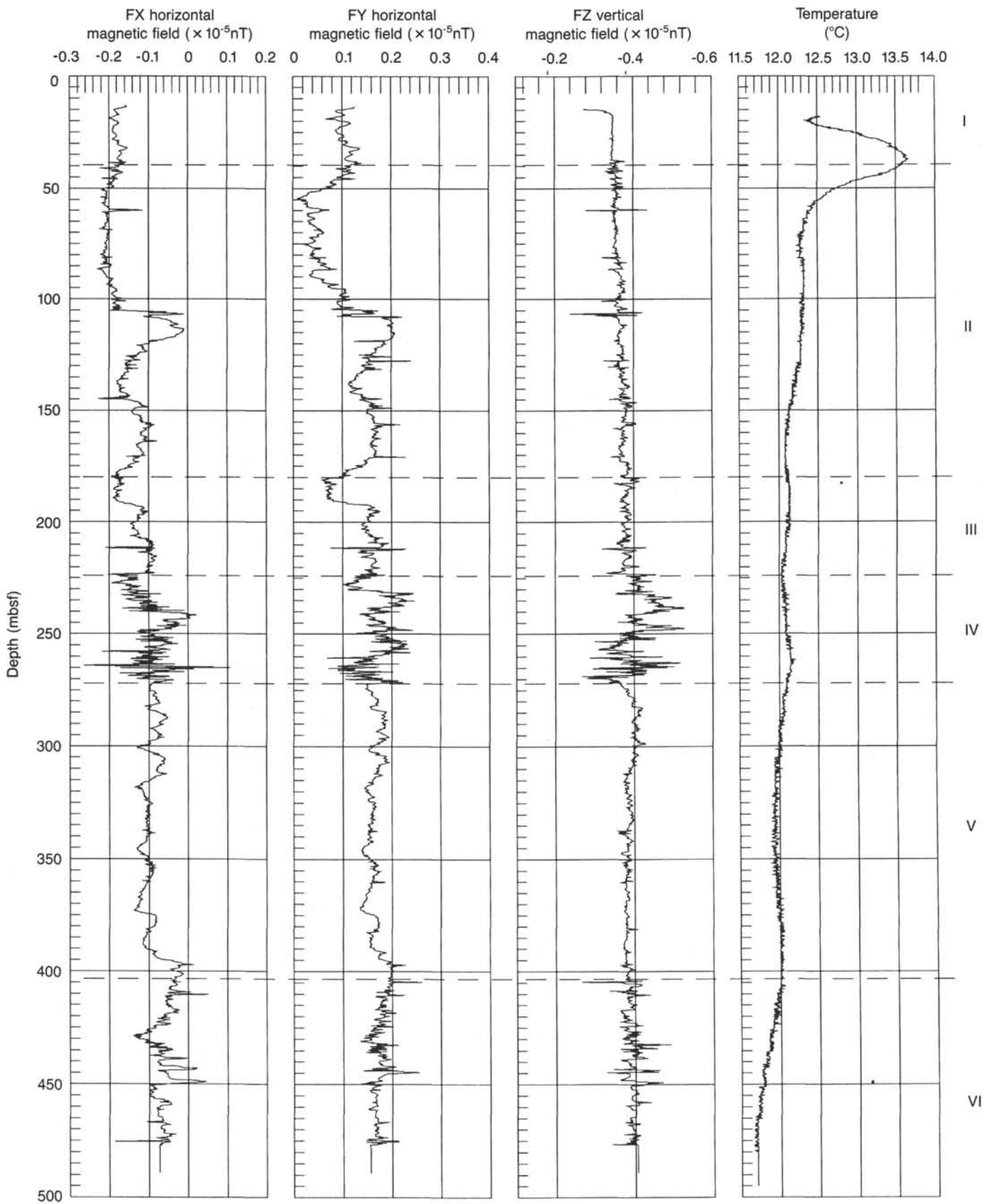


Figure 73. Schlumberger magnetometer and temperature logs. Horizontal dashed lines indicate lithologic boundaries of Figure 72.

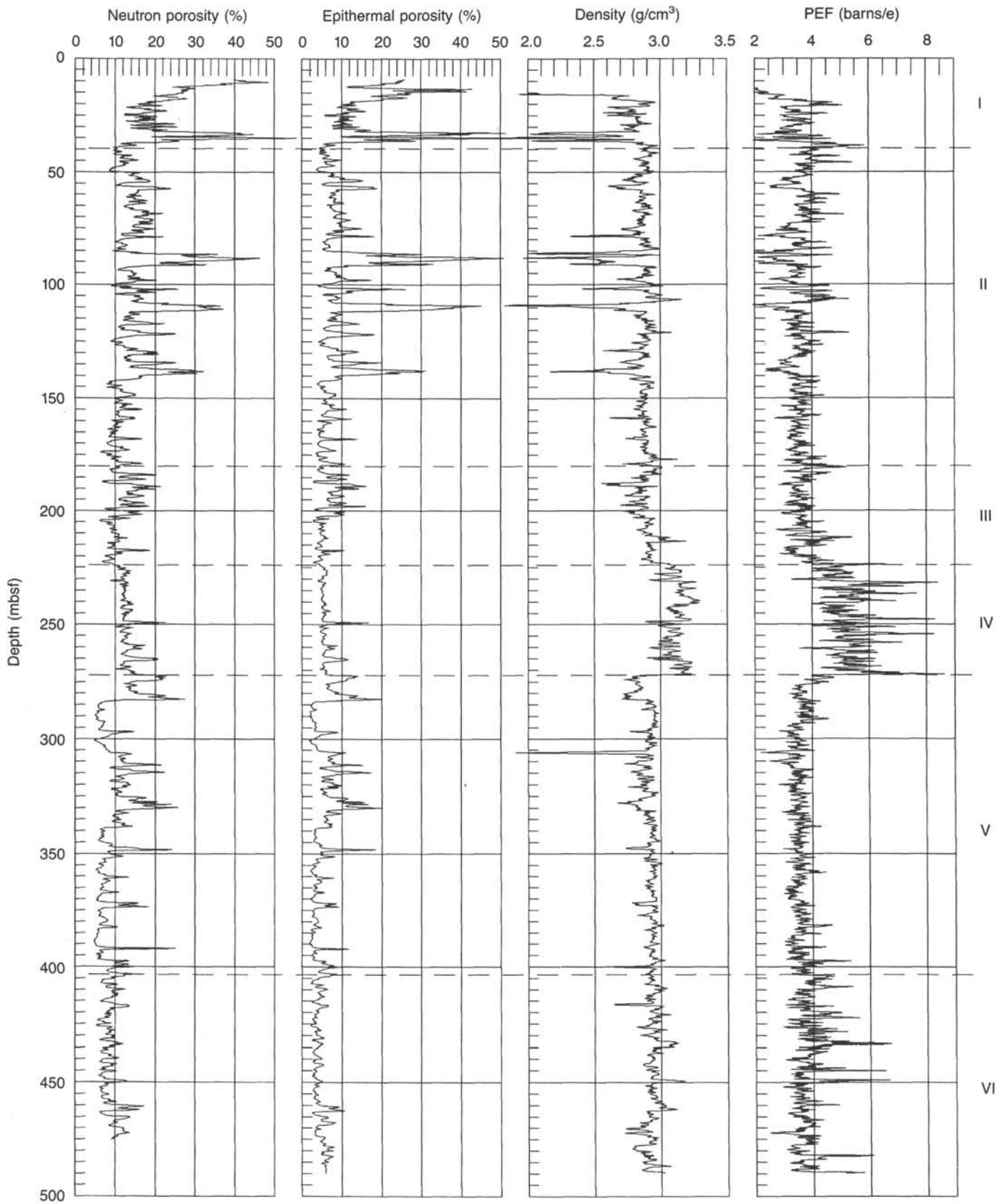


Figure 74. Porosity and density logs. Horizontal dashed lines indicate lithologic boundaries of Figure 72. PEF = Photoelectric factor.

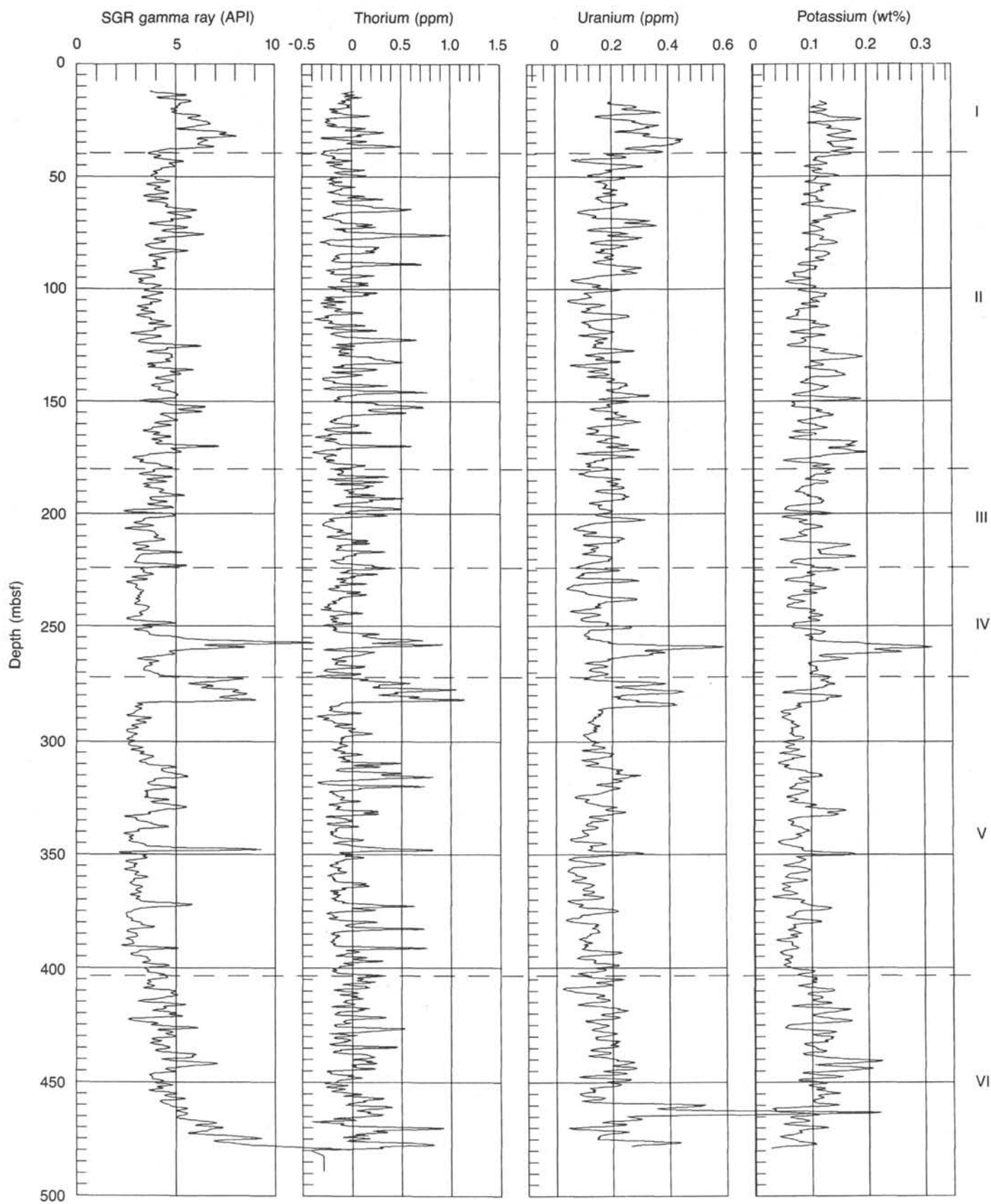


Figure 75. Natural gamma radiation logs. Horizontal dashed lines indicate lithologic boundaries of Figure 72.

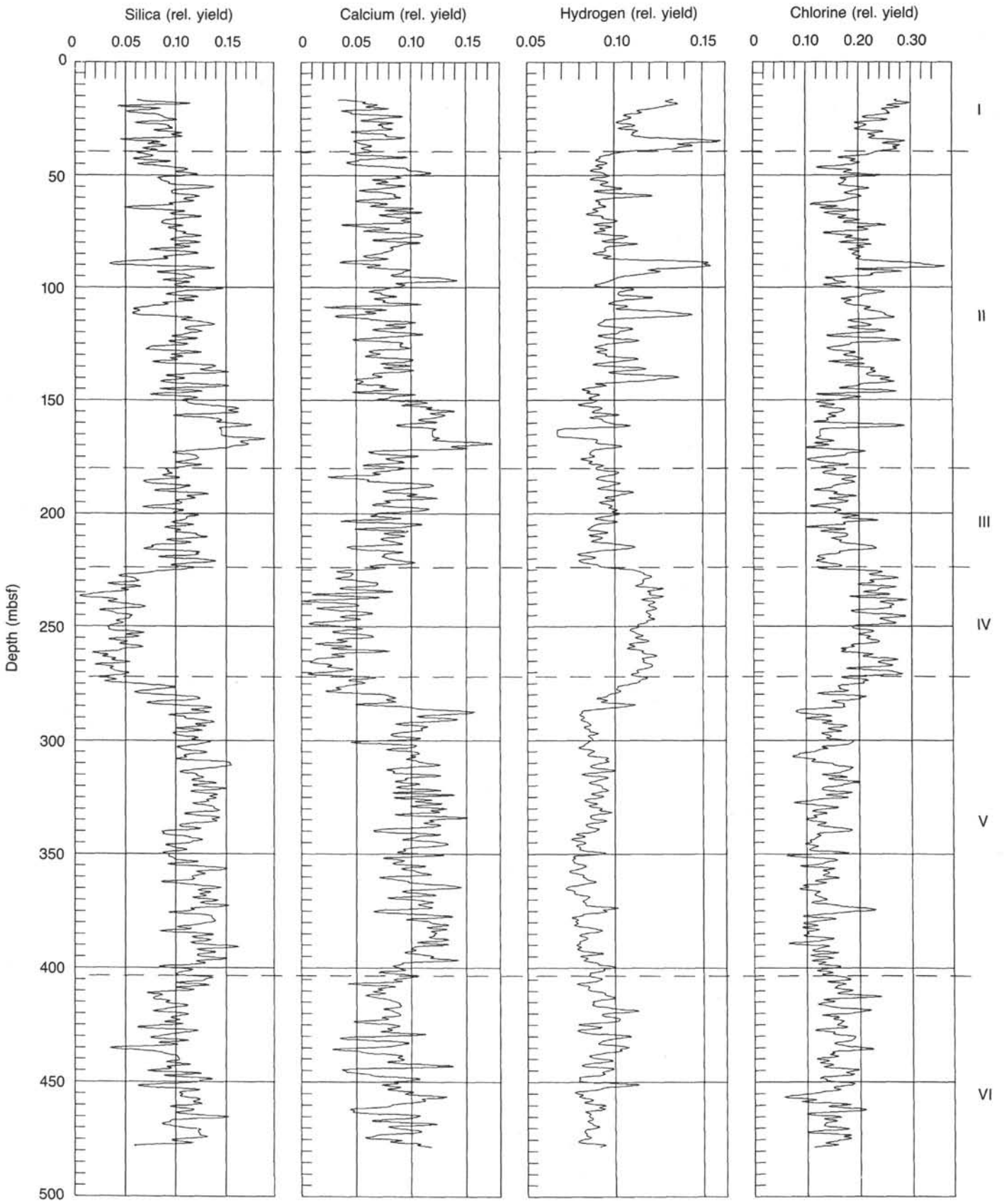


Figure 76. Silica, calcium, hydrogen, and chloride geochemical logs. Horizontal dashed lines indicate lithologic boundaries of Figure 72.

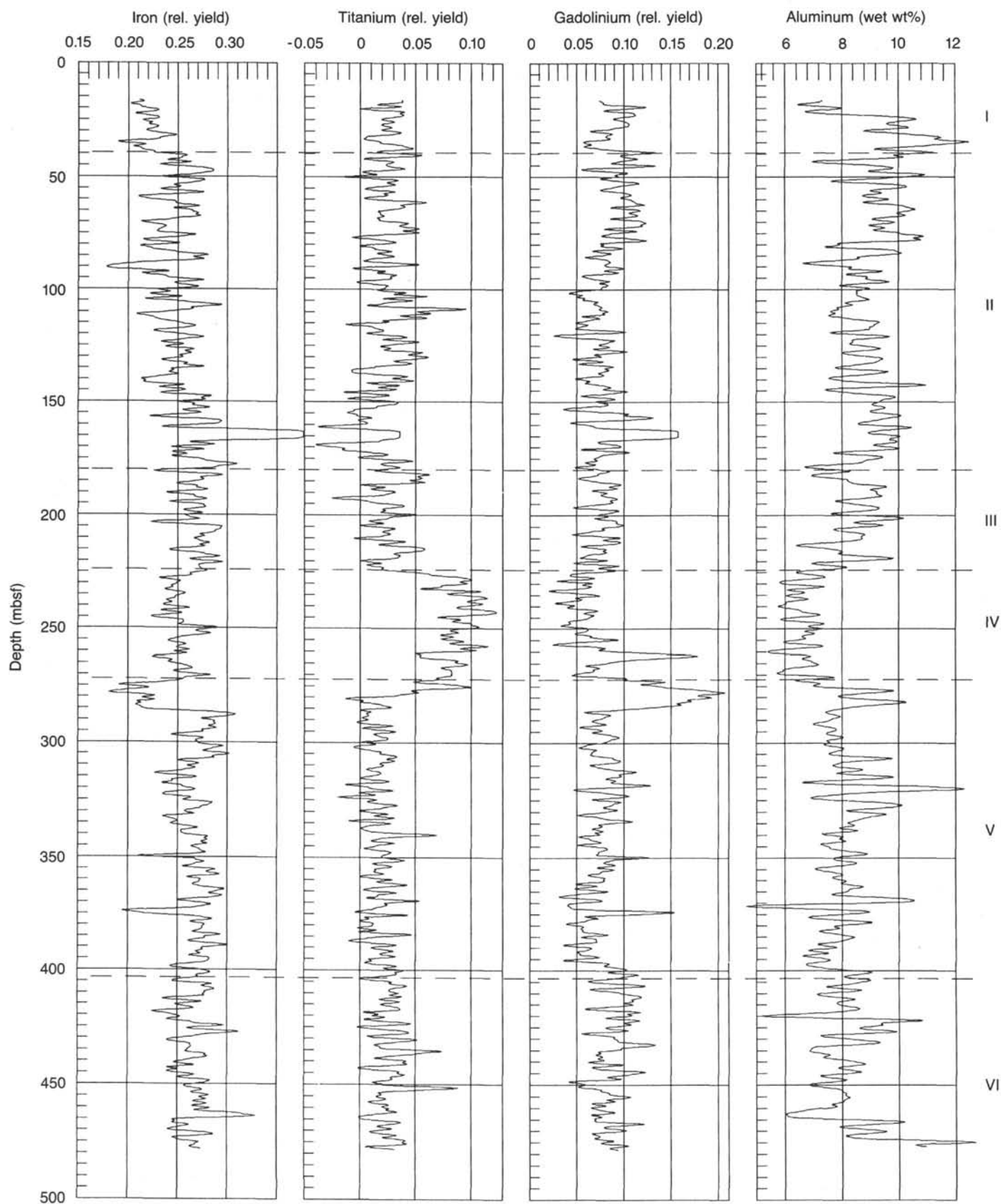


Figure 77. Iron, titanium, gadolinium, and aluminum geochemical logs. Horizontal dashed lines indicate lithologic boundaries of Figure 72.

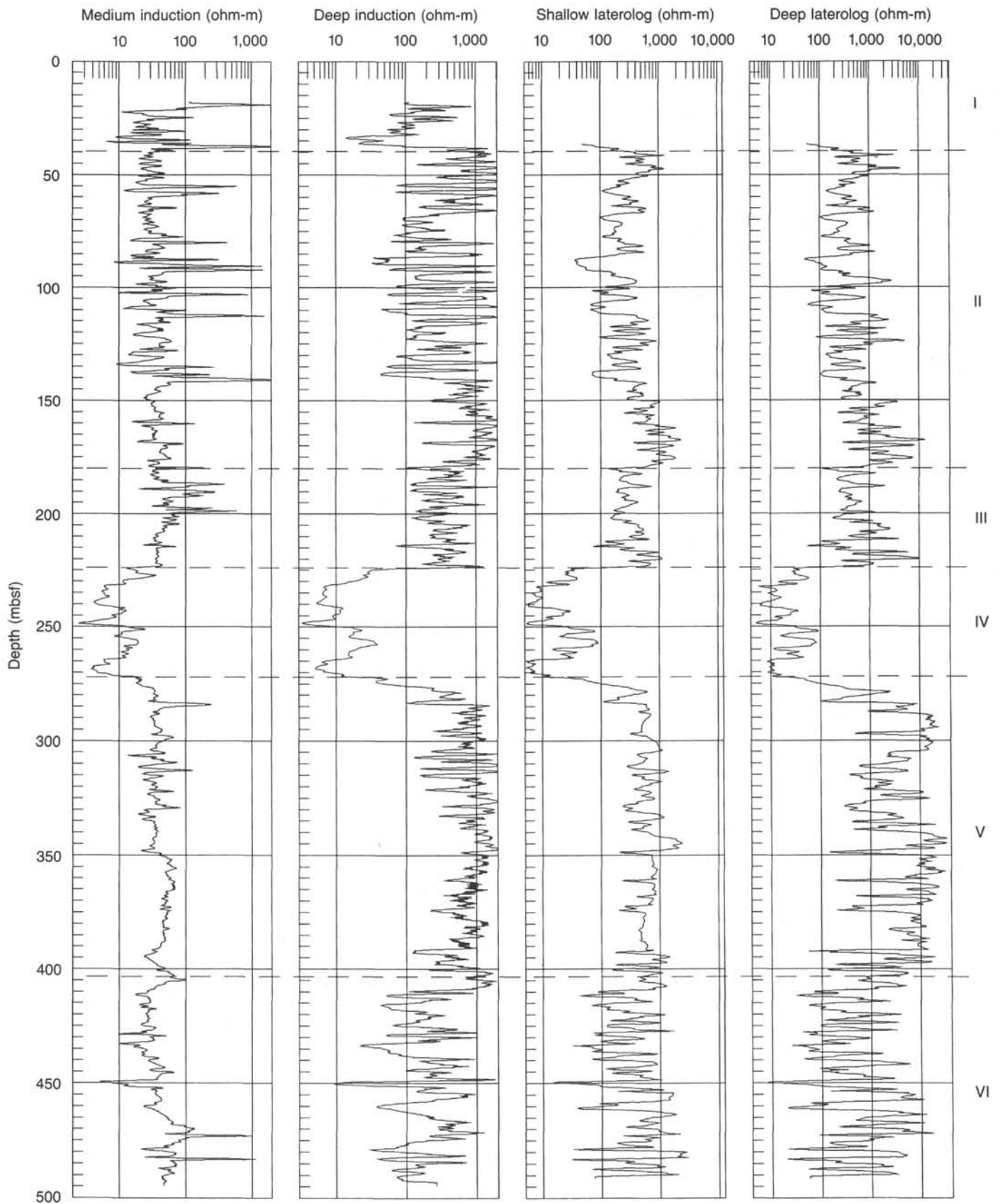


Figure 78. Resistivity logs. Horizontal dashed lines indicate lithologic boundaries of Figure 72.

The neutron porosity varies between 0% and 55% in Hole 735B. The high porosity zones correlate with low-density and high-hydrogen concentration zones from the geochemical log. Zones of interest include:

Depth (mbsf)	Porosity (%)	Lithology
32	55	Massive altered gabbro/missing core
88	52	Mylonitized gabbro
110	45	Amphibolitized metagabbro
139	32	Amphibolitized metagabbro
279	20	Highly altered olivine gabbro

The epithermal neutron porosity was measured at a low energy level, at which the effects of matrix-bound oxygen (i.e., water) were not measured. Owing to the lower energy level, the log measurement statistics produced a slightly smoother curve, as was observed. At Hole 735B, the epithermal porosity was lower than the log measurement statistics, which does not necessarily indicate bound water.

The density log from Hole 735B provided a continuous profile of bulk density in the borehole (Fig. 74). The tool averages the density of the rock over an approximately 30-cm spherical interval. The density log clearly indicates the same zones of alteration that are evident in the neutron log. In addition, Unit IV shows a significantly higher density than any other lithologic unit in the hole. Low density values may correspond to high porosity zones, where fractures intersect the borehole. Preliminary borehole results show fracturing at 288, 292.5, and 302.5 mbsf. The low density zone at 306 mbsf may correspond to a fracture observed in the borehole televiewer near that depth.

The photoelectric factor (PEF) was measured along with the density (Fig. 74). The PEF measures low-energy gamma-ray absorption. Laboratory measurements of the photoelectric absorption index (Pe) of various elements and minerals have been compiled (see Tables 2 through 4 in *ODP Wireline Logging Manual*, 1987). The log measurement represents the total absorption index of the formation.

At Hole 735B, the rise in the PEF within Unit IV corresponds with the increase in iron and titanium concentrations. For comparison, note that the Pe of magnetite is 22.08, that of ilmenite is 16.63, and hematite is 21.48, while the Pe of quartz is 1.806 and that of salt water is 0.807 barns/electron.

Also of interest are the potential effects of uranium and thorium (Fig. 75) on the PEF log. The laboratory-measured Pe of uranium is 2948.74 and that of thorium is 2724.4 barns/electron. We observed that the highly altered zone just below the Unit IV/Unit V boundary, which has a high concentration of thorium and uranium, does not appear as an increase in PEF. We concluded that although the concentrations of thorium and uranium are relatively high in the alteration zone, the effect on the PEF log may be balanced by the reduced concentration of various other high-PEF minerals.

Resistivity Measurements

The results of the laterolog (curves LLS and LLD) and induction resistivity tools (curves ILM and ILD) are presented in Figure 78 and have been smoothed with a 5-point (0.760-m) boxcar filter. The limitations of each tool must be considered during analysis; the operational limits of the tools were reached in Hole 735B.

The saltwater in the borehole and the initial pore fluid have a low resistivity compared to the rock matrix. Thus, an increase in fracture or connected intergranular porosity results in a decrease in measured resistivity. The matrix resistivity is controlled by rock composition, particularly iron oxides. An increase in iron oxide concentration will significantly reduce the measured resistivity.

Resistivity tools measure the bulk resistivity of the rock and fluid within various size zones of investigation, which are specific to each tool. For this reason, their results are controlled by the relative amount of conductive borehole fluid and resistive rock matrix within the zone. Tools with deeper zones of penetration are influenced less by the conductive borehole fluid.

The method by which the laterolog measures resistivity is significantly different from that of the induction log (Serra, 1985). The laterolog is inaccurate for that range in which the induction log is more accurate. The induction log measurement should be used when the resistivity decreases below 100 ohm-m, while the laterolog should be used when the resistivity is above this value.

Induction Logs

The medium induction log (ILM) measures the resistivity within approximately 0.5 m of the borehole. Induction logs are designed to give accurate measurements of resistivities below 100 ohm-m. At Hole 735B this occurs only in the iron-titanium oxide-rich zone.

The deep induction log (ILD) has a greater depth of investigation than the ILM and reaches approximately 5 m. Owing to the greater penetration, the log provides a more accurate measure of rock resistivity because it is influenced less by borehole fluid. However, this log is accurate only below 100 ohm-m.

Laterologs

The deep laterolog (LLD) has a depth of investigation of greater than 1.0 m and provides the closest measure of the true resistivity of the rock for zones where resistivity is greater than 100 ohm-m. However, this log does not have the vertical resolution of the shallow laterolog (LLS). The response of the LLD spans four orders of magnitude, between 4 and 40,000 ohm-m. The variation in the resistivity may be attributed to different factors at different locations in the borehole. The low resistivity zones in Unit II are probably caused by changes in porosity, as confirmed by the neutron and density logs at 87, 108, and 138 mbsf. Lithologic Units III and IV also show reductions in resistivity, which are attributed to increased iron oxide concentrations. The LLD log was saturated at about 4000 ohm-m owing to a malfunctioning electrode. For this reason, the difference in resistivity between the LLS and LLD curves at high resistivity is exaggerated.

The spherically focused resistivity log (SFLU) was run in Hole 735B, although results are of little value and are not shown. The tool has a very shallow depth of investigation and thus is influenced greatly by the contrast between the matrix and borehole fluid resistivity. The oscillations in log response, which occur in the high-resistivity zones, indicate that the tool was operating beyond its measurement limit. The tool was designed to provide a resistivity measure over a 15-cm vertical interval.

Geochemical Measurements

The geochemical measurements of natural gamma, potassium, thorium, uranium, silicon, calcium, hydrogen, iron, titanium, gadolinium, and aluminum are presented in Figures 75, 76, and 77. These measurements have been smoothed with a 7-point (1.064 m) boxcar filter. The raw data (relative yield) are presented in these figures, and further processing should allow us to calculate the weight percent of these elements and oxides. Note that the geochemical data between 161 and 165 mbsf are poor because of temporary operational problems.

The gamma-ray log or Standard Gamma Ray (SGR) measures the total natural gamma radiation emitted by the rock into the borehole. The log is recorded in API units, the standardized units of the American Petroleum Institute. The most significant characteristic of the gamma log from Hole 735B is the very low API values. For comparison, 10–30 API is typical for a sand-

stone, whereas 80–140 API is typical of shales. Three significant zones of higher gamma radiation occur in the borehole. The first, at 258 mbsf, corresponds to the trondjemite layer in lithologic Unit IV. The second zone occurs immediately below the lower boundary of Unit IV and corresponds to a zone of high alteration. The third increase in natural gamma radiation below 465 mbsf is unexplained and conflicts with the natural gamma-ray spectral logs.

While the SGR log measures total gamma radiation, the thorium, uranium, and potassium measurements provide concentration of the three most common sources of gamma radiation. The peak in the SGR log at 258 mbsf corresponds to the only significant peak in the potassium log, which indicates that potassium is more concentrated in the trondjemite layer. This is confirmed by the XRF measurements.

Comparison of the shape of the thorium and uranium logs with the gamma-ray log indicates that these elements are the primary source of radiation in the borehole at various depths. This is particularly evident in the alteration zone below Unit IV.

The silica, calcium, and aluminum logs show a distinct decrease in relative yield in Units III and IV, as observed in the XRF data. The hydrogen and chlorine logs exhibit a shape similar to the neutron log, which allows identification of high-porosity zones. The gadolinium log shows a significant increase in response within the trondjemite interval at 258 mbsf, and within the alteration zone immediately below Unit IV. The relative yield of iron does not show the expected increase in response within the iron-titanium oxide-rich zone; further investigation will be necessary.

Figure 79 allows us to compare geochemical log results with XRF analyses performed on board the ship. Within the iron-titanium oxide-rich unit, the thin silicon-rich trondjemite zone appears as a slight increase in silicon concentration. However, the geochemical tool does not have the vertical resolution to detect true concentrations in the zone (for a discussion of the factors affecting tool response, refer to Serra, 1985). Comparison of the titanium measurements indicates a close correlation of log results with laboratory data. Depth offset between peaks in the laboratory and log results (e.g., at 100 mbsf) may be caused by sample offset from vertical shifting of core where recovery was poor.

Conclusions

The logging results at Hole 735B clearly delineate the iron-titanium oxide-rich gabbros encountered between 223 and 272 mbsf. The resistivity logs responded dramatically to the increased oxides in this zone owing to their electrical conductivity (Clark, 1966). Also evident was an increase in density, along with a distinct reduction in silicon concentrations. A felsic trondjemite interval within the oxide layer is evident from the small increase in silicon and the significant increase in potassium concentration.

Immediately below the iron-titanium oxide-rich gabbro lies a 12-m-thick zone, where increased alteration is evident. Logs show an increase in silicon, thorium, and neutron porosity, along with reduced density and iron concentration.

In general, the lower section of the borehole is marked by uniform log signatures. The laterolog resistivity, however, shows many intervals of reduced resistivity that may possibly correlate with zones of alteration or increased oxide concentration.

MULTICHANNEL SONIC LOGS

Introduction

Sonic logs are run routinely in ODP wells using a two-source, two-receiver Schlumberger (LSS) sonic tool. The Lamont-Doherty multichannel sonic (MCS) tool was used during ODP Legs 102, 109, and 111 to investigate basaltic basement.

This tool is a multireceiver signal-source logging device that records 12 sonic waveforms at each source depth. At Site 735, both LSS and MCS tools were run into gabbroic basement to investigate elastic properties and fracturing.

Sonic waveforms may be analyzed to yield compressional, shear, and Stoneley velocities across a receiver span using a semblance correlation to measure the coherence of energy between receivers. The semblance value may also be used to estimate the energy loss across the receiver array. Amplitude thresholds typically are used to provide accurate measurements of compressional and sometimes shear velocity. The low signal/noise ratio of the compressional wave in this gabbro precluded our selecting amplitudes directly and required the use of semblance processing. Generally, in fast formations such as gabbro, dense receiver spacings and long source offsets enable greater precision and higher semblance when computing velocities (i.e., MCS tool). Sonic data are commonly used to determine lithology and to estimate porosity from compressional velocities, fracture location, and structural analysis from semblance values, as well as to estimate pore aspect ratios from calculated V_p/V_s ratios (O'Connell and Budiansky, 1974; Paillet and White, 1982; Kimball and Marzetta, 1984; Goldberg and Gant, 1988).

Description of Tools

The MCS tool is configured with the source above the receiver string and is separated by a variable-length spacer assembly (Fig. 80). The MCS receiver geometry is similar to that of a surface refraction survey rotated 90°, with 12 receivers spaced 15 cm apart over a 1.65-m linear receiver array aligned along the hole. The LSS tool is configured with two transducers 0.61 m apart and two receivers also 0.61 m apart that are located 2.44 m above the upper transducer. During logging, both tools are centered in the borehole by means of bowspring centralizers. The energy that arrives at each receiver travels as a compressional pulse from the source in the borehole fluid, is refracted at the borehole wall, and then is refracted back into the borehole fluid. Additional guided-wave modes also are produced in the borehole environment, and their propagation is controlled by the properties of both the formation and the fluid-filled borehole. One such mode, the Stoneley (or tube) wave, propagates as a surface mode slightly slower than the fluid velocity. The propagation of waves in a borehole was discussed completely by Paillet and White (1982). The spectral signature of the MCS source was recorded at 80 cm horizontal offset in a water bath at Lamont-Doherty Geological Observatory. Figure 81 shows that the peak power in the spectrum occurs at 22 kHz. The peak is centered on a broad shoulder about 8–10 dB below the peak between 10 and 27 kHz and is at least 6 dB down outside the 18 to 26 kHz frequency band.

Computer control of the tool during logging allowed us to select the depth increment between recorded suites as well as the number of receivers to be used. The data are transmitted uphole in analog format and digitized and recorded on magnetic tape during the logging run. The MCS logging rate depends on the depth increment and the number of receivers per source depth. For the 0.3-m depth increment and the 12 receivers per source depth used in the MCS survey, the logging rate required for the MassComp acquisition software was about 3 m/min. The logging rate was about 10 m/min for the LSS tool.

Operations

On 6 December 1987, Schlumberger LSS waveforms were recorded during the first logging run in Hole 735B. High-quality waveforms were recorded at a sampling rate of 5 μ s for 2.5 ms over most of the interval. However, due to an electrical short in the cable head, two intervals in the hole were missed: 140–160 and 380–450 mbsf. The low signal/noise ratio of the compress-

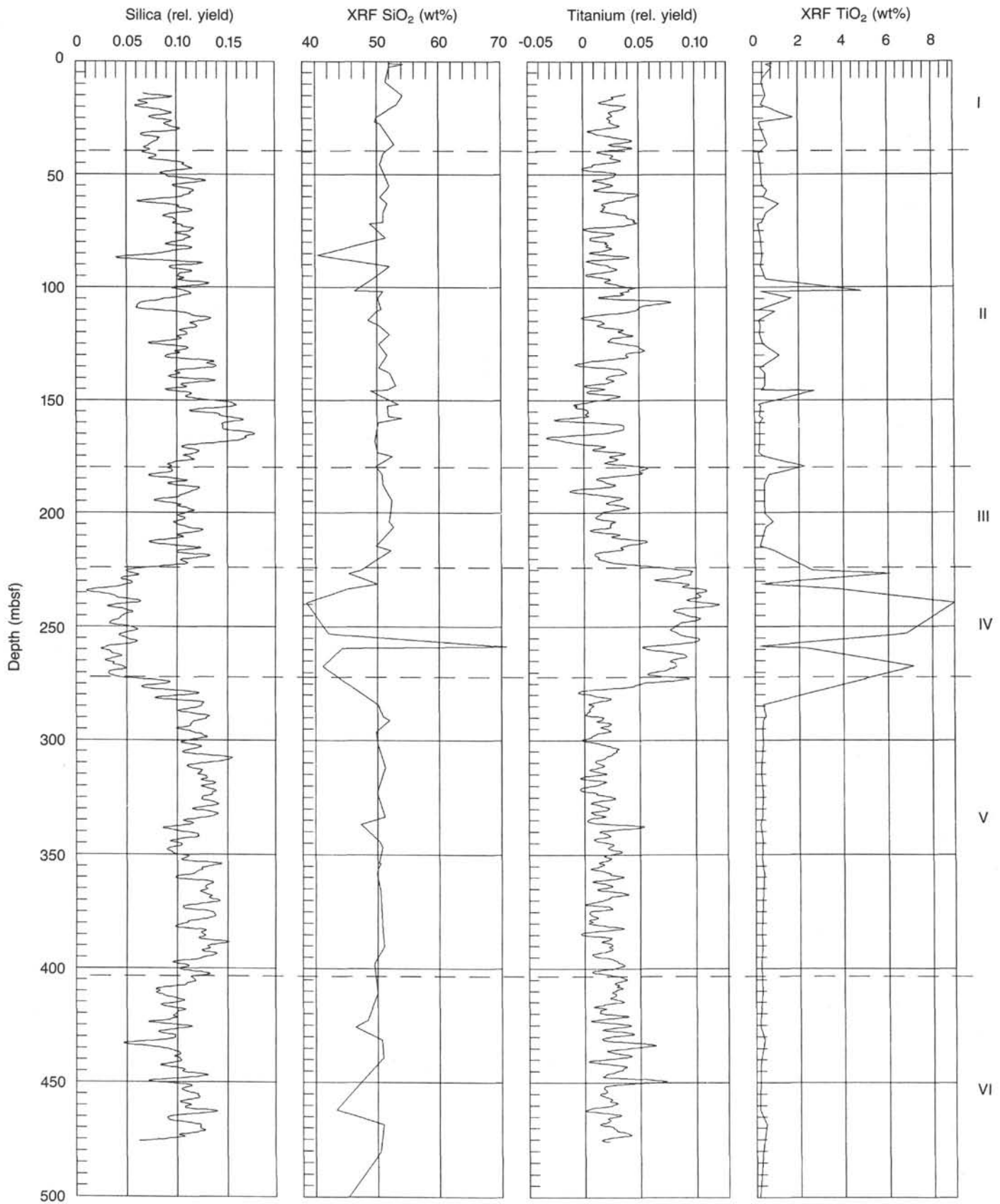


Figure 79. Comparison of geochemical logs with XRF analyses. Horizontal dashed lines indicate lithologic boundaries of Figure 72.

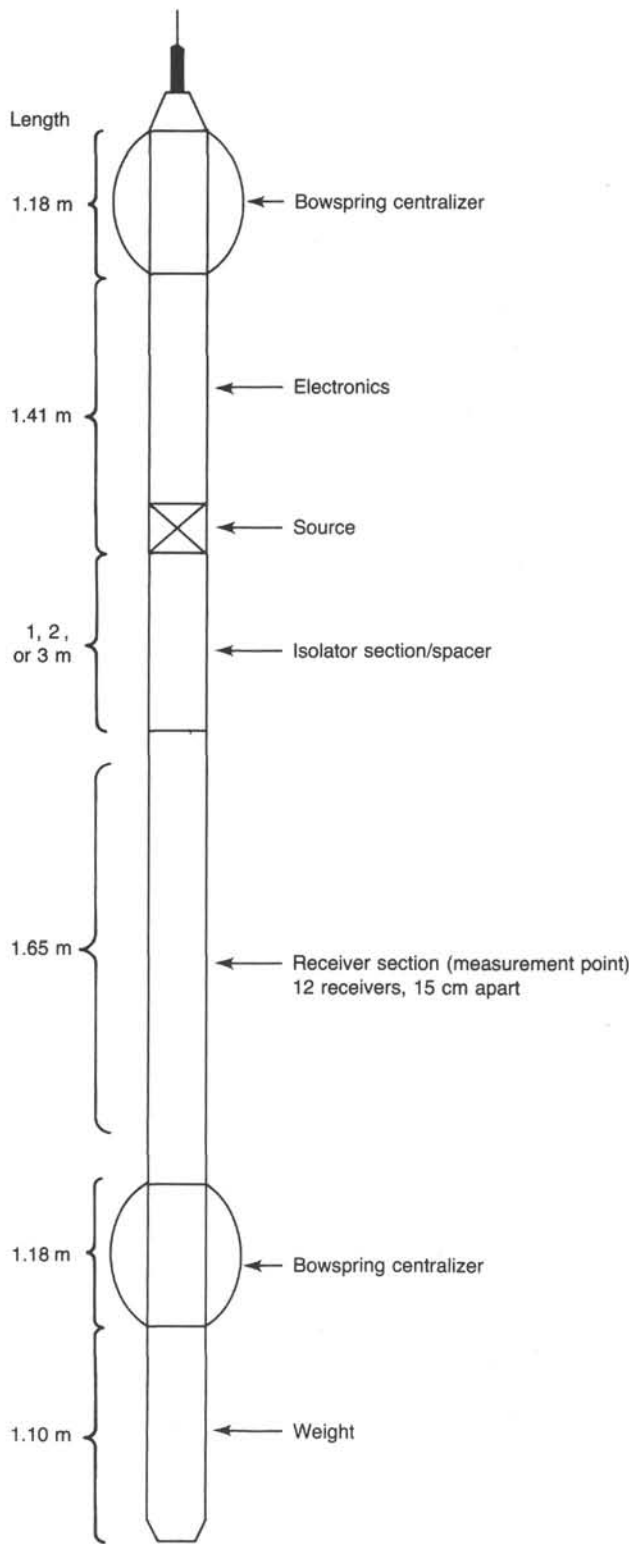


Figure 80. Schematic diagram of the MCS logging sonde.

sional wave in this formation required that the recorded waveforms be processed using a modified semblance calculation for this tool geometry after the log was completed.

On 7 December, MCS data were recorded in Hole 735B from a depth of 484.6 to 13.0 mbsf using a tool configuration that resulted in a separation of 3.81 m between the source and the receiver array. Digital waveforms were recorded for successive

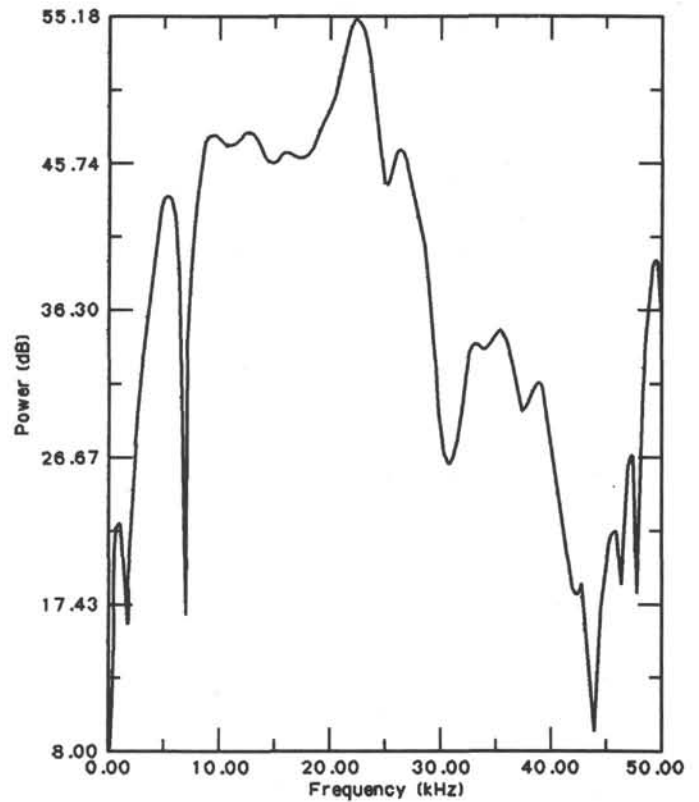


Figure 81. Spectral signature of the MCS sonic source recorded at LDGO in a water bath with an 80-cm horizontal offset. Peak power occurs at 22 kHz and is at least 6 dB down outside the 18 to 26 kHz frequency band.

source locations at 0.3-m intervals. The waveforms were digitized at a sampling rate of $5 \mu\text{s}$ for 5 ms. At 125.9 mbsf, one of two spacers between the source and the receiver array shorted by flooding at a failed epoxy joint, and the log had to be aborted. The upper 100.0 m of Hole 735B was logged on 8 December using one spacer at a reduced source-receiver separation of 3 m. In addition, the computer interface that controls the source firing was not operating correctly, and the upper 100 m interval had to be logged using unsynchronized source firing. Data throughout the open-hole interval of the well are good; however, data from the upper 100 m had to be reordered by sequential receiver number before receiver amplitude analysis could proceed.

Single-receiver MCS waveforms at 4.57 m source offset are shown in a variable-density format over a 4-ms recording interval for the entire hole in Plate 1. Depths shown in this plate are meters below rig floor. The data are unprocessed, with the exception of the upper 100 m interval that was reordered after asynchronous recording, based on a pick of the high-amplitude and stable fluid arrival (see Fig. 82). The amplitude of the waveforms (blackness) changes in certain depth intervals and over time. In particular, the upper 100-m interval is more chaotic and has lower amplitudes (it is also plotted at a $5\times$ scale). This results partly from receiver gain changes from recording without computer synchronization and partly from physical-property changes in the formation. The lower amplitude of compressional waves in this interval can also be seen in the LSS waveform log. The relative amplitudes of compressional, shear, and Stoneley wave modes observed qualitatively in Plate 1 are quantified by the subsequent semblance calculation.

A sample suite of 12 MCS waveforms recorded at 126.0 mbsf with reduced spacing (3 m source-receiver offset) is shown in Figure 82A. Compressional and shear wavemodes are suffi-

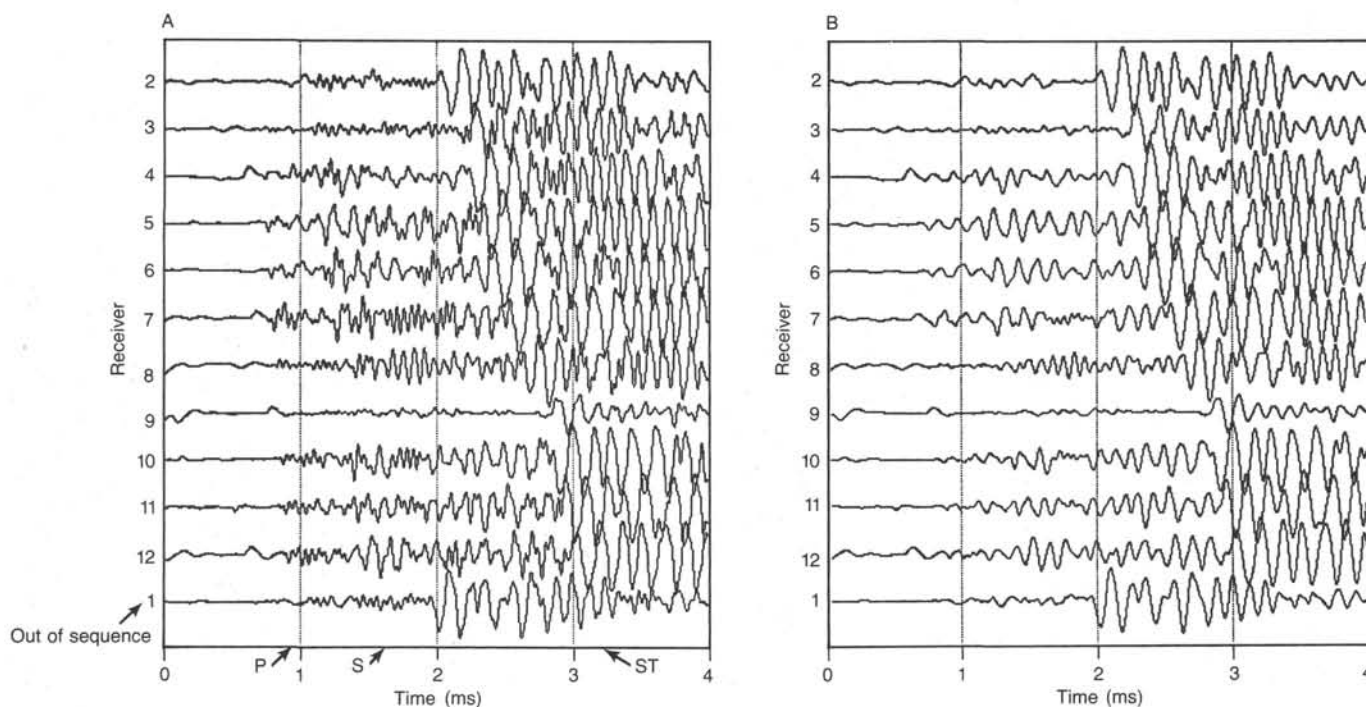


Figure 82. A. MCS waveforms recorded at 126 mbsf by asynchronous computer control (Note that receiver 1 is recorded at the farthest offset location and that compressional (P), shear (S), and Stoneley (ST) arrivals occur near those at receiver 2). B. Bandpass filtering of the waveforms show the dominant received frequency band as 2.5 to 17.5 kHz.

ciently separated for velocity analysis using this geometry. Compressional (P), shear (S), and the later-arriving Stoneley (ST) wavemodes are identified. In addition, this example shows the misordering of receiver 1 to the farthest offset as a result of asynchronous recording. The waveforms were recorded based on the pick of the high-amplitude Stoneley/fluid arrival.

Figure 82B shows the same suite processed using a frequency filter to eliminate high-frequency noise and low-frequency instrument bias. A Butterworth bandpass operator was convoluted twice with each waveform to ensure a zero-phase outcome. The dominant frequency band of the waveforms is 2.5–17.5 kHz, as shown by a comparison of the unfiltered with the filtered waveforms, and is considerably lower than the peak source output band resulting from propagation losses through the formation and borehole. The data for the entire interval were processed using this filter before semblance analysis.

An expanded time scale for a suite of waveforms recorded at 214.4 mbsf is shown in Figures 83A and 83B. The high-amplitude shear arrival is prominent near 1250 μ s at receiver 1 and 1700 μ s at receiver 12; however, the compressional arrival is emergent only for the longer source-receiver offsets. This may result from both poorer sensitivity of MCS receivers 1, 2, 3, and 9 and from better far-field wave-mode separation farther from the source. Receivers 4, 5, 6, 7, 8, 10, 11, and 12 thus were used in the compressional semblance computation, and the others were rejected over the entire interval.

The MCS and LSS data were processed for compressional and shear velocities using a modified semblance calculation to correlate energy traveling over the receiver array at progressive time steps. Peak semblance occurs when the time lag equals the receivers offset, divided by the velocity. Compressional- and shear-wave velocities were calculated separately by restricting the time window of correlation over the wavefield and the range of possible velocities. For additional discussion of semblance pro-

cessing for sonic waveforms, the reader should consult Kimball and Marzetta (1984) and Goldberg and Gant (1988).

Semblance results for LSS data are plotted as a function of depth in Figure 84. Compressional, shear, and Stoneley slowness values (the inverse of velocity) in microseconds per foot and the peak compressional amplitudes in millivolts for 2.44-, 3-, and 3.81-m receivers also are shown. The LSS log is unreliable in the intervals from 140 to 160 mbsf and 380 to 450 mbsf because of the shorted cable head. Elsewhere, mean compressional, shear, and Stoneley velocities are reliable and equal to about 6.5, 3.5, and 1.5 km/s, respectively. Of particular interest is that compressional and shear slownesses increase (velocities decrease) and compressional amplitudes decrease in the upper 140 mbsf, which suggests that physical-property variability is scattering energy in this interval. Below 140 mbsf, the MCS compressional-wave velocity is inverted and plotted on scale with the LSS log for comparison. MCS velocity and semblance curves are indicated by heavy lines. The correlation of MCS and LSS velocities is generally good in the overlapping zones, and the semblance correlates roughly with changes in compressional amplitude. The low amplitudes observed in the upper interval of the hole suggest that the MCS data also may be expected to have lower semblance values in the upper interval owing to formation changes.

Figure 85 depicts the processed MCS semblance velocity logs. V_p varies from 5.0 to 7.5 km/s over the interval, and peak semblance varies between 0.10 and 0.75, where a value of 1.0 represents perfectly coherent signals. Low semblance (less than 0.15) is used to discriminate against unreliable velocities that are not plotted. This generally occurs when the shear wave is severely attenuated by fracturing or borehole washout. V_s is less variable than V_p because of the proportion of sonic energy partitioned into the guided-wave modes in fast formations that dominates the group velocity (Paillet and White, 1982). These logs were

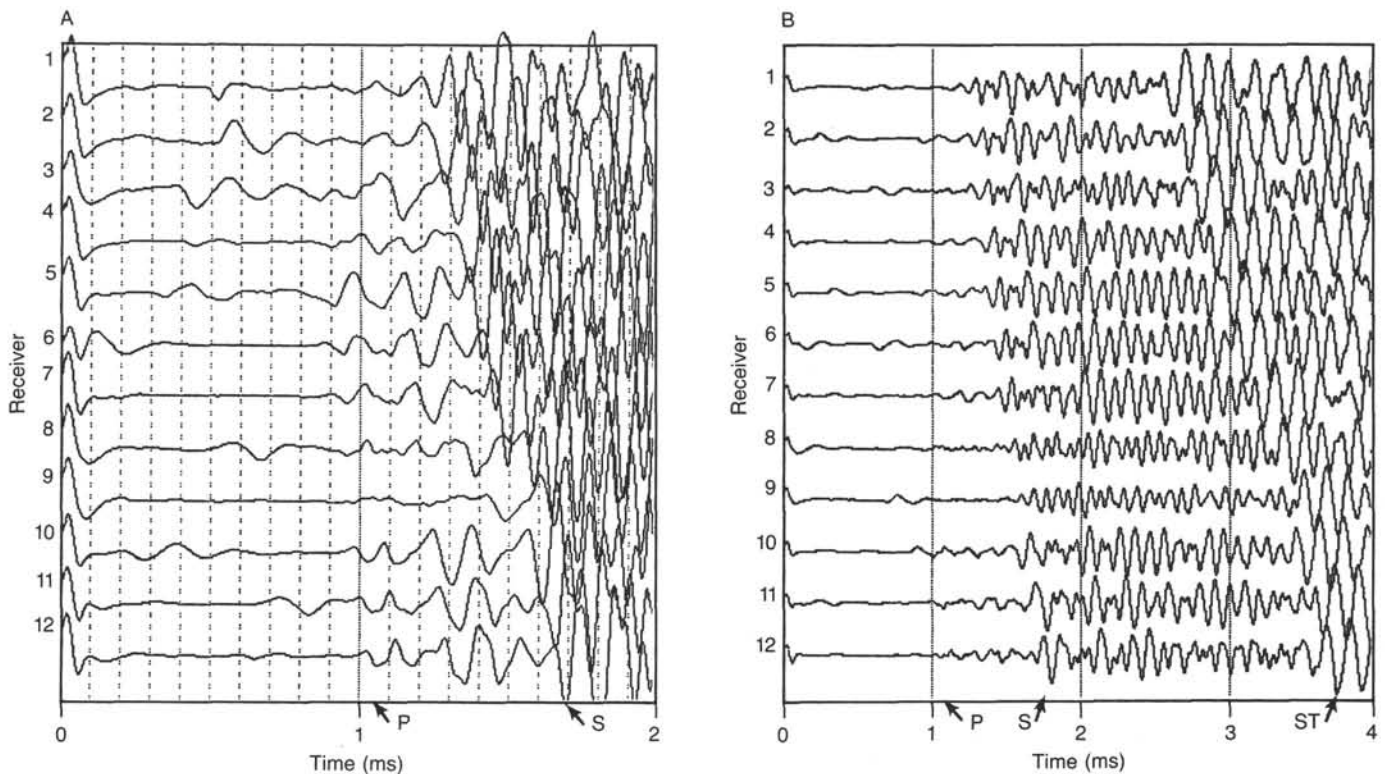


Figure 83. A. Filtered MCS waveforms recorded at 214.4 mbsf show that compressional arrivals (P) have low amplitude at the nearest receivers. B. Full 4-ms time scale shows strong shear (S) and Stoneley (ST) arrivals at all receivers.

smoothed using a ± 0.9 -m boxcar filter. The smoothing filter is shorter than the receiver span and thus does not influence the vertical resolution of velocity.

The V_p/V_s ratio is primarily governed by the compressional velocity and varies about a mean of 1.9 (Fig. 85). Variable V_p/V_s ratios and reduced semblance values occur in the foliated interval above 140 mbsf and are probably due to scattering losses in zones of deformation (see "Metamorphism and Alteration" section, this chapter). The most dramatic localized decreases in shear semblance and compressional velocity appear to be associated with isolated fractures that may occur near 275, 310, and 335 mbsf (see "Borehole Televier" section, this chapter). This correlation also might be used to predict the occurrence of fractures near 95, 135, and 195 mbsf, where the borehole televier data have not yet been processed. Further analysis of the sonic logs may reveal detailed correlation as well as subtle changes in lithology and physical properties in oceanic layer 3.

VERTICAL SEISMIC PROFILING

Introduction

A vertical seismic profile (VSP) differs from a conventional reflection profile in that the receiver is clamped successively at different borehole depths within the earth (Fig. 86; Hardage, 1983; Balch and Lee, 1984). The seismometer records both the direct, downgoing waves and upgoing waves reflected from acoustic impedance changes below the clamping depth. Interval velocities may be calculated from the difference in arrival time of the direct wave between different receiver depths. Processing techniques can be applied to separate the upgoing and downgoing wavefields, which can then be analyzed for attenuation properties of rock, prediction of acoustic properties below the bottom of the hole, and correlation with borehole lithology, wireline logs, and events on conventional seismic-reflection pro-

files. Resolution of structure is limited by the signal/noise level, bandwidths of source and receiver, and rock velocity. In marine usage, the frequency of the source ranges from 5–30 Hz (air guns and explosives) to about 120 Hz (water gun). In rocks having velocities of 4–8 km/s, the finest scales resolvable (about one quarter wavelength) with a broad band receiver under good signal/noise conditions are 8–200 m.

Objectives

The purpose of Leg 118 was to drill in or near an oceanic fracture zone offsetting a slow-spreading ridge to sample igneous and metamorphic rocks from the lower oceanic crust and upper mantle. The VSP for Leg 118 was planned (1) to provide seismic interval velocities with which the rock sequence drilled could be put into the context of seismic-refraction velocity structure of oceanic crust in general (Spudich and Orcutt, 1980; White, 1984; Bratt and Purdy, 1984) and fracture zones in particular (Detrick and Purdy, 1980; Cormier et al., 1984), (2) to estimate fracturing on scales greater than 0.5 m by comparing seismic interval velocities with velocities measured in the laboratory using core samples and measured *in situ* by sonic logging tools, (3) to correlate borehole lithology with the upgoing seismic reflected wavefield, (4) to predict structure and lithology changes below the drill hole, and (5) to estimate physical properties of rock on seismic scales by studying particle motion and downhole seismic attenuation.

Previous Oceanic Borehole Seismology

VSPs are a standard industry tool used most often to tie surface seismic-reflection profiles to borehole geology and logs (Gal'perin, 1974; Hardage, 1983; Balch and Lee, 1984). In scientific ocean drilling, oblique seismic experiments were conducted during DSDP Legs 52, 65, 70, 78B, 88, and 91 and during ODP Leg 102 to investigate the seismic structure of upper

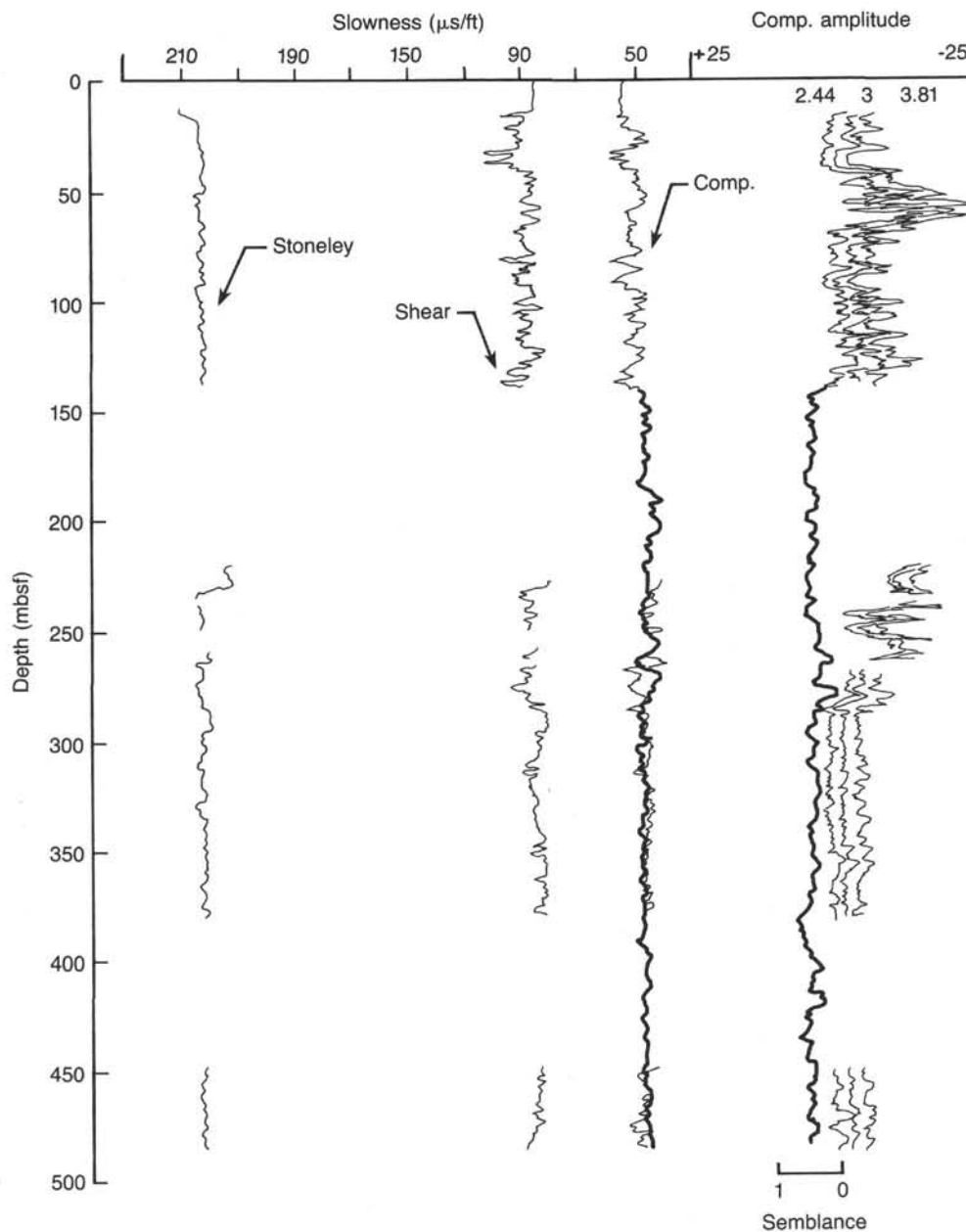


Figure 84. Compressional, shear, and Stoneley slowness (inverse of velocity) by semblance analysis of LSS waveforms. Electrical shorting in the tool caused the loss of data from 140 to 260 mbsf and from 380 to 450 mbsf. The MCS compressional slowness and semblance curves (heavy curves) are shown for comparison and are in general agreement with the LSS slowness and relative amplitudes, respectively. Compressional and shear slownesses increase and compressional amplitudes (in millivolts) decrease in the foliated gabbro interval (40–140 mbsf). Stoneley velocity remains constant at about 1.4 km/s over the entire interval.

oceanic crust (Stephen, 1979, 1983; Stephen et al., 1983; Jacobson et al., 1984; Little and Stephen, 1985; Shipboard Scientific Party, 1986; Duennbier et al., 1987; Swift et al., in press). In these experiments, a three-component borehole seismometer was clamped at one to five depths within oceanic basement, while a second ship fired airgun and explosive shots in radial lines and concentric circles around the drill ship. Conventional zero-offset VSPs were performed in oceanic basement during ODP Legs 104 and 111. These VSPs rigorously confirmed correlation of sub-basement seismic reflectors with borehole lithology and predicted the presence of significant changes in acoustic impedance below the total depth drilled (Shipboard Scientific Party, 1987, 1988a).

Setting

Hole 735B is located in 720 m of water on top of the fracture zone ridge that forms the eastern wall of the Atlantis II Fracture Zone (see “Geologic and Tectonic Setting” section, this chapter). Unprocessed, single-channel seismic profiles across the ridge crest, collected during the *Conrad* site survey and the site approach by *Resolution* (see “Operations” section, this chapter) could resolve no sediment above acoustic basement and no sub-basement reflectors in the area of Hole 735B. No refraction studies have been conducted on the eastern transform wall.

In general, not much is known about the seismic structure of fracture zone ridges. At the Kane Fracture Zone, delay-time

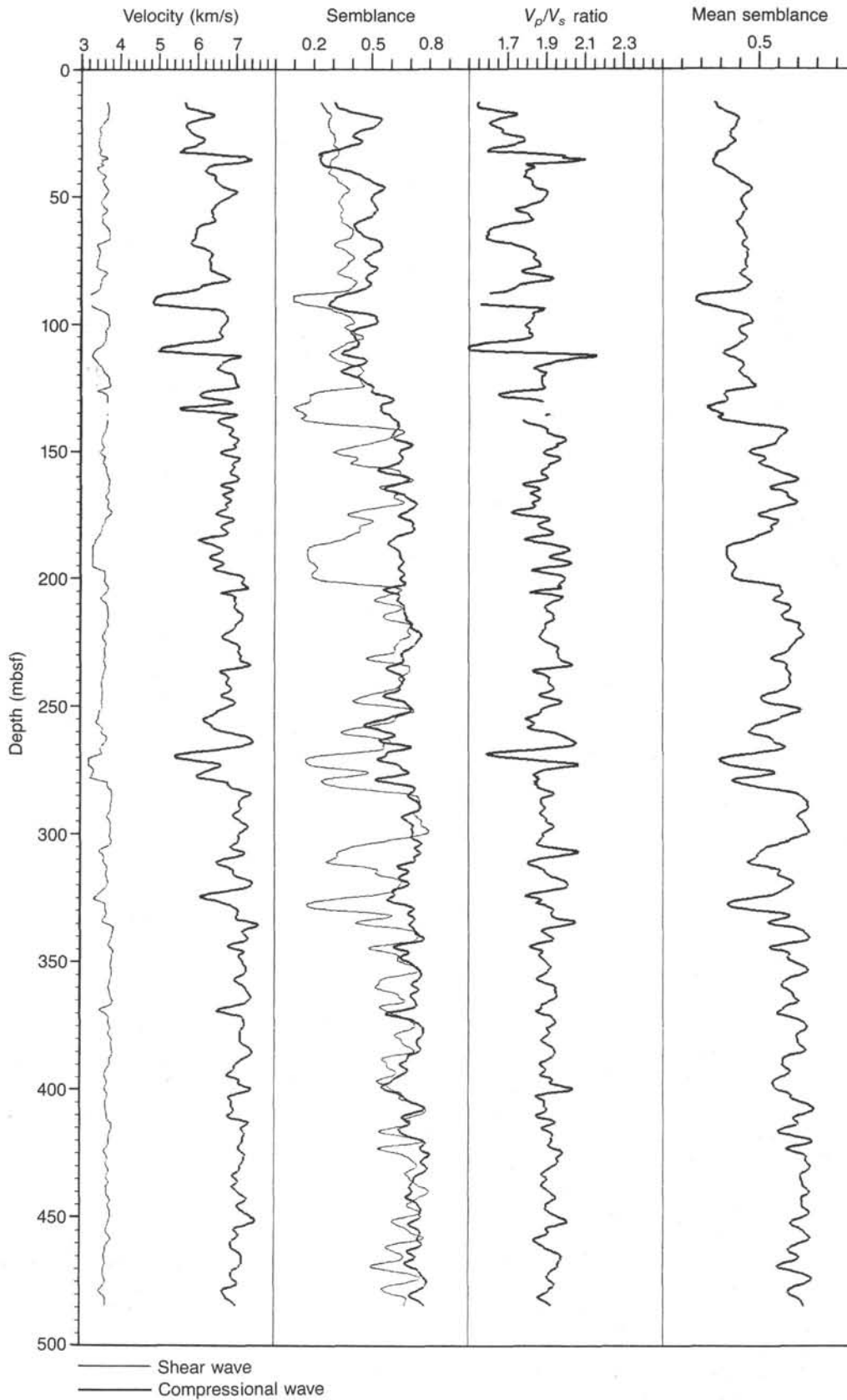


Figure 85. Compressional and shear velocity logs from 13.0 to 484.6 mbsf in Hole 735B. Peak semblance (see text) and V_p/V_s also are shown. Low velocities and semblance occur in isolated intervals below the iron-titanium oxide gabbro (265–285 mbsf) and in the foliated gabbro (40–140 mbsf) where localized fracturing or deformation occurs.

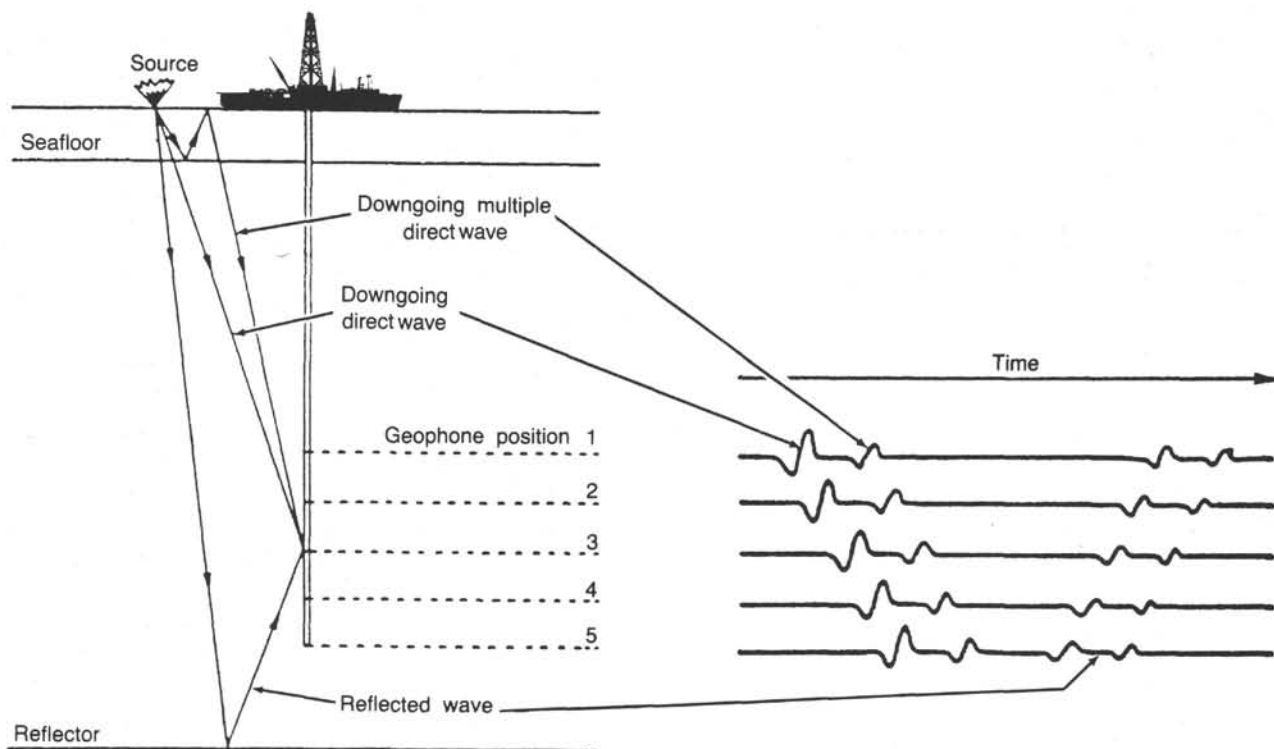


Figure 86. Schematic diagram of VSP geometry and record section illustrating how direct and reflected arrivals differ with changes in receiver depth. (Modified after Mons and Barbour, 1981).

analysis of refracted arrivals passing beneath the northern fracture zone ridge found high velocities (7.7–8.0 km/s) at shallow depths (3–4 km bsf) (Detrick and Purdy, 1980; Cormier et al., 1984). Structure within the ridge itself could not be resolved with the data. Similar results were found at the Oceanographer Fracture Zone using refraction methods (Sinha and Loudon, 1983).

METHODS

Two seismic logging tools were used to collect VSPs during Leg 118: the Schlumberger Well Seismic Tool (WST), a vertical-component seismometer, and the WHOI three-component seismometer.

Vertical-Component Seismometer

The Schlumberger WST contains four vertically oriented, 10-Hz geophones wired in series and a single-step preamplifier (60 dB). The signal is transmitted via the seven-conductor logging cable to the Schlumberger CSU logging data acquisition system. Signals were recorded for 3 s at a sampling rate of 1 kHz with no deep-water delay using both air- and water-gun sources (described next). At each receiver clamping depth, air- and water-gun shots (5–25 each) having a good signal/noise ratio were recorded and stacked. Transit time to the first arrival was detected by Schlumberger software and recorded with the stacked data on digital tape. Plots of the seismograms could not be provided on board ship because of time constraints. Later, the data tapes will be converted from Schlumberger LIS format to SEG-Y at the Lamont-Doherty Borehole Research Laboratory for further processing.

Three-Component Seismometer

The acquisition methods used during Leg 118 with the WHOI three-component tool were similar to those used in the oblique seismic experiments from earlier ocean drilling legs (Stephen, 1979; Shipboard Scientific Party, 1988a, 1988b).

Receivers

The receiver used was a Geospace Wall-Lock Seismometer with a three-channel preamplifier that can be remotely stepped through six gain settings in increments of 12 dB. Optimally, signals are sent up the

logging cable with a maximum amplitude of 25 V peak-to-peak. The sensing package consists of three sets of two 4.5-Hz geophones wired in series and aligned vertically and horizontally in two orthogonal directions. The geophones have a flat response at 4.5 to 100 Hz. After pre-amplification, the three voltage signals are sent via the seven-conductor, 10,000-m-long logging cable to the logging winch aft of the pipe racker on the helicopter deck of the *Resolution* from which they are patched into the data acquisition system in the Underway Geophysics Laboratory (UGL) (Fig. 87). Receiver depths are read from the meter wheel in the logging winch hut. To monitor the far-field source signature of the guns, an A-1 hydrophone with a preamplifier gain of +20 dB was suspended at a depth of about 250 meters below sea level (mbsl) from the starboard tautline mooring boom abeam the moon pool (Fig. 88).

Unlike VSPs run during Legs 104 and 111, the pipe could not be clamped off in the reentry cone. Because the hole was not cased and was located off center of the hard-rock guidebase, clamping the pipe into the reentry cone increased the risk of losing the bottom-hole assembly.

Recording Systems

Three signals from the seismometer and one from the hydrophone were recorded in the UGL in two ways (Fig. 89). The primary acquisition system was the ODP digital logging program HI-RES (M. Weidenspahn, Univ. of Texas, Austin) installed in a Masscomp M-500 minicomputer. After analog gain adjustment with an Ithaco Model 445 amplifier, the signals were passband filtered (Wavetek filter) between 1 and 250 Hz (115 dB per octave rolloff) to prevent aliasing and to eliminate low-frequency noise. Each of four channels was digitized at 100 Hz and stored as 32-bit IBM floating-point data in SEG-Y format on nine-track magnetic tape. A total of 4 s of signal in each channel was recorded after a sequence start and field time-break signal generated by the "Black Box" (Fig. 90).

An eight-channel Hewlett-Packard Model 3968A audio tape recorder was used as a backup recording system (Fig. 89). Four seismic signals were recorded (on 1/4 in. tape at 3-3/4 in./s) in FM channels, while time code and field time break from the blast phone were recorded on two direct channels.

Testing and Calibration

Before the experiment, we tested the attenuation effect of the seven-conductor cable in the frequency passband used by the VSP (5–250 Hz).

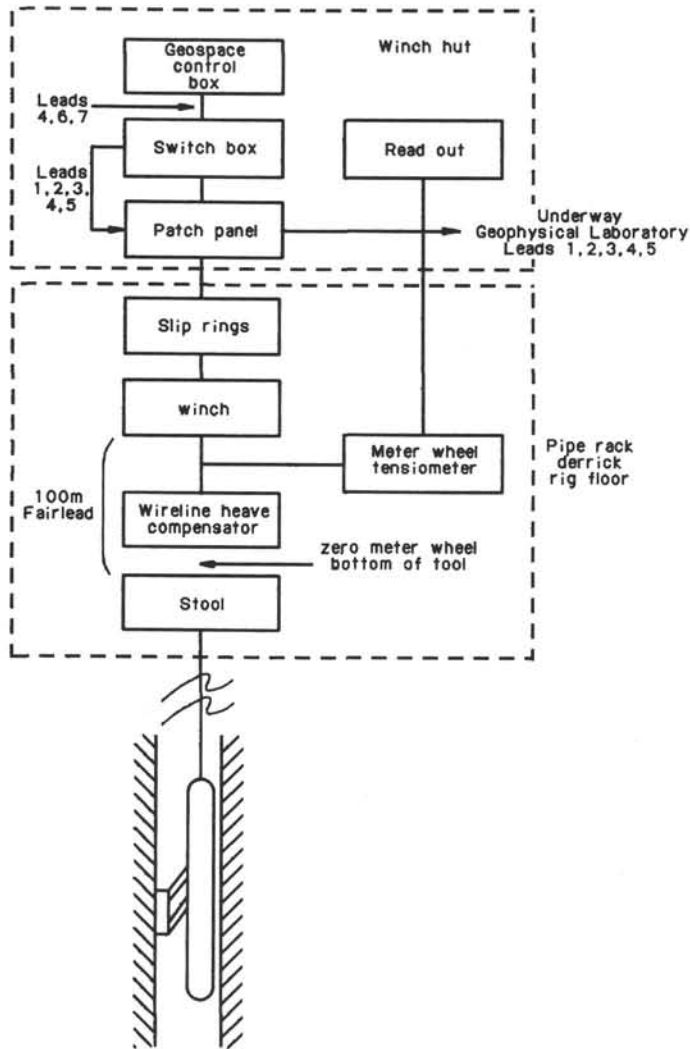


Figure 87. Block diagram of components outside the Underway Geophysics Laboratory (not to scale).

Logging Cable Attenuation

Specific details of the ODP logging cable are as follows:

1. Vector Cable Company, Type 7-46P, seven conductors, torque-balanced, double-armored logging cable.
2. Condition: new, unused.
3. Length: 31,497 ft.
4. Resistance of each conductor per 1000 ft: 10.3 ohms. Resistance of total length: 330 ohms.
5. Capacitance of each conductor to the two layers of armor per 1000 ft: 0.04 μ farads. Capacitance for total length: 1.27 μ farads.
6. The "RC" time constant of the cable from its resistance and capacitance is 0.43 ms or a frequency response of 2.3 kHz.
7. The cable is wound on a reel having a 22-in. diameter drum (62 in. outside diameter, 50 in. wide).

The test was conducted in the ODP logging winch hut with the following setup: A Wavetek Model 191, 20 MHz Pulse/Function Generator with a 50-ohm output was connected to the inboard (ship) end of the cable. Its level was set at a maximum 30 V, less the 10-dB switch, which gives about 9.6 V peak-to-peak. A two-channel Tektronix Model 485 oscilloscope was used to monitor the input to the cable from the Wavetek function generator and the output from the outboard (tool) end of the cable. The inboard end passes through a set of slip rings. The outboard end is "headed" with a Schlumberger torpedo connection (using the BCC connector). A 1.5-m-long pendant of additional cable terminates in a Gearhart-Owen female seven-pin connector assembly. Wiring con-

nections are labeled clockwise looking down the cable. For measuring purposes, an additional patch cable with a male Gearhart-Owen connector and Cannon 2-1/2 in. 10-banana pin connector was used to lead into the winch hut to the oscilloscope.

Amplitudes were measured on conductors 1, 2, and 3 using 5 as ground at frequencies of 10, 20, 50, 100, 200, and 500 Hz; 1, 2, 5, 10 kHz into a high-impedance load and into a 50-ohm load. For the high-impedance load, the 1/e point at 2.3 kHz agreed with that predicted. No measurable loss was observed up to 200 Hz; the loss at 500 Hz was about 10%, increasing to 89% at 10 kHz (Table 12, Fig. 91). No discernible 60 Hz or other noise was observed on the traces. With 50-ohm terminating load, the input loaded the signal generator heavily at the lower frequencies, but the cable losses were comparable (Fig. 91). The rolloff began at 200 Hz (20%) and was faster because of the load resistance shunting the line capacitance. Given the small amount of pickup with the high-impedance load, there was no need for a low-impedance termination.

The cross-talk between connectors (unterminated) was measured at the same frequencies between leads 2 and 3 (Table 12, Fig. 93). The cross-talk up to 100 Hz was about 0.085%, increasing to 0.1% at 200 Hz and 1% at 500 Hz.

Results of this test indicated that the 5- to 250-Hz signals from the three geophones in the WHOI seismometer can be run through the cable with little loss of signal or cross-talk between channels.

Also, before conducting the VSP experiment, the complete acquisition system was calibrated by passing a sine wave signal of various known frequencies and amplitudes into the seismometer above the geophone package, through the cable, and into both the HI-RES acquisition system and the audio tape recorder. The results of this calibration will allow us (1) to compare accurately between amplitudes in different channels, (2) to plot particle motions, and (3) to analyze downhole losses in the pressure field quantitatively. The high level of electrical noise on board the ship required considerable care in shielding and grounding, particularly in cases where single-point grounding was not feasible.

Seismic Sources

Two seismic sources were used to discriminate true seismic response of the earth from structure produced by spectral characteristics peculiar to a particular gun type. Following methods used by J. Phillips during ODP Legs 104 and 111 (Shipboard Scientific Party, 1987, 1988b), both air and water guns were suspended from a pair of Norwegian floats (Fig. 92). A Bolt Model PAR 1500 air gun having a 1000-in.³ chamber and an SSI P400 Model 2 water gun having a 400-in.³ chamber were hung with vent ports at 8.7 and 4.8 mbsl, respectively. Gun depths for the experiment were chosen after measuring far-field waveforms with the gun suspended at depths from 1.5 to 11.3 mbsl, using the source monitor hydrophone at a depth of 250 mbsl (Fig. 93). Both guns were operated at 1900 psi (higher pressure shots might damage ship thruster seals). A blast phone for detecting the shot instant was rigged 5.5 mbsl, below the water gun, but was not used during most of the experiment because of a malfunction in the timing signal system. The buoys were moored to the drill ship's aft port crane (Fig. 94). In this position, the sources were 38 m aft of the drill string, 39 m to port of the drill ship's centerline, and 53 m diagonally from the center of the moon pool. The horizontal separation between the blocks from which the hydrophone and guns were hung was about 80 m, but the actual gun-to-hydrophone distance may have varied as much as 8 m owing to currents. Because gun depth remained relatively fixed with respect to the sea surface, the source signature, which includes the reflection of the pressure field from the sea surface, remained relatively constant.

The guns were not fired simultaneously. At each receiver clamping depth, sequences of about 5-10 air-gun shots alternating with 5-10 water-gun shots were fired. Tests performed during Leg 111 comparing gun performance rigged alone and in tandem showed that the most significant shadow effects of rigging the guns on the same vertical mooring were an increase of about 5% in the peak pressure of the air-gun radiated pulse and a slight decrease in the water-gun peak pressure pulse (Shipboard Scientific Party, 1988b). During the Leg 111 test, there was no significant change in the frequencies of the guns' primary or bubble pulse.

Processing

Seismic data from the VSP were processed in the *Resolution's* computing center on a VAX 11/750 minicomputer. The SEG-Y tapes gener-

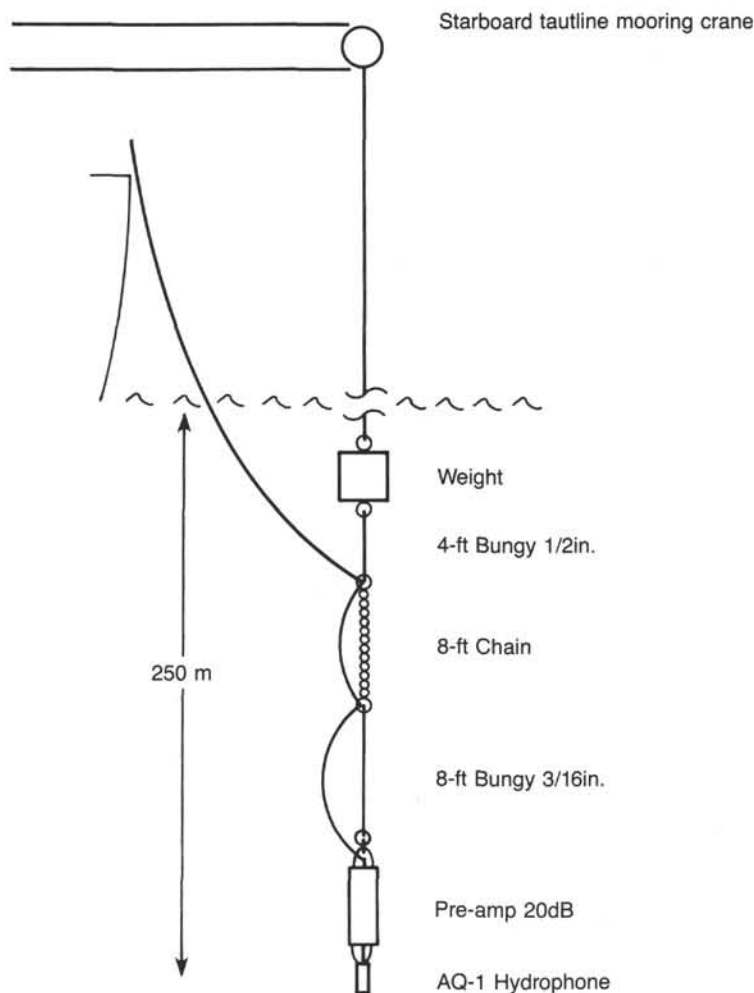


Figure 88. Schematic diagram of source monitor mooring (not to scale).

ated on the MassComp acquisition computer were reformatted to ROSE format (LaTraille, 1983) to use processing programs developed by the seismology group at WHOI. During reformatting, the gun type, gun depth, and seismometer depth below seafloor were merged into the ROSE shot headers. Shots were sorted by gun type and receiver depth and then stacked. The first arrivals of the direct wave were selected visually using a computer display and cursor program. Following standard VSP analytical procedures (Hardage, 1983; Balch and Lee, 1984), seismograms were plotted vs. depth before and after offsetting the seismograms by the direct-wave arrival time.

Navigation and Weather

The Honeywell Automatic Station Keeping (ASK) system is designed to position the *Resolution* within a horizontal offset from the hole of 1% to 1.5% of the water depth. Thus, at Hole 735B the drill pipe was nominally maintained within 10 m or 0.6° of the vertical above the receiver. Because of good weather, the deviations during the experiment were only 0 to 2 m, as determined from the ship's Honeywell ASK system. Sea state was 0 to 1 and wind was 5–10 kt from the west-northwest. A slight 8-s period northerly swell existed, and heave on the drill-pipe compensator was about 0.6 m. Ship's heading for the whole series of experiments was N36°E. The angular offset of the source was about 3.2° from the vertical above the guidebase. The Honeywell ASK system determines horizontal offsets between the ship and hole by comparing traveltimes differences to four transducers lowered 5.5 m below the ship's hull from a Datasonics

seafloor beacon and by logging the ship's heading every second. We stripped 1-min data from the ASK tapes. Transit satellite fixes, where available, also were recorded.

Operations

The VSP was scheduled near the end of logging operations in case failure of the clamping arm caused blockage and we had to abandon the hole. Considerable difficulties were initially encountered when acquiring data with the three-component seismometer. On 8 December, the tool was run into the hole, signal levels were tested, and gain levels on the tool and laboratory amplifiers were set to allow complete resolution during recording of the signal without clipping. Data were acquired at two clamping points near the bottom of the hole. On the third clamping, the signal deteriorated into random, high-amplitude fluctuations. We suspected malfunction of the pre-amplifier. The tool was pulled, and a backup tool run into the hole. The clamping arm on the second tool failed to open, and that tool also was pulled to continue other logging operations.

Both tools were opened and restored to apparent functioning condition in the downhole measurement laboratory. Eleven hours later, the first tool was run into the pipe, where it failed again. The backup tool failed to open its clamping arm on deck. On the morning of 9 December, the Schlumberger tool was run into the hole. The guns were rerigged to include a Schlumberger shot-detection blast phone and gun-triggering connections. Noise

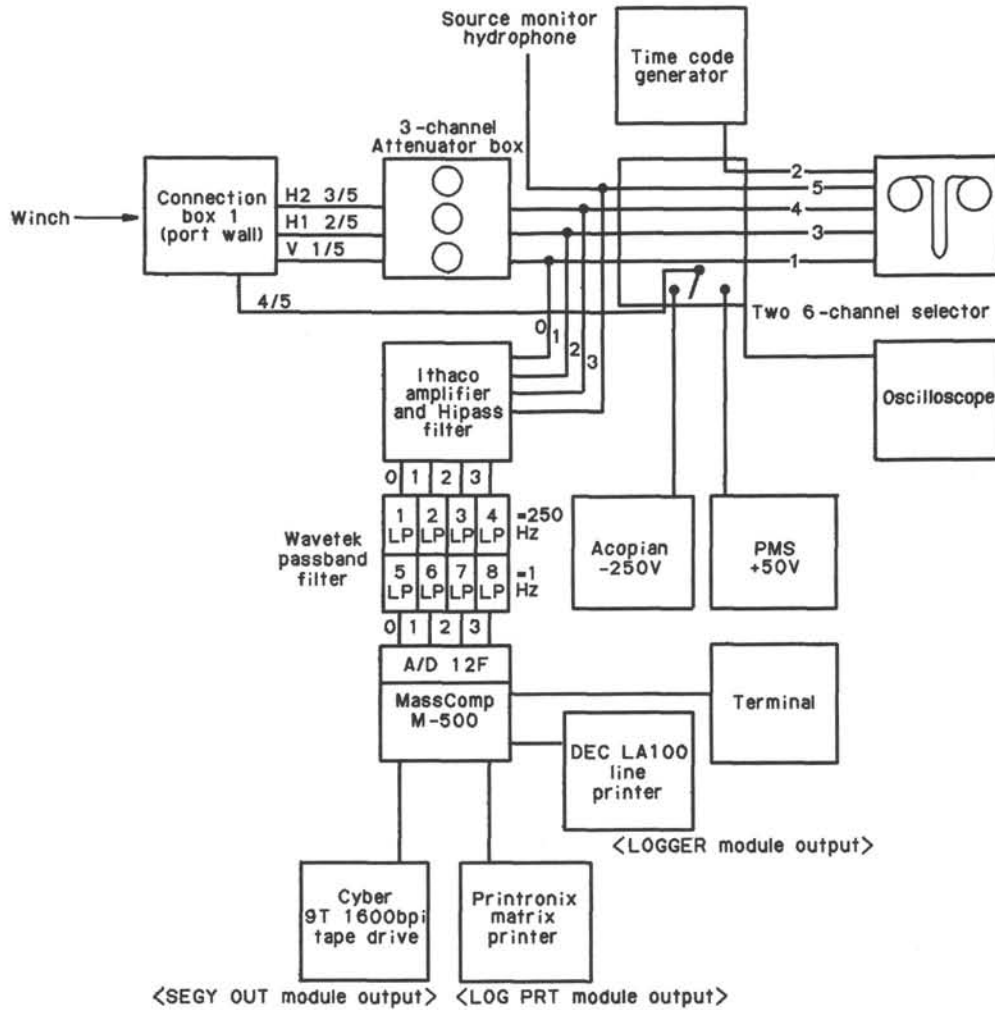


Figure 89. Schematic diagram of the processing and recording components in the Underway Geophysics Laboratory for signals from the WHOI three-component seismometer.

problems similar to those sustained by the first WHOI seismometer were initially encountered at several depths. The trouble was finally diagnosed as tool slippage on the smooth walls of the borehole. When the tool was dragged up the hole a short distance at each clamping, a firm clamp to the walls was achieved. The cable then was slacked 2 m. The tensiometer was monitored to see if the tool slipped. The change in load that occurred when the tool was adequately clamped could be better detected when not using the wireline heave compensator. The entire hole was logged at 20-m increments, and the tool recovered in good condition.

The three-component tool was then redeployed using the new clamping procedure. At the first depth, the tool was clamped firmly, and a good signal was received. The entire hole then was logged with a total of 329 air- and water-gun shots to 22 receiver depths (in addition to the two depths occupied on 8 December) in 15- to 25-m increments. In addition, background noise was recorded for 1-2 min with both guns off at six tool locations (29, 44, 74, 174, 249, and 394 mbsf). Data were also intentionally recorded while the pipe was raised and lowered to assess the

signal spectrum of noise generated by pipe motions. Qualitatively, the background noise increased as the tool approached the bottom of the drill pipe, which was suspended 12 m into the hole. The pipe appeared to make more noise at 5 m than at 12 m in the hole. This was corroborated by greater flexural motion observed on the video camera suspended immediately above the guidebase. In all, VSP operations lasted about 25 hr in the hole (Table 13).

Results and Discussion

During shooting to the two deepest WHOI receiver depths on December 8, the blast phone was used to detect shot instants and initiate the recording sequence. During shooting to the WHOI seismometer on 9 December, however, shot instants could not be determined using the blast phone signal; thus a constant, internal time break was used to trigger recording of the HI-RES system before the gun fired. The delay between the time of the first sample and the shot instant was determined by comparing average traveltimes to the hydrophone for shots using the blast phone with traveltimes for shots without the blast phone. The

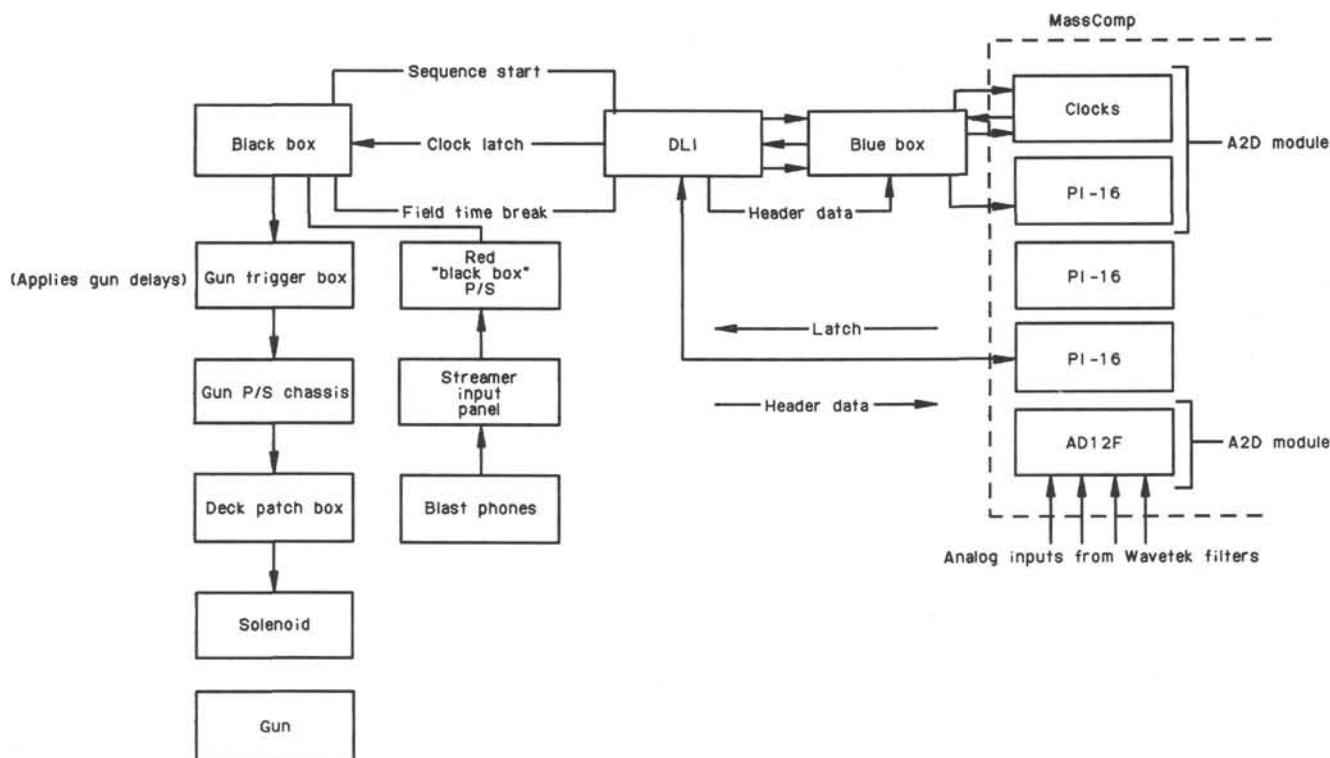


Figure 90. Timing signal flow in the Underway Geophysics Laboratory. P/S = port and starboard; DLI = data logger interface; clock = clock interface board; PI-16 = 16-bit parallel interface board; AD12F = analog to digital converter, 12-bit resolution; A2D = software acquisition module for analog to digital controller.

Table 12. Downhole time required for vertical seismic profiling.

Date (1987)	Time	Activity
8 December	5 hr 30 min	Log bottom 20 m of hole. Both 3-component tools fail.
8 December	2 hr	Rerun WHOI tools. Both tools fail.
8 December	11 hr 30 min	Schlumberger 1-component tool. Log entire hole.
9 December	5 hr 45 min	WHOI tool. Finished logging upper 480 m of hole.

differences in traveltimes for water and air guns (0.073 and 0.075 s, respectively) were applied as static corrections to the stacked shot files.

Most of the data on the vertical channel using either gun are of good quality and have fair signal-to-noise characteristics. Figure 95 indicates for each gun type an example of the data in each of the four channels. Figures 96 and 97 show the stacked record sections for air and water guns, respectively. Random noise is more common at depths below 350 mbsf and exceeds the signal level in some shots. Because tool clamping took longer at these depths, we suspect that the noise was caused by slow slippage of the tool. The caliper log indicated that the hole was smoother at depth.

Data from the horizontal channels are generally ringy with few, if any, distinct events after the first arrival. Since little noise preceded the first arrival, pipe banging is not a likely source. The ringing may be horizontal oscillation of the tool set up by the passage of the compressional wave.

Coherent noise is the most significant problem when identifying coherent reflectors in the record sections. The air-gun signature has strong bubble pulses at 0.1 and 0.2 s after the primary pulse. Later arrivals were obscured by a water bottom

multiple that arrived at about 1.5 s (Figs. 96 and 97). When the data are shifted by subtracting the one-way traveltime to the receiver (Fig. 98), the downgoing wave trains are aligned. Two additional water bottom multiples are apparent at about 2 and 3 s. Post-cruise processing of the signal using source signature deconvolution with the hydrophone recordings of the outgoing pulse may suppress coherent noise.

The traveltimes selected from the vertical component of the stacked seismograms for both VSP runs are presented in Tables 14 and 15 and Figure 99. The waveform and phase of the initial arrival was similar at all receiver depths. Sources of error include a small systematic uncertainty in shot time ($+0.004$ s, 95% confidence limit). Additional sources of error are imprecision in selecting arrivals in seismograms and obscuring of the first arrival by noise. These random errors contribute $+0.006$ to 0.008 s. Thus, total systematic and random error is about $+0.010$ to 0.012 s. Traveltime differences between receiver clampings spaced 20 to 25 m apart are about 7 to 8 ms. Because errors in transit times are twice the time differences, little significance should be given to incremental gradient changes between clampings in Figure 99.

The vertical channel traveltime data sets from VSPs with the three-component tool and the Schlumberger tool are consistent. The slopes of both traveltime curves are relatively constant downhole. Straight lines were fit by least squares to the individual water- and air-gun data sets and to all traveltimes from each receiver (Table 16). There are no significant differences between traveltimes selected from air- and water-gun data. When all data are included, the slopes of the single and three-component tool data are similar: 6.38 and 6.51 km/s, respectively. The 95% confidence limits of the slopes determined in the better constrained data sets are about ± 0.15 km/s. These velocities are consistent with velocities measured on hand samples that are representative of the general lithology (see "Physical Properties" section, this chapter). Fracturing on scales much greater

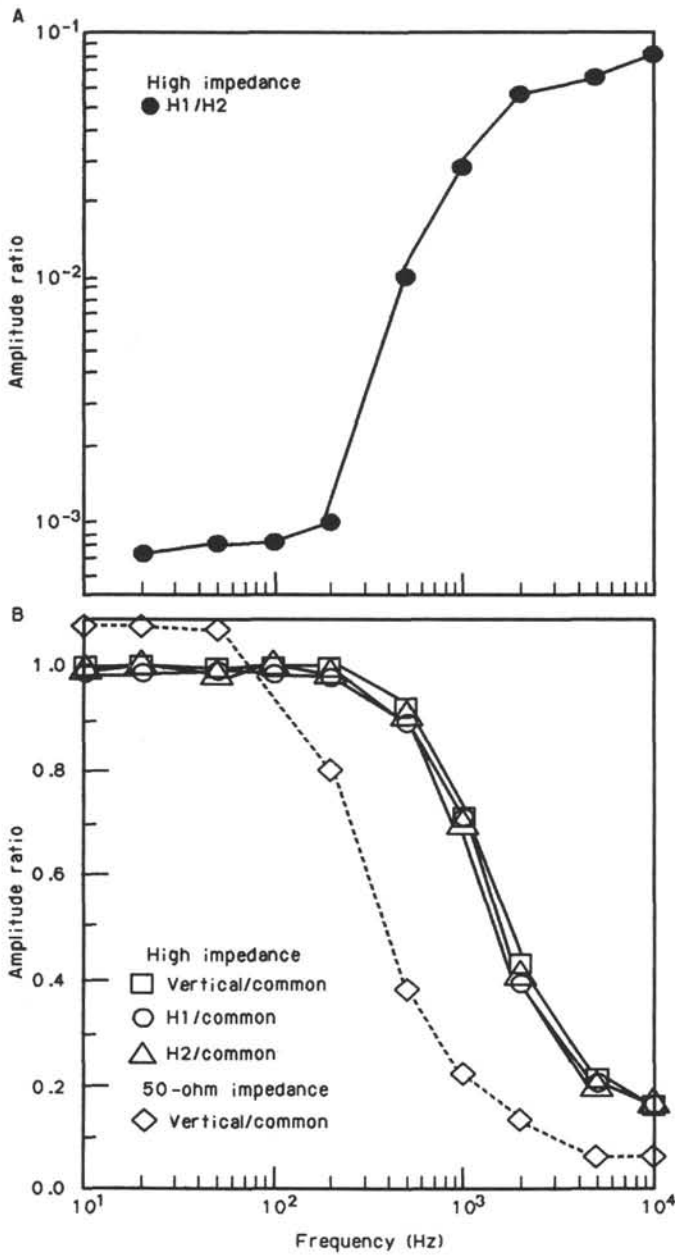


Figure 91. A. Amplitude ratio of high-impedance load. B. Amplitude ratio of 50-ohm impedance load.

than that resolvable by core studies, which would have the effect of reducing seismic velocities relative to laboratory measurements, appears to be relatively insignificant at Hole 735B.

In Figure 100, the stacked air-gun data are offset by the traveltimes to the first arrival; thus, the upgoing reflections from below the seafloor are aligned at their two-way traveltimes. Record sections with and without automatic gain control (AGC) scaling are shown. Most of the coherent signal dips and thus can be considered coherent noise. At about 1.4 s in the AGC seismograms from the shallowest seismometer depths, the reflector amplitude decreases and cannot be distinguished from the downgoing compressional-wave train. Any reflectors earlier than this event are too weak to be resolved without further processing, as compared to the high-amplitude downgoing pulse.

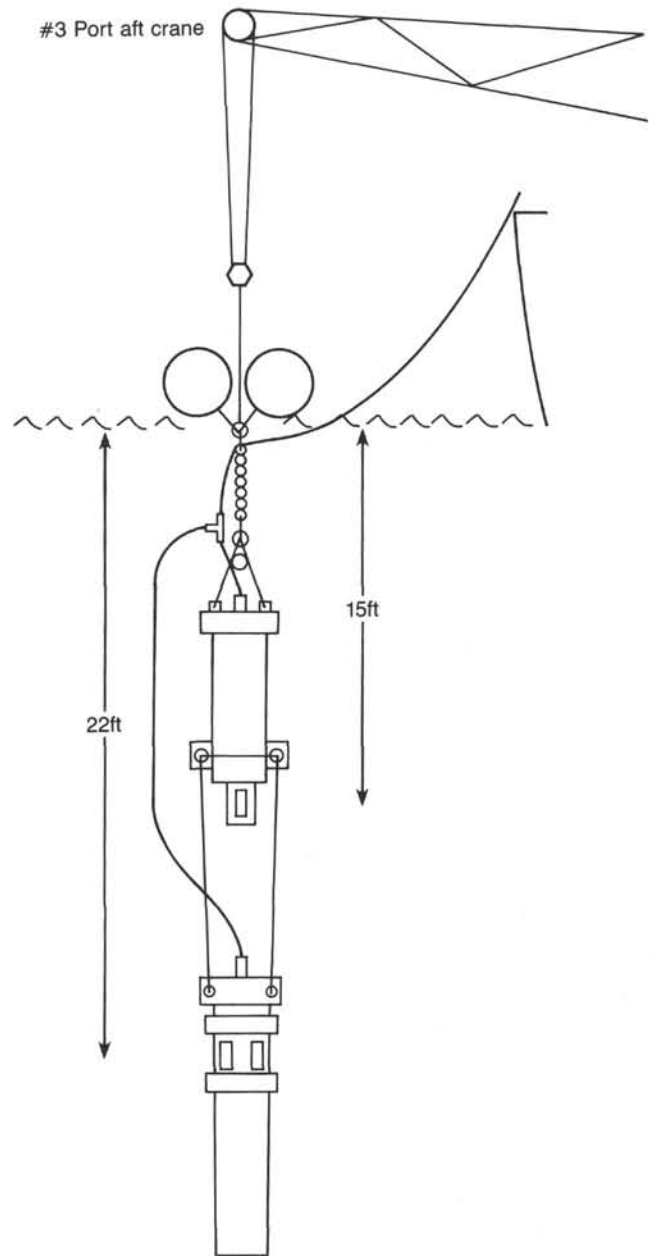


Figure 92. Schematic diagram of gun mooring (not to scale).

The reflector occurs about 0.3 s after the first arrival to the shallowest receiver depth. Allowing for two-way traveltimes and using a velocity of 6.5 km/s, the reflector occurs at about 1 km below the seafloor. This places the impedance change causing the event at about 4 km above the floor of the fracture zone. Speculatively, the event might be a reflection off a fault surface or a 50- to 200-m-thick transition in physical properties or lithology. The possibility cannot be excluded with these data that the event marks upwelling mantle, as suggested by the high velocities found below the Kane Fracture Zone ridge (Cormier et al., 1984).

Conclusions

Seismic velocities are uniform on the scale of 50–200 m throughout Hole 735B. Seismic velocity averages 6.4–6.5 km/s.

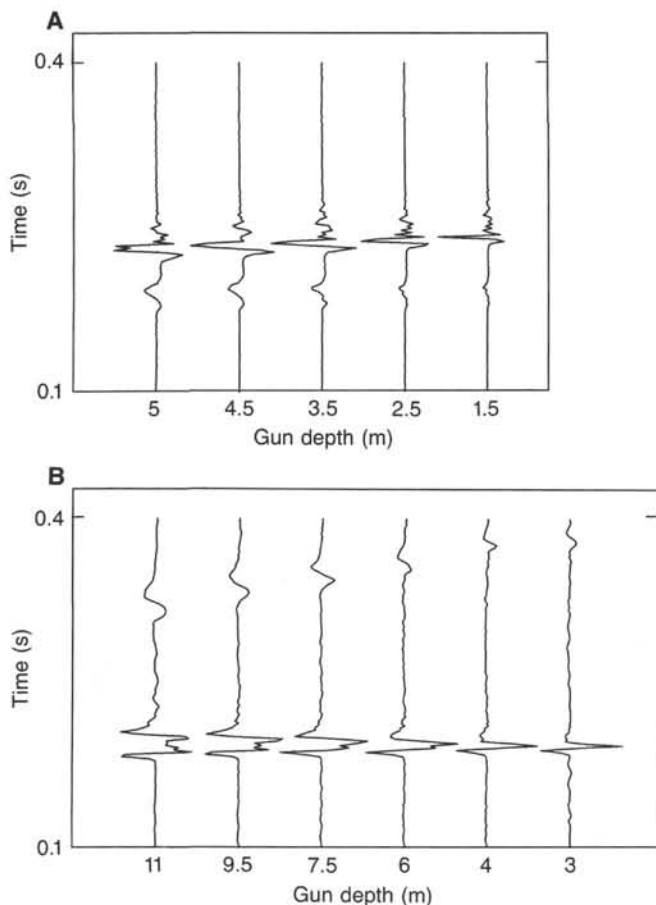


Figure 93. Gun signatures, received by source monitor hydrophone at 250 mbsl, as a function of nominal port depth. A. Water gun. B. Air gun. Amplitude scaling of water-gun traces is six times that of air gun.

No evidence in the seismic data exists for lower velocities associated with the deformation zones and faulting determined in cores.

A weak reflector occurs at 1.4 s two-way traveltime, about 1 km below seafloor. A long, high-amplitude downgoing pulse obscures any reflectors occurring at shallower depths.

MAGNETOMETER LOGS

Background

Magnetic logging was first attempted during DSDP Legs 68 (Hole 501), 69 (Holes 504B and 505B), and 78B (Hole 395A) by Ponomarev and Nechoroshkov (1983, 1984) using a combination three-component magnetometer and magnetic-susceptibility probe designed and built in the U.S.S.R. The three fluxgate elements of the magnetometer were oriented by gravity in a gimbal suspension system that positioned one of the elements in line with the probe axis, another one horizontal and perpendicular to the direction of inclination of the borehole, and the third perpendicular to the first two and in the plane of inclination of the borehole. The gravitational orientation of the horizontal elements depended on the borehole being somewhat deviated from the vertical, and as the DSDP holes were nearly vertical, the azimuthal orientation was not well controlled and the magnetic declination could not be measured accurately. However, because of the near verticality of the holes, the element in line with the probe axis was positioned appropriately to measure the vertical component, and so it was possible to determine the inclination of the Earth's field; and because the rocks were strongly mag-

netized, it was possible to determine the inclination of the remanent vector *in situ*. Downhole susceptibility measurements using the combination probe were inaccurate because of temperature problems, and so core susceptibilities were used in their place for interpreting the downhole magnetometer data.

During ODP Leg 102, a three-component magnetometer probe with inclinometer and gyro orientation was provided by the Federal Institute for Geosciences and Natural Resources (BGR) of the Federal Republic of Germany (F.R.G.), and a susceptibility probe was provided by the USGS for logging Hole 418A (Bosum and Scott, 1988). The borehole measurements, which showed a clear reversal in the direction of polarization of the lower basalt section, were interpreted to determine the amplitude and direction of the remanent vector in this interval. The downhole susceptibility measurements were relatively stable because the sensing coil was kept at a nearly constant temperature in a heated chamber near the bottom of the probe. The interpreted results of the downhole magnetic field and susceptibility measurements agreed favorably with those obtained from paleomagnetic laboratory measurements of cores made during DSDP Leg 53 (Levi, 1979).

During ODP Leg 109, magnetometer logs were run in Hole 395A with three different probes (Shipboard Scientific Party, 1988b). One was the same BGR probe used during Leg 102, another was an unoriented, high-temperature, three-component magnetometer probe of Japanese design, and the third was the unoriented, three-component magnetometer in the Schlumberger General Purpose Inclinometer Capsule (GPIC) that was run with the Schlumberger Litho-Density Tool (LDT). The Japanese magnetometer logs were interpreted to determine the total field, vertical and horizontal components, and inclination. Although the BGR probe was equipped with inclinometers and a gyro for orientation, this system was not completely operational during Leg 109 because the lower assembly of the probe broke off and was lost in the hole. Therefore, only the vertical component of the Earth's field was recorded. The Schlumberger magnetometer, though relatively insensitive, was used to record the three measured components and the total field. An experimental three-coil magnetic-susceptibility probe developed by the Institute of Applied Geophysics (University of Munich, F.R.G.) was also run successfully during Leg 109.

During Leg 111, the same Japanese and Schlumberger three-component magnetometer probes were run in Hole 504B. Unfortunately, the rechargeable battery power supply of the Japanese probe shorted out, causing the batteries to explode, which made data retrieval impossible. Although the sensitivity of the Schlumberger magnetometer was fairly low, the log revealed two features very clearly: (1) a change of *in-situ* inclination between pillow basalts and the sheeted dike complex and (2) abrupt changes in remanent magnetic intensity between the pillow basalts and pillow-dike transition and between the sheeted dike complex (Shipboard Scientific Party, 1988a).

Leg 118 Magnetic Logging Equipment

During Leg 118, downhole magnetic measurements were performed with the same USGS susceptibility probe used during Leg 102: a USGS three-component magnetometer probe similar to the BGR probe with gyro and inclinometer orientation, and a combination three-component magnetometer and susceptibility probe developed by the University of Washington (UW) in coordination with the Lamont-Doherty Borehole Research Group. The unoriented magnetometer in the Schlumberger GPIC capsule was also run in conjunction with the Schlumberger LDT tool. The magnetic logging tools run during Leg 118 are described in detail in the following paragraphs.

The USGS magnetic-susceptibility probe contains a solenoid sensing coil connected in the measuring arm of a Maxwell

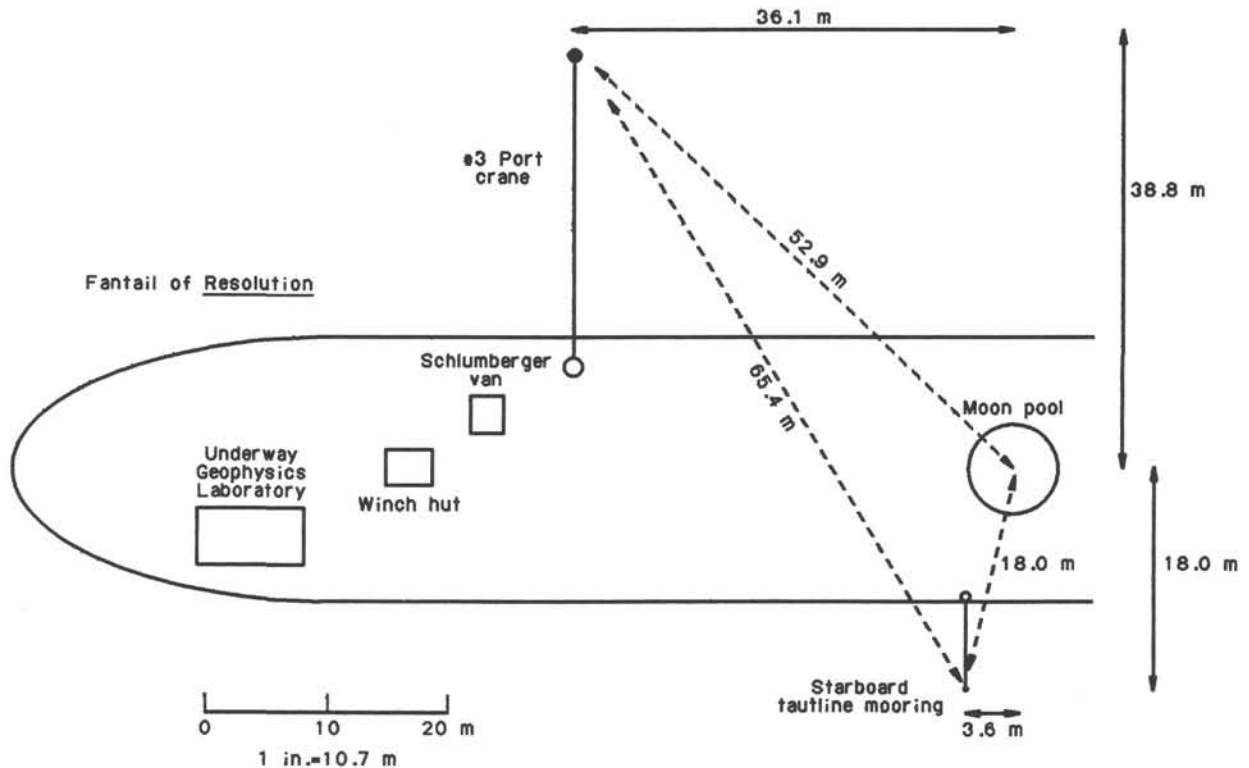


Figure 94. Scaled layout of VSP showing relative positions of receiver (center of moon pool), sources (outboard end of number 3 port crane), and source monitor (starboard tautline mooring).

Table 13. Amplitude ratio between connectors.

Frequency (Hz)	Vertical (1/5) high imp.	Horiz. 1 (2/5) high imp.	Horiz. 2 (3/5) high imp.	Vertical (1/5) 50-ohm imp.	H1/H2 (2/3) high imp.
10	1.00	0.99	0.99	1.08	—
20	1.00	0.99	1.00	1.08	0.00075
50	1.00	0.99	0.98	1.07	0.00083
100	1.00	0.99	1.00	1.00	0.00084
200	1.00	0.98	0.98	0.80	0.001
500	0.92	0.89	0.90	0.38	0.010
1,000	0.71	0.71	0.69	0.22	0.028
2,000	0.43	0.39	0.40	0.13	0.056
5,000	0.21	0.20	0.19	0.06	0.064
10,000	0.16	0.16	0.16	0.06	0.080
20,000	—	—	—	0.02	0.070

bridge, which is nulled in a zero-susceptibility environment (air) prior to logging (Scott et al., 1981). The sensing coil is contained in a thermally insulated chamber where the temperature is held nearly constant (at 82°C) to minimize drift. The off-null signal from the bridge is sent up the logging cable along with a reference signal from the 1000-Hz oscillator (both in analog form) to the surface module, where a phase detector is used to separate the susceptibility component from the conductivity component. The amplitude of the susceptibility signal is a nearly linear function of the susceptibility of rock near the borehole in the range 0–20,000 × 10⁻⁶ cgs. The conductivity signal is useful only for detecting concentrations of highly conductive minerals such as graphite and metallic sulfides because at the operating frequency of 1000 Hz, the bridge is relatively insensitive to changes in resistivity above 0.1 ohm-m, although it is quite sensitive to susceptibility at this frequency. A block diagram of the USGS borehole magnetic-susceptibility system is shown in Figure 101. A Hewlett-Packard HP-9845B desktop computer was

used to control data acquisition; digitization was accomplished by an HP-3455A DVM. Data were recorded by an HP-9875A digital magnetic tape unit. The depth of the probe was obtained from the ship's wireline winch system, which was monitored by the MassComp computer in the Downhole Measurements Laboratory and transferred to the HP-9845B computer via an RS-232 cable link. During logging, weight sections were added to the bottom of the probe, which made the total weight 143 kg and total length 8 m.

The USGS three-component magnetometer probe is shown schematically in Figure 102 (Scott and Olson, 1985). The probe's gyroscopic azimuthal reference is read to the nearest 0.1° from 0–358° (with a dead band from 358° to 360°), and must be corrected for drift, which usually is 1° or 2°/hr. Gyro drift is assumed to be linear with time, and time is recorded to the nearest second when each probe reading is taken. Azimuthal reference readings are made with the X-axis of the probe oriented in a known direction before and after logging by means of a telescopic sight that is temporarily attached to the top of the probe for that purpose. A gyro drift correction is computed for each probe reading from the azimuthal sightings made before and after the logging run and from the time recorded for each reading. The probe contains two inclinometers aligned with the probe's horizontal X- and Y-axes that are used to measure the tilt of the probe to 0.01°. The three orthogonally oriented fluxgate magnetometer elements measure the Earth's magnetic field to a resolution of 10 nT. The internal temperature of the probe is measured to 0.1°C and is used to correct the inclinometer and magnetometer readings for temperature effects. The offset voltage of the downhole power supply is also monitored while the other measurements are being conducted. These eight parameters are digitized downhole and sent up the cable as a pulse-coded FM signal that is decoded by a surface control module. The control module is connected to the Hewlett-Packard 9845B desktop

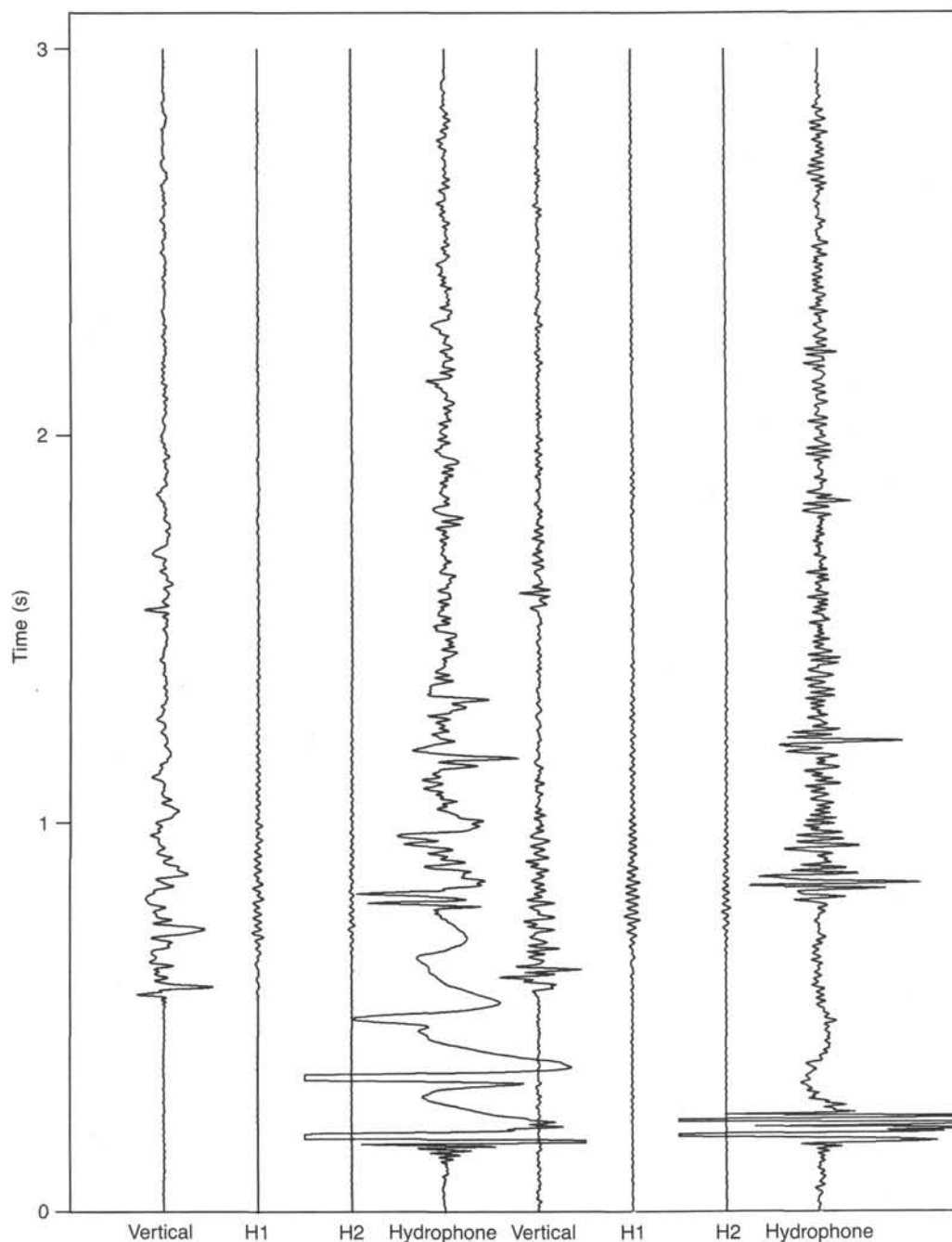


Figure 95. Examples of stacked seismograms. Four channels shown for air gun (left) and water gun (right). Receiver at 489 mbsf. True amplitude scaling with amplitude of water-gun traces scaled up by about twice that of air-gun traces. Passband filtered at 5 to 80 Hz. Highest peaks in the first 0.3 s on hydrophone traces were clipped intentionally to improve clarity of display.

computer by an RS-232 interface cable. The computer is used to control the acquisition of borehole data and to record all of the downhole measurement parameters, along with time and depth information obtained from computer peripherals (clock and depth modules). Depth values are obtained via an RS-232 link to the MassComp computer, which is used to monitor the ship's wireline winch measurement system. Depth, time, and probe readings are transferred by a Hewlett-Packard IB interface cable to an HP-9875A tape deck that records them on digital tape. During logging, centralizer springs and weight sections were attached to the top and bottom of the probe, increasing the total weight to 206 kg and length to 12 m.

The UW combination magnetometer-susceptibility tool was recently developed in conjunction with the Lamont-Doherty Borehole Research Group for routine use during ODP legs that include downhole logging measurements. A large portion of the probe was designed by IFG Corporation of Toronto, Canada, which made several modifications to the basic design of the probe specifically for ODP logging. The tool contains three orthogonally oriented ring-core fluxgate magnetometers and a susceptibility coil and can operate at temperatures up to 125°C. Although the tool is not oriented azimuthally at the present time, this is a feature that will be included eventually. Data are digitized downhole, and a total of eight parameters can be mon-

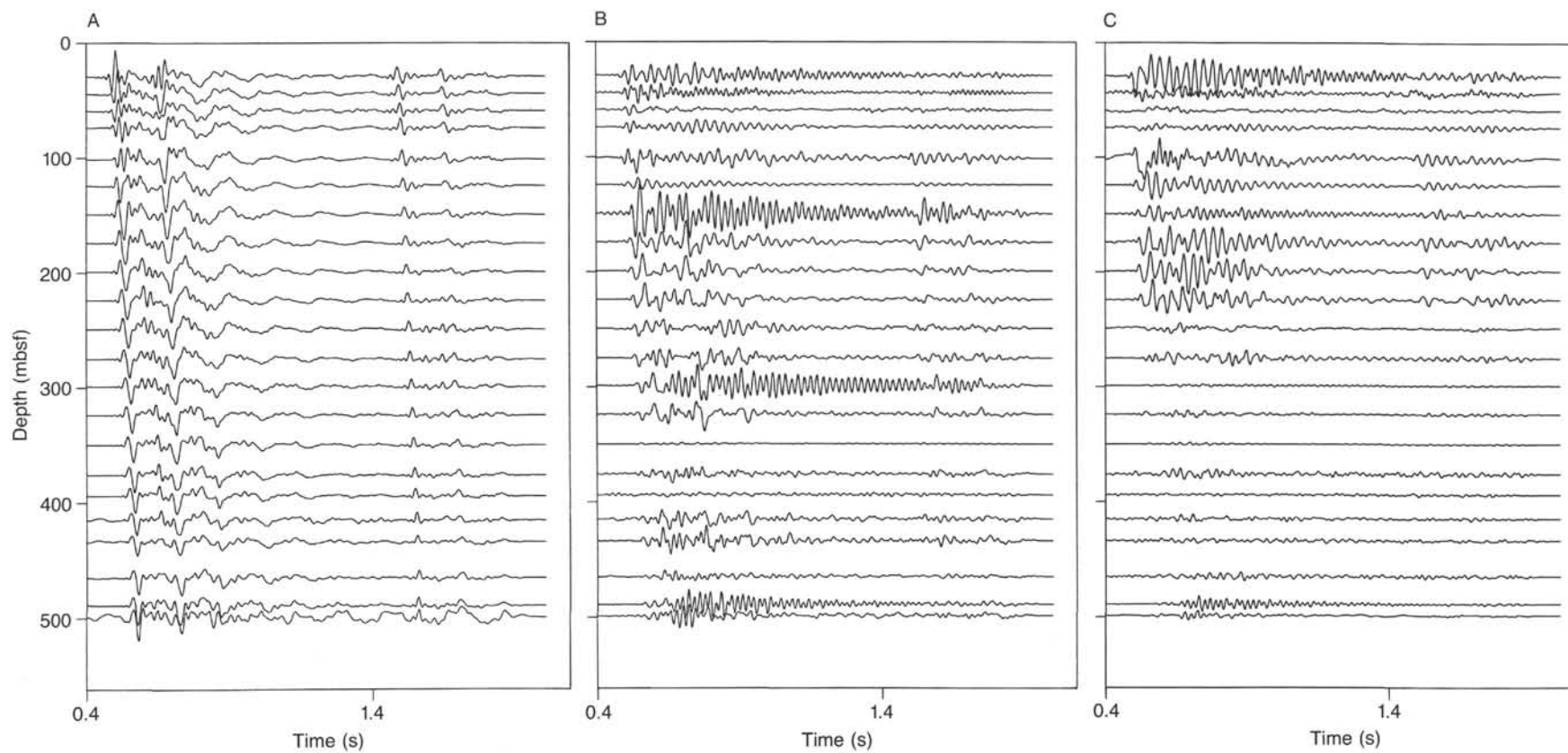


Figure 96. Stacked air-gun seismograms plotted vs. receiver depth below seafloor. Vertical (A), horizontal 1 (B), and horizontal 2 (C) channels. Passband filtered at 5 to 50 Hz. True amplitude scaling. Vertical channel: all seismograms scaled the same; horizontal 1: 3.3X vertical channel at 0–80 mbsf and 12X vertical channel at 80–500 mbsf; horizontal 2: 3.3X vertical channel at 0–80 m and 36X vertical channel at 80–500 mbsf. Azimuth of H1 and H2 varies with depth.

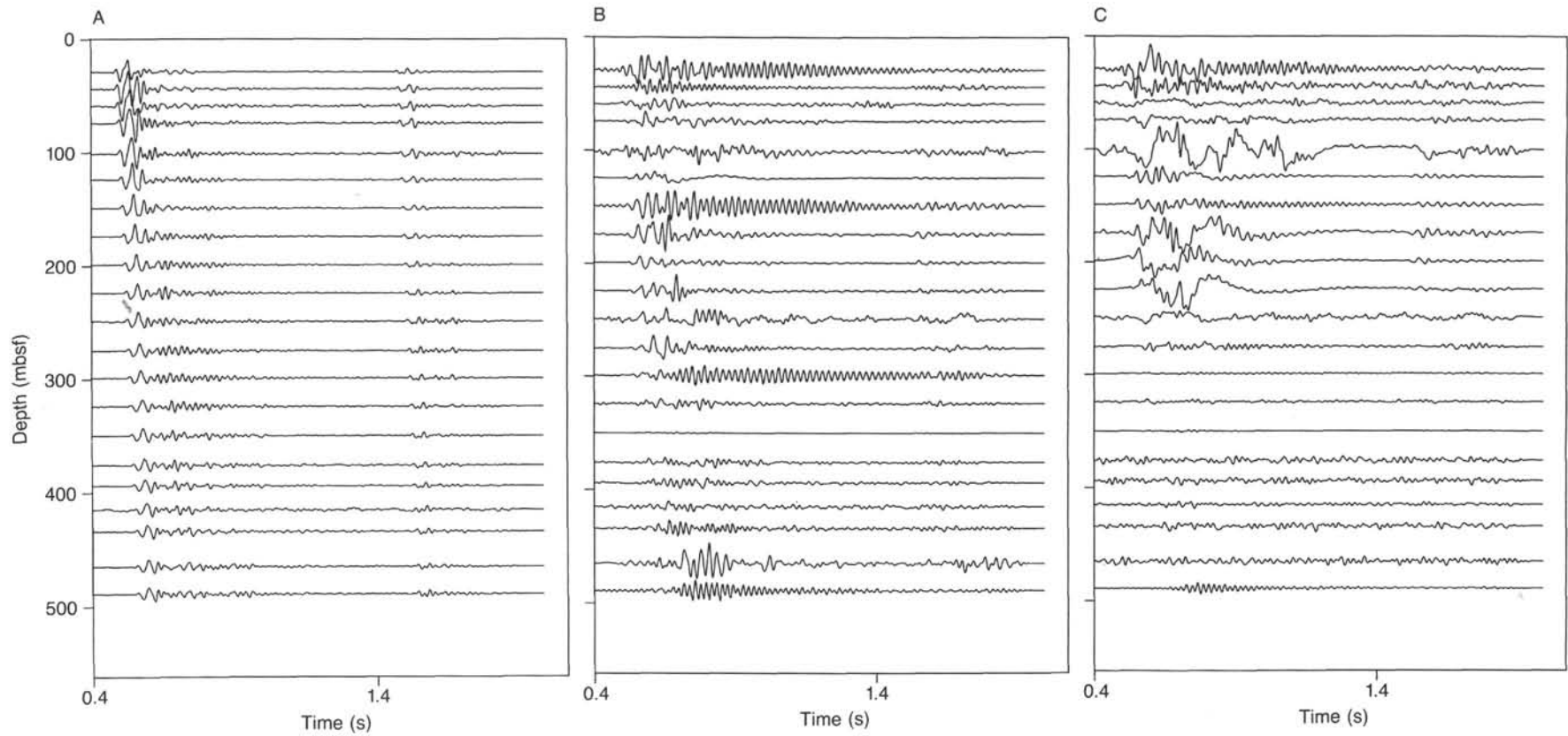


Figure 97. Stacked water-gun seismograms plotted vs. receiver depth below seafloor. Vertical (A), horizontal 1 (B), and horizontal 2 (C) channels. Passband filtered at 5 to 50 Hz. True amplitude scaling. Vertical channel: all seismograms scaled the same; horizontal 1: 3X vertical channel at 0–80 mbsf and 10X vertical channel at 80–500 mbsf; Horizontal 2: 3X vertical channel at 0–80 mbsf and 30X vertical channel at 80–500 mbsf. Azimuth of H1 and H2 varies with depth.

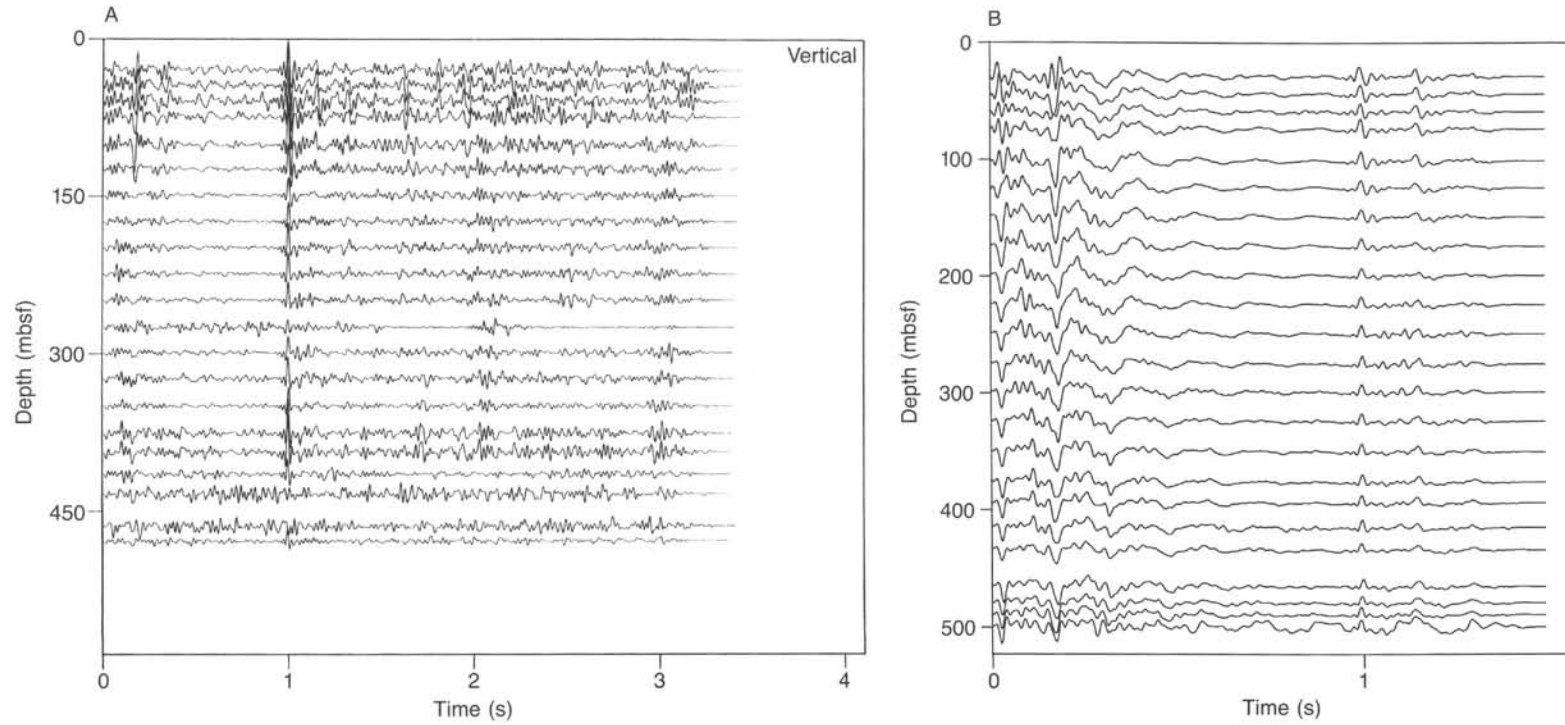


Figure 98. Air-gun (vertical channel) seismograms. Traces have been shifted to earlier time by subtracting the first arrival time. A. True amplitude scaling. Passband filtered at 5 to 50 Hz. B. Automatic gain control using a window of 0.5 s. Deconvolved with a Burg filter 0.2 s long.

Table 14. First compressional-wave arrival time selected from seismograms recorded using the WHOI three-component seismometer.

Receiver depth (mbsf)	Air gun		Water gun	
	Number of shots in stack	Arrival time (s)	Number of shots in stack	Arrival time (s)
29	6	0.482	6	0.482
44	5	0.485	6	0.485
59	7	0.489	5	0.489
74	6	0.491	6	0.492
101	8	0.495	6	0.496
124	6	0.499	6	0.501
149	6	0.503	3	0.503
174	7	0.507	5	0.508
199	6	0.509	8	0.511
224	8	0.515	5	0.515
249	6	0.518	6	0.518
275	6	0.521	6	0.522
299	7	0.526	5	0.526
324	4	0.530	5	0.530
350	7	0.534	4	0.534
376	6	0.537	6	0.538
394	11	0.541	5	0.538
415	4	0.545	5	0.545
434	6	0.548	5	0.547
465	9	0.549	4	0.552
479	5	0.553	4	0.602
489	11	0.552	4	—
499	7	0.554	—	—

Table 15. First compressional-wave arrival time selected from seismograms recorded using the Schlumberger vertical-component seismometer.

Receiver depth (mbsf)	Air gun		Water gun	
	Number of shots in stack	Arrival time (s)	Number of shots in stack	Arrival time (s)
29	5	0.483	—	—
39	6	0.485	4	0.488
59	7	0.488	6	—
70	5	—	6	—
99	5	—	5	—
115	6	0.497	5	0.468?
119	7	—	7	—
139	5	0.301?	6	0.505
151	—	—	5	—
159	—	—	—	—
160	5	—	—	—
179	5	—	5	0.508
199	5	0.511	5	—
214	6	0.513	5	0.515
219	5	0.514	5	—
239	4	0.515	2	0.671?
259	5	0.520	5	—
279	5	0.524	5	0.527
299	5	0.527	5	—
319	5	0.527	5	—
320	6	0.530	5	0.530
339	6	0.533	5	—
359	5	—	5	0.538
379	—	—	6	—
390	5	0.540	6	0.440?
415	5	—	5	0.545
428	5	—	5	—
450	5	—	5	0.550
466	6	—	1	—
491	5	—	4	—

itored on the surface. These include the *X*, *Y*, and *Z* components of the magnetic field, total magnetic intensity, magnetic susceptibility, internal voltage, the temperature of the electronics section, and the temperature of the magnetometer section.

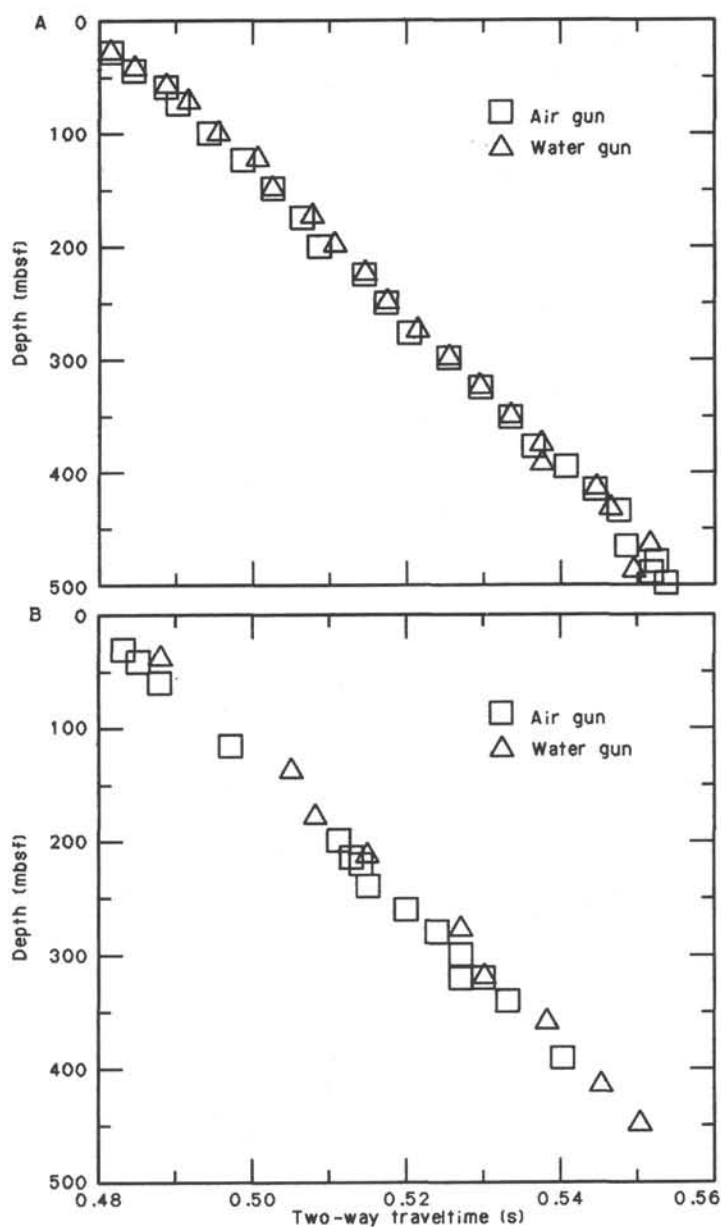


Figure 99. Plot of two-way traveltimes of first compressional arrival selected from stacked seismograms vs. depth below seafloor. A. WHOI three-component seismometer. B. Schlumberger vertical-component seismometer.

Logging Data

The susceptibility log obtained with the USGS tool was made by logging uphole at a speed of 9 m/min after allowing the probe to approach thermal stability at the bottom for about 30 min. Data reduction included applying a correction for hole diameter and applying a five-point smoothing filter. Results indicate that the susceptibility of gabbro in the upper 200-m section of the hole is extremely variable, with one thin zone approaching 7000×10^{-6} cgs and many thin anomalies peaking out between 1000 and 2000×10^{-6} cgs, but with many other values approaching zero (Fig. 103). Midway down the hole, a 60-m zone of high susceptibility (2000 – 4000×10^{-6} cgs) occurs in a gabbroic section containing anomalously high concentrations of magnetite and ilmenite. Below the magnetite-ilmenite-

Table 16. Linear regression fits of first arrival times from vertical channel seismograms.

Data	Intercept (s)	Inverse slope (km/s)	Number of points	Regression coefficient (r)
WHOI Seismometer				
Air gun, all depths	0.4796	6.530	23	0.9987
Air gun, 0–435 m	0.4788	6.327	19	0.9993
Water gun, all depths	0.4798	6.459	20	0.9987
Water gun, 0–435 m	0.4798	6.467	19	0.9984
Both guns, all depths	0.4797	—	43	0.9986
Both guns, 0–435 m	0.4793	6.396	38	0.9988
Schlumberger Seismometer				
Air gun	0.4788	6.321	15	0.9987
Water gun	0.4827	6.617	9	0.9981
Both guns	0.4799	6.384	24	0.9968

rich gabbros a magnetically quiet zone 100 m thick occurs, with susceptibility averaging $200\text{--}300 \times 10^{-6}$ cgs. Below this zone another highly variable 100-m-thick interval occurs near the bottom of the hole, with susceptibilities in the range $200\text{--}3000 \times 10^{-6}$ cgs. This interval is also characterized by high magnetite and ilmenite concentrations in the drill cores.

The logs obtained with the USGS magnetometer tool are shown in Figures 104 and 105. Logs of probe orientation vs. depth are shown in Figures 104A and 104B. In Figure 104A the azimuth of the probe (direction that the bottom of the probe points toward) is referenced to the gyro, and in Figure 104B, it is referenced to the magnetometer. In both cases, 0° represents magnetic north and $\pm 180^\circ$ represents magnetic south. The log in Figure 104A is referenced to magnetic north at sea level, and the log in Figure 104B is referenced to local magnetic north, as measured in the borehole by the magnetometer in the probe. Local magnetic north varies throughout the hole in the sections containing strongly magnetized rocks. An example of this variability can be seen in Figure 104B in the depth interval 230–280 mbsf, where the azimuth referenced to the magnetometer deviates as much as 90° from the azimuth referenced to the gyro in Figure 104A. Figure 104C shows the tilt of the probe (and the borehole) with respect to the vertical. Near the top of the hole, the tilt is about 6° and the hole points about 30° east of magnetic north (almost directly toward true north because the magnetic declination is 32° west at the site). The bottom of the hole tilts about 4° from the vertical and points toward magnetic east (equivalent to $N60^\circ E$ with respect to true north).

Figure 106 shows the direction and magnitude of the magnetic vector representing the Earth's field, as measured in Hole 735B. Figure 105A gives the azimuthal direction of the horizontal component of the Earth's field referenced to magnetic north at sea level above the hole. Figure 106B shows the inclination of the field in the borehole, and Figure 106C gives the total field. The iron-titanium oxide-rich zones midway down the hole and near the bottom of the hole show up on all three logs as strongly anomalous intervals having magnetic polarizations approximately opposite to the direction of Earth's present field.

The UW magnetometer-susceptibility tool was run for the first time in Hole 735B. The hole was logged at two different speeds, going uphole and downhole, to check repeatability. The overall performance of the tool was good, although there appears to have been a problem with the initial zeroing and calibration of the susceptibility coil. Unfortunately, the short time interval between logging and the termination of Leg 118 did not allow for a thorough examination of this problem.

Data from the uphole log are displayed in Figure 106. Although the magnetometer log agrees well with that of the USGS

tool, the susceptibility appears to be very noisy, which is probably a result of the aforementioned problems. The most salient features of the magnetic field data are the abrupt increases in signal amplitude that occur within the magnetite-ilmenite-rich gabbros between 224 and 272 mbsf and below 405 mbsf. Between the magnetite- and ilmenite-rich zones, the signal amplitude is low and has only intermittent, narrow zones of high field intensity. Further interpretation of the logging data will occur when the contribution of the Earth's magnetic field can be removed accurately and the contribution of remanent magnetization of the surrounding rock has been examined independently.

Vertical magnetic field measurements in Hole 735B from the Schlumberger, USGS, and UW magnetometers are compared in Figure 107. Although sampling density and sensitivity are different in each tool, the overall character of the logs agrees well. All three logs show an abrupt increase in vertical magnetic field between 224 and 272 mbsf and below 405 mbsf, which correlates with the presence of magnetite-ilmenite-rich gabbro. In addition, the quietest part of each log occurs from 272 to 405 m within lithologic Unit V, which consists of olivine with a distinct absence of magnetite-ilmenite-rich zones.

Summary of Magnetic Measurements of Cores, Hole 735B

Results of shipboard laboratory measurements of minicores from Hole 735A (see "Paleomagnetism" section, this chapter) indicated that the gabbroic rocks have the following approximate magnetic properties before demagnetization.

Susceptibility:	Average 500×10^{-6} cgs	Range $20\text{--}10,500 \times 10^{-6}$ cgs
Intensity of remanent magnetization:	1000×10^{-6} emu/cm ³	$5\text{--}100,000 \times 10^{-6}$ emu/cm ³
Inclination:	65°	-80° to 80°

The extreme variability and broad range of the magnetic properties of rocks penetrated by the borehole are indicated by both the laboratory and the downhole magnetic measurements. However, the borehole measurements indicate that the entire section is reversely polarized *in situ*, suggesting that the negative NRM inclinations measured in the laboratory were induced by drilling, or perhaps by pulling the core through the pipe (730–1230 mbrf) during wireline core recovery. In any case, the normal component is soft and easily removed by AF demagnetization.

Geomagnetic Field at Site 735

The total force of the geomagnetic field at Site 735 was measured by the ship's towed magnetometer system during a site survey just before drilling began and again just after the ship left the site. The vertical component was computed from the total force and the inclination. Inclination and declination of the Earth's field were estimated for Site 735 from published IGRF charts (IGRF, 1980).

Total force:	37,250 nT (± 50)
Vertical component:	32,259 nT
Inclination:	-60° (up)
Declination:	$32^\circ W$

These values will be used for the final interpretation of downhole magnetic measurements with the objective of estimating the direction and intensity of the remanent vector *in situ*. If this is successful, it should be possible to determine the azimuthal orientation of the cores for which the direction of the remanent

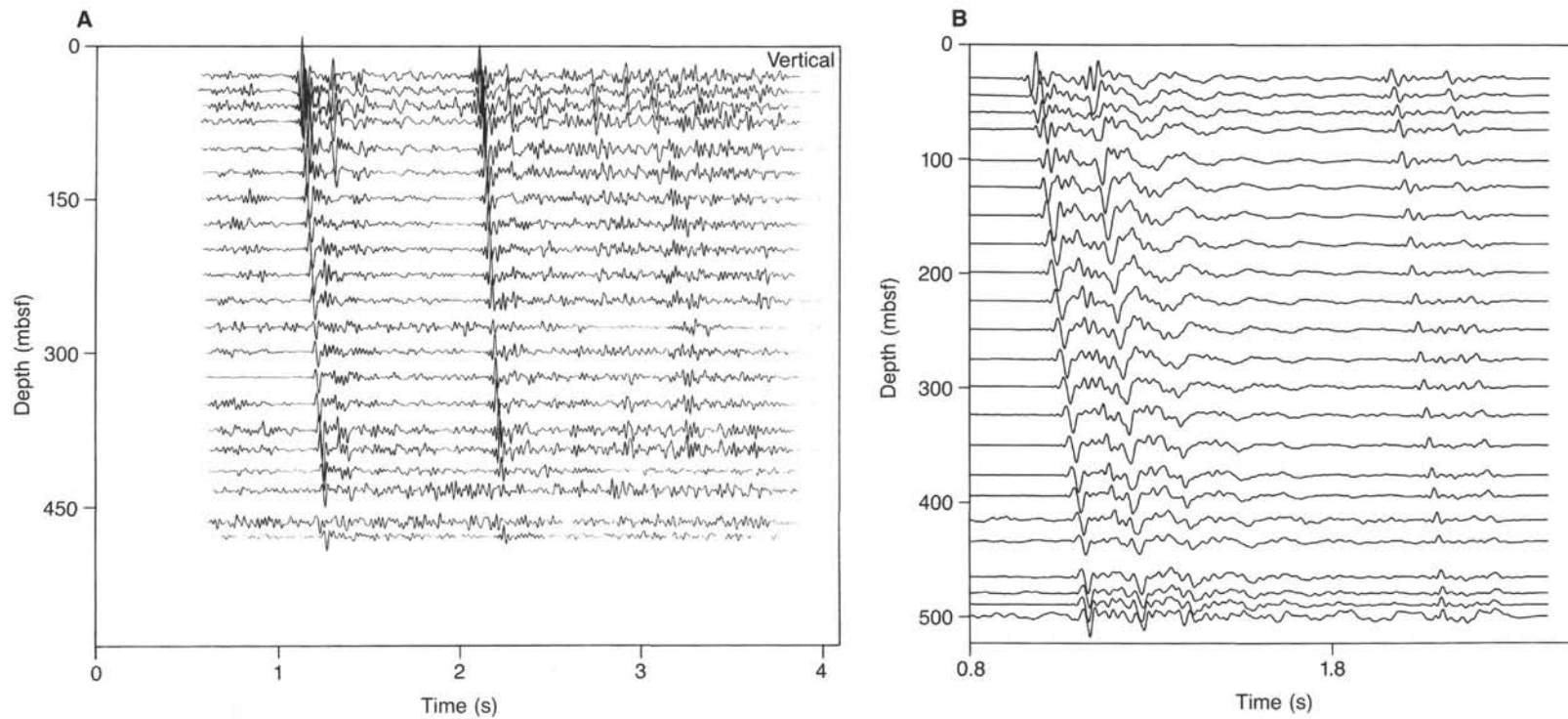


Figure 100. Stacked seismicograms shot with air-gun source and plotted vs. receiver depth below seafloor. Traces are offset to later time by the one-way traveltime. A. True amplitude scaling. B. Automatic gain control and deconvolution as in Figure 98B.

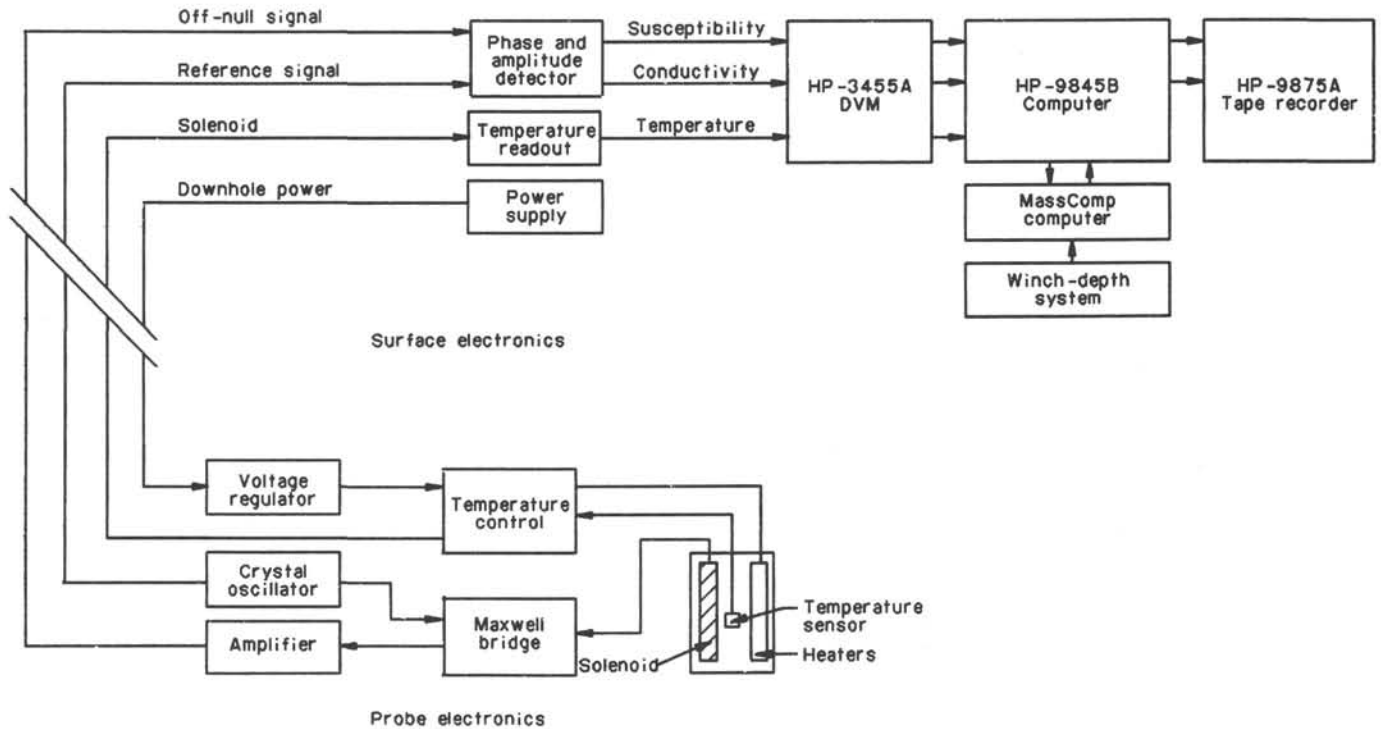


Figure 101. Block diagram of the USGS magnetic-susceptibility well logging system.

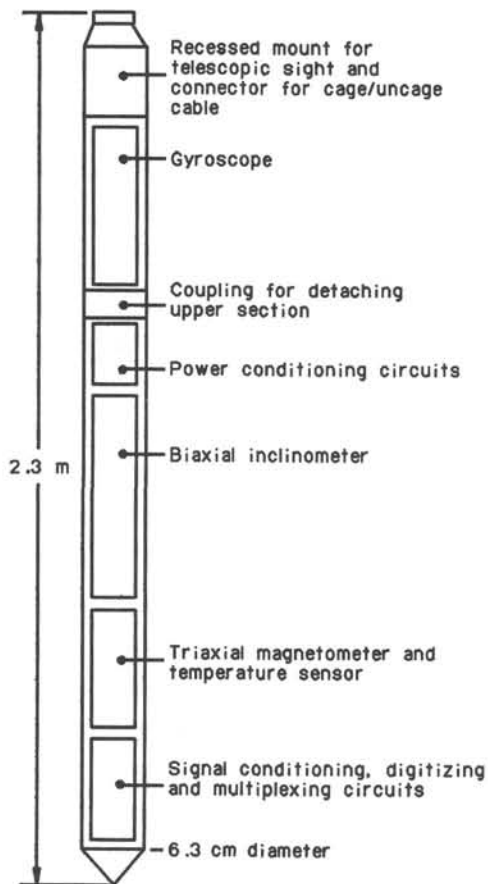


Figure 102. Diagram of the USGS three-component magnetometer probe (not to scale).

vector has been determined after AF demagnetization has stripped off the soft induced normal polarization.

Conclusions

The success of magnetic logging conducted during Leg 118 will contribute significantly to our overall understanding of the vertical magnetic structure of the crustal section penetrated by Hole 735B. The *in-situ* logging measurements will be used together with laboratory measurements of discrete samples to provide an integrated interpretation of the paleomagnetic character of gabbro at Site 735. In particular, logging data will be very important in constraining the *in-situ* magnetic directions and intensities of the ilmenite-magnetite-rich gabbros. Future interpretation of magnetic data will draw heavily on the petrographic and geochemical data that are obtained from the drill core of Hole 735B.

PERMEABILITY MEASUREMENTS IN THE GABBROS OF HOLE 735B

Introduction

The circulation of seawater and pore fluids through the oceanic crust plays a vital role in the development of the physical and chemical nature of the crust. The modes and effects of circulation are largely controlled by the variable permeability and porosity of the basaltic and gabbroic formations that constitute the oceanic crust. As crustal permeability and porosity probably vary with irregular fractures and voids of unknown scale, they cannot be reliably determined from dredged or cored samples. Instead, bulk permeability and porosity must be measured *in situ*, at averaging scales large enough to include the effects of irregular fracture porosity and to avoid the disturbance of drilling on the formation.

There are several downhole logs and experiments with which porosity can be estimated (e.g., "Schlumberger Logs" section, this chapter). However, while it is intuitive that there must be

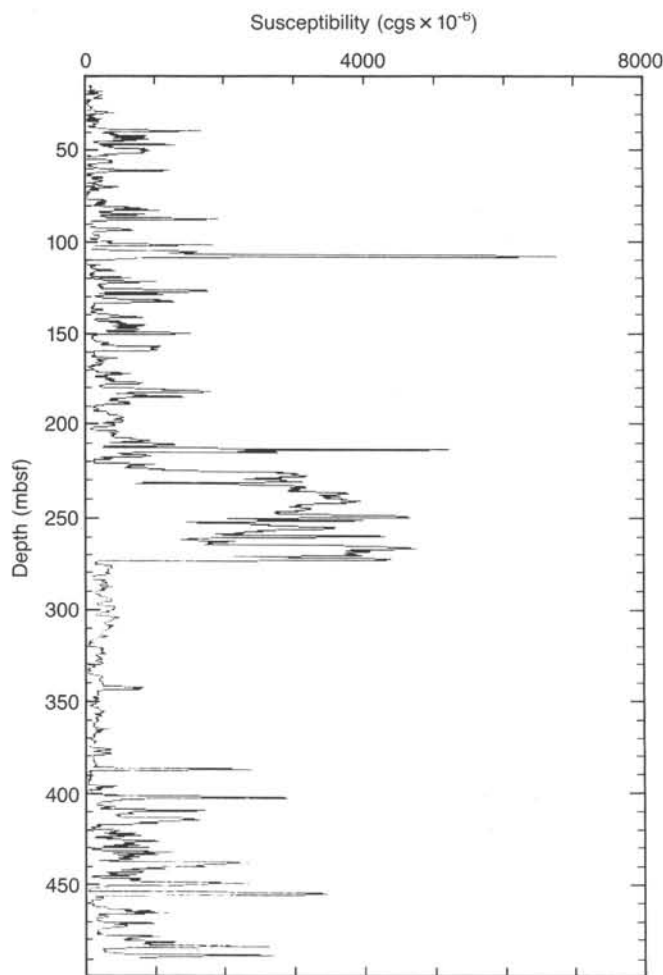


Figure 103. Magnetic susceptibility log of Hole 735B made with the USGS susceptibility tool. Hole diameter correction and 5-point smoothing filter (1-m span) applied.

some relationship between permeability and porosity, the permeability of the oceanic crust cannot be reliably determined from its porosity. Many scales of crustal porosity occur, among them intergranular or pore porosity, cracks, and large fractures, not all of which contribute to permeability. The permeability of the oceanic crust is probably dominated by large-scale, interconnected porosity, which cannot be unequivocally distinguished from other forms of porosity by logging.

To date, the only reliable means of assessing crustal permeability is by actively testing the formation *in situ*, which is usually done using a packer to isolate a section of a borehole that penetrates the formation. Before Leg 118, drill-string packers had been deployed several times during DSDP and ODP cruises, but only Holes 395A and 504B were the rare holes that penetrate deeply into the oceanic crust. The permeability of the pillow lavas and sheeted dikes in Hole 504B was measured during Legs 69, 70, 83, and 111 by Anderson and Zoback (1982), Becker et al. (1983), Anderson et al. (1985), and Becker (unpubl. data), respectively. The permeability of the pillow lavas cored in Hole 395A was measured during Leg 78B by Hickman et al. (1984) and during Leg 109 by Becker (unpubl. data).

The permeability of oceanic gabbros has never before been measured *in situ*. Thus, Hole 735B presented an outstanding opportunity to significantly augment our knowledge about the permeability of the oceanic crust, even though the tectonized

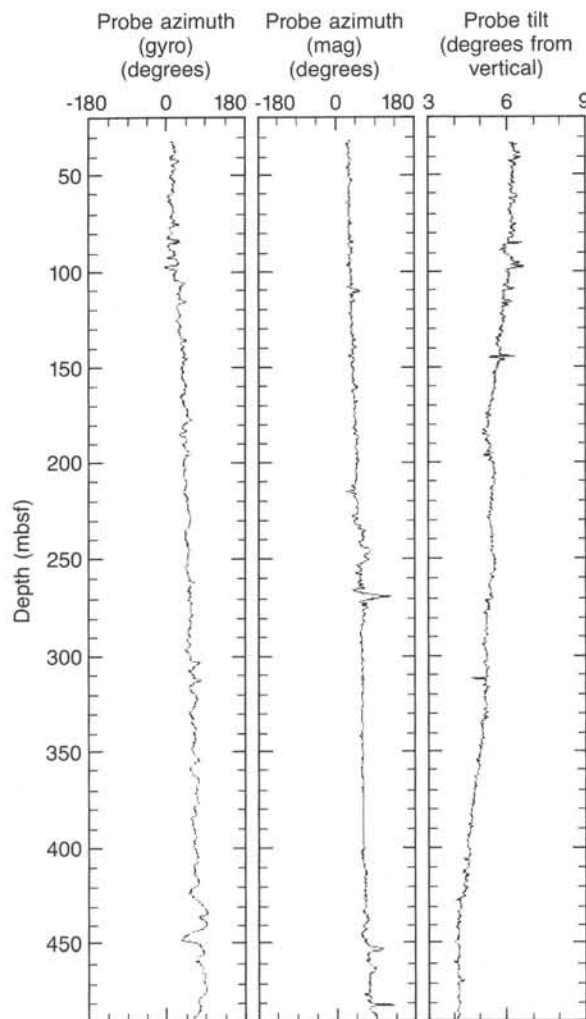


Figure 104. Magnetometer-derived logs of probe orientation in Hole 735B. A. Probe azimuth referenced by the gyro to magnetic north at sea level directly above Hole 735B. B. Probe azimuth referenced by the magnetometer to local magnetic north in the borehole. C. Probe tilt computed from the biaxial inclinometers. A 5-point smoothing filter (1.5-m span) was applied to all three panels.

gabbros cored in the hole do not fully represent "normal" oceanic layer 3. During the last drill-pipe trip of Leg 118, a drill-string packer was set six times in Hole 735B to measure the bulk permeability of several zones of the gabbroic formations cored (listed in the order that the measurements were performed):

1. From 49 mbsf to the bottom of the hole at 500.7 mbsf, encompassing lithologic Units II through VI.
2. From 47 mbsf to hole bottom (a reset to check the packer performance).
3. From 389 mbsf to hole bottom, Unit VI.
4. From 299 mbsf to hole bottom, Units V and VI.
5. From 223 mbsf to hole bottom, Units IV, V, and VI.
6. From 223 mbsf to hole bottom (a reset to verify the important result from the previous set).

The depths at which the packer was set were chosen primarily on the basis of logging results, particularly resistivity, density, and borehole televiewer measurements, which clearly distinguished the deepest five of the six major lithologic units (see "Lithostratigraphy" section, this chapter).

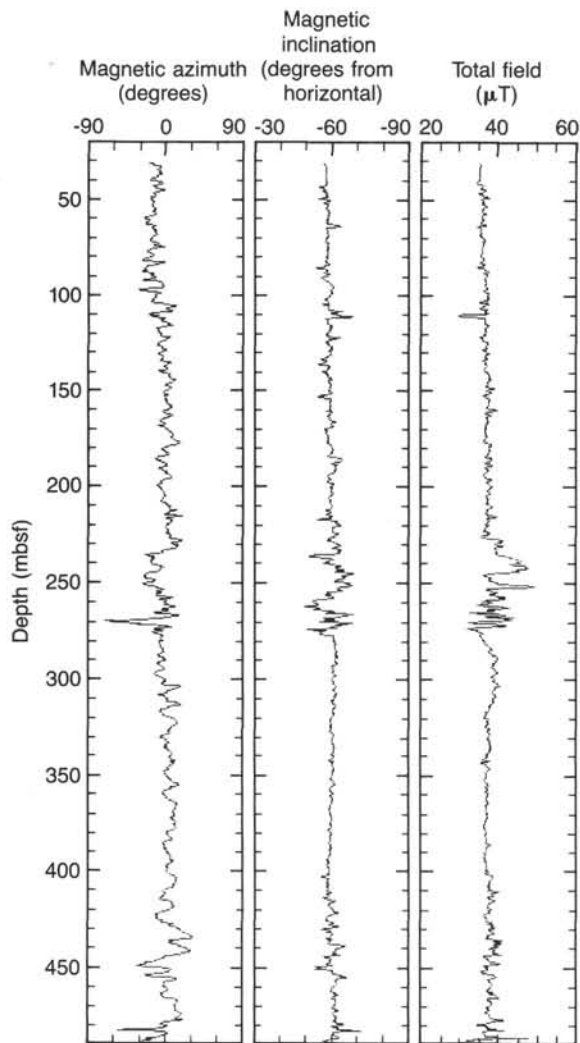


Figure 105. Magnetometer-derived logs of magnetic vector parameters in Hole 735B. A. Magnetic azimuth referenced by the gyro to magnetic north at sealevel. Magnetic north, east and west are 0° , 90° , and -90° , respectively. B. Magnetic inclination computed from the gyro inclinometer-referenced magnetometer measurements. C. Total field in micro-Teslas ($T \times 10^{-6}$) computed as the vector sum of the three-axis magnetometer measurements. A 5-point smoothing filter (1.5-m span) was applied to all three panels.

Because these measurements were performed when only three days of Leg 118 remained, none of the data could be analyzed. Here, we first review the measurement of permeability using a packer and then describe the operational procedures followed for the measurements performed in Hole 735B. We present only the basic downhole pressure data and can only briefly discuss a few preliminary, qualitative inferences that can be drawn about the permeability of the gabbros in Hole 735B from the character of these data.

Experimental Procedures

Permeability Measurements Using Drill-String Packers

A packer can be defined as a device that produces a hydraulic seal in a borehole (Fig. 108). If the integrity of this hydraulic seal is properly maintained, the hydrologic properties of the formation can be tested by applying differential fluid pressures to the isolated section. Formation properties that can be measured using a packer include pore pressure, transmissivity (from which

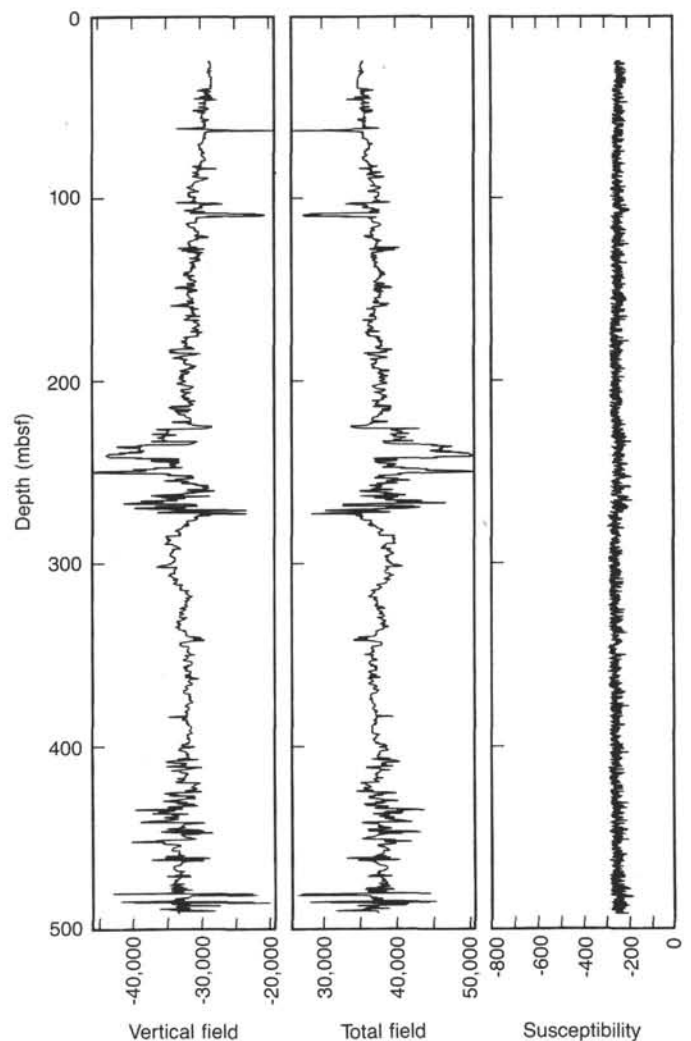


Figure 106. UW magnetometer measurements made within Hole 735B. Vertical magnetic and total magnetic field are in nannoTeslas. Susceptibility is plotted on relative scale.

permeability can be derived), and storage coefficient (which is closely related to bulk formation porosity). During Leg 118, these properties were tested using two types of experiments:

1. Pulse or "slug" tests, in which downhole pressure recorders monitor the decay of short, effectively instantaneous pressure pulses applied to the formation using the surface pumps. In a relatively impermeable formation, the period of decay of such a pulse will be long compared to the duration of the pulse, and the permeability can be determined using the theory for an instantaneous pulse (Cooper et al., 1967; Papadopoulos et al., 1973; Bredehoeft and Papadopoulos, 1980). In a permeable formation, a pressure pulse will decay rapidly, and injection tests must be run.

2. Constant-rate injection tests, in which downhole pressure recorders monitor the approach of downhole pressure to a nearly steady-state value as fluid is pumped into the isolated formation at a constant rate. The permeability can be estimated from the rise of downhole pressure using a form of Darcy's Law (e.g., Matthews and Russell, 1967).

During Leg 118, we used a drill-string packer made by TAM International of Houston and described by Becker (1986). This is a nonrotatable packer that is installed in the bottom-hole as-

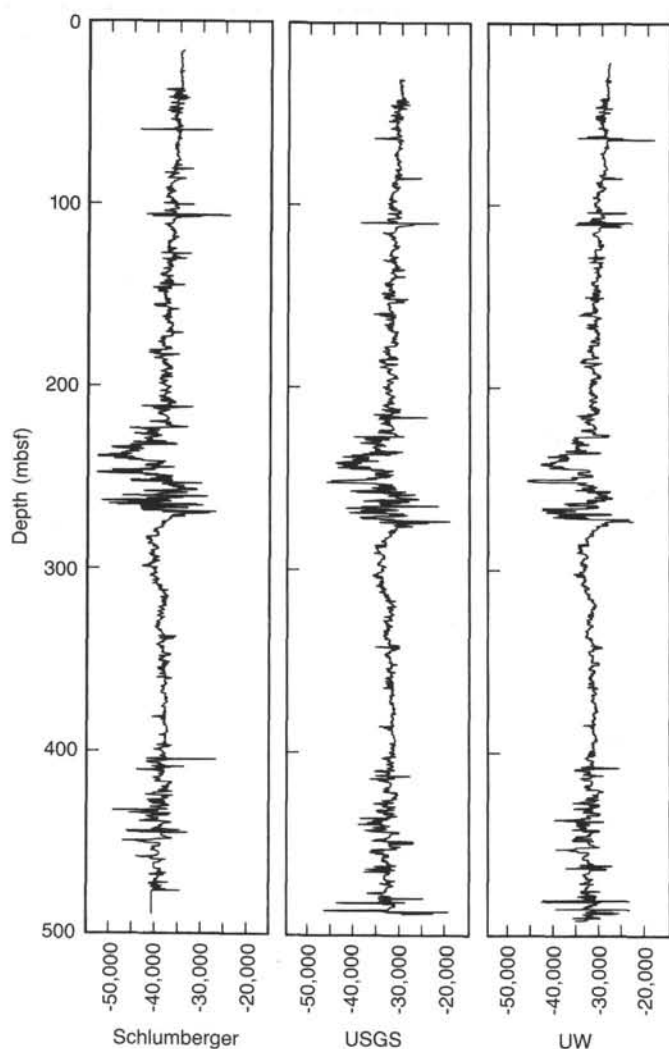


Figure 107. Vertical magnetic field measured in Hole 735B by the Schlumberger tool (left), the USGS tool (center), and the UW tool (right). Magnetic field is in nanoTeslas (nT). Center log has been corrected for drill-hole inclination, while the other two logs have not.

sembly immediately above the bit. It had been tested during Leg 102 and was successfully used during Legs 109 and 111 to measure permeability in the basalt layer of Holes 395A and 504B. This packer can be configured as either a single packer or a straddle packer; during Legs 109, 111, and 118, it was used as a single packer. With a single packer, permeability and pore pressure are determined as bulk values averaged over the interval between the packer seal and the bottom of the hole. Setting a single packer at several depths allows the permeability of the intervening zones to be determined.

With the TAM packer, the required hydraulic seal is achieved by pumping seawater down the drill pipe to fill an inflatable rubber and steel element, which expands and deforms against the borehole wall to isolate the formation below the seal (Fig. 108). The inflation mechanism is set in motion by first dropping a "go-devil," which performs two major functions:

1. To form a hydraulic seal within the packer and to direct the fluids pumped down the pipe first into the element for inflation, and then into the isolated formation for testing.
2. To carry the recorders that monitor the pressure data from which pore pressure and permeability are calculated.

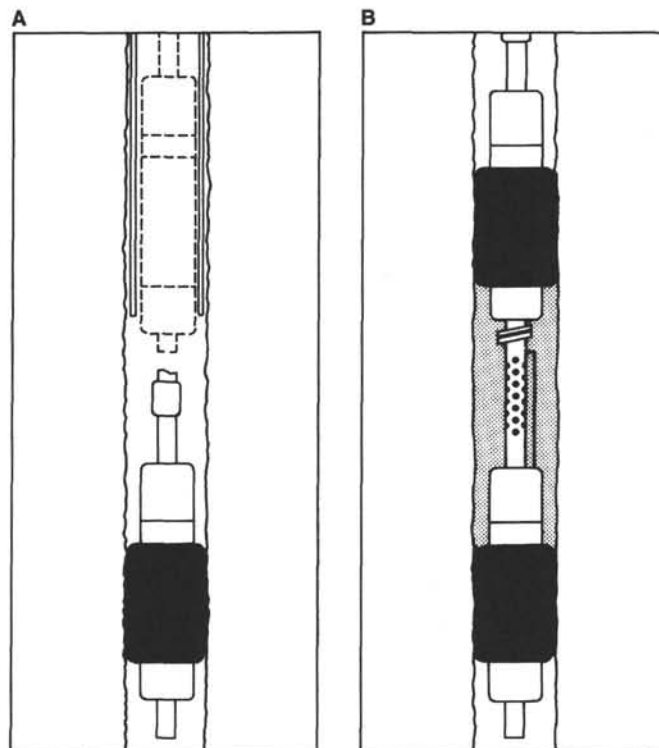


Figure 108. Sketches of inflatable drillstring packers. A. Single-element packer, which isolates the formation between the element and the bottom of the hole. B. Straddle packer, which separately isolates the zone between the elements and the zone between the lower element and the bottom of the hole.

The go-devil is allowed to fall freely down the pipe to the packer and is retrieved using the coring winch when the pressure recorders need to be reset.

During the Leg 118 permeability measurements, downhole pressure was monitored using two Kuster K-3 pressure recorders, S/N 9542 and 9685. These are self-contained, mechanical recorders that performed flawlessly, as they did during Legs 109 and 111. Their pressure sensors had been calibrated recently at the factory, and their time scales were carefully checked during Legs 109, 111, and 118. For each packer inflation point, both recorders were attached to the go-devil, for redundancy of data collection in the (unrealized) case of an instrument failure. These recorders can be set to run 3, 6, or 12 hr; for the Leg 118 experiments, they were set to run 6 hr, which was enough time to run two to four pulse and/or flow tests at each of two or three packer seats, before retrieving and redressing the go-devil while the packer was moved to another setting depth.

Operational Summary

Leg 118 Permeability Measurements in Hole 735B

The last day of scientific operations at Hole 735B was committed to a drill-pipe trip to run the drill-string packer into the hole. During this period, the go-devil was dropped and retrieved three times, and the packer was inflated six times to assess the variation of permeability in the formation (Table 17). During this sequence of measurements, fluid pressure, flow rate, and total volume pumped were measured at the surface, and fluid pressure was measured below the go-devil in the isolated intervals. During pulse tests, the small volume of fluid pumped was carefully recorded, to allow the compressibility of the pressurized system to be checked, as suggested by Neuzil (1982).

Table 17. Summary of Leg 118 packer measurements in Hole 735B.

Run	Activity
Go-Devil 1	Packer Set 1 — packer at 49 mbsf (780 mbrf) 4 pulse tests — fast decay due to high permeability? unset packer with 20,000 lb pull. Packer Set 2 — reset packer at 47 mbsf (778 mbrf). 2 pulse tests — fast decay due to high permeability. 3 flow tests 100 strokes/min, with mud slug to verify packer seal. 50 strokes/min 30 strokes/min
Go-Devil 2	Packer Set 3 — packer at 389 mbsf (1120 mbrf). 2 pulse tests — very slow decay due to very low permeability. Packer Set 4 — packer at 299 mbsf (1030 mbrf). 4 pulse tests — slow decay due to moderately low permeability. Packer Set 5 — packer at 223 mbsf (954 mbrf). 3 pulse tests — fast decay due to high permeability. 1 flow test — 50 strokes/min
Go-Devil 3	Packer Set 6 — reset packer at 223 mbsf to verify previous results. 1 pulse tests — fast decay due to high permeability. 2 flow tests 30 strokes/min 50 strokes/min, with mud slug to verify packer seal.

One pump stroke equals 5 gal.

Throughout the series of measurements, special care was taken to verify the hydraulic integrity of the testing system, which consisted of the rig pumps and lines, the drill string, the go-devil seals, and the inflated packer. Before dropping the first go-devil, the hydraulic integrity of the rig-floor circulation system was satisfactorily tested to 2000 psi, about twice the pressure used to inflate the packer or test the formation. At each packer-setting depth, the integrity of the drill-string and go-devil seals was satisfactorily tested by holding inflation pressure for about 10 min before locking the packers while inflated. The effectiveness of the packer seal against the borehole was demonstrated by the excellent quality of the slowly decaying slug test records in impermeable sections, and was tested in permeable zones by a method described next.

As mentioned above, the depths at which the packer was set were planned primarily based on logging results. The order in which the packer was inflated at these depths was left flexible, pending the results at the first setting depth, which was very shallow in the hole. We decided first to set the packer shallowly in the hole because there were a number of indications (e.g., superb core recovery, very high electrical-resistivity values and low-density values from the logs) that most of the formation might be quite impermeable. Setting the packer first as shallowly as possible allowed us to assess the permeability of the entire cored section; if the entire section had been impermeable, the remaining time on site would have been used for other purposes. However, the results at the first setting depth showed that there was significant permeability in the hole, and subsequent setting depths were run from deep in the hole back uphole to determine the variation of permeability with lithology and to locate the permeable zone(s).

The complete sequence of measurements is summarized in Table 17. All operations went smoothly, except for the very first packer setting, as follows: When the pulse test results at the first setting indicated surprisingly high permeability, we decided to verify that the packer element was properly sealing by resetting the packer at the same depth and repeating the measurements. However, we were unable to unset the packer smoothly as it required much more pull (20,000 lb) than normal to release the fluid inside the inflated element. For a short time, the packer was actually stuck in the hole, and we were not sure whether it was working properly. Nevertheless, when the packer was pressured up again 2 m shallower in the hole, it was reset smoothly and gave similar indications of high permeability somewhere in

the isolated interval. Such indications could also have been produced by a “leaky” packer seal if the element had been damaged when pulling it free. The seal was tested by monitoring the television/sonar system, which was hanging immediately above the reentry cone, and a small slug of mud was pumped into the isolated interval, which was followed immediately by a standard constant-rate injection test that involved pumping seawater at 500 gal/min for more than 20 min. This amount of seawater was more than twice that required to pump the mud back out of the hole if the packer had not been sealing properly. No mud or other fluid was seen exiting the cone on the video, and the fluid pressure followed a reasonable curve for a successful injection test.

Thus, we concluded that the packer was operating correctly and was sealing properly; there was indeed highly permeable formation in the hole. The go-devil was retrieved and redressed, and the packer was moved deep in the hole and set at successively shallower depths to locate the permeable zone(s). The packer and go-devil operated smoothly until the drill string had to be pulled to depart the site. At the end of the last packer setting, the mud-slug/flow test described above was repeated; it again verified that the packer was sealing properly. When the packer was brought back on deck, the element was in nearly perfect condition, unlike several previous examples of shredded, melted, or otherwise frazzled elements.

Preliminary Results

The pressure-time records from the downhole Kuster pressure recorders carried in the three go-devils are shown in Figures 109 through 111. It is clear from the variation in the responses to similar types of tests that there is a wide range of permeability in the formations cored in Hole 735B.

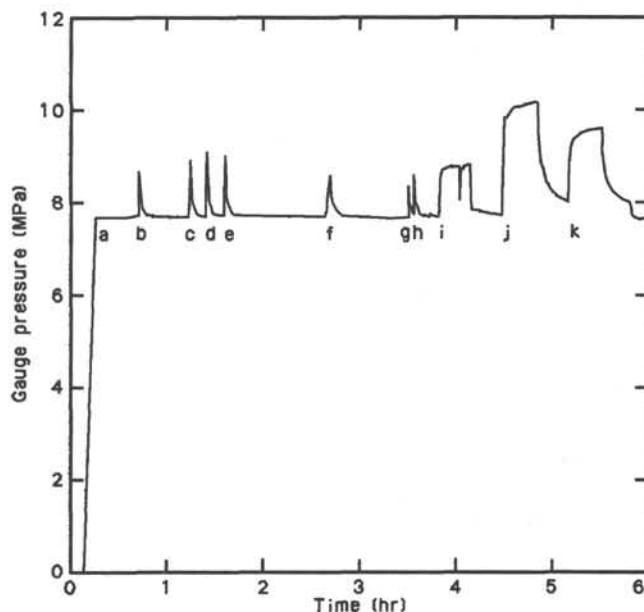


Figure 109. Pressure-time records from Kuster K-3 S/N 9582 for the two packer setting depths (49 and 47 mbsf) during the first run of the go-devil. a = Go-devil lands in packer and monitors hydrostatic pressure baseline. b = Pulse test resulting from packer inflation at 49 mbsf. c, d, e = Pulse tests. f = Deflate and pull packer free. g = Pulse test resulting from packer inflation at 47 mbsf. h = Pulse test. i, j, k = Constant-rate injections tests at 100, 50, and 30 strokes/min, respectively. The injection test at 100 strokes/min produced questionable data that are not a valid test of formation permeability, probably because of problems in switching from one rig-floor pump to the other.

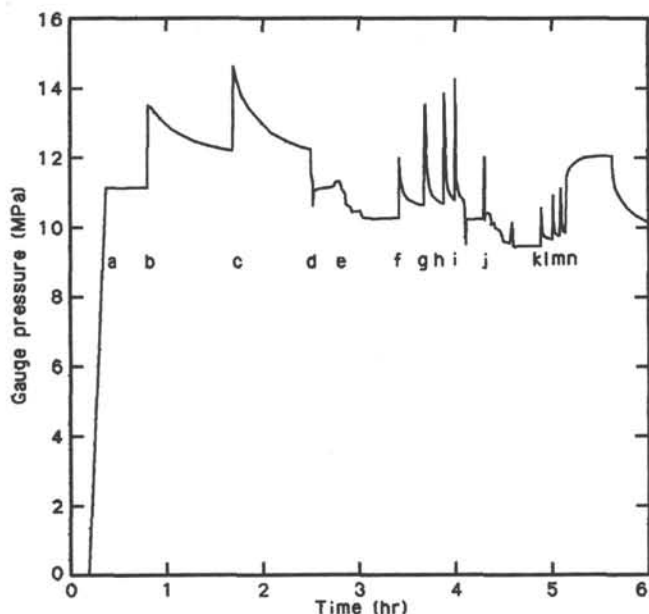


Figure 110. Pressure-time records for the three packer setting depths (389, 299, and 223 mbsf) during the second run of the go-devil. a = Go-devil lands in packer and monitors hydrostatic pressure baseline. b = Pulse test resulting from packer inflation at 389 mbsf. c = Pulse test. d = Packer deflation. e = Move packer to 299 mbsf. f = Pulse test resulting from packer inflation at 299 mbsf. g, h, i = Pulse tests and packer deflation. j = Move packer to 223 mbsf. k = Pulse test resulting from packer inflation at 223 mbsf. l, m = Pulse tests. n = Injection test at 50 strokes/min.

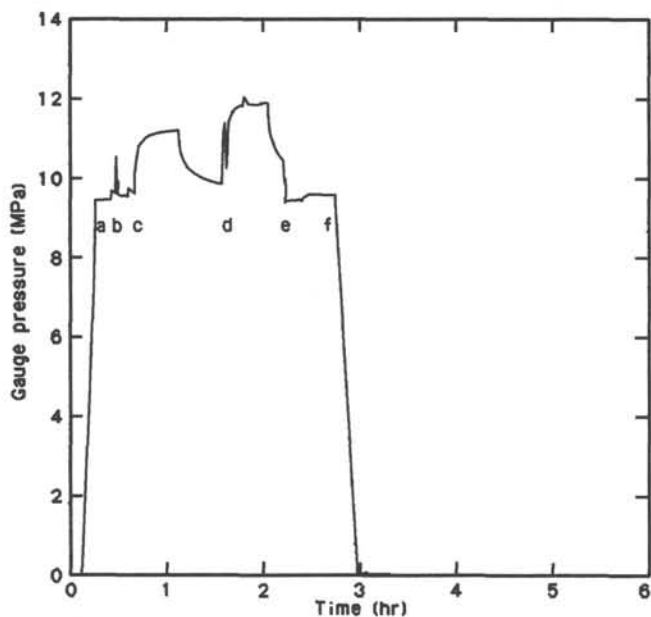


Figure 111. Pressure-time records for single-packer setting depth (223 mbsf) during the third run of the go-devil. The run ended after 3 hr for pulling pipe to depart the site on time. a = Go-devil lands in packer and monitors hydrostatic pressure baseline. b = Pulse test resulting from packer inflation at 223 mbsf. c = Injection test at 30 strokes/min. d = Mud slug and injection test at 50 strokes/min. e = Packer deflation. f = Retrieve go-devil and pull pipe to leave site.

When the packer was first set shallowly in the hole, pulse tests decayed very rapidly and the isolated zone accepted fluids pumped at high constant rates, indications of highly permeable formation(s) somewhere in the cored section. The second and third packer settings deep in the hole resulted in pulse tests of long decay times, indicative of low permeability in lithologic Units V and VI, particularly in the gabbros and troctolites of Unit VI. When the packer was set just above Unit IV at 223 mbsf, just 76 m above the impermeable gabbros of Units V and VI, pulse tests decayed rapidly and the isolated zone accepted fluids at similar rates and pressures as during the first packer set another 174 m shallower. Thus, it appears that the zone between 223 and 299 mbsf may contain most of the permeable formation in the entire cored section. However, the data must be processed carefully to assess whether all the transmissivity indicated below 49 mbsf is indeed concentrated between 223 and 299 mbsf.

The permeable zone between the packer sets at 223 and 299 mbsf includes the Unit IV iron- and titanium-rich, oxidized gabbros that are somewhat more porous than gabbros recovered from the rest of the hole, and the contact between Units IV and V. This sharp contact consists of a mylonite immediately above a brecciated zone (see "Lithostratigraphy" section, this chapter) that probably marks a major fault. The high injection rates achieved during the permeability measurements suggest that the breccia zone and fault may still be quite open.

As pressure data have not been completely processed, we are unable to determine accurately the values of permeability in Hole 735B. However, these values clearly span a large range, probably several orders of magnitude, as in Holes 395A and 504B. From the similarities in decay curves and constant flow results among the measurements in DSDP Holes 395A and 504B and ODP Hole 735B, we estimate that the permeabilities in the gabbros of Hole 735B span a similar range, as in the basalts of Hole 504B, on the order of 10^{-13}m^2 in the upper section to 10^{-17}m^2 in the deepest 100 m.

BOREHOLE TELEVIEWER

Introduction

The borehole televiewer (BHTV) is an acoustic device that scans the wall of the borehole, producing an image of the reflectivity of the rock surrounding the hole as a function of depth and azimuth. A piezoelectric transducer, which is mounted on a central shaft rotating three times per second, transmits and receives a high-frequency acoustic pulse 600 times per revolution. Two transducers are mounted on this shaft, which allows either a 1.3-MHz or a 400-kHz pulse to be used as a source. The higher-frequency source reveals more details of the wall surface, while the lower-frequency source has better penetration and can produce an improved image in a rough-walled borehole. The pulse is transmitted through the borehole fluid, reflected from the wall of the borehole, and received again at the transducer. The amplitude of the returning signal is recorded and displayed as brightness on a three-axis oscilloscope. The oscilloscope image is thus an acoustic picture of the reflectivity of the borehole wall, where the azimuth varies along the X-axis and depth varies along the Y-axis. The left-hand edge of the image is aligned with the local magnetic north in the borehole using a downhole fluxgate magnetometer.

The raw data are recorded on a specially formatted video cassette for final playback and processing. The amplitudes and traveltimes of the received pulses are also recorded on magnetic tape by digitizing the televiewer signal during playback. This traveltime log may be used to yield a three-dimensional cylindrical projection of the borehole as a function of depth and azimuth in the well, producing a 360° caliper log.

The scientific objectives addressed by BHTV logs include (1) the location and orientation of fractures intersecting the hole; (2) the determination of structural features, such as bedding or brecciation; (3) the measurement of borehole diameter, ellipticity, and surface roughness; and (4) the determination of the orientation of the principal horizontal stresses from the azimuth of borehole breakouts observed in the time-domain images. However, some limitations of the BHTV log should be recognized. First, as the log is effectively a point measurement with depth, ship heave may cause irregular tool motion and confuse the analysis and interpretation of the log. Second, severe borehole deviation or ellipticity or decentralization of the tool will degrade the image because the beam will no longer be perpendicular to the borehole wall at all azimuths. This effect can be recognized in the time-domain image. Third, the BHTV cannot recognize features that do not affect either the roughness, reflectivity, or radius of the borehole. BHTV images recorded in Hole 735B are briefly discussed next.

Operations

The BHTV log from Hole 735B was recorded on 8 December 1987 while logging upward at a rate of 1.5 m/min from 489.0 to 13.0 mbsf. The borehole caliper log shows hole diameter varying from 10 to 12 in., and borehole deviation logs show that the hole was inclined between 4° and 6° from vertical. The first BHTV pass on 7 December was aborted because of severe centralization problems with the tool in the noncylindrical hole, although at the time, an electronic malfunction was suspected. The effects of poor centralization and ellipticity remained as dark vertical bands apparent in the BHTV amplitude images even after improved centralization using three 3-armed bow-spring sections: the standard upper BHTV centralizer, the lower multichannel sonic centralizer, and a through-wired temperature tool centralizer borrowed from J. Scott (USGS). Determining the effect of borehole shape requires additional digital processing of travelt ime data.

The BHTV log in Hole 735B was recorded with the wireline heave compensator, although its operation was not optimal in the low sea state present during logging. In addition, between 207 and 277 mbsf, the wireline heave compensator was not operating because of a malfunction of the heat exchanger. Ship heave introduced some periodic changes in scanning coverage, but these effects were easily observed and corrected in the digital images.

Data

The BHTV log was digitally processed from 489.0 to 240.0 mbsf using shore-based MassComp computer equipment. The upper 240 m must still be processed. The gabbro interval studied has smooth and cylindrical borehole walls and isolated fracturing. Planar features, such as fractures, appear as dark bands (low amplitude and longer travelt ime) in horizontal or sinusoidal curves in the unwrapped BHTV image. Two examples of steeply dipping, planar features are shown as travelt ime images in Figures 112 and 113 at 288 and 417 mbsf. Fractures are also more clearly observed in travelt ime images than in amplitude images. The effects of eccentricity of the tool are obvious as wide vertical banding and can be easily distinguished from the effects of fractures. These two isolated fractures both strike north-northwest and dip 73° to 77° west-southwest.

In Figures 114 and 115, cylindrical net projections of two fractures at 292.5 and 302.5 mbsf are presented at three viewing angles. These isolated features dip about 70° west-southwest, consistent with the other fractures depicted in Figures 112 and 113. Horizontal offsets in the fracture plane and variable spacing of the travelt ime net result from uncompensated ship heave. This effect may be corrected later by editing the data.

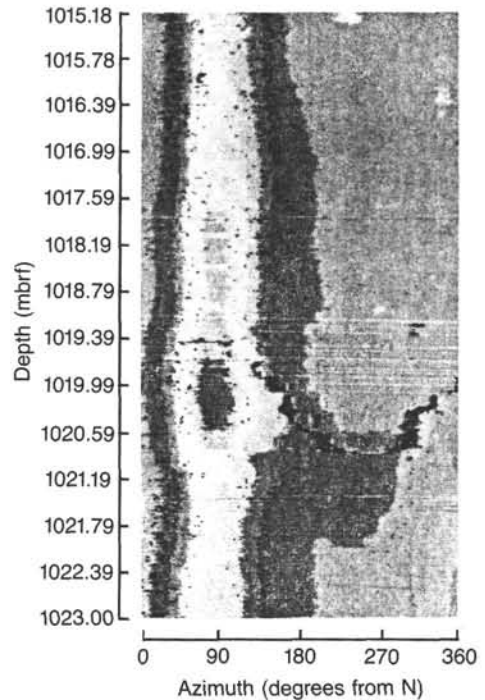


Figure 112. Digitally processed borehole televiewer travelt ime image. Tool decentralization appears as diffuse vertical banding. An isolated fracture at 1020 mbrf (288 mbsf) is evident as a dark sinusoidal band that dips about 73° west-southwest (see text).

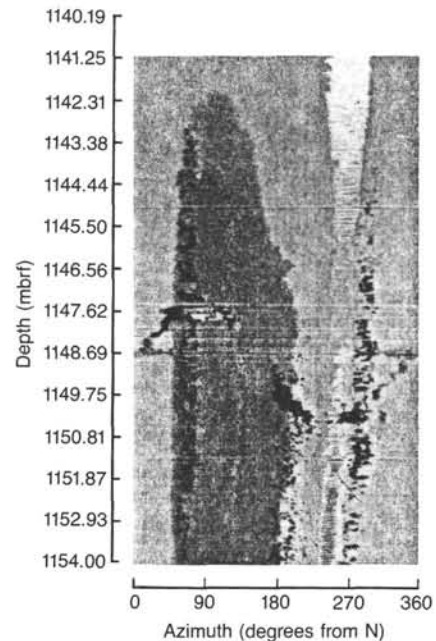


Figure 113. Digitally processed borehole televiewer travelt ime image showing some tool decentralization and a large fracture dipping about 77° west-southwest.

The location of these major fractures at 288, 292.5, and 302.5 mbsf corresponds to the location of decreases in compressional velocity and shear semblance (see “Sonic Logs” section, this chapter). These also occur where fluid permeability, as determined from packer tests, may decrease with depth, although

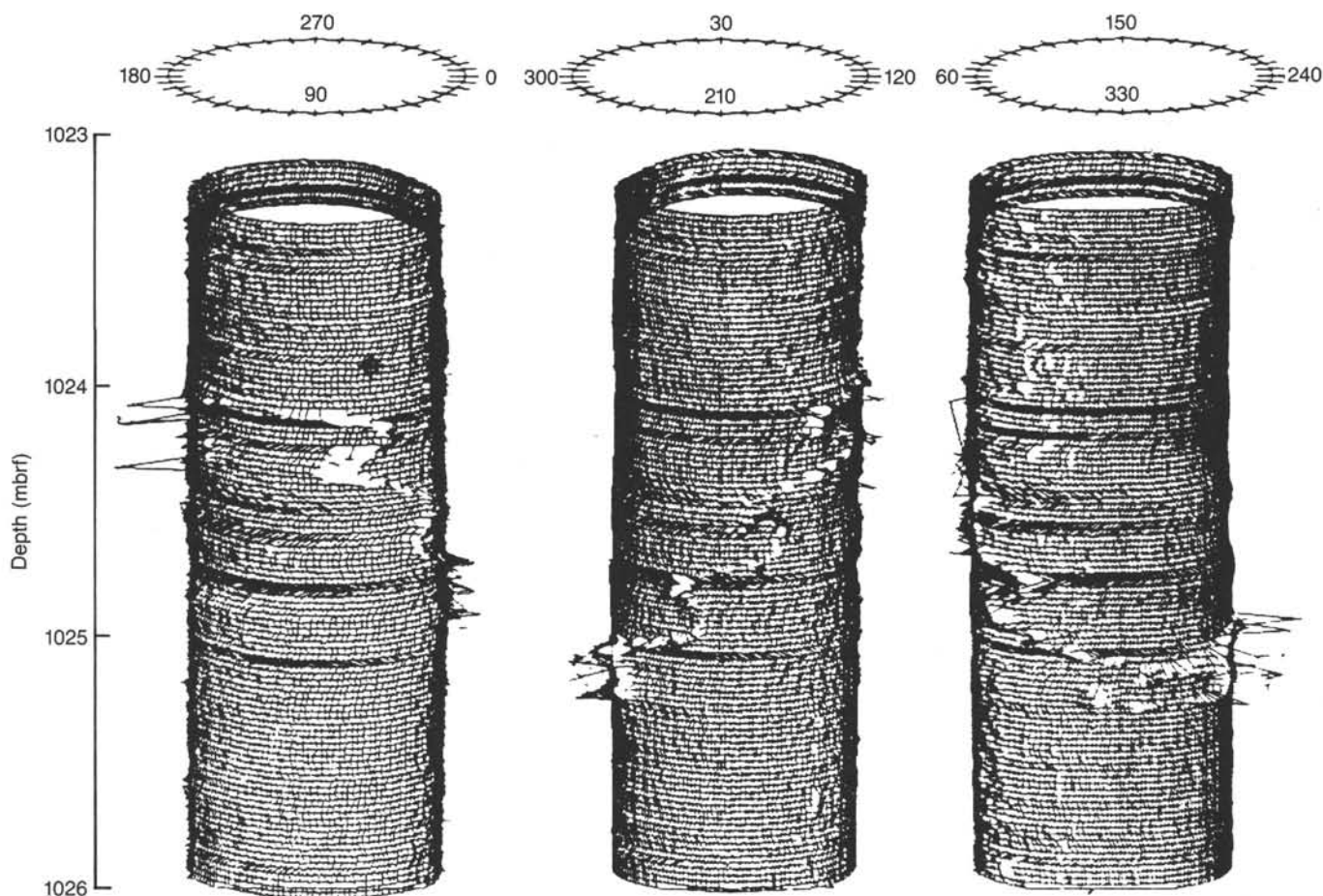


Figure 114. Cylindrical net projections at three viewing angles (90°, 210°, 330°) showing the intersection of a dipping fracture with the borehole at 1024.5 mbrf (292.5 mbsf). Horizontal offsets in the fracture plane and variable spacing of the travelttime net result from uncompensated ship heave.

the precise depth of this change cannot be determined (see "Permeability Experiments" section, this chapter). The fracture observed at 417 mbsf is not associated with major decreases in sonic velocity or semblance, nor with high permeability. The interval just below the iron-titanium oxide-rich gabbro is also rich in hydrothermal alteration minerals (see "Metamorphism and Alteration" section, this chapter) and corresponds to a positive temperature anomaly (see "Temperature Measurements" section, this chapter). It appears, then, that at least some of the fractures near 290 mbsf are open and active in fluid transport. The fracture at 417 mbsf, or others in the lower interval of this hole, is filled or closed and apparently does not transmit fluids.

In the lower 250 m of the hole, only these major fractures were observed from preliminary data processing. Smaller and subhorizontal features may appear after additional processing of the BHTV data. Note, however, that the resolution of low-angle features in BHTV images is about 20°, i.e., features dipping between 0° and 20° do not appear significantly different from horizontal ones. In any event, further examination and processing of the BHTV images in the upper interval of the hole will be necessary to produce a complete log. These results may show the severe fracturing and foliated intervals usually observed from the recovered core or indicated from high sonic attenuation and porosity observed from logging results.

SUMMARY AND CONCLUSIONS

A major long-term goal of ODP has been to sample *in-situ* sections of the lower oceanic crust and upper mantle. Prior to

Leg 118, only small amounts of gabbro and peridotite had been cored from anomalous occurrences, chiefly along the Mid-Atlantic Ridge and some continental margins.

At Site 735, we continuously cored a 500.7-m-thick section of gabbro on the wall of the Atlantis II Fracture Zone. Core recovery averaged 87% for the entire hole and exceeded 95% in the lower 350 m. The recovered core provides a unique opportunity to study (1) the petrology and structure of the lower oceanic crust, (2) the nature of magma chamber evolution at a slow-spreading ridge, and (3) the physical properties of layer 3 as determined from downhole and sonic measurements.

Site 735 is located on a shallow platform in about 700 m of water on the east rim of the transform. This platform, about 9 km long in north-south direction and 4 km wide, is one of a series of uplifted blocks that are connected by saddles to form a long, linear ridge parallel to the Atlantis II transform. The entire ridge is elevated from 2 to nearly 6 km relative to the floor of the adjacent transform and from 1 to 4 km relative to the ridge-generated crust lying to the east. The topographic relief along this "transverse ridge" varies considerably, particularly between uplifted blocks, which may be as much as 2 or 3 km higher than the intervening saddles. The uplifted blocks are highly irregular in shape, defined by steep slopes commonly associated with major normal faulting in such terrains, and may represent simple horsts uplifted relative to both the rift valley floor at which the crust originated and the adjacent ocean crust to the east. Such topographic features are found in many fracture zones and are commonly underlain by upper mantle and

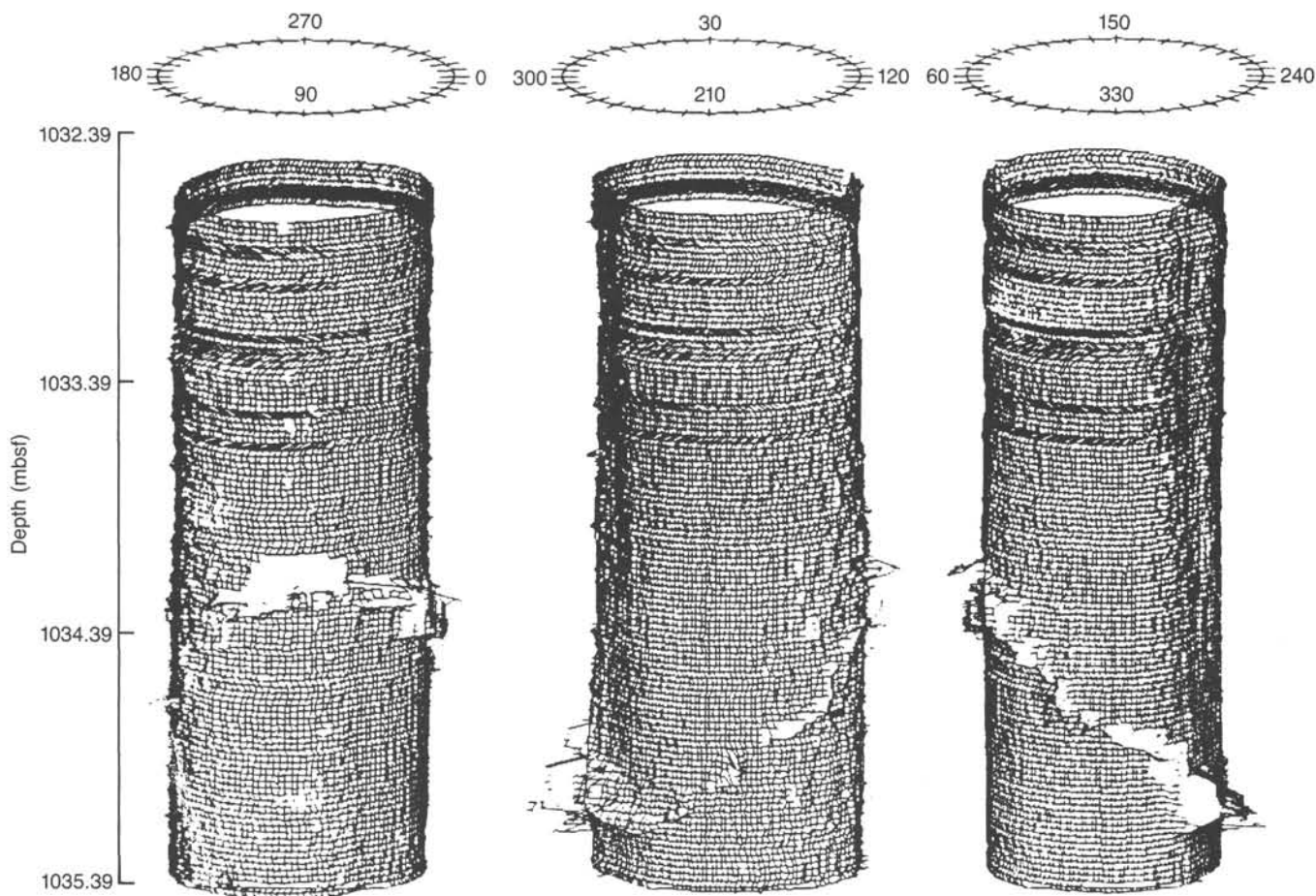


Figure 115. Cylindrical net projections showing the intersection of a dipping fracture at 1034.5 mbrf (302.5 mbsf).

lower crustal rocks (Bonatti, 1978; Engel and Fisher, 1975; van Andel et al., 1971).

The platform at Site 735 has a remarkably flat surface, which suggests that it is a wave-cut feature. Its position in the magnetic anomaly pattern on the east transform wall suggests a crustal age of about 12 Ma. A television/sonar survey conducted before drilling revealed basement outcrops locally mantled with thin layers of sediment. Many of the outcrops have a well-developed, steeply dipping foliation and are cut by a regular pattern of faults or joints.

An unsupported test spud-in, using the turbine coring motor, recovered 0.1 m of gabbro from Hole 735A. Consequently, the hard-rock guidebase was deployed and drilling commenced in Hole 735B. Although this was only the second time that a guidebase had been used, deployment proceeded smoothly and required only two days. Once the guidebase was cemented in place on the seafloor, the coring motor was used to start a hole and to drill to a depth of 60 m. When the hole was deep enough to provide lateral support for the standard rotary coring system, we used it to drill to 500 mbsf. A newly developed navidrill was then tested in the hole and cut another 70 cm. The entire 500.7-m-deep hole was drilled in 17 days, resulting in an average rate of penetration of 30 m/day.

A total of 435 m of igneous and metamorphic rock was recovered from Hole 735B for an average recovery of 87%. However, below about 150 m the recovery averaged 95%, providing a nearly complete section of part of crustal layer 3. The recovered material includes olivine gabbro, olivine-bearing gabbro, two-pyroxene gabbro, iron-titanium oxide gabbro, troctolite, and microgabbro with rare basalt and trondjemite. These rocks

have undergone varying degrees of plastic and brittle deformation and many have well-developed foliations.

Six major lithologic units were recognized in the sequence, based primarily on igneous mineralogy, mineral compositions, and degree and style of deformation.

Lithologic Unit I is a 39.5-m-thick sequence of foliated meta-gabbro with porphyroclastic to mylonitic textures. Rock types include poorly foliated metagabbro, porphyroclastic metagabbro, mylonite, gneissic metagabbro, and augen gneissic metagabbro. Igneous textures have been completely destroyed, and the rocks now consist chiefly of neoblasts of plagioclase, clinopyroxene, and amphibole. Relic porphyroclasts of plagioclase, orthopyroxene, clinopyroxene, iron-titanium oxides, and rare olivine suggest that the protolith was a two-pyroxene gabbro or olivine gabbro. A few iron-titanium oxide-rich layers in this unit are probably secondary because the oxides fill fractures and pore spaces in the gabbros.

Lithologic Unit II consists of 140.5 m of olivine and olivine-bearing gabbro. The upper contact is drawn at the first appearance of clearly igneous textures, and the lower boundary is a rapid transition to gabbro with more orthopyroxene and more sodic plagioclase. Most of the rocks are mesocumulates that commonly have primary layering defined by size variations. Alternating bands of olivine-rich and olivine-poor gabbro reflect rare modal layering. These gabbros consist of plagioclase (40%–70%), clinopyroxene (30%–50%), olivine (0%–25%), and orthopyroxene (0%–3%), along with traces of iron-titanium oxides, primary brown amphibole, and sulfides. Chemically, they are fairly primitive rocks with MgO contents between 9 and 12 wt% and magnesium numbers between 0.78 and 0.85. Inter-

layered iron-titanium oxide-bearing gabbros commonly have igneous textures in which the oxide minerals are closely intergrown with pyroxenes. A few pyroxene-rich layers containing inverted pigeonite were probably formed from significantly more evolved liquids than those from which the olivine gabbros crystallized. Some mylonitic and porphyroclastic intervals are present, particularly in the upper part of the unit.

Lithologic Unit III is a 44-m-thick sequence of olivine gabbro with intervals of iron-titanium oxide gabbro. These gabbros are macroscopically similar to those of Unit II but have significantly more enriched compositions. The upper contact is gradational and is defined by the appearance of sodic plagioclase (An_{40-45}), low-calcium pyroxene, and iron-rich olivine. This contact coincides with a change in chemical composition from olivine gabbro with 12–13 wt% MgO to gabbro with 8–9 wt% MgO. A reappearance of more magnesian olivine gabbro at 211 mbsf coincides with a geochemical break between the upper and lower parts of Unit III. A well-developed igneous lamination is steeply dipping in the upper part of the unit but flattens with depth. Mylonitic and foliated zones are common, and the lower contact of Unit III is marked by a 60-cm-thick zone of mylonite.

Lithologic Unit IV is composed of 48 m of iron-titanium oxide-rich gabbro. The Unit III/Unit IV contact is gradational, and the lower boundary is marked by a 3-m-thick layer of mylonite. These gabbros have more abundant opaque minerals (10% or more) and less olivine than those of Unit III. They consist chiefly of plagioclase, clinopyroxene, and iron-titanium oxide, with minor amounts of olivine, calcium-poor pyroxene, reddish-brown hornblende, apatite, and sulfide. Like those of Unit III, these rocks have relatively sodic plagioclase and iron-rich olivine. The iron-titanium oxide gabbros have granular textures, commonly with cumulus plagioclase and clinopyroxene. Olivine is typically intergranular and the iron-titanium oxides, mostly ilmenite and magnetite, form intergranular to poikilitic masses enclosing plagioclase and clinopyroxene. These rocks have iron oxide contents up to 30 wt% and TiO_2 contents up to 9 wt%. The magnesium numbers of these rocks are the lowest of all samples analyzed from Hole 735B and range from 0.32 to 0.51. On land, these rocks might be investigated as a possible ore deposit. A felsic intrusion breccia having trondjemite veins occurs at two levels in the unit.

Lithologic Unit V consists of 131.5 m of relatively uniform olivine gabbro characterized by a scarcity of iron-titanium oxides and low-calcium pyroxene. Most of the gabbros are mesocumulates, and some exhibit primary grain size layering. They are mineralogically and chemically similar to those of Unit II. Small changes in mineral proportions are shown by the presence of a thin troctolite layer and several plagioclase-rich zones. Zones of brecciation are common and contain felsic veins of epidote and albite.

Lithologic Unit VI is an interval of olivine-rich gabbro having frequent layers and intrusions of troctolite. The gabbros are similar to those of Unit V but have consistently higher modal percentages of olivine. Grain size layering is common, and some lenses and layers of microgabbro occur. The troctolite and troctolitic gabbros are interlayered with the olivine gabbros. Most are fine-grained rocks with granular textures and are interpreted as small intrusive layers. They consist on average of 43% olivine, 53% plagioclase, 3% clinopyroxene, and 1% spinel, with trace amounts of sulfides. These are the most mafic rocks encountered in Hole 735B, with up to 25 wt% MgO and magnesium numbers that range from 0.83 to 0.87. The fine-grained, granular textures indicate a noncumulate origin. These compositions are probably close to the original liquids. A few coarse-grained iron-titanium oxide gabbros are also present; there is an intrusion of orthopyroxene plus oxide plus apatite gabbro near

the upper contact. Unit VI also has frequent intervals of meta-gabbro characterized by mylonitic to porphyroclastic textures.

Contacts between Units I and II and IV and V are clearly tectonic. Undeformed or poorly foliated gabbros are commonly juxtaposed with augen gneissic or mylonitic gabbros and meta-gabbros, which indicates very high strain gradients. The foliated gabbros obviously experienced less total strain than the augen gneissic gabbros, which in turn are less strained than the mylonites. However, the strain was far from linear, and that accommodated by a 10-cm-thick mylonitic band probably was greater than that accommodated by a 100-m-thick section of poorly foliated gabbro.

Veins and fractures generally dip 40° to 90° , with a strong peak at 60° to 65° . Vein dips are skewed toward steep inclinations, and the skewness increases below 90 mbsf, suggesting that the stress field deeper in the hole was rotated with respect to that higher in the hole. The mean dip of both veins and foliation decreases downward in the hole, which suggests that deformation took place along listric normal faults that flatten downward.

The rocks from Hole 735B were subjected to varying degrees of metamorphism and alteration. An early stage of dynamothermal metamorphism produced highly foliated porphyroclastic, gneissic, and mylonitic textures. Highly deformed rocks are most abundant in lithologic Unit I but also occur intermittently elsewhere in the section. This high-temperature event was followed by brecciation and static alteration associated with brittle deformation. The static alteration was controlled by permeability and is manifested by numerous veins (0.5–2 cm wide) filled largely with hornblende and sodic plagioclase. Clinzoisite, epidote, and minor prehnite occur in the lower parts of the core. A few silicic veins containing diopside, hornblende, sphene, clinzoisite, and albite are also present. In undeformed gabbros, static alteration resulted in development of coronas of hornblende, tremolite, talc, clinzoisite, magnetite, chlorite, sphene, epidote, and phlogopite(?) around the primary igneous minerals. A late stage of oxidative alteration is reflected in carbonate plus hematite plus smectite pseudomorphs of olivine and orthopyroxene. These occur sporadically in the upper 256 m of the core and are particularly abundant from 33 to 39 mbsf. Oxidative alteration is also observed in brecciated zones at 180, 275, and 330 mbsf.

Paleomagnetic intensities are variable, generally in the range of other oceanic gabbros but up to > 2.5 emu/cm³ in some of the iron-titanium oxide gabbros. Magnetic susceptibilities average about 100×10^{-6} cgs and are significantly lower than values from gabbros of the Kane Fracture Zone (Fox and Opdyke, 1973). Again, the highest values are in the iron-titanium oxide gabbros. Natural remanent inclinations are all steep and about equally divided between normal and reverse. Stable inclinations are reversed and average $65^\circ \pm 15^\circ$. The theoretical inclination for the site is -52° , so the observed inclinations are somewhat steeper than expected. Logging in the hole shows that it has an average tilt from vertical of about 5° in a north and east direction, so that the inclinations are even more anomalous with respect to the present mean field.

Results of logging and downhole measurements reveal interesting structural and physical properties of the rock penetrated by the hole. Compressional-wave seismic velocities in the gabbros range from 6.5 to 7.0 km/s, both on rock samples and *in situ*, confirming expectations from the low porosities measured (less than a few percent) for relatively high velocities in the bulk rock and that fracture porosity is not significant throughout the section. Physical-properties measurements show seismic anisotropy up to 10%, particularly in some of the foliated rock. A borehole multichannel seismic experiment indicated that *in-situ* seismic velocity increases somewhat (5%–10%) with depth over

the hole. Grain (matrix) densities obtained average about 2.9 g/cm³ over the hole from logs, and the caliper log showed a relatively uniform diameter (± 1 in. or less), generally changing only gradually with depth.

One of the more interesting logs at this site was the laterolog, which showed variations of electrical resistivity of four orders of magnitude downhole (~ 4 to 40,000 ohm-m). The highest values are to be expected from silicate rock of low porosity, but lower values are not generally correlated with higher porosity. The most prominent low-resistivity zone occurs throughout Unit IV and probably results from the high mineral conductivity of the iron-titanium oxides. Smaller-scale variations (a few meters) in the units below may reflect the same conductivity mechanisms.

The borehole televiewer showed that most of the hole wall is relatively smooth, with occasional linear and sinusoidal features, which probably indicate small fractures that cut the borehole. Broader, near-vertical bands of light and dark reflectivity may indicate noncircularity of the borehole cross section, although further processing and analysis may be needed to distinguish the similar effects of a decentralized tool.

Four magnetometer sondes were run in the hole: (1) the Schlumberger three-component tool used primarily for hole inclination and orientation, (2) a USGS three-component magnetometer, (3) a USGS susceptibility tool and a UW/LDGO combined 3-component magnetometer, and (4) a susceptibility tool. The magnetometers showed large and similar variations in the fields measured in the hole, especially in the iron-titanium oxide-rich zone where the fields are up to 50% greater and more variable. Although susceptibility also varies more in this zone, most of the variability is probably due to the remanent component, much of it unstable, as deduced from samples examined in the Paleomagnetism Laboratory aboard ship.

A borehole packer experiment indicated low fluid permeability below about 272 mbsf, with higher values (by several orders of magnitude) above this level. Because of the low porosity, the higher permeability is unlikely to be related to bulk properties of the rock, but probably reflects fracture permeability, at least at a few zones. The temperature log shows a very low or even negative gradient in the hole, further evidence of the effects of seawater advection even with low porosity.

More comprehensive studies of the rock samples recovered and the data obtained will better define the origin, tectonics, and physical state of this unique section of material believed to represent the lower oceanic crust.

REFERENCES

- Anderson, R. N., and Zoback, M. D., 1982. Permeability, underpressures, and convection in the oceanic crust near the Costa Rica Rift, eastern equatorial Pacific. *J. Geophys. Res.*, 87:2860-2868.
- Anderson, R. N., Zoback, M. D., Hickman, S. H., and Newmark, R. L., 1985. Permeability vs. depth in the upper oceanic crust: *in-situ* measurements in DSDP Hole 504B, eastern equatorial Pacific. *J. Geophys. Res.*, 90:3659-3669.
- Atwater, T. M., and Mudie, J. D., 1973. Detailed near-bottom geophysical study of the Gorda Rise. *J. Geophys. Res.*, 78:8665-8686.
- Balch, A. H., and Lee, M. Y., 1984. *Vertical Seismic Profiling: Techniques, Applications, and Case Histories*: Boston (Int. Human Resources Co.).
- Banerjee, S. K., 1984. The magnetic layer of the oceanic crust—how thick is it? *Tectonophysics*, 105:15-27.
- Barton, P. B., Jr., and Skinner, B. J., 1979. Sulfide mineral stabilities. In Barnes, H. L. (Ed.), *Geochemistry of Hydrothermal Ore Deposits, 2nd Ed.*: New York (John Wiley & Sons), 278-403.
- Becker, K., 1986. Drillstring packers in the Ocean Drilling Program. *JOIDES J.*, June 1986.
- Becker, K., Langseth, M. G., and Von Herzen, R. P., 1983a. Deep crustal geothermal measurements, Hole 504B, Deep Sea Drilling Project Legs 69 and 70. In Cann, J. R., Langseth, M. G., Honnorez, J., Von Herzen, R. P., White, S. M., et al., *Init. Repts. DSDP*, 69: Washington (U.S. Govt. Printing Office), 223-235.
- Becker, K., Langseth, M. G., Von Herzen, R. P., and Anderson, R. N., 1983b. Deep crustal geothermal measurements, Hole 504B, Costa Rica Rift. *J. Geophys. Res.*, 88:3447-3457.
- Bloomer, S. H., Natland, J. H., and Fisher, R. L., 1985. Mineralogic studies of gabbros from the Central and Southwest Indian Ridges. *EOS*, 66:405.
- Bonatti, E., 1978. Vertical tectonism in oceanic fracture zones. *Earth Planet. Sci. Lett.*, 37:369-379.
- Bonatti, E., and Hamlyn, P. R., 1978. Mantle uplifted block in the western Indian Ocean. *Science*, 201:249-251.
- Bosum, W., and Scott, J. H., 1988. Interpretation of magnetic logs in basalt, Hole 418A. In Salisbury, M. H., Scott, J. H., et al., *Proc. ODP Sci. Results*, 102: College Station, TX (Ocean Drilling Program), 77-96.
- Boyd, F. R., 1959. Hydrothermal investigations of amphiboles. In Ableson, P. H. (Ed.), *Researchs in Geochemistry*: New York (John Wiley & Sons), 377-396.
- Bratt, S. R., and Purdy, G. M., 1984. Structure and variability of oceanic crust on the flanks of the East Pacific Rise between 11° and 13°N. *J. Geophys. Res.*, 89:6111-6125.
- Bredehoeft, J. D., and Papadopoulos, S. S., 1980. A method for determining the hydraulic properties of tight formations. *Water Resour. Res.*, 16:223-238.
- Bullard, E. C., 1947. The time necessary for a borehole to attain temperature equilibrium. *R. Astron. Soc. Geophys. Suppl.*, 5:127-130.
- Christensen, N. I., 1982. Seismic velocities. In Carmichael, R. S. (Ed.), *Handbook of Physical Properties of Rocks*, Vol. II: Boca Raton, FL (CRC Press), 1-228.
- Clark, S. P. (Ed.), 1966. *Handbook of Physical Constants*. Geol. Soc. Am. Mem., 97:1-587.
- Cooper, H. H., Bredehoeft, J. D., and Papadopoulos, S. S., 1967. Response of a finite-diameter well to an instantaneous charge of water. *Water Resour. Res.*, 3:263-269.
- Cormier, M. H., Detrick, R. S., and Purdy, G. M., 1984. Anomalous thin crust in oceanic fracture zones: new constraints from the Kane Fracture Zone. *J. Geophys. Res.*, 89:10249-10266.
- Crampin, S., 1981. A review of wave motion in anisotropic and cracked elastic media. *Wave Motion*, 3:343-391.
- Detrick, R. S., and Purdy, G. M., 1980. The crustal structure of the Kane Fracture Zone from seismic refraction studies. *J. Geophys. Res.*, 85:3759-3778.
- Duennebieber, F. K., Lienert, B., Cessaro, R., Anderson, P., and Mallick, S., 1987. Controlled-source seismic experiment at Hole 581C. In Duennebieber, F. K., Stephen, R. A., Gettrust, J. F., et al., *Init. Repts. DSDP*, 88: Washington (U.S. Govt. Printing Office), 105-125.
- Engel, C. G., and Fisher, R. L., 1975. Granitic to ultramafic rock complexes of the Indian Ocean Ridge system, western Indian Ocean. *Geol. Soc. Am. Bull.*, 86:1553-1578.
- Fox, P. J., and Opdyke, N. D., 1973. Geology of the oceanic crust: magnetic properties of oceanic rocks. *J. Geophys. Res.*, 78:5139-5154.
- Fox, P. J., and Stroup, J., 1981. The plutonic foundation of the oceanic crust. In Emiliani, C. (Ed.), *The Sea: The Oceanic Lithosphere*: New York (John Wiley & Sons), 119-218.
- Gal'perin, E. I., 1974. *Vertical Seismic Profiling*: Tulsa (Soc. Explor. Geophys.) Spec. Publ. 12, 1-270.
- Gilbert, M. C., Helz, R. T., Popp, R. K., and Spear, F. S., 1982. Experimental studies of amphibole stability. In Veblen, D. R., and Ribbe, P. H. (Eds.), *Amphiboles: Petrology and Experimental Phase Relations*. *Rev. Mineral.*, 9B:229-353.
- Hardage, B. A., 1983. *Vertical Seismic Profiling, Part A: Principles*: London (Geophysical Press), 1-450.
- Harrison, C.G.A., 1981. Magnetism of the oceanic crust. In Emiliani, C. (Ed.), *The Sea: The Oceanic Lithosphere*: New York (John Wiley & Sons), 219-239.
- Hickman, S. H., Langseth, M. G., and Svitek, J. F., 1984. *In-situ* permeability and pore-pressure measurements near the Mid-Atlantic Ridge, Deep Sea Drilling Project Hole 395A. In Hyndman, R. D., Salisbury, M. H., et al., *Init. Repts. DSDP*, 78 (Pt. B): Washington (U.S. Govt. Printing Office), 699-708.
- Holloway, J. R., 1973. The system pargasite-H₂O-CO₂: A model for melting of a hydrous mineral with a mixed-volatile fluid-I. *Geochim. Cosmochim. Acta*, 37:651-666.

- International Geomagnetic Reference Field, 1980: Scotland (Inst. of Geol. Sci.).
- Jacobson, R. S., Adair, R., Orcutt, J., 1984. Preliminary seismic refraction results using a borehole seismometer in Deep Sea Drilling Project Hole 395A. In Hyndman, R. D., Salisbury, M. H., et al., *Init. Repts. DSDP*, 78 (Pt. B): Washington (U.S. Govt. Printing Office), 783-792.
- Jaeger, J. C., 1956. Conduction of heat in an infinite region bounded internally by a circular cylinder of a perfect conductor. *Aust. J. Phys.*, 9: 167-169.
- Johnson, H. P., 1979. Magnetization of the oceanic crust. *Rev. Geophys. Space Phys.*, 17:215-226.
- Johnson, G. R., and Olhoeft, G. R., 1984. Density of rock and minerals. In Chalmers, R. S. (Ed.), *Handbook of Physical Properties of Rocks*, Vol. VIII: Boca Raton, FL (CRC Press), 1-38.
- Kempton, P. D. 1985. An interpretation of contrasting nucleation and growth histories from the petrographic analysis of pillow and dike chilled margins, Hole 504B, Deep Sea Drilling Project, Leg 83. In Anderson, R. N., Honnorez, J., Becker, K., et al., *Init. Repts. DSDP*, 83: Washington (U.S. Govt. Printing Office), 165-181.
- Kent, D. V., Honnorez, B. M., Opdyke, N. D., and Fox, P. J., 1978. Magnetic properties of dredged oceanic gabbros and the source of marine magnetic anomalies. *Geophys. J. R. Astron. Soc.*, 55:513-537.
- Kimball, C. V., and Marzetta, T. L., 1984. Semblance processing of borehole acoustic array data. *Geophysics*, 49:274-281.
- Kirby, S. H., and Kronenberg, A. K., 1987. Rheology of the lithosphere: selected topics. *Rev. Geophys.*, 25:1219-1244.
- Klitgord, K. D., Huestis, S. P., Mudie, J. D., and Parker, R. L., 1975. An analysis of near-bottom magnetic anomalies, seafloor spreading and the magnetized layer. *Geophys. J. R. Astron. Soc.*, 43:387-424.
- LaTraille, S. L., 1983. Archiving and exchange of a computerized marine seismic database: the ROSE data archive system. *Hawaii Inst. Geophys. Data Rept.*, 43:1-65.
- Levi, S., 1979. Paleomagnetism and some magnetic properties of basalts from the Bermuda triangle. In Donnelly, T., Francheteau, J., Bryan, W., Robinson, P., et al., *Init. Repts. DSDP*, 51, 52, 53 (Pt. 2): Washington (U.S. Govt. Printing Office), 1363-1378.
- Liou, J. G., Maruyama, S., and Cho, M., 1985. Phase equilibria and mineral parageneses of metabasites in low-grade metamorphism. *Mineral. Mag.*, 49:321-333.
- Little, S. A., and Stephen, R. A., 1985. Costa Rica borehole seismic experiment, Deep Sea Drilling Project Hole 504B, Leg 92. In Anderson, R. N., Honnorez, J., Becker, K., et al., *Init. Repts. DSDP*, 83: Washington (U.S. Govt. Printing Office), 517-528.
- Macdonald, K. C., 1977. Near-bottom magnetic anomalies, asymmetric spreading, oblique spreading and tectonic of the Mid-Atlantic Ridge near lat. 37°N. *Geol. Soc. Am. Bull.*, 88:541-555.
- MacKenzie, W. S., Donaldson, C. H., and Guilford, C., 1982. *Atlas of Igneous Rocks and Their Textures*: New York (John Wiley & Sons), 1-148.
- Mathez, E., and Yeats, R., 1976. Magmatic sulfides in basalt glass from DSDP Hole 319A and Site 320, Nazca Plate. In Yeats, R., Hart, S., et al., *Init. Repts. DSDP*, 34: Washington (U.S. Govt. Printing Office), 363-374.
- Matthews, C. S., and Russell, D. G., 1967. *Pressure Build-up and Flow Tests in Wells*: Dallas (Soc. Pet. Eng., AIME), Mono. 1.
- McFaddin, P. L., and Reid, A. B., 1982. Analysis of paleomagnetic inclination data. *Geophys. J. R. Astron. Soc.*, 69:307-319.
- Merrill, R. T., and McElhinny, M. W., 1983. *The Earth's Magnetic Field*: London (Academic Press), 20-23.
- Meyer, P. S., Dick, H.J.B., and Thompson, G., in press. Cumulate gabbros from the Southwest Indian Ridge 54°S, 7°E. *Contrib. Mineral. Petrol.*
- Miyashiro, A., 1973. *Metamorphism and Metamorphic Belts*: London (George Allen & Unwin).
- Mons, R., and Barbour, K., 1981. Vertical seismic profiling. *Schlumberger Wireline Atlantic-Marketing Geophys.*, SMP-1108.
- Neuzil, C. E., 1982. On conducting the modified "slug" test in tight formations. *Water Resour. Res.*, 18:439-441.
- O'Connell, R. J., and Budianski, B. 1974. Seismic velocities in dry and saturated cracked solids. *J. Geophys. Res.*, 79:5412-5426.
- ODP Wireline Logging Manual, 2nd Ed.: Palisades, NY (Lamont-Doherty Geol. Observatory).
- Papadopoulos, S. S., Bredehoeft, J. D., and Cooper, H. H., 1973. On the analysis of "slug test" data. *Water Resour. Res.*, 9:1087-1089.
- Pariso, J. E., and Johnson, H. P., in press. Magnetic properties of an analog of the lower oceanic crust: magnetic logging and paleomagnetic measurements from drillhole CY-4 in the Troodos Ophiolite. *Init. Repts. Cyprus Crustal Study Project, Hole CY-4*.
- Ponomarev, V. N., and Nechoroshkov, V. L., 1983. First measurements of the magnetic field within the ocean crust: Deep Sea Drilling Project Legs 68 and 69. In Cann, J. R., Langseth, M. G., Honnorez, J., Von Herzen, R. P., White, S. M., et al., *Init. Repts. DSDP*, 69: Washington (U.S. Govt. Printing Office), 271-279.
- _____, 1984. Downhole magnetic measurements in oceanic crustal Hole 395A on the Mid-Atlantic Ridge. In Hyndman, R. D., Salisbury, M. H., et al., *Init. Repts. DSDP*, 78 (Pt. B): Washington (U.S. Govt. Printing Office), 731-739.
- Scott, J. H., and Olson, G. G., 1985. A three-component borehole magnetometer probe for mineral investigations and geologic research. *Trans., SPWLA 26th Annu. Logging Symp.*, June 17-20, 1985, Pap. E:E1-E16.
- Scott, J. H., Seeley, R. L., and Barth, J. J., 1981. A magnetic susceptibility well-logging system for mineral exploration. *Trans., SPWLA 22nd Annu. Logging Symp.*, June 23-26, 1981, Pap. CC:CC1-CC21.
- Serra, O., 1985. *Fundamentals of Well-Log Interpretation*, Vol. 1 (2nd Ed.): New York (Elsevier).
- Schouten, M., and Klitgord, K. D., 1982. The memory of the accreting plate boundary and the continuity of fracture zones. *Earth Planet. Sci. Lett.*, 59:255-266.
- Shearer, P. M., Orcutt, J. A., Jordon, T. H., Whitmarsh, R. B., Kim, I. I., Adair, R. G., and Burnett, M. S., 1987. The Ngendei seismic refraction experiment at Deep Sea Drilling Project Hole 595B—ocean bottom seismometer data and evidence for crustal and upper mantle anisotropy. In Menard, H. W., Natland, J. H., Jordon, T. H., Orcutt, J. A., et al., *Init. Repts. DSDP*, 91: Washington (U.S. Govt. Printing Office), 385-435.
- Shipboard Scientific Party, 1986. Site 418: Bermuda Rise. In Salisbury, M. H., Scott, J. H., et al., *Proc. ODP, Init. Repts.*, 102: College Station, TX (Ocean Drilling Program), 95-149.
- _____, 1987. Site 642: Norwegian Sea. In Eldholm, O., Thiede, J., et al., *Proc. ODP, Init. Repts.*, 104: College Station, TX (Ocean Drilling Program), 198-209.
- _____, 1988a. Site 504: Costa Rica Rift. In Becker, K., Sakai, H., et al., *Proc. ODP, Init. Repts.*, 111: College Station, TX (Ocean Drilling Program), 124-136.
- _____, 1988b. Site 395. In Bryan, W. B., Juteau, T., et al., *Proc. ODP, Init. Repts.*, 109: College Station, TX (Ocean Drilling Program), 175-202.
- Sinha, M. C., and Loudon, K. E., 1983. The Oceanographer Fracture Zone, 1, crustal structure from seismic refraction studies. *Geophys. J. R. Astron. Soc.*, 75:713-737.
- Smith, G. M., and Banerjee, S. K., 1986. The magnetic structure of the upper kilometer of the marine crust. *J. Geophys. Res.*, 91:10337-10354.
- Spear, F. S., 1980. NaSi-CaAl exchange equilibrium between plagioclase and amphibole, an empirical model. *Contrib. Mineral. Petrol.*, 72: 33-41.
- _____, 1981. An experimental study of hornblende stability and compositional variability in amphibole. *Am. J. Sci.*, 281:697-734.
- Spudich, P., and Orcutt, J., 1980. A new look at the seismic velocity structure of the oceanic crust. *Rev. Geophys. Space Physics*, 18:627-645.
- Stephen, R. A., 1979. The oblique seismic experiment in oceanic crust: experiment and technique. *Mar. Geophys. Res.*, 4:213-226.
- _____, 1983. The oblique seismic experiment on Deep Sea Drilling Project Leg 70. In Cann, J. R., Langseth, M. G., Honnorez, J., Von Herzen, R. P., White, S. M., et al., *Init. Repts. DSDP*, 69: Washington (U.S. Govt. Printing Office), 301-308.
- Stephen, R. A., Johnson, S., and Lewis, B.T.R., 1983. The oblique seismic experiment on Deep Sea Drilling Project Leg 65. In Lewis, B.T.R., Robinson, P., et al., *Init. Repts. DSDP*, 65: Washington (U.S. Govt. Printing Office), 319-327.

- Swift, B. A., and Johnson, H. P., 1984. Magnetic properties of the Bay of Islands ophiolite suite and implications for the magnetization of oceanic crust. *J. Geophys. Res.*, 89:3291-3308.
- Tiezzi, L. J., and Scott, R. B., 1980. Crystal fractionation in a cumulate gabbro, Mid-Atlantic Ridge, 26°N. *J. Geophys. Res.*, 85:5438-5454.
- van Andel, T. H., Von Herzen, R. P., and Phillips, J. D., 1971. The Vema fracture zone and the tectonics of transverse shear zones in oceanic crustal plates. *Mar. Geophys. Res.*, 1:261-283.
- Vacquier, V., 1985. The measurement of thermal conductivity of solids with a transient linear heat source on the plane surface of a poorly conducting body. *Earth Planet. Sci. Lett.*, 74:275-279.
- Von Herzen, R. P., and Maxwell, A. E., 1959. The measurement of the thermal conductivity of deep-sea sediments by a needle probe method. *J. Geophys. Res.*, 64:1557-1563.
- Vine, F. J., and Matthews, D. H., 1963. Magnetic anomalies over ocean ridges. *Nature*, 199:947-949.
- Wager, L. R., Brown, G. M., and Wadsworth, W. J., 1960. Types of igneous cumulates. *J. Petrol.*, 1:73-85.
- White, R. S., 1984. Atlantic oceanic crust: seismic structure of a slow-spreading ridge. In Gass, I. G., Lippard, S. J., and Shelton, A. W. (Eds.), *Ophiolites and Oceanic Lithosphere*: Oxford (Blackwell), 101-111.

Ms 118A-107

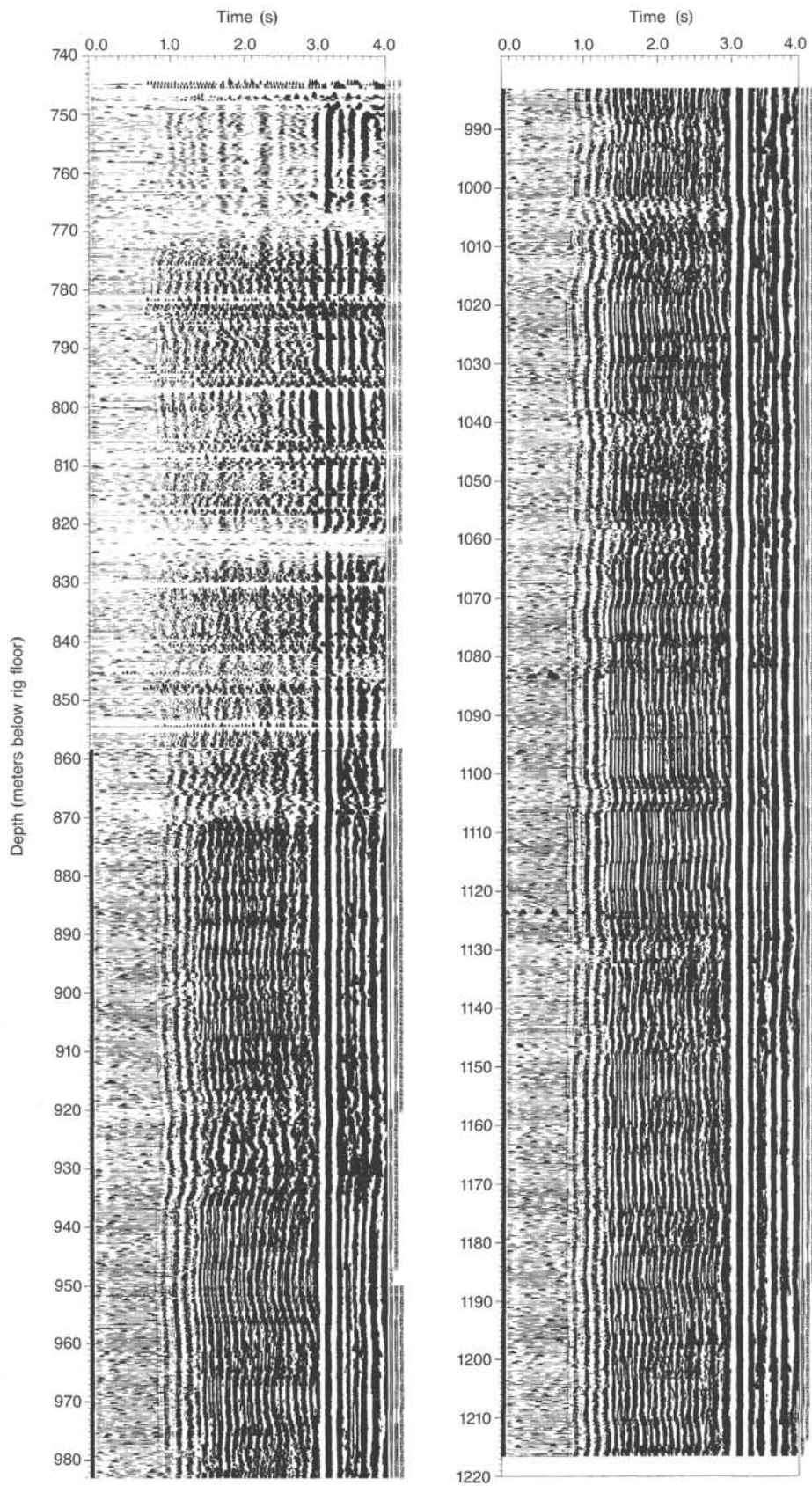
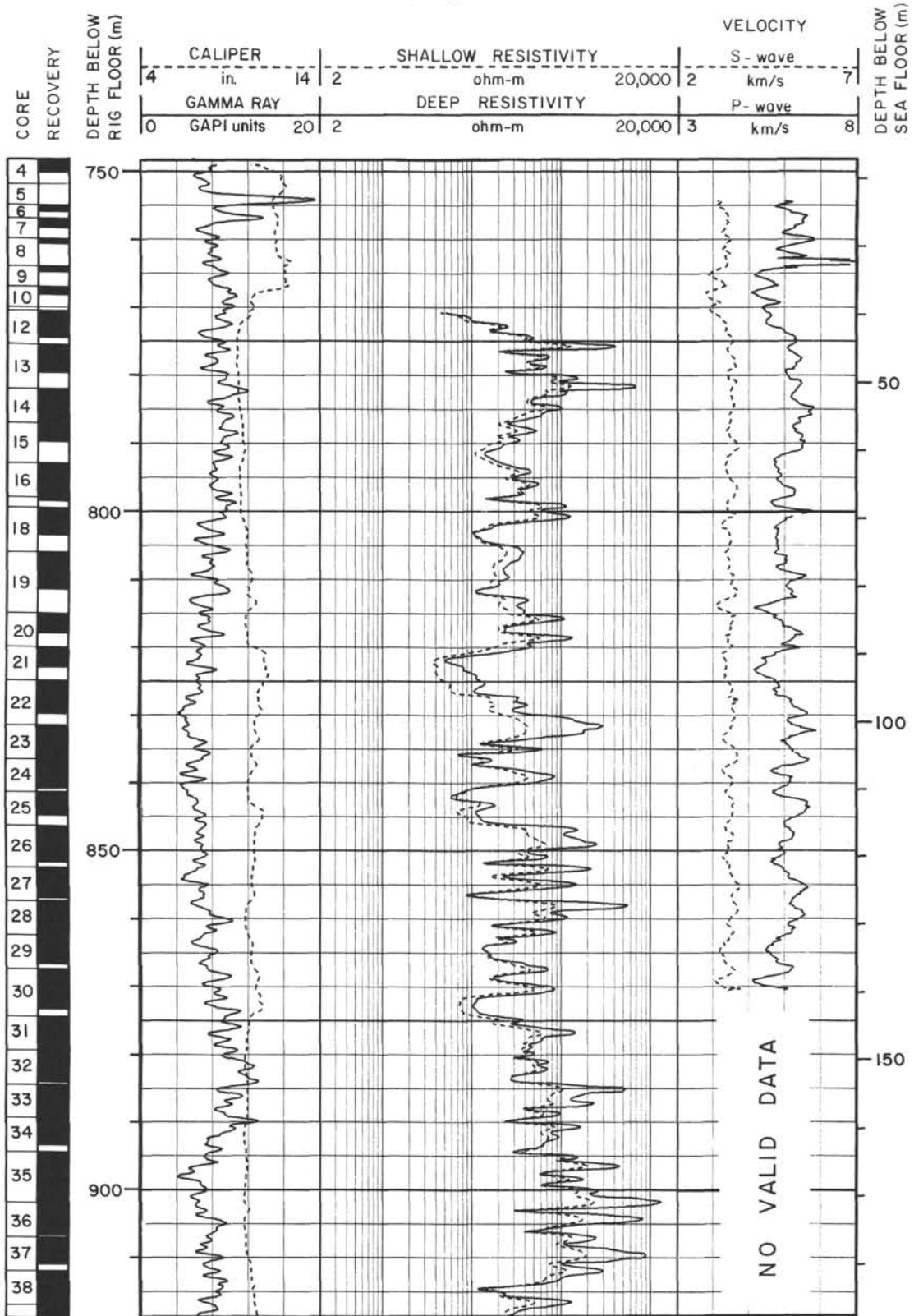
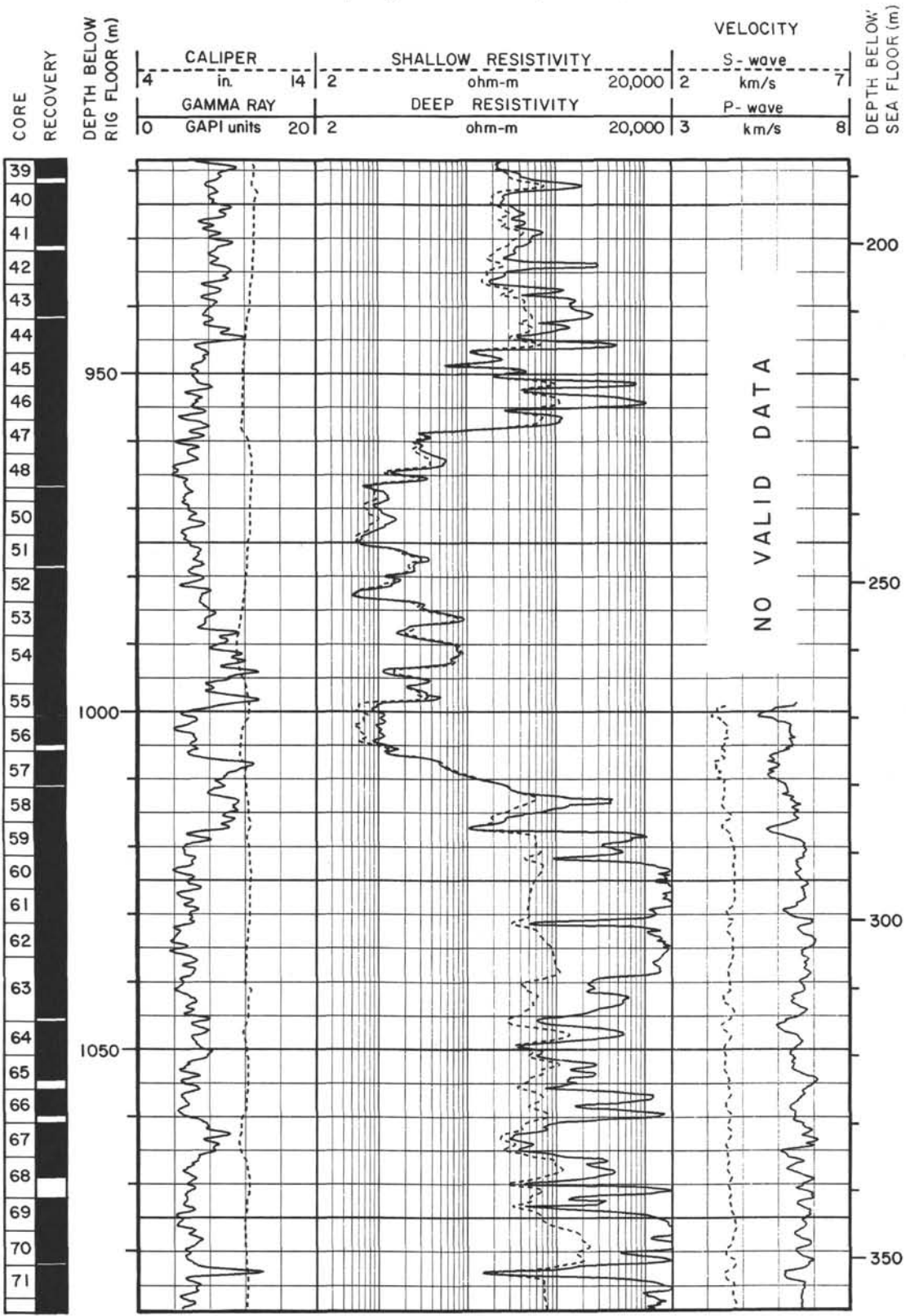


Plate 1. Variable density plot of receiver 6 (4.57 m offset) waveforms from 745.0 to 1216.6 mbrf (13.0–484.6 mbsf). Waveforms from receiver 12 are shown for the upper 100-m interval to provide consistent source-receiver offset for the plot. This interval also is plotted at a scale of 5X.

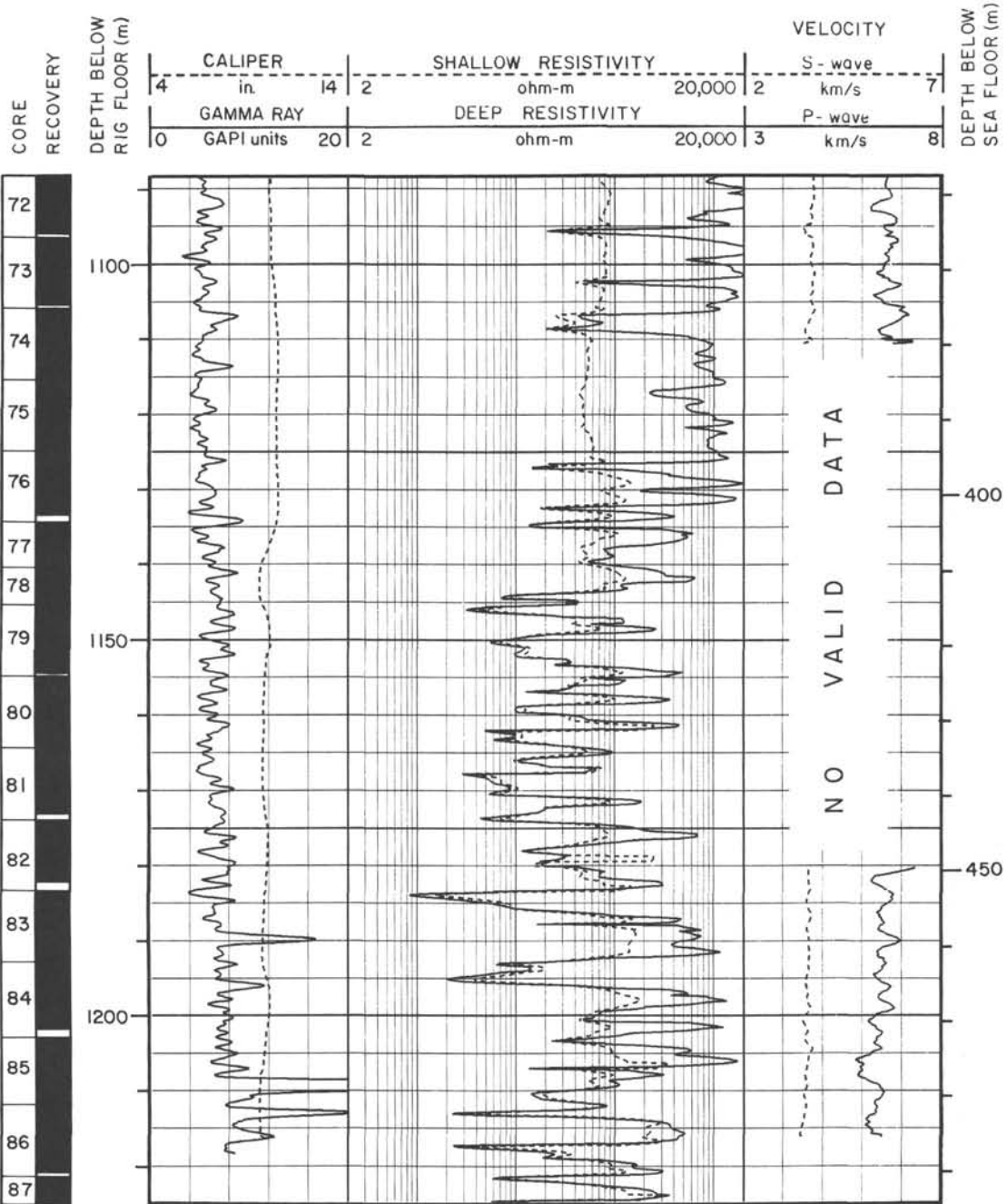
Summary Log for Hole 735B



Summary Log for Hole 735B (continued)

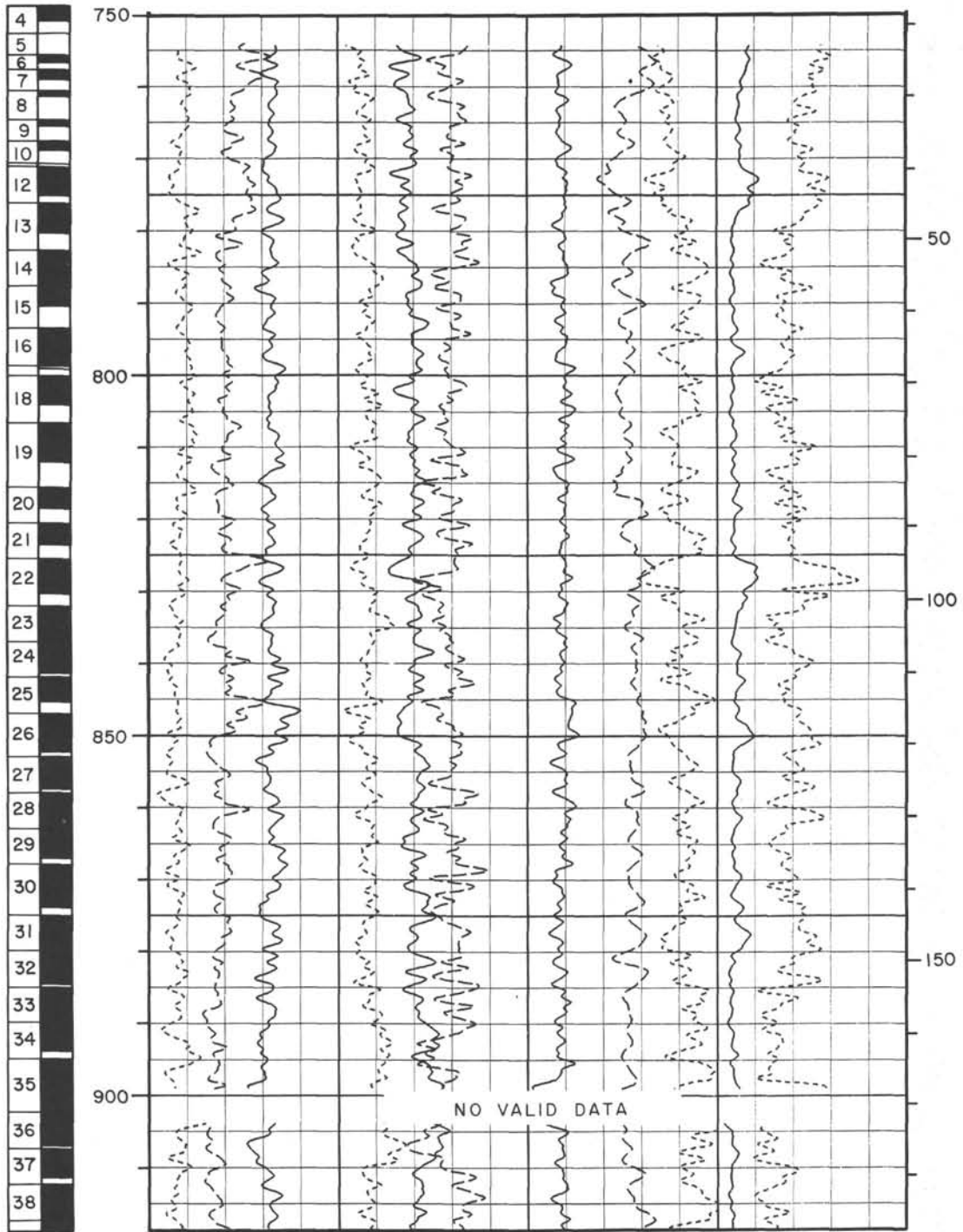


Summary Log for Hole 735B (continued)



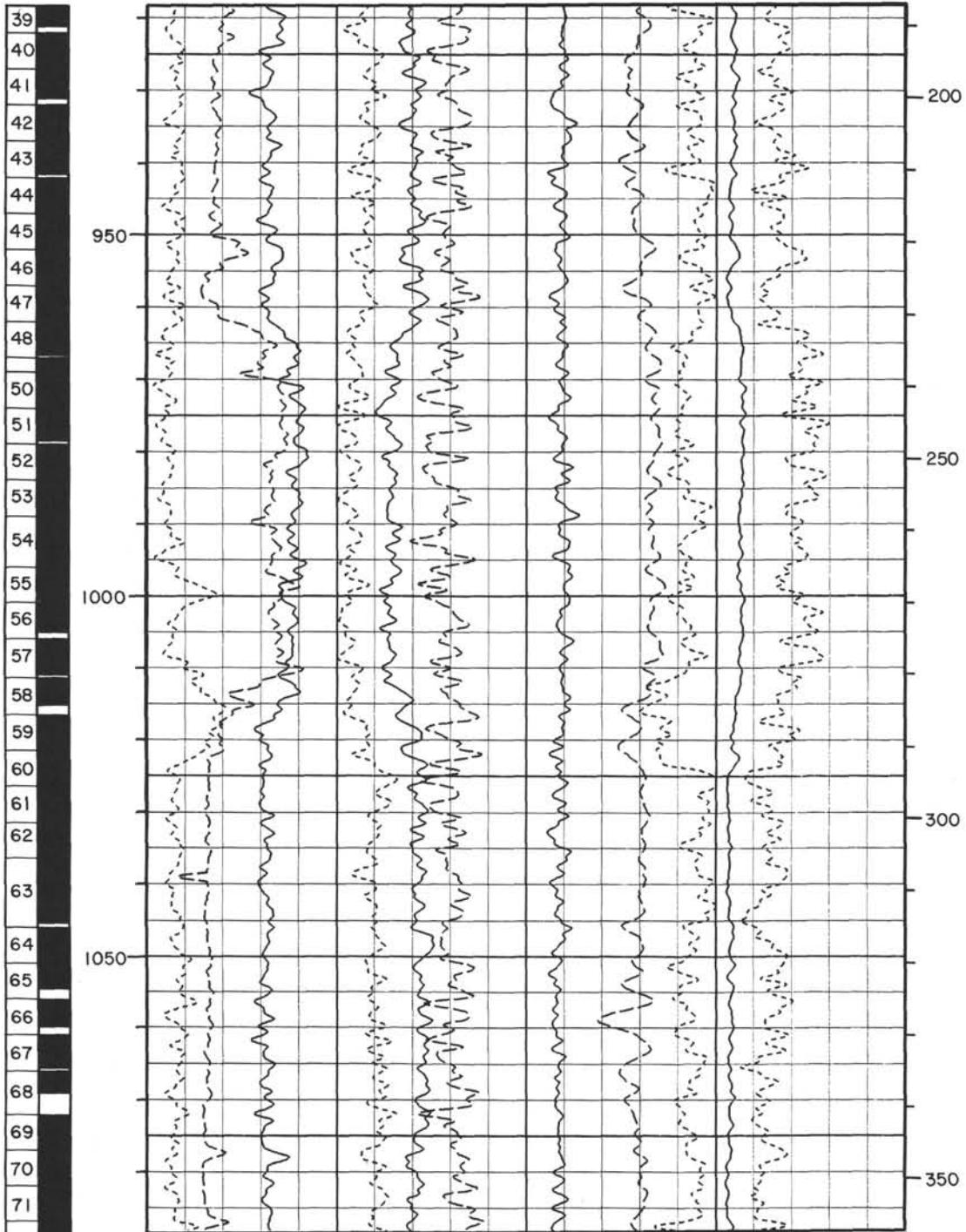
Summary Log for Hole 735B (continued)

CORE RECOVERY	DEPTH BELOW RIG FLOOR (m)	CAPTURE		POTASSIUM	YIELD	ALUMINUM	DEPTH BELOW SEA FLOOR (m)				
		CROSS SECTION	50	-0.3	0.2	20		wet weight %	0		
		GADOLINIUM YIELD	0	0.5	0	0.5		0	0.3	0	0.5
		TITANIUM YIELD	-0.3	0.2	-0.1	0.4		-0.1	0.4	0.05	0.55



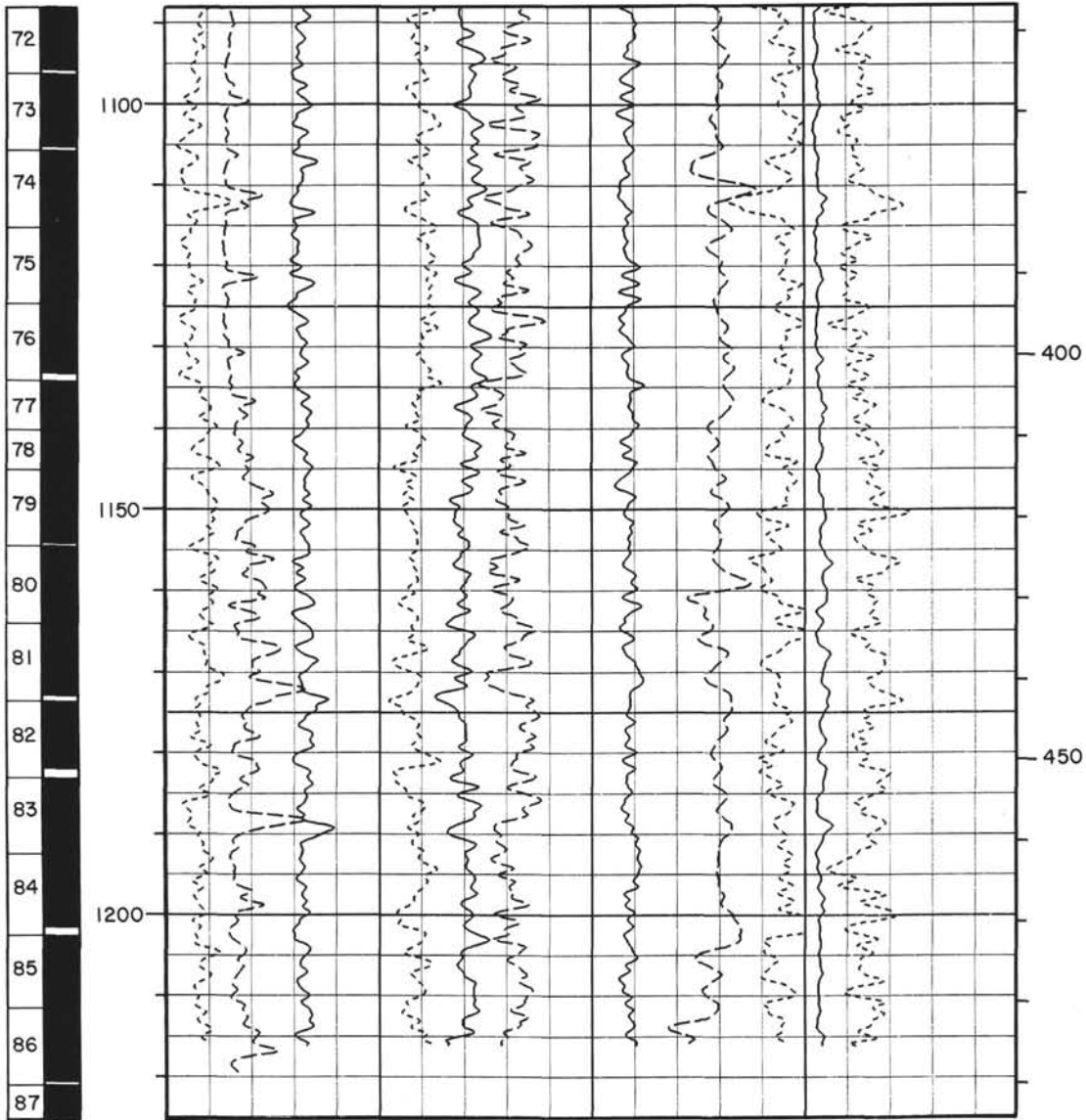
Summary Log for Hole 735B (continued)

CORE RECOVERY	CAPTURE CROSS SECTION															
	0 capture units 50				POTASSIUM YIELD 0.3				ALUMINUM 0.2 wet weight % 0							
	GADOLINIUM YIELD 0.5				CALCIUM YIELD 0.5				IRON YIELD 0.3				CHLORINE YIELD 0.5			
	TITANIUM YIELD 0.3				SILICON YIELD 0.2-0.1				SULFUR YIELD 0.4				HYDROGEN YIELD 0.05 0.55			
DEPTH BELOW RIG FLOOR (m)													DEPTH BELOW SEA FLOOR (m)			

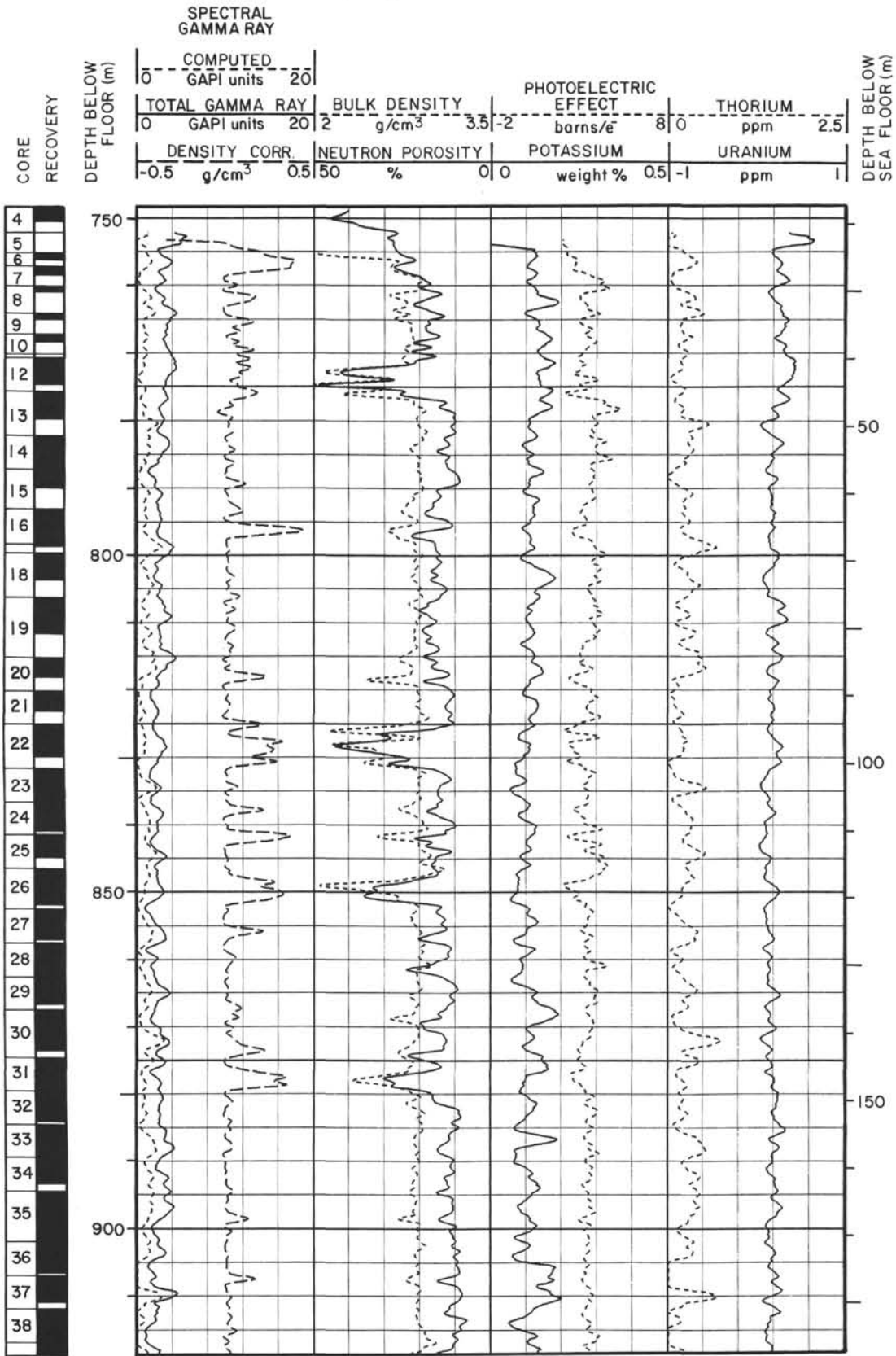


Summary Log for Hole 735B (continued)

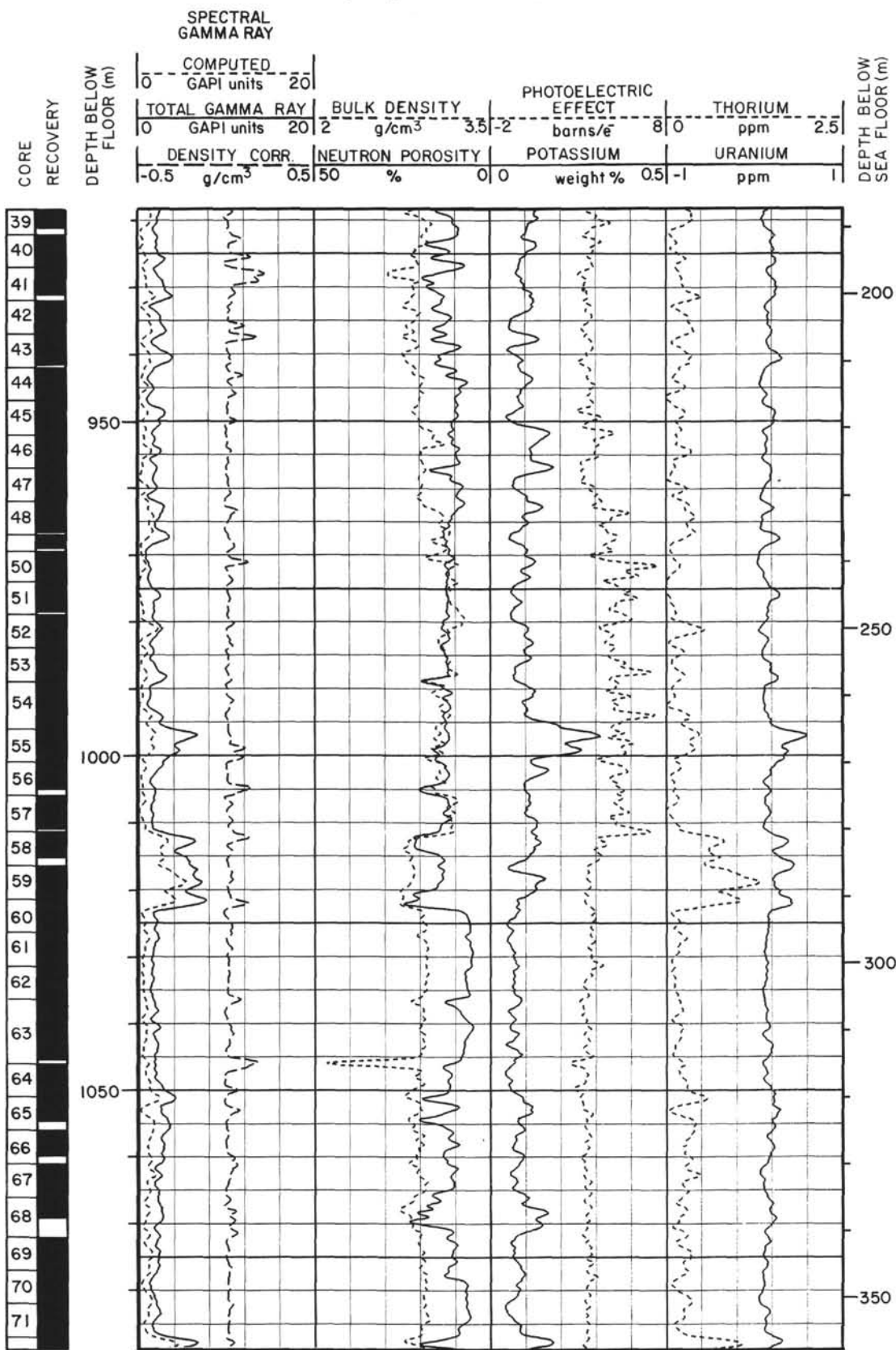
		CAPTURE CROSS SECTION		POTASSIUM YIELD	ALUMINUM				
		0	50	0.3	0.2	20	0		
		capture units		wet weight %					
CORE RECOVERY	DEPTH BELOW RIG FLOOR (m)	GADOLINIUM YIELD		CALCIUM YIELD		IRON YIELD		CHLORINE YIELD	
		0	0.5	0	0.5	0	0.3	0	0.5
		TITANIUM YIELD		SILICON YIELD		SULFUR YIELD		HYDROGEN YIELD	
		-0.3	0.2	-0.1	0.4	-0.1	0.4	0.05	0.55



Summary Log for Hole 735B (continued)



Summary Log for Hole 735B (continued)



Summary Log for Hole 735B (continued)

